THÈSE
de DOCTORAT de l'UNIVERSITÉ PARIS VI

présentée par

Ivica Puljak

pour obtenir le grade de
DOCTEUR de l'UNIVERSITÉ PARIS VI

Spécialité:
Champs, Particules, Matière

Potentiel de découverte du boson de Higgs dans le canal $H \to ZZ^* \to 4e^{\pm}$ avec le détecteur CMS. Contribution à la construction du calorimètre électromagnétique de CMS.

Soutenue le 21 septembre 2000 devant le jury composé de:

M. Pierre Billoir	*président*
M. Claude Charlot	*directeur de thèse*
M. Daniel Denegri	
M. Abdelhak Djouadi	*rapporteur*
M. Ludwik Dobrzynski	
M. Jean-Louis Faure	*rapporteur*
M. Miroslav Furić	

FERMILAB LIBRARY

Thèse préparée au sein du
Laboratoire de Physique Nucléaire des Hautes Energies - Ecole Polytechnique

A Toma, Ema et Marijana
A mes parents

Remerciements

Je voudrais tout d'abord exprimer toute ma gratitude à l'Ambassade de France à Zagreb, au Ministère de la science et de la technologie de la République de Croatie et à l'Institut National de Physique Nucléaire et de Physique des Particules pour avoir financé mon séjour à l'École Polytechnique lors de l'élaboration de ma thèse.
Je désire exprimer ma reconnaissance à Messieurs François Jacquet et Henri Videau, directeurs du Laboratoire de Physique Nucléaire des Hautes Énergie qui m'ont accueilli dans leur laboratoire et ont fait tout pour m'assurer des conditions de travail extraordinaires.
Je remercie tout particulièrement Monsieur Claude Charlot, qui a choisi le sujet de ma thèse et a accepté de me guider dans mon travail. Ses connaissances exceptionnelles, son enthousiasme et son intuition ont été toujours pour moi un stimulant et m'ont donné l'assurance si nécessaire dans ce travail. Merci de tout coeur surtout pour l'aide et la patience au cours des derniers mois de la rédaction de ma thèse. J'ai été très heureux d'avoir pu travailler avec une personne toujours disposée à discuter et à vous offrir son aide, avec quelqu'un qui peut analyser un problème de plusieurs côtés et qui propose sans cesse de nouvelles idées. Mon travail avec Claude restera un de mes plus beaux souvenirs de mon séjour en France.
Je remercie également Monsieur Ludwik Dobrzynski de sa contribution à cette thèse. Il était présent depuis la premier instant lors de mon arrivée au CERN et plus tard à l'École Polytechnique, me montrant son énorme savoir, sa chaleur humaine et sa sagesse, me donnant son appui et m'aidant à persévérer.
J'adresse ma gratitude à Messieurs Abdelhak Djouadi et Jean-Louis Faure pour avoir accepté de juger mon travail, et d'avoir lu, avec beaucoup de patience et d'empressement la première version de ma thèse. Merci pour toutes les correction et suggestions qui ont contribué à l'amélioration de ce travail.
Merci également à tous les autres membres du jury, Messieurs Pierre Billoir, Daniel Denegri et Miroslav Furic. Leur présence était pour moi un grand honneur.
Je remercie tous mes collègues du LPNHE, et en particuliers ceux du groupe CMS, pour leur aide et surtout pour m'avoir fourni une atmosphère de travail stimulante. Ma reconnaissance particulière s'adresse à Messieurs Jean Badier, Alain Debraine et Akli Karar pour leur aide, leur conseils et la chaleur humaine que j'ai pu sentir lors de mes contacts avec eux.
Je voudrais également remercier Messieurs Csaba Balázs, Joey Huston et Slava Ilyin pour notre travail commun et pour la contribution qu'ils ont apportée à cette thèse. Cela a été un plaisir exceptionnel de pouvoir travailler avec eux.
La physique est devenue mon premier amour alors que j'assistais aux cours du professeur Josip Tudoric-Ghemo et de la professeur Jadranka Vuletin, et c'est ici que je voudrais les remercier d'avoir partagé avec moi l'inépuisable richesse de leurs dons pédagogiques et humains. Je remercie également tous les autres membres de la chaire de physique de la FESB - Université de Split, pour leur aide et leur soutien.
Mon séjour en France a été enrichi par de nombreuses amitiés nouvellement acquises. Je souhaite exprimer ici ma gratitude à Geun-Beom Kim, pour son soutien inconditionnel dans toutes les circonstances. C'était un plaisir exceptionnel pour moi de passer trois ans en compagnie d'une personne si riche de dons. Merci à Karim Chine et à Luca Quaglia pour leur amitié et les nombreux moments que nous avons passés ensemble dans une atmosphère des plus agréables.
Les moments passés a l'École Polytechnique resteront toujours dans ma mémoire, surtout grâce à mon équipe de basket. Les matchs et le médailles que nous avons gagnés seront pour moi un souvenir inoubliable de l'atmosphère amicale où je me trouvais si bien en leur compagnie. Je leur adresse tous mes remerciement les plus chaleureux.
Ce doctorat n'aurait jamais vu le jour sans le soutien de ma famille. Il m'est impossible d'exprimer en quelques mots combien je leur suis reconnaissant, aussi je ne le tenterai même pas. Je leur dis simplement: MERCI!

Table des matières

Introduction

Chapitre 1 *Physique du boson de Higgs*

Le boson de Higgs 8
Limites sur la masse du Higgs - expériences 9

Chapitre 2 *LHC et CMS*

LHC - grand collisionneur des hadrons 12
Compact Muon Solenoid - CMS 13
Trajectomètre - conception 14
Calorimètre électromagnétique 15
Calorimètre électromagnétique - résolution. 16

Chapitre 3 *Contribution à la construction du calorimètre électromagnétique*

Structures alvéolaires 18
Contrôle de qualité 19
Contrôle optique - MONICA 20
MONICA - mesure des structures 21
Procédure de contrôle 22
Résultats sur les structures du Module 0 23
Contrôle qualité - conclusion 24

Chapitre 4 *Etude de signal et de bruits de fonds*

Production du Higgs dans LHC (1) 26
Production du Higgs dans LHC (2) 27
Production et désintégration du Higgs 28
Bruit de fond ZZ^*/γ^* et $t\bar{t}$ 29
Bruit de fond $Zb\bar{b}$ 30
Coupures d'analyse 31
Résultats de l'étude au niveau générateur 32

Chapitre 5 *Etude de la reconstruction de $H \rightarrow ZZ^* \rightarrow 4e^{\pm}$*

Problème de bremsstrahlung 34
Reconstruction des traces Reconstruction des agrégats. 35
Méthode de poids 37
Modèle de gerbe 38
Matrice des covariances 39
Méthode de poids - résultats (1). 40
Méthode de poids - résultats (2). 41
Estimateur final d'impulsion 42
Résultats sur la reconstruction du Higgs (1) 43
Résultats sur la reconstruction du Higgs (2) 44

Conclusion

Introduction

La question centrale de la physique des particules actuelle est l'origine des masses des particules ou, en termes de théorie quantique des champs, le mécanisme de brisure de la symétrie électrofaible. Le scénario le plus plausible pour cette brisure de la symétrie électrofaible est le mécanisme dit de Higgs. Il permet de rendre compte des masses des leptons et des bosons vecteurs, et prédit l'existence d'au moins une particule scalaire, le boson de Higgs.

Les recherches directes du boson de Higgs, effectuées auprès des accélérateurs LEP et Tevatron, n'ont pas encore donné de résultats positifs, établissant ainsi pour sa masse une limite basse d'environ 100 GeV. Des arguments théoriques basés sur la cohérence du Modèle Standard et des recherches indirectes donnent une limite supérieure à la masse du boson de Higgs de plusieurs centaines de GeV. La région de masses restantes sera efficacement explorée par un nouvel accélérateur, le Grand Collisionneur de Hadrons (Large Hadron Collider LHC). Sa construction est en cours au Laboratoire Européen pour la Physique des Particules (CERN), près de Genève, et son démarrage est prévu pour 2005. Le détecteur «Solénoïde Compact à Muons» (Compact Muon Solenoid CMS), un des deux détecteurs à vocation généraliste, sera utilisé pour explorer la physique accessible au LHC.

Le sujet de cette thèse est l'étude du potentiel de découverte du boson de Higgs dans le canal $H \rightarrow ZZ^* \rightarrow 4e^{\pm}$. Il est prévu d'utiliser ce canal pour la recherche du Higgs dans la région de masses s'étendant de 120 à 180 GeV environ. Le calorimètre électromagnétique est essentiel pour la détection des électrons. Notre contribution à sa construction est également présentée dans cette thèse.

Au premier chapitre nous donnons un bref survol de la partie du Modèle Standard relative au Higgs, de récentes limites théoriques et expérimentales pour la masse du boson de Higgs, et les grands traits du secteur de Higgs des théories au-delà du Modèle Standard. Nous présentons de manière plus détaillée les calculs théoriques récents qui concernent notre étude : les principaux mécanismes de production du Higgs au LHC et les rapports de branchement du Higgs.

Une brève description du Grand Collisionneur à Hadrons et du détecteur «Solénoïde Compact à Muons» est faite dans le second chapitre. Les principaux sous-systèmes de détection de CMS sont présentés. Les caractéristiques du calorimètre électromagnétique sont plus particulièrement développées, car c'est un des détecteurs les plus importants pour la détection des électrons.

Pour atteindre et conserver les performances spécifiées du calorimètre électromagnétique, il est important de vérifier les caractéristiques de chacun de ses composants. Au chapitre 3 nous décrivons un système pour le contrôle qualité des structures alvéolaires destinées à contenir

les cristaux. Nous insistons sur la description du système de contrôle de la qualité optique, et présentons l'instrument, la procédure développée, ainsi que les résultats obtenus.

Notre étude de la sensibilité de $H \rightarrow ZZ^* \rightarrow 4e^{\pm}$ est exposée au chapitre 4. Cette étude est basée sur une analyse au niveau des particules utilisant les calculs théoriques les plus récents et la dernière version des générateurs Monte Carlo de particules. L'accent est mis sur le moment transverse du Higgs et le bruit de fond en $Zb\bar{b}$, qui sont des aspects importants pour lesquels des études plus approfondies ont été nécessaires. Les caractéristiques cinématiques des événements du signal et du fond, l'optimisation des coupures cinématiques et topologiques ainsi que quelques coupures supplémentaires seront présentées de même que les résultats sur la visibilité attendue du Higgs dans ce canal.

Au chapitre 5 nous étudions les effets de détecteur dans la recherche $H \rightarrow ZZ^* \rightarrow 4e^{\pm}$ à CMS. Les algorithmes récemment proposés pour la reconstruction des électrons sont programmés et utilisés avec une simulation détaillée du détecteur. L'accent est mis sur le bremsstrahlung dans la matière du trajectomètre, le principal problème pour la reconstruction des électrons. Les algorithmes développés pour récupérer les photons de bremsstrahlung sont également présentés. Pour utiliser efficacement ces algorithmes, un estimateur optimisé pour l'énergie des électrons a été nécessaire. Nous avons développé une nouvelle méthode pour cette estimation de l'énergie, basée sur un modèle de gerbe pour prédire la répartition des dépôts d'énergie dans le calorimètre électromagnétique. Comme ultime estimateur de l'impulsion de l'électron, une combinaison de mesures du calorimètre électromagnétique et du trajectomètre est utilisée. Les algorithmes développés sont ensuite appliqués à la reconstruction d'événements Higgs, et les résultats sont comparés à ceux obtenus par l'analyse au niveau des particules.

Chapitre 1

Physique du boson de Higgs

Le boson de Higgs

- Question centrale de physique des particules: **l'origine de masse des particules**
  c.à.d. **le mécanisme de la brisure de symétrie électrofaible**
- Le plus plausible: **le mécanisme du Higgs**
- Il prédit au moins un **boson de Higgs**
- La théorie ne prédit pas la masse du boson de Higgs, mais elle peut la contraindre:

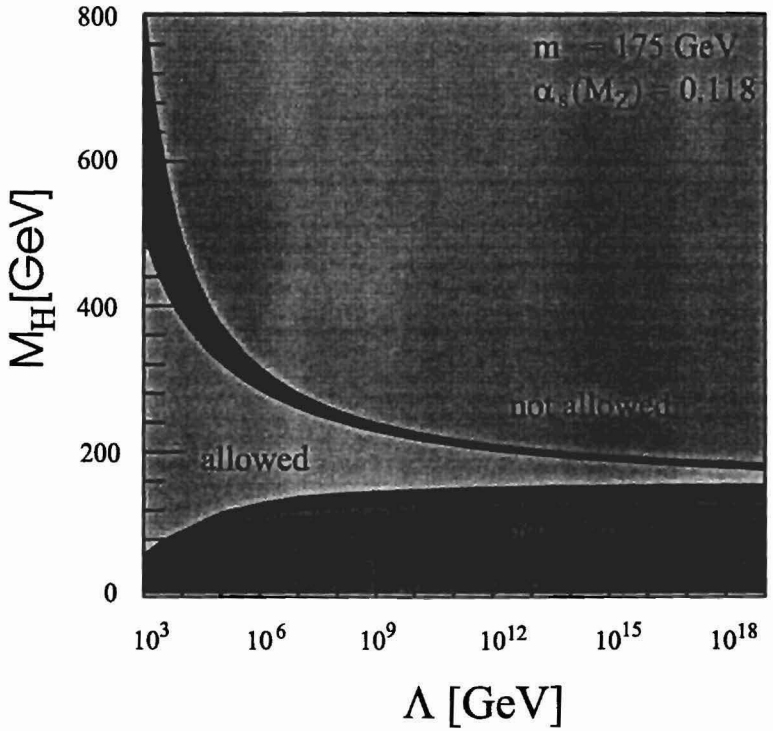

- limites supérieures: trivialité
- limites inférieures: stabilité du vide

Echelle d'énergie à laquelle le Modèle Standard n'est plus valable

Limites sur la masse du Higgs - expériences

- **Recherches indirectes** - mesures de précision électrofaibles

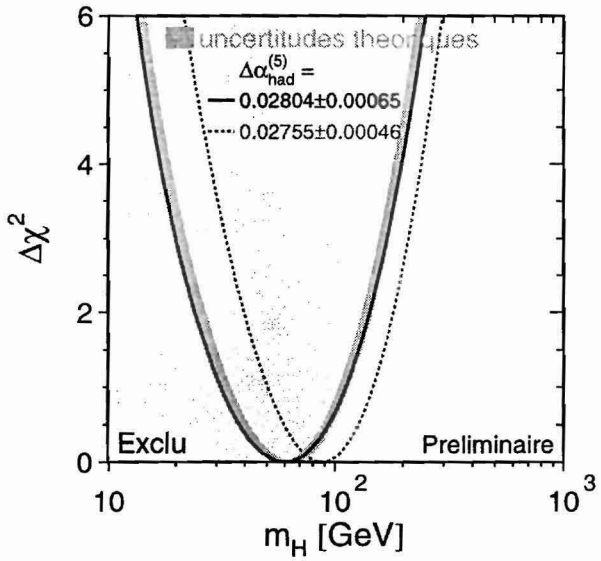

ICHEP (Osaka, août 2000):

$$M_H = 62^{+53}_{-30} \text{ GeV}$$

$$M_H < 170 \text{ GeV dans } 95\% \text{ NC}$$

- Cependant, ces limites sont relativement faibles, à cause des *dépendances logarithmiques* des corrections radiatives sur la masse du Higgs

- **Recherche directe** - les résultats les plus récents proviennent de LEP II
  - les données collectées à $\sqrt{s} \approx 200 - 210$ GeV donnent une limite inférieure de

$$M_H > 112.3 \text{ GeV dans } 95\% \text{ NC},$$

  - très récemment: un surplus d'événement pour $M_H \approx 114$ GeV
  - LEP II est prolongé jusqu'à début novembre 2000

  - Tevatron - découverte du Higgs possible juste quelques mois avant LHC

Chapitre 2

LHC et CMS

LHC - grand collisionneur des hadrons

- LHC produira des collisions:
  - **proton-proton,** avec une énergie dans le centre de masse de **14 TeV**
  - **ions lourds**, avec une énergie supérieure à **1150 TeV**
- ***Programme de physique:***
  mécanisme de BSE - recherche des Higgs, recherche de SUSY, violation CP, tests du Modèle Standard, le plasma de gluons et de quarks etc

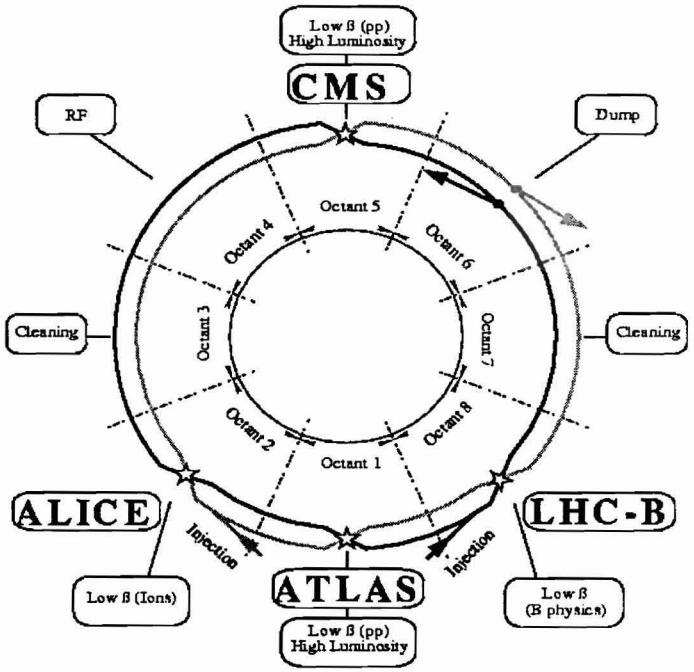

- *quelques paramètres de la machine*
  - nombre de paquets: 2835
  - nombre des particules par paquet: 10^{11}
  - temps de croisement des paquets: 25 ns
  - champ magnétique des dipôles: 8.33 T
  - luminosité nominale (haute): 10^{34} cm^{-2}s^{-1}
  - un an à **haute** luminosité
    $$\int L dt = 10^5 \text{ pb}^{-1} = 100 \text{ fb}^{-1}$$
  - un an à **basse** luminosité
    $$\int L dt = 10^4 \text{ pb}^{-1} = 10 \text{ fb}^{-1}$$

- ***exigences sur la conception de détecteur:***
  - une granularité très fine
  - une réponse très rapide
  - une très bonne résistance aux radiations
  - un système de déclenchement et d'acquisition des données très rapide et très efficace

Compact Muon Solenoid - CMS

:

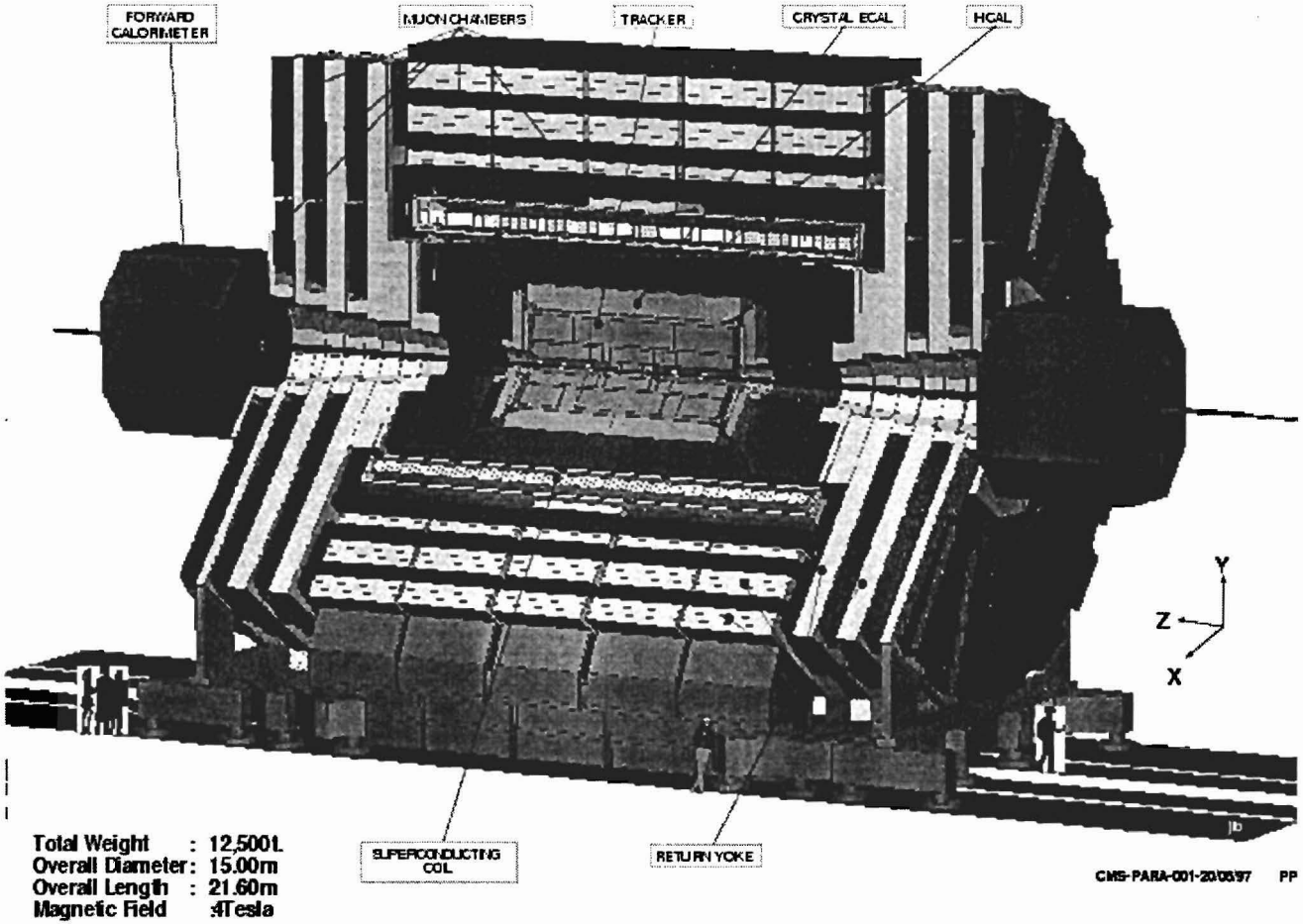

Trajectomètre - conception

- ***objectif***

  Reconstruire les traces isolées de grands p_T avec une efficacité meilleure que 95%, et les traces de grands p_T dans les jets avec une efficacité meilleure que 90% dans la région de pseudorapidité $|\eta| < 2.5$

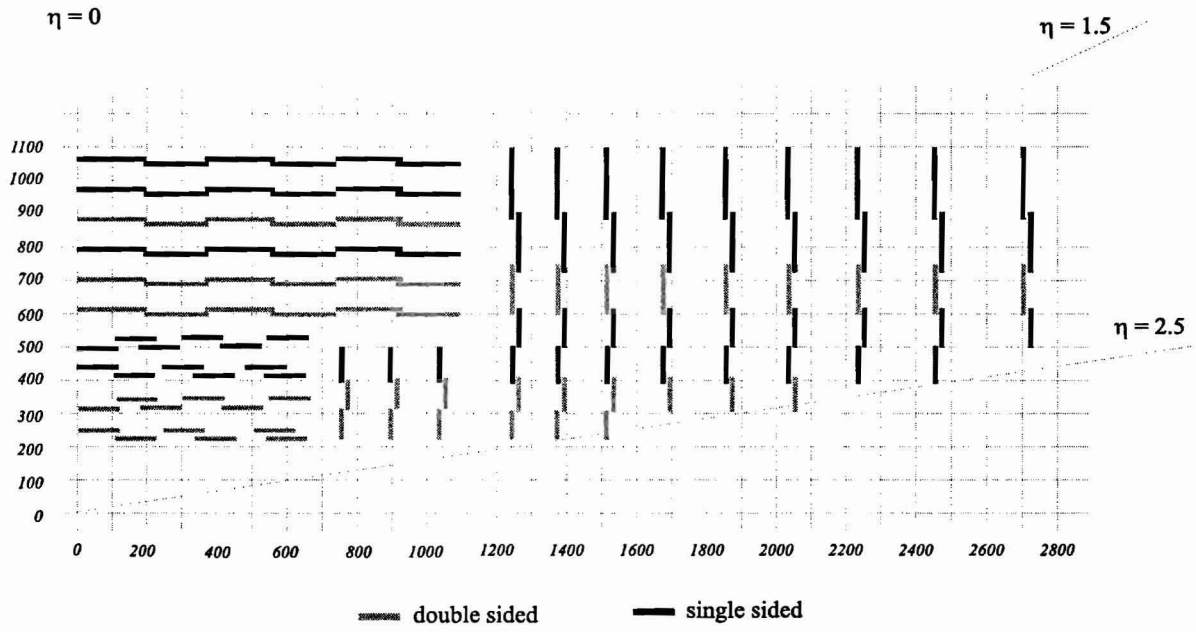

- détecteurs à pixels de silicium près du point d'interaction
- détecteurs à micro-pistes de silicium à plus grands rayons
- ***résolutions attendues***
  - électrons: $(\delta p_T / p_T)^2 \approx (0.15 \cdot p_T)^2 + 0.005^2$, avec p_T en TeV, et pour $|\eta| \leq 1.6$
  - muons: $\delta p / p \approx (4.5 \cdot \sqrt{p})\%$, en combinaison avec des chambres à muons

Calorimètre électromagnétique

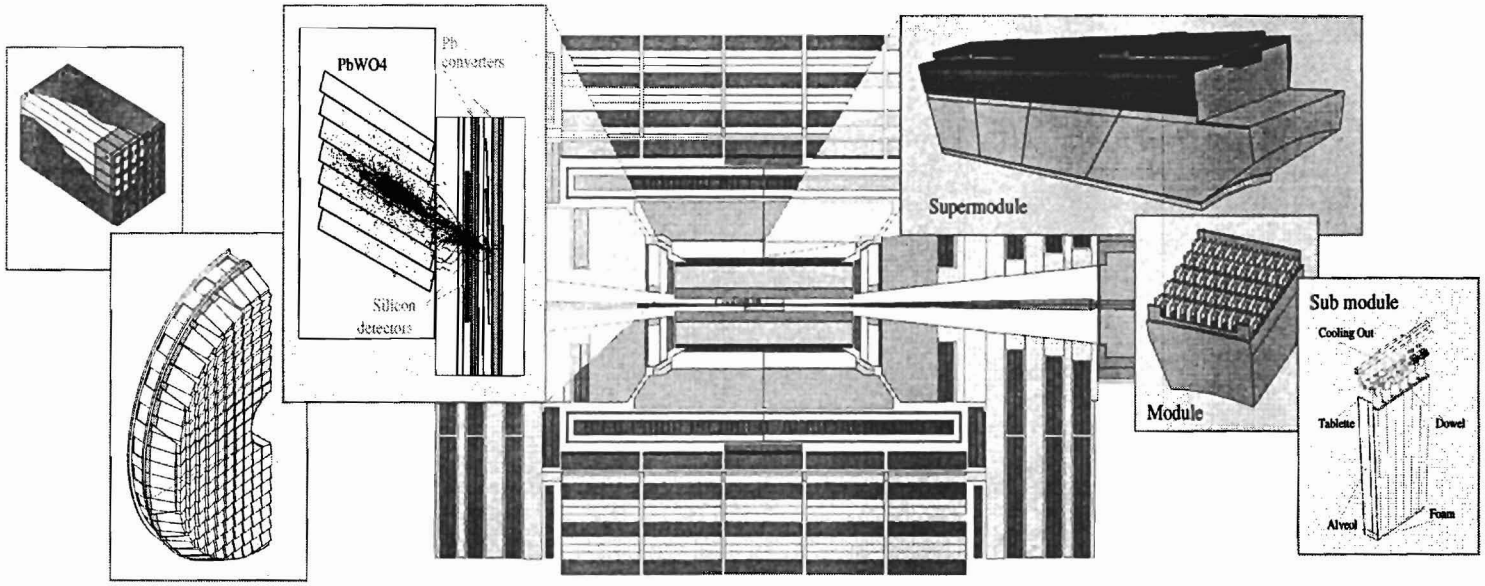

- ***Paramètres principaux:***
  - *Tonneau:*
    - $|\eta| < 1.48$
    - 61 200 cristaux de tungstate de plomb
    - $22 \times 22 \times 230$ mm^3
    - photodétecteur: diodes à avalanche (2 par cristal)
  - *Bouchons:*
    - $1.48 < |\eta| < 3.0$ (2.6)
    - 16 000 cristaux de tungstate de plomb
    - $28.6 \times 28.6 \times 220$ mm^3
    - détecteur de pied de gerbe ($3X_0$)
    - photodétecteur: phototriodes à vide

Calorimètre électromagnétique - résolution

- résolution en énergie:

$$\left(\frac{\sigma}{E}\right)^2 = \left(\frac{a}{\sqrt{E}}\right)^2 + \left(\frac{b}{E}\right)^2 + c^2$$

- ***a - terme stochastique***
  fluct. intrinsèque + photostatistique ($\sim \sqrt{1/N_{tot}}$)
- ***b - terme du bruit***
  électronique + courant du fuite + empilement
- ***c - terme constant***
  non-uniformité longit.+intercalib.+imperfections géom.

- résolution exigée ***(matrice 5x5)***

	Tonneau	Bouchons
a (stoch.)	$2.7\%/\sqrt{E}$	$5.7\%/\sqrt{E}$
c (const.)	0.55%	0.55%
b (bas lumi.)	155 MeV	770 MeV
b (haut lumi.)	210 MeV	915 MeV

- résolution mesurée dans les tests en faisceaux ***(matrice 3x3)***

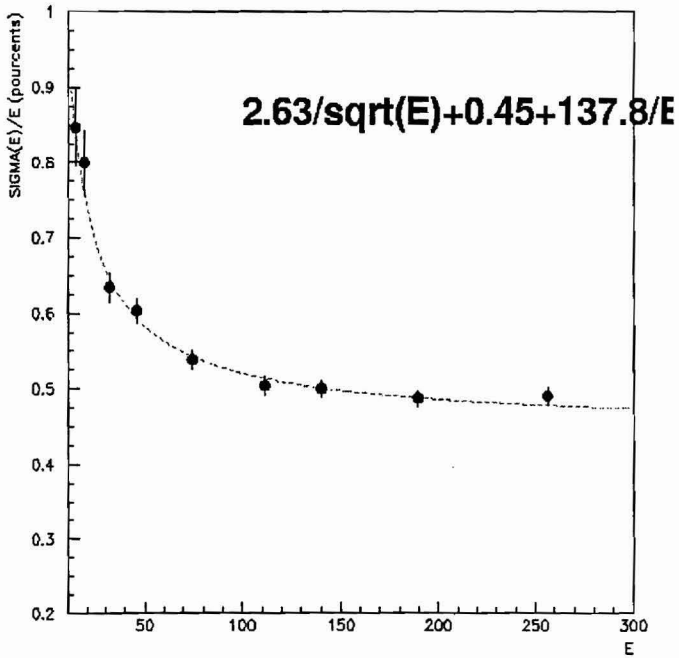

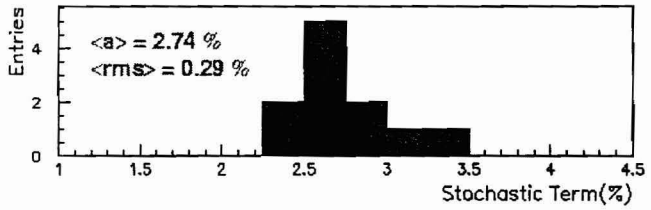

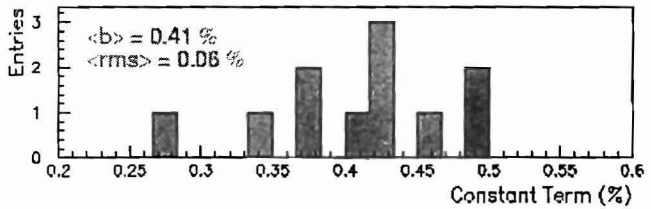

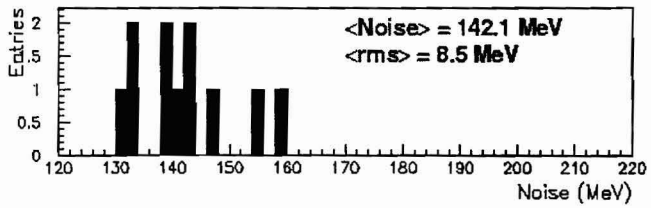

Chapitre 3

Contribution à la construction du calorimètre électromagnétique

Structures alvéolaires

- ***Le choix des structures alvéolaires est basé sur:***
  - *les exigences mécaniques*:
    le poids du cristal ≈ 1 kg, fragilité des cristaux, grand nombre des cristaux ≈ 80000
  - *les exigences physiques:*
    l'espace entre deux cristaux ≤ 0.5 mm, propriétés optiques ne détériorent pas la résolution en énergie
- ***Propriétés optiques*** - deux aspects importants:
  - *lumière totale collectée*
  - *uniformité longitudinale de la collection de lumière*
- ***Les structures alvéolaires sont constituées de deux types de matériaux:***
  - couche extérieure:
    fibre de verre préimprégnée d'époxy,
    75 μm d'épaisseur
  - couche intérieure: *aluminium traité*,
    30 μm d'épaisseur
- ***6120 structures pour le tonneau***

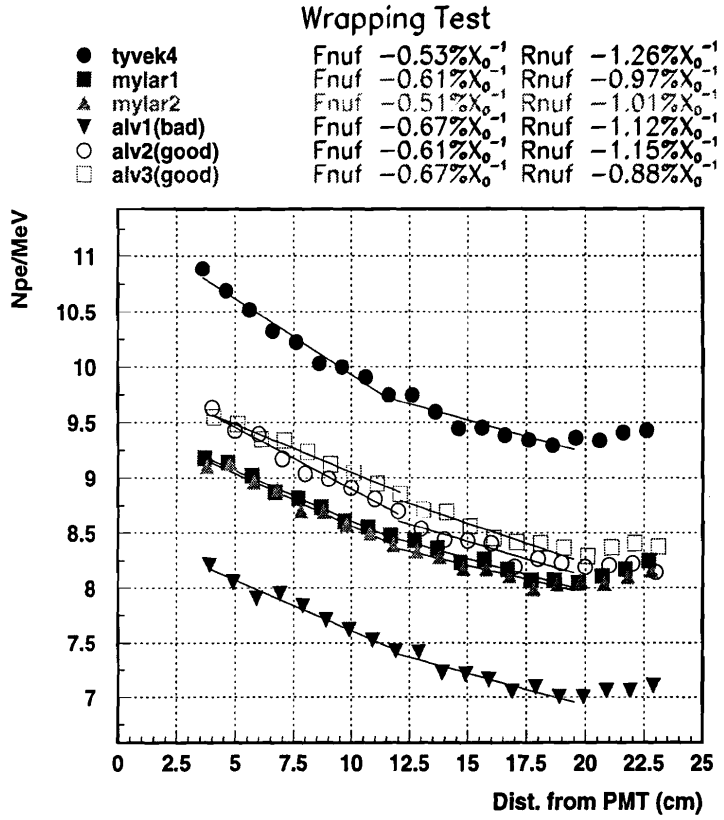

Conclusion:

les structures alvéolaires assurent que la résolution en énergie reste au niveau requis par la physique

Contrôle de qualité

- Pour s'assurer que toutes les structures alvéolaires produites auront des propriétés mécaniques et optiques conformes aux tolérances, nous avons conçu le

processus de contrôle de qualité

qui consiste en:

- ***suivi du procédé de production***

  - chaque tâche du procédé de production a été optimisée dans le laboratoire, pour minimiser le temps de production et le nombre des pièces rejetées,
  - un système de suivi de l'exécution des tâches a été développé et installé chez le fabricant

- ***mesures dimensionnelles***

  - après la production, mesures très détaillées pour vérifier les dimensions
  - les structures ne satisfaisant pas les critères seront rejetées

- ***mesures optiques***

  - mesure d'un échantillon d'aluminium traité avant la production
  - mesure de la structure après la production
  - comparaison des résultats
  - si la structure ne passe pas les critères, elle sera étudiée en détails et éventuellement rejetée

Contrôle optique - MONICA

- *Exigences:*
  - mesure des caractéristiques optiques significatives dans une courte période de temps
  - simple à utiliser
  - de dimensions appropriées pour l'insertion dans la structure
  - stabilité sur une période courte
- *Mesure de:*
  - réflexivité spéculaire: ***la réflexion***
  - réflexivité diffusée: ***la diffusion***

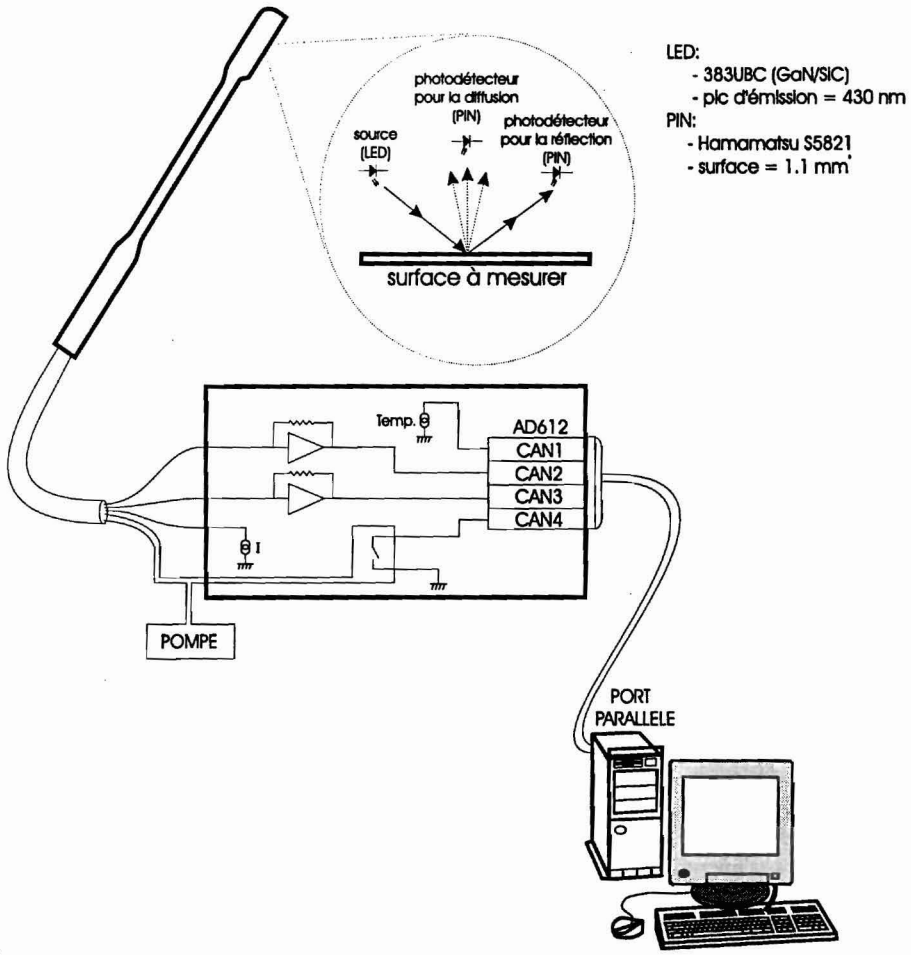

- Les mesures démarrent automatiquement par un interrupteur électronique déclenché par un manomètre

- instabilités possibles:
  - durée de vie de la LED (~ 2000 heures)
  - variations de réponse de la LED avec la température
- stabilité satisfaisante pour des mesures locales
- pour une comparaison des mesures une référence a été prévu

MONICA - mesure des structures

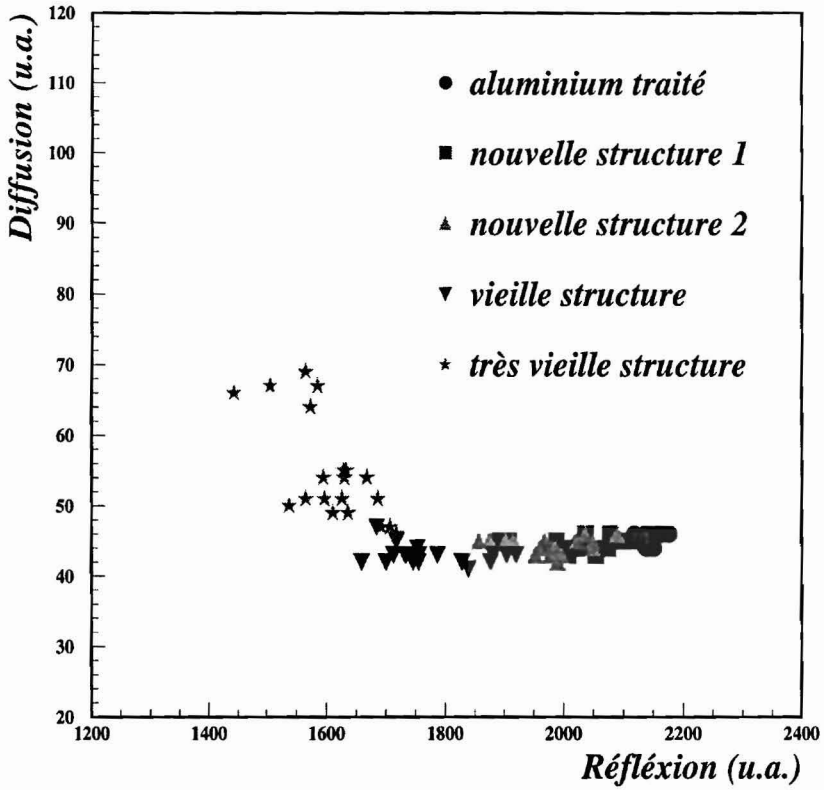

surface	réflexivité	diffusivité
aluminium	2132 ± 33	45.2 ± 0.7
nouv. struct. 1	2013 ± 56	44.3 ± 0.9
nouv. struct. 2	1979 ± 57	44.2 ± 1.1
vieille struct.	1779 ± 74	42.9 ± 1.3
très vieille struct.	1610 ± 69	55.8 ± 7.3

- structures nouvelles / aluminium $\approx -7\%$
- vieille structure / aluminium $\approx -15\%$
- très vieille structure / aluminium $\approx -25\%$

- Conclusion:

le rapport des réflexivités des structures alvéolaires / aluminium traité
est du même ordre que
le rapport de la collection de lumière avec les cristaux / tyvek

Procédure de contrôle

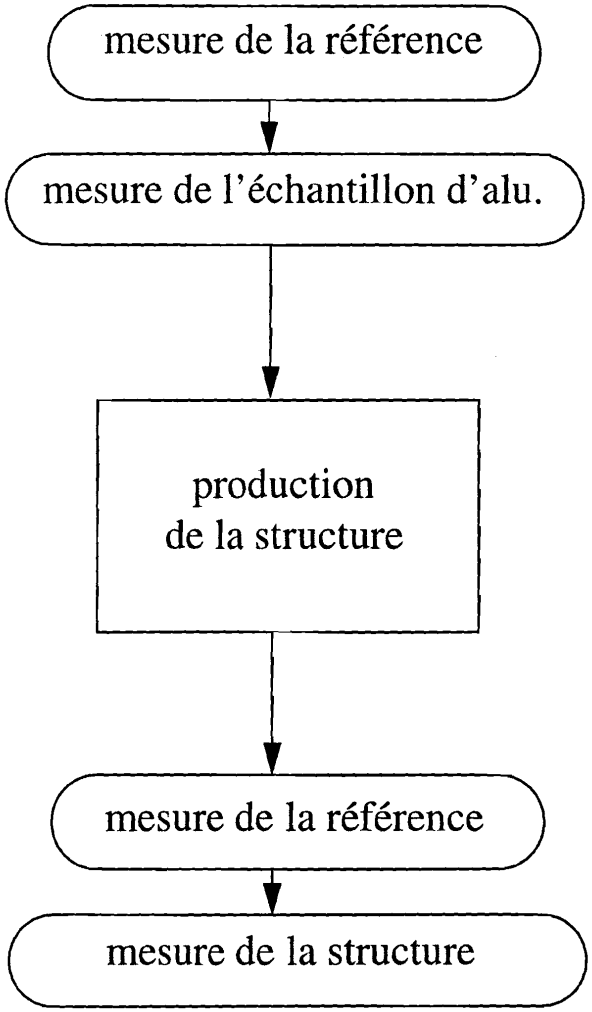

- résultats de chaque mesure: $M^{refl}_{edian}, RMS^{refl}_{eff}, M^{diff}_{edian}, RMS^{diff}_{eff}$
- **critère local:** $\frac{RMS_{eff}}{M} < A_{loc}$
- **critères globaux:**

référence

$$M/M_{etalon} \in [A^{ref}_{glob}, B^{ref}_{glob}]$$

échantillon

$$\frac{M_{ech}}{M_{ref}}/R_{etalon} \in [A^{ech}_{glob}, B^{ech}_{glob}]$$

structure alvéolaire

$$\frac{M_{struct}}{M_{ref}}/\frac{M_{ech}}{M'_{ref}} \in [A^{struct}_{glob}, B^{struct}_{glob}]$$

les valeurs des critères

	local réfl. et diff.	**global** réflexivité		diffusivité	
	A_{loc}	A_{glob}	B_{glob}	A_{glob}	B_{glob}
référence	2%	0.5	1.2	0.5	1.2
éch. d'alu	3%	0.9	1.2	0.8	1.2
structure	4%	0.85	1.	0.8	1.1

Résultats sur les structures du Module 0

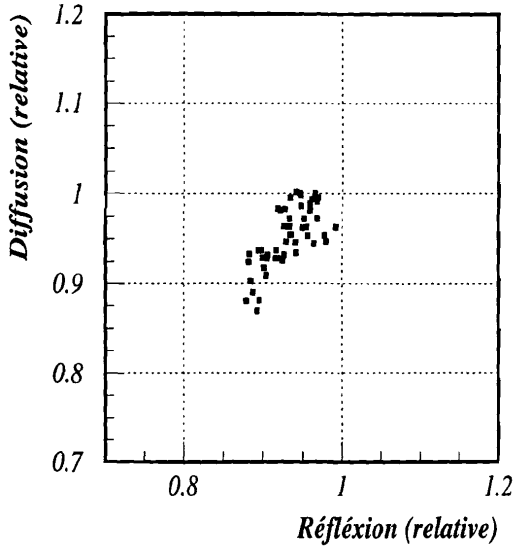

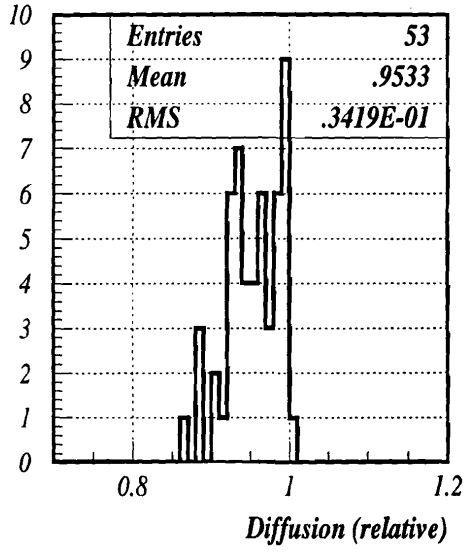

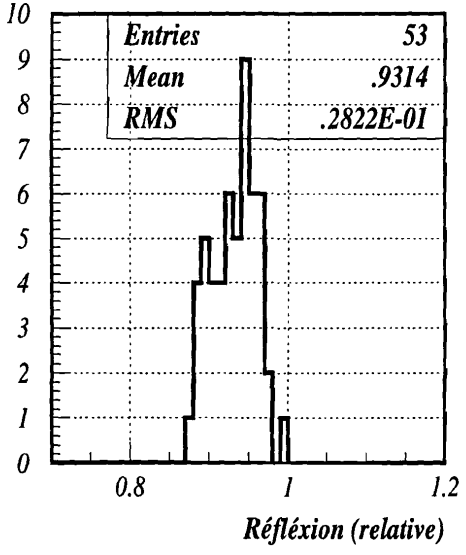

Contrôle qualité - conclusion

- La production des structures alvéolaires a été confiée à *MOC Composite*

- Le système développé pour le contrôle qualité des structures alvéolaires consiste en:
  - **suivi de la production**
  - **mesures dimensionnelles**
  - **contrôle optique**

- Le système de contrôle assure que les structures produites ne détérioreront pas les performances du calorimètre électromagnétique

- Après vérification des résultats dans le laboratoire:
  - *les structures alvéolaires seront envoyées aux centres régionaux pour l'assemblage*
  - *les résultats de contrôle (suivi de la production et toutes les mesures) seront entrés dans la base de données CRISTAL*

Chapitre 4

Etude de signal et de bruits de fonds

Production du Higgs dans LHC (1)

- ***fusion des gluons*** $gg \rightarrow H$:

  - diagramme de premier ordre(LO)

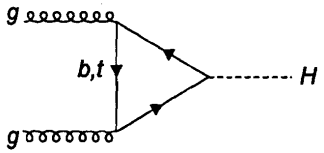

  - exemples de diagrammes à l'ordre suivant (NLO)

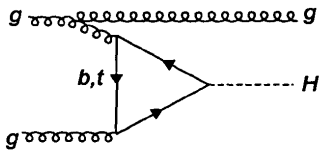

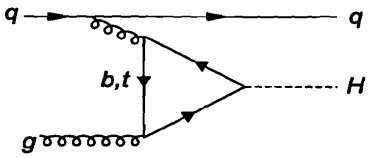

- facteur K - utilisé pour exprimer la quantité de corrections des ordres supérieurs
- dans NLO: $K = \sigma_{NLO}/\sigma_{LO}$
- $M_H \in (120, 180)$ GeV $\Rightarrow K \approx 1.6$
- application du facteur K aux événements générés exige un accord de la cinématique $\longrightarrow$ étude de p_T
- pour les études inclusives du Higgs il y a accord avec les calculs analytiques

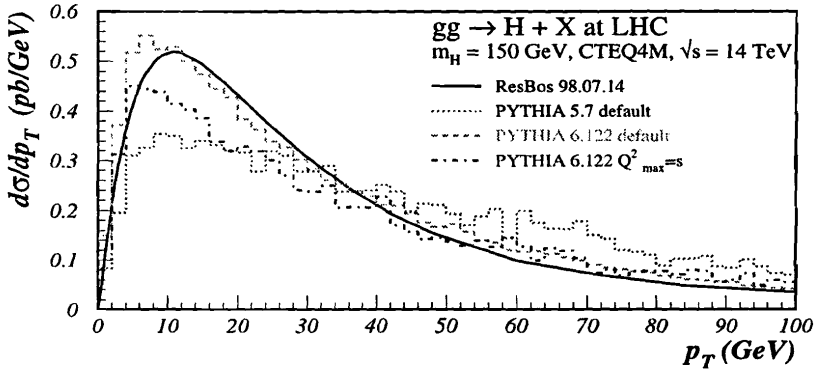

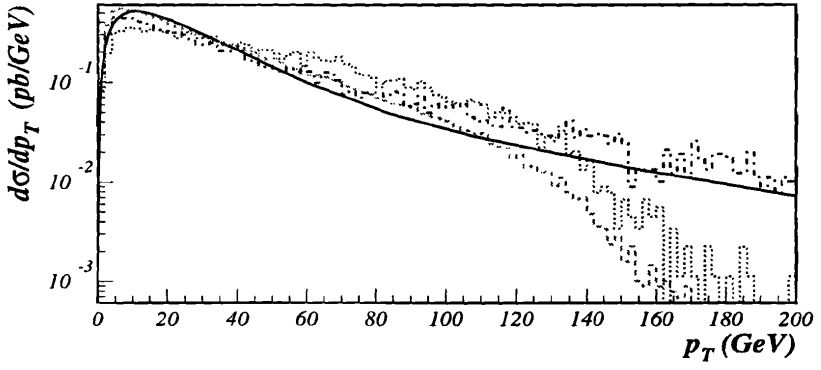

- ***incertitudes théoriques:***
  - fonctions des structures ≈ 10 %
  - variations de σ_{NLO} avec l'échelle de renormalisation et de factorisation ≈ 15 %
  - calculs NNLO encore inconnus

Production du Higgs dans LHC (2)

- ***fusion des W et des Z:*** $qq \to V^*V^*qq \to Hqq$

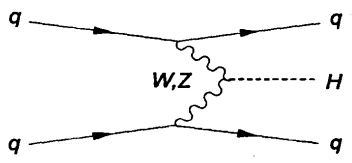

- les corrections QCD sont d'environ 8-10%
- les deux jets avec des petits angles peuvent être utilisés pour la suppression de bruit de fond

- ***Higgs-strahlung:*** $q\bar{q} \to V^* \to VH$

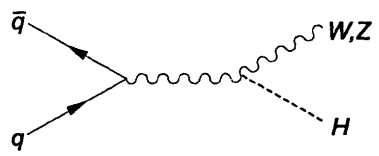

- les corrections QCD sont d'environ 25-40%
- l'utilisation de Z ou W peut améliorer la visibilité du signal

- ***production associée avec une paire*** $t\bar{t}$

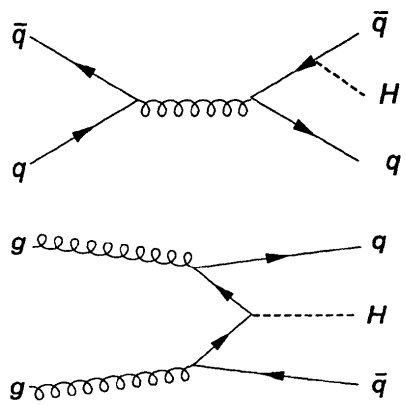

- détection possible de paire $t\bar{t}$
- les corrections QCD sont encore inconnues

Production et désintégration du Higgs

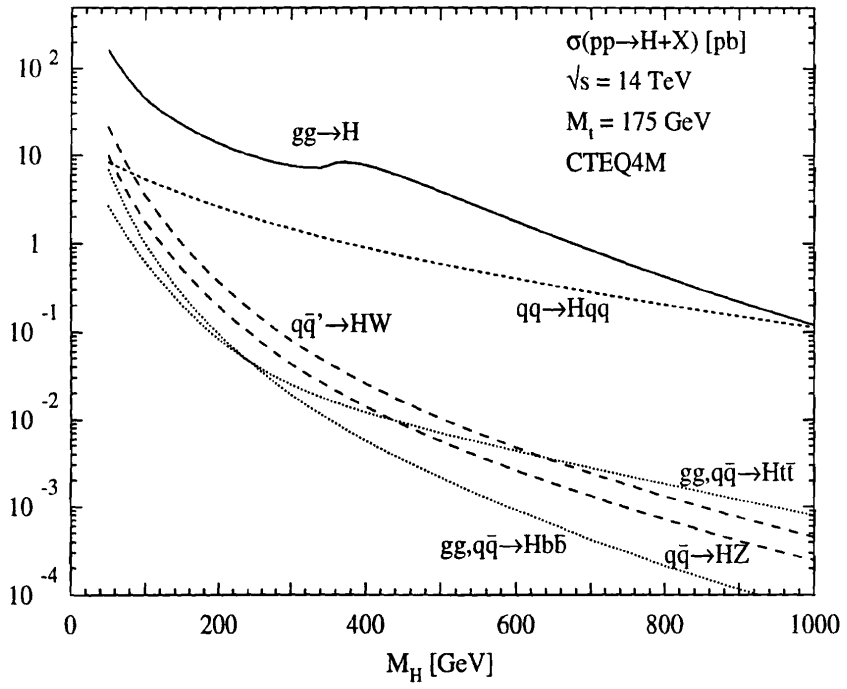

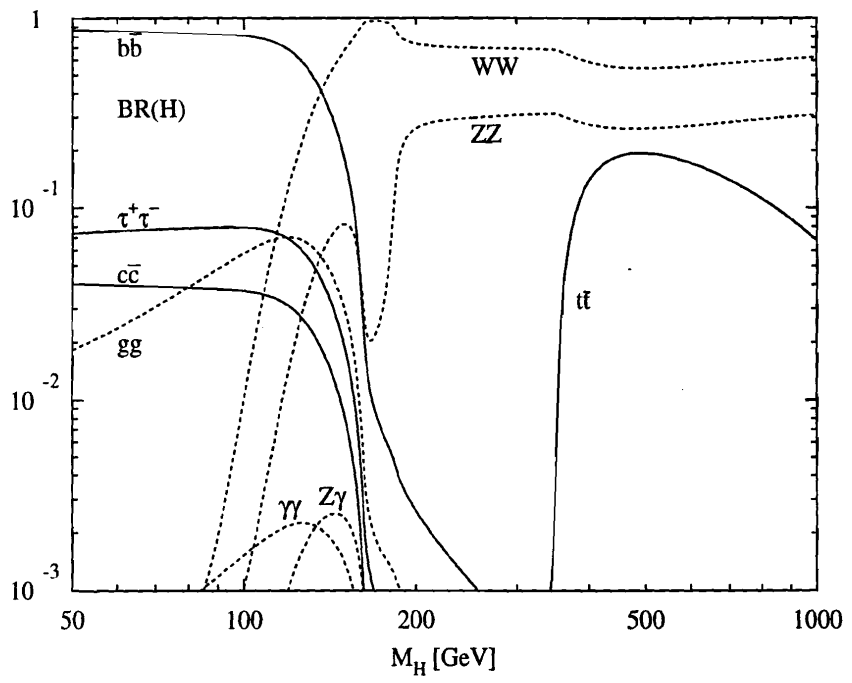

- Environ 2 000 000 événements de Higgs attendus pour $m_H \in (130, 180)$ GeV pour 10^5 pb^{-1}
- $M_H \in (130, 180)$ GeV $BR(H \to ZZ^*) \approx 2 - 10\%$
- $BR(Z \to ee)^2 = 3.4\%^2 = 0.11\%$
- Environ de 40 à 200 événements $H \to ZZ^* \to 4e^{\pm}$ attendus pour 10^5 pb^{-1}

Bruit de fond ZZ^*/γ^* et $t\bar{t}$

- ZZ^*/γ^*
  - deux processus au premier ordre: $q\bar{q} \to ZZ^*/\gamma^*$ et $gg \to ZZ^*/\gamma^*$
  - seul $q\bar{q} \to ZZ^*/\gamma^*$ implémenté dans PYTHIA
    - corrections QCD:
      - le facteur K pour le $q\bar{q} \to ZZ$ vaut 1.44
      - PYTHIA sous-estime les prédictions pour $p_T(ZZ) > 100$ GeV
  - pour $gg \to ZZ^*/\gamma^*$ nous utilisons les résultats:
    - $\sigma(gg \to ZZ)/\sigma(q\bar{q} \to ZZ) = 0.35$, en négligeant les différences cinématiques
    - les corrections QCD sont inconnues, mais potentiellement importantes
  - préselection: au moins $2e^-$ et $2e^+$ avec $p_T > 6.5$ GeV et $|\eta| < 2.5$
  - après présélection: $\sigma(ZZ^*/\gamma^* \to 4e) = 2.66$ fb, c.à.d. 266 événements attendus pour 100 fb^{-1}
- $t\bar{t}$

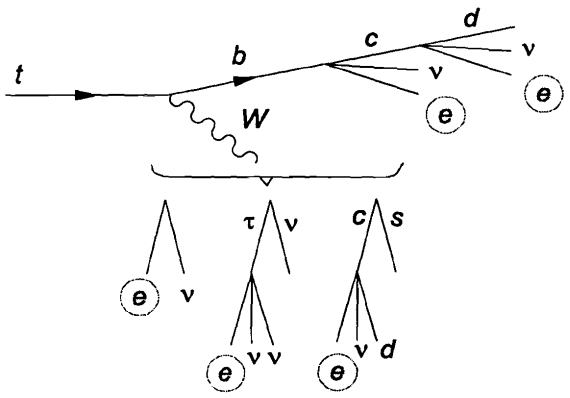

  - plusieurs sources d'électrons
  - sections efficaces:

$$\sigma_{LO}(t\bar{t}) = \left(515\ ^{+128}_{-95}\ ^{+167}_{-228}\right) \text{ pb}, \quad \sigma_{NLO}(t\bar{t}) = \left(758.8 \pm 75\ ^{+167}_{-228}\right) \text{ pb}$$

  - nous avons forcé $W \to e\nu$,
    la contribution des autres canaux de W constitue une source d'erreur systématique
  - après présélection: $\sigma(t\bar{t} \to 4e) = 27.06$ fb, c.à.d. 2706 événements attendus pour 100 fb^{-1}

Bruit de fond $Zb\bar{b}$

- Production dans LO:

$g + g \to Z + b + \bar{b}$

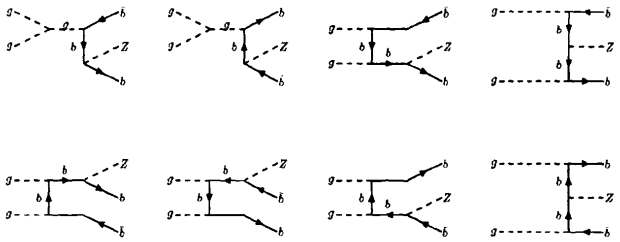

$q + \bar{q} \to Z + b + \bar{b}$

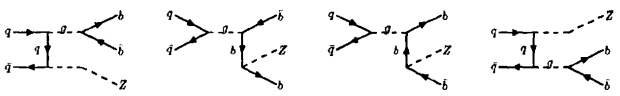

$b + \bar{b} \to Z + b + \bar{b}$

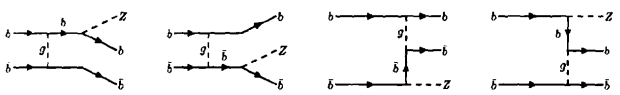

- ***problèmes dans PYTHIA***
  - génération incorrecte d'espace de phase
  - n'existe plus dans PYTHIA 6.x
  - la génération par gerbe de parton sous-estime la section efficace et la cinématique

- ***nous utilisons:***
  - CompHEP - pour le calcul de section efficace et pour la génération des $Zb\bar{b}$ dans l'état final
  - PYTHIA - pour la désintégration et la fragmentation

- ***section efficace au LO***

  (CTEQ4L, $Q = m_Z$, $\alpha_s^{LO} = 0.132$)

état initial	gg	$q\bar{q}$
σ_{LO}(pb)	780.79	148.79

  - les variations de σ_{LO} sont d'environ $\pm 20\%$ autour $Q = m_Z$
  - c.à.d. les corrections QCD sont importantes

- après présélection: $\sigma(Zb\bar{b} \to 4e) = 20.65$ fb, c.à.d. 2065 événements attendus pour 100 fb^{-1}

Coupures d'analyse

- ***coupures et acceptances (relatives):***

	p_T des électrons	m_{Z^*}	m_Z	isolation	acc. totale
	$p_T > 20, 15, 10, 7$ GeV	$15 < m_{ee} < 80$ GeV	$m_{ee} > m_Z - 13$ GeV $< m_Z + 6$ GeV	pas de traces chargés avec $p_T > 2.5$ GeV dans un cône $R = 0.2$	
$m_H = 130$ GeV	***0.94***	***0.90***	***0.82***	***0.93 (0.80)***	***0.64 (0.55)***
$m_H = 150$ GeV	***0.98***	***0.95***	***0.91***	***0.94 (0.80)***	***0.80 (0.67)***
$m_H = 170$ GeV	***0.99***	***0.96***	***0.94***	***0.94 (0.80)***	***0.84 (0.71)***
ZZ^*/γ^*	***0.91***	***0.81***	***0.91***	***0.95 (0.81)***	***0.63 (0.54)***
$t\bar{t}$	***0.87***	***0.64***	***0.70***	***0.014***	***0.0055***
$Zb\bar{b}$	***0.77***	***0.38***	***0.90***	***0.067***	***0.018***

  - les nombres entre parenthèses correspondent à la haute luminosité

- ajustement des coupures possible après une première étape d'analyse

Résultats de l'étude au niveau générateur

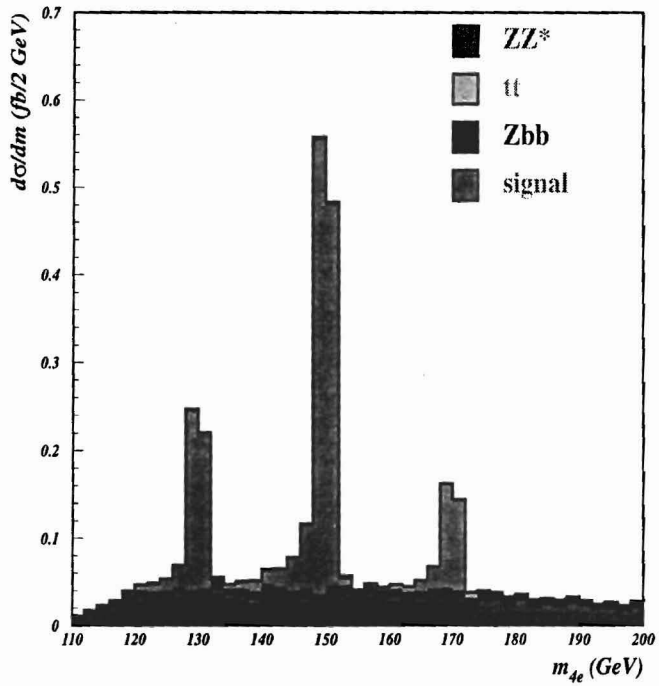

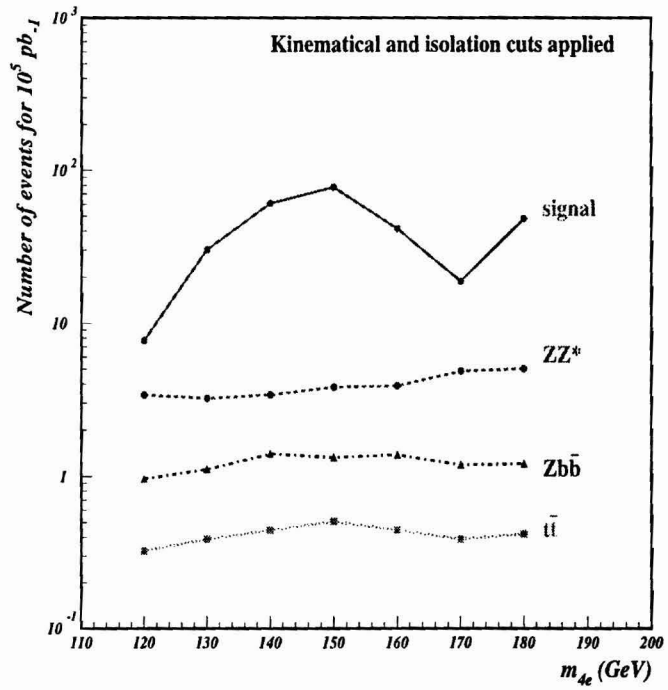

Cette visibilité du signal est très optimiste,
car elle dépend très fortement de l'efficacité et de la précision de reconstruction des électrons dans le détecteur

Chapitre 5

Etude de la reconstruction de $H \rightarrow ZZ^* \rightarrow 4e^{\pm}$

Problème de bremsstrahlung

- ***Problèmes potentiels:***
  - perte en efficacité
  - perte en précision

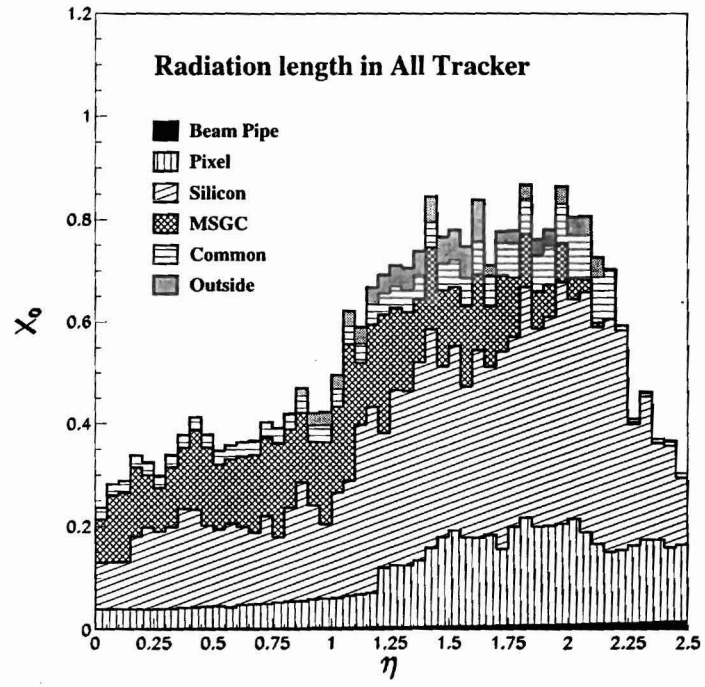

- Fraction des électrons avec

$$\frac{E_{\text{impact}}}{E_{\text{généré}}} < 0.1 = 12\%$$

- Fraction des particules secondaires avec

$$E_{\text{sec}} > 1 \text{ GeV} = 13\%$$

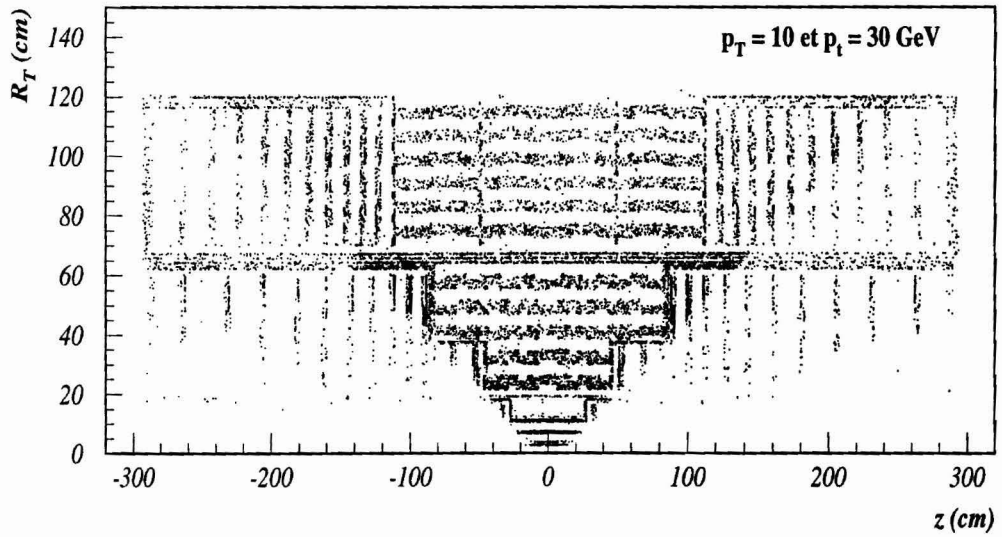

Reconstruction des traces

- L'algorithme utilisé est basé sur un filtre de Kalman
  - démarre avec une prétrace (pixels)
  - prédiction + inclusion de la mesure
  - itération (de l'intérieur vers l'extérieur)

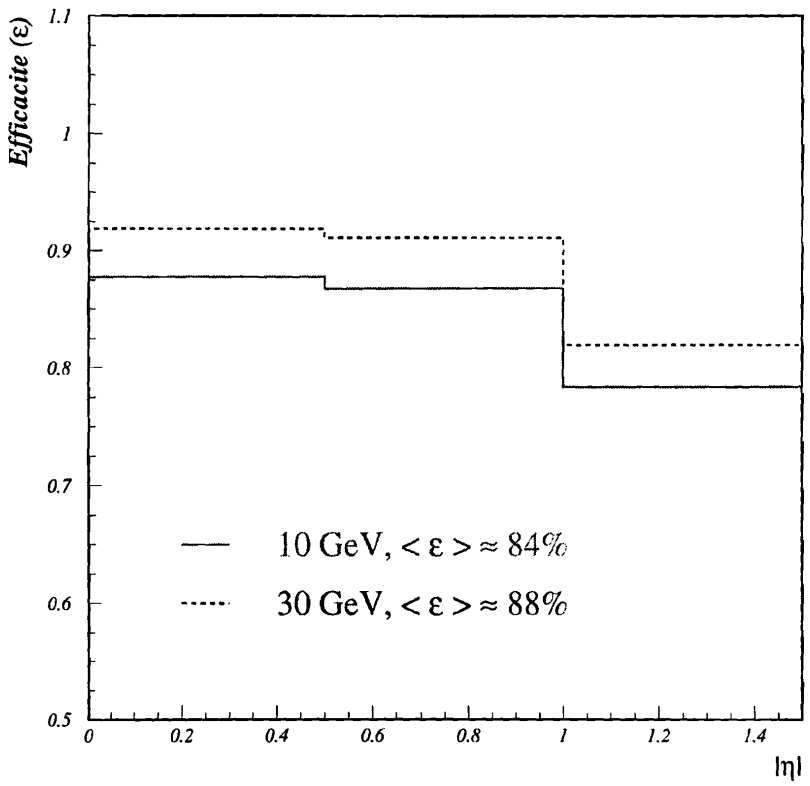

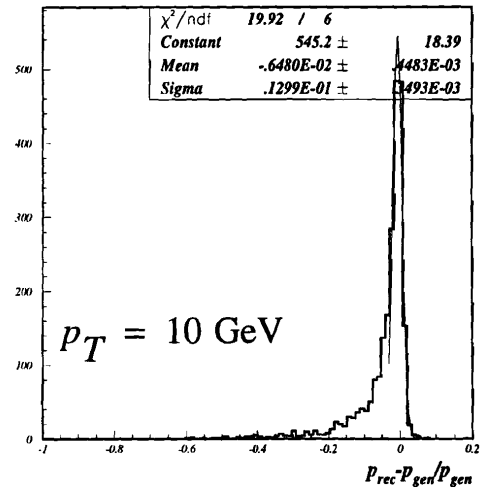

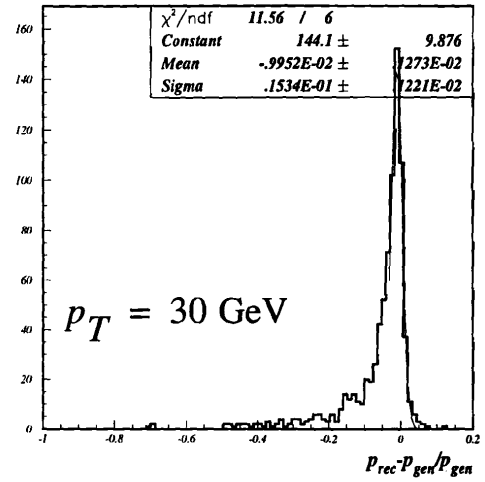

Reconstruction des agrégats

- ***Exigences pour un algorithme d'agrégation:***
  - adapté aux fluctuations événement par événement de la position et de la direction de l'impact de la particule
  - agrégat pas trop grands, pour éviter l'influence du bruit
  - suffisamment local pour distinguer deux gerbes proches
- ***Algorithme dynamique:***

  1. **recherche d'un germe**

     cristal avec un maximum local d'énergie plus grande qu'un seuil ($E_{germe}^{seuil} = 3.3\sigma_{bruit}$)

  2. **construction de l'agrégat**

     Attachement des cristaux qui sont voisins par un côté d'un cristal de l'agrégat et qui ont moins d'énergie que ce cristal

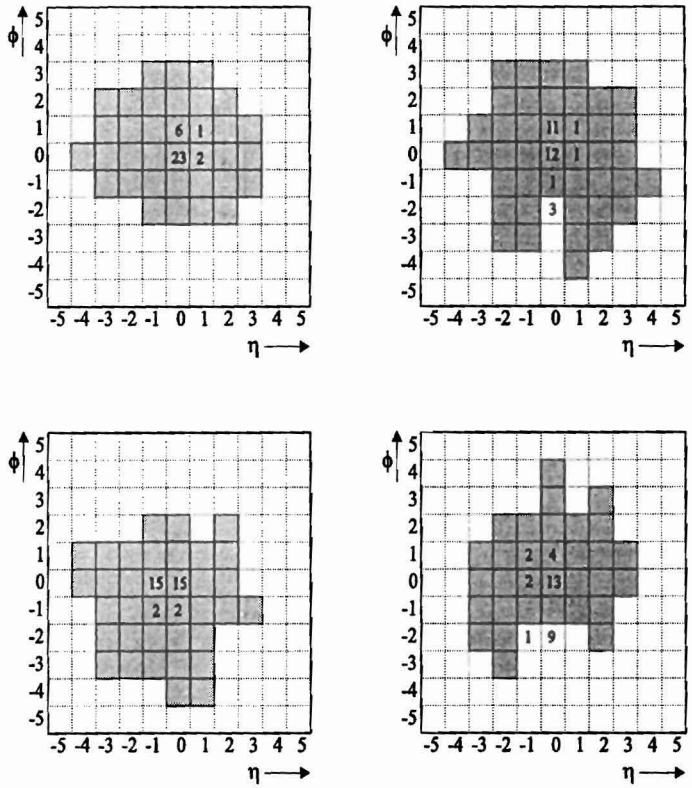

- ***Recherche des photons émis par bremsstrahlung***
  - depuis l'énergie transverse de l'agrégat de l'électron on peut prédire où chercher des agrégats de photons
  - les agrégats trouvés sont attachés à l'agrégat de l'électron
  - pour les cas de photons durs, on a besoin de changer d'algorithme d'association

Méthode de poids

- ***estimateur d'énergie le plus simple: 'somme des énergies dans l'agrégat'***

$$E_s = \sum e_i$$

  - traitement de bruit inadéquat; N cristaux avec un bruit non correlé (σ_{bruit}) contribuent $N\sigma^2_{bruit}$ à la variance
  - le bruit commence à dominer la résolution quand l'énergie est inférieure à environ 20 GeV

- ***une autre estimateur peut être construit dans la façon suivante:***
  - chaque cristal dans laquel la particule dépose une fraction (f_i) de son énergie donne un estimateur de l'énergie totale

$$\left\{\tilde{E}_i = \frac{e_i}{f_i}\right\} \quad i = 1, \ldots, n$$

  - la combinaison optimale de ces estimateurs est une somme pondérée

$$\tilde{\mathrm{E}} = \sum w_i' \tilde{E}_i = \sum w_i' \frac{e_i}{f_i} = \sum w_i e_i$$

  - la contrainte pour que cet estimateur ne soit pas biaisé $\langle \tilde{\mathrm{E}} \rangle = E$ est équivalent à $\sum w_i f_i = 1$
  - les poids sont obtenus en minimisant la variance, avec la contrainte introduite par le multiplicateur de Lagrange

$$\Theta = \sigma^2_{\tilde{\mathrm{E}}} - 2\lambda(\sum w_i f_i - 1)$$

  - comme résultat on obtient la matrice des poids:

$$W = \frac{S^{-1}F}{F^T S^{-1} F}$$

- S est la matrice des covariances
- F est la matrice des fractions

Modèle de gerbe

- pour l'implémentation de la méthode de poids on a besoin:
  - d'un ***modèle de gerbe*** électromagnétique pour la prédiction des fractions
  - d'une modélisation de la ***matrice des covariances***

- **modèle de gerbe**

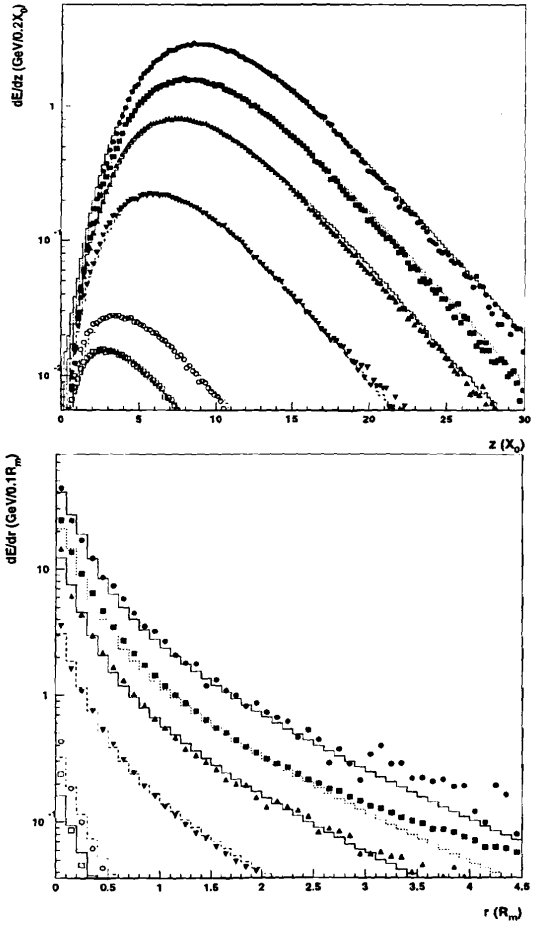

- paramétrisation des profils longitudinal et transverse

  - profil longitudinal

$$\frac{dL}{dz} = E_{inc}\frac{\beta^{\alpha}}{\Gamma(\alpha)}z^{\alpha-1}e^{-\beta z}$$

  - profil transverse

$$\frac{dT(r,z)}{drdz} = a\frac{2(\gamma-1)rR_1^{2(\gamma-1)}}{(r^2+R_1^2)^{\gamma}} + (1-a)\frac{2(\gamma-1)rR_2^{2(\gamma-1)}}{(r^2+R_2^2)^{\gamma}}$$

- implémentation dans la géométrie de CMS
- pour atteindre la précision nécessaire des prédictions:
  - ajustement du profil transverse au profil simulé avec GEANT, en changeant les paramètres R_1, R_2 et a
  - modélisation des effets du champ magnétique

Matrice des covariances

- fortes corrélations entre les énergies déposées dans des cristaux voisins

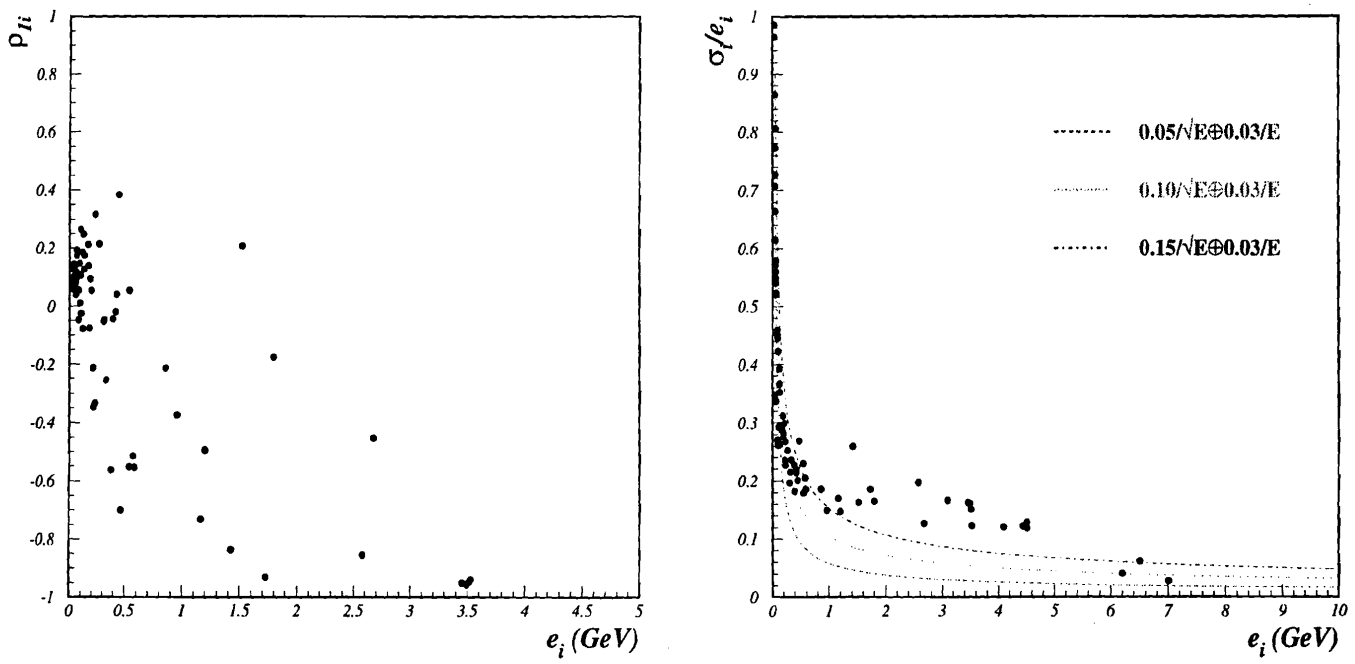

- pas de paramétrisation simple
- nous choisissons $\sigma_i \sim \sqrt{e_i}$
- tous les poids deviennent les mêmes, et l'estimateur d'énergie est $\tilde{E}_{sw} = \dfrac{\sum_{i=1}^{n} e_i}{\sum_{i=1}^{n} f_i}$

Méthode de poids - résultats (1)

- ***sans trajectomètre:***

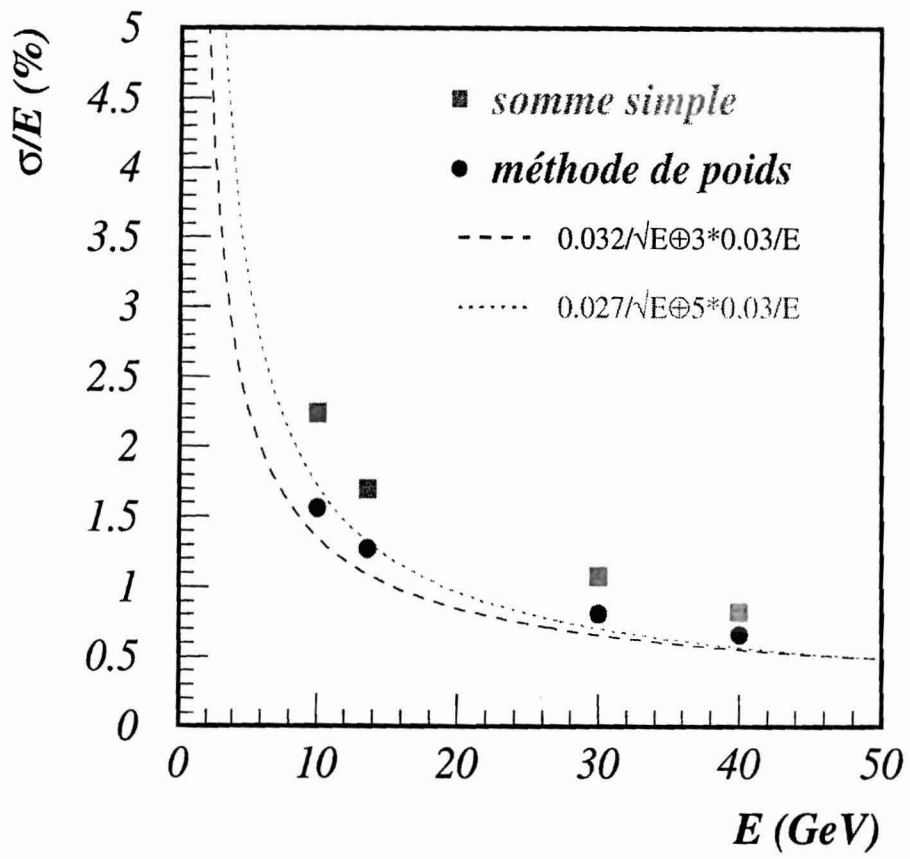

1. Entrée du ECAL:

- $E = 10$ GeV
- $E = 30$ GeV

2. Depuis le vertex

- $p_T = 10$ GeV, ($\langle E \rangle \approx 14$ GeV)
- $p_T = 30$ GeV, ($\langle E \rangle \approx 42$ GeV)

- points d'impact distribués uniformément
- direction et point d'impact extraits de GEANT

Méthode de poids - résultats (2)

- **avec trajectomètre:**
  - *exemple:* $p_T = 10$ *GeV*

tous les événements

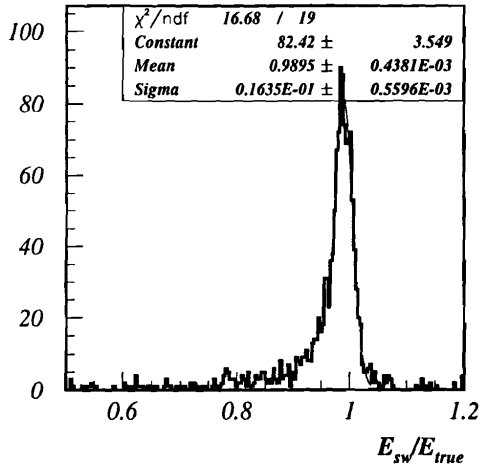

$\Delta^2 < 15$

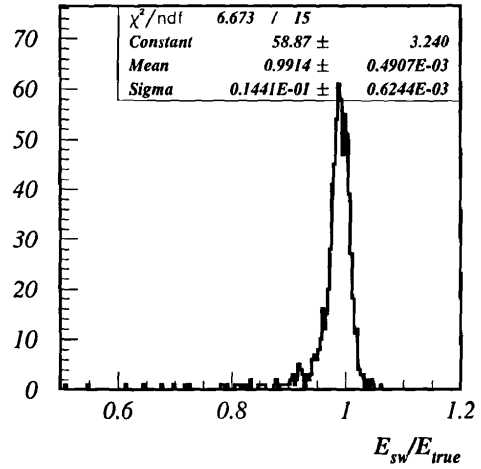

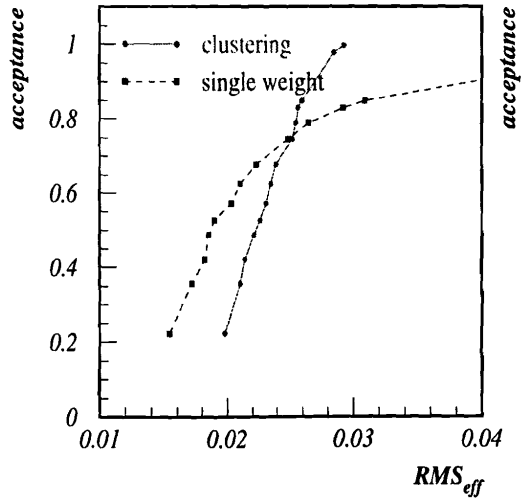

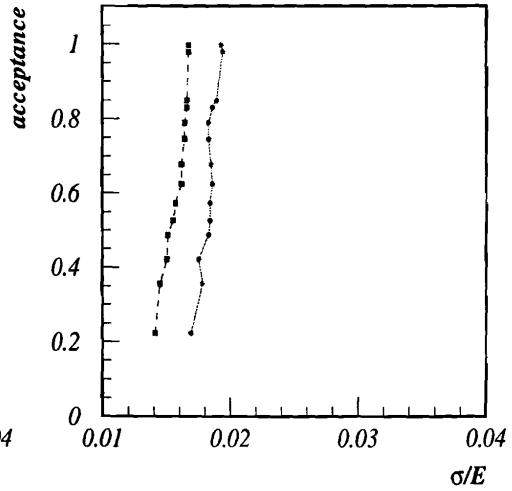

- *influence du trajectomètre:*
  - bremsstrahlung
  - extrapolation
- seulement les cristaux avec $e_i > 2\sigma_{bruit}$ considérés dans la méthode des poids

résultats: 1 – méthode de poids / somme simple

	accept.	RMS_{eff}	σ
10 GeV (30 MeV bruit)	50%	15%	19%
10 GeV (100 MeV bruit)	60%	18%	29%
30 GeV (30 MeV bruit)	70%	10%	15%

Estimateur final d'impulsion

- ***Estimateur final = une combinaison des mesures du ECAL et du trajectomètre***
- exemple: $p_T = 10$ GeV

$$\tilde{p} = \begin{cases} w_E \cdot E + w_p \cdot p \ , \text{if } \left|\frac{E}{p} - 1\right| \le 2\sigma_{E/p} \\ E \qquad , \text{if } \frac{E}{p} > 1 + 2\sigma_{E/p} \\ p \qquad , \text{if } \frac{E}{p} < 1 - 2\sigma_{E/p} \end{cases}$$

résultats

		RMS_{eff}	σ	$\varepsilon(\pm 2\sigma)$ (%)	$\varepsilon(\pm 3\sigma)$ (%)
p_T = 10 GeV	E	0.029	0.0164	71.5	78.5
	p	0.025	0.0120	67.1	74.2
	$\tilde{p}$	0.017	0.0127	79.1	86.5
p_T = 30 GeV	E	0.020	0.0080	62.3	69.9
	p	0.045	0.0175	59.7	68.1
	$\tilde{p}$	0.016	0.0084	69.4	75.5

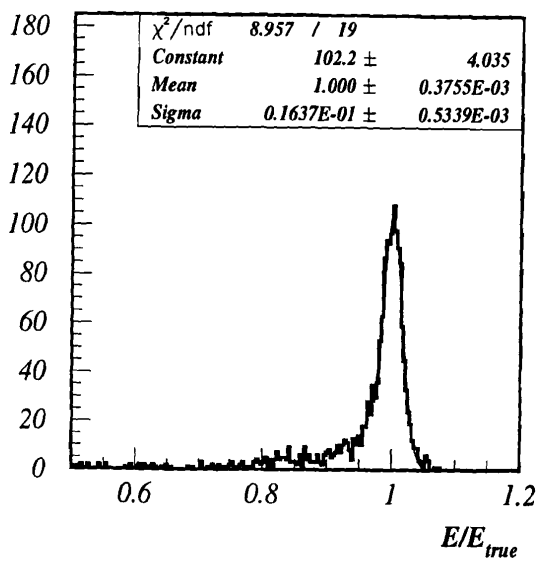

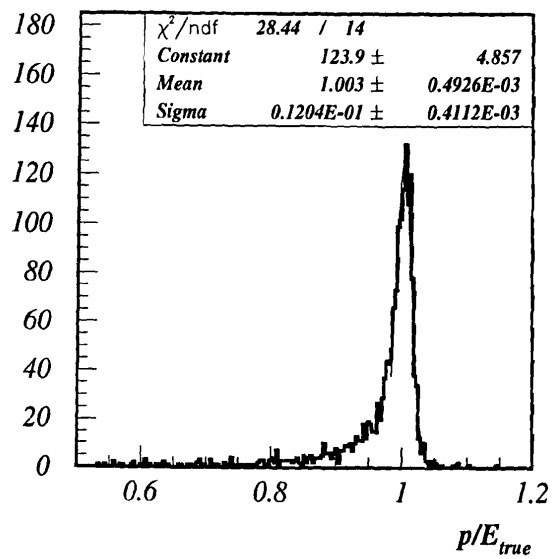

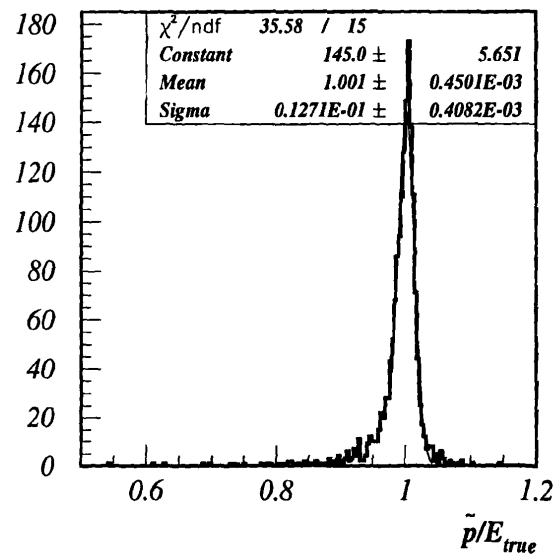

Résultats sur la reconstruction du Higgs (1)

	m_H = 130 GeV	m_H = 150 GeV	m_H = 170 GeV
acc. de reconstr. des $e^{\pm}$	**0.64**	**0.65**	**0.67**
coupures en p_T des $e^{\pm}$	**0.89**	**0.91**	**0.94**
coupure en masse de Z*	**0.90**	**0.94**	**0.95**
coupure en masse de Z	**0.77**	**0.86**	**0.92**
σ_{m_H} (GeV)	**1.29**	**1.58**	**1.78**
efficacité 2σ	**0.68**	**0.67**	**0.67**
efficacité 3σ	**0.77**	**0.77**	**0.76**
acc. totale	**0.26**	**0.31**	**0.37**
acc. totale niveau génér.	**0.56**	**0.68**	**0.67**

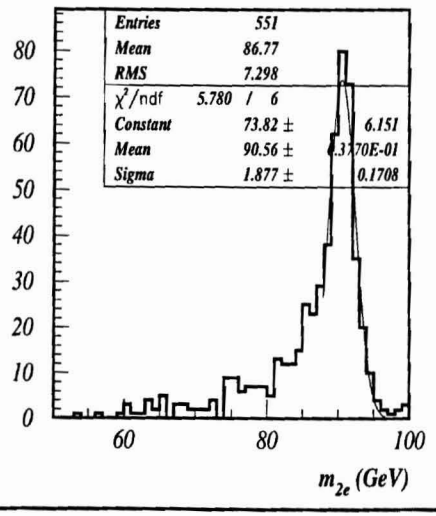

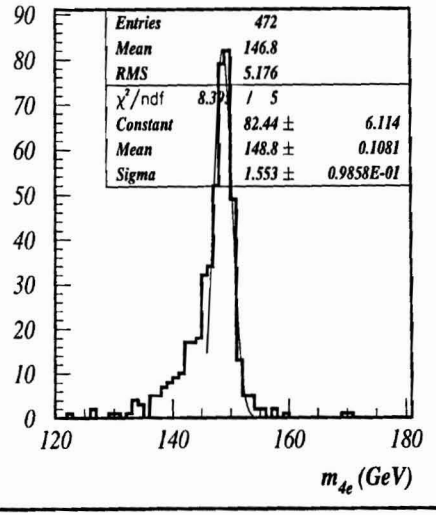

Résultats sur la reconstruction du Higgs (2)

- une combinaison des résultats de reconstruction et d'analyse au niveau de générateur

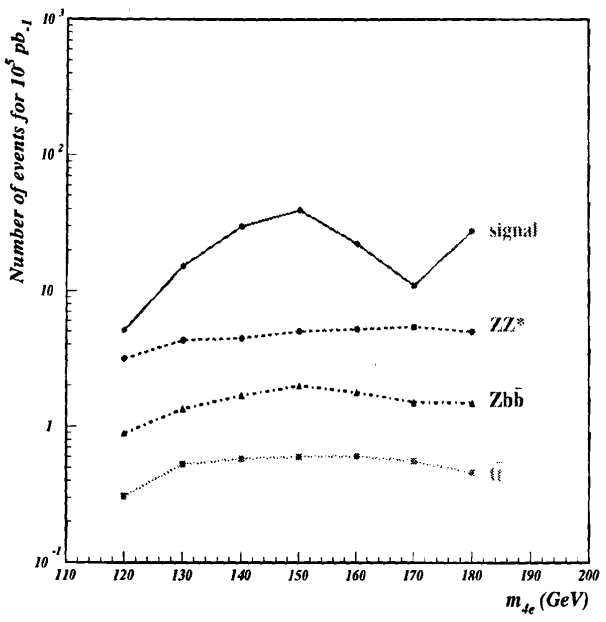

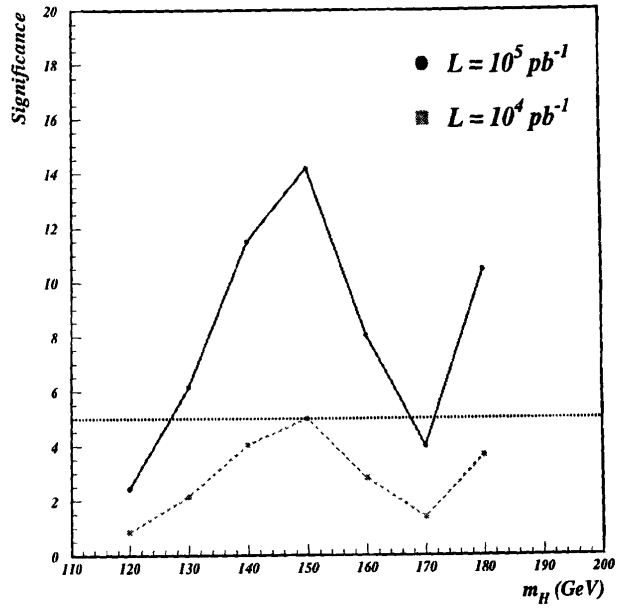

- ***améliorations possibles:***
  - efficacité pour trouver les traces
    maintenant $\varepsilon \approx 0.9$, pour $\varepsilon \approx 0.95$ $\Delta S \approx 10\%$
  - recherche des photons de bremsstrahlung interne

- avec $Z \to \mu\mu$, significance augmente d'un facteur d'environ 2 et le Higgs pourrait être découvert dans l'intervalle d'environ 120 GeV jusqu'à $2m_Z$ pour $\int Ldt = 10^5$ pb^{-1}

Conclusion

Le travail présenté dans cette thèse consiste en l'étude du potentiel de CMS pour la recherche du Higgs dans le canal $H \rightarrow ZZ^* \rightarrow 4e^{\pm}$. Cette recherche n'est possible que grâce à un calorimètre électromagnétique (ECAL) de hautes performances. Notre contribution à la construction du calorimètre électromagnétique fut le développement d'un procédé de contrôle qualité pour la production des structures alvéolaires. Pour estimer le potentiel de découverte du Higgs par le canal $H \rightarrow ZZ^* \rightarrow 4e^{\pm}$, une analyse au niveau des particules, suivie d'une étude détaillée de reconstruction ont été effectuées.

Après plusieurs années de recherches et développements, le calorimètre électromagnétique de CMS est entré dans une phase de production en série pour la plupart de ses composants. Les structures alvéolaires, conçues pour maintenir les cristaux, ont été développées au laboratoire, et toute leur production a été confiée à une entreprise. Les deux caractéristiques les plus importantes des structures alvéolaires sont la précision de leurs cotes mécaniques et la qualité optique de leur revêtement réfléchissant interne. Pour s'assurer que ces qualités se maintiennent au niveau demandé par la physique, nous avons développé une procédure de contrôle qualité consistant en un suivi du procédé de production, en des mesures géométriques précises et en des mesures optiques détaillées. Pour le contrôle optique nous avons développé un instrument permettant la mesure de la réflexivité et de la diffusivité du matériau interne des structures alvéolaires, qui est une feuille d'aluminium traité. La procédure de contrôle optique consiste à mesurer un morceau d'aluminium avant la production et la structure alvéolaire après le processus complet de production. Le critère le plus important demande que la réflexivité du matériau interne de l'alvéole soit supérieur à 85% de la réflexivité du matériau brut. La procédure proposée a été testée sur les structures alvéolaires faites au laboratoire pendant la phase de pré-production. Elle a confirmé que toutes les structures alvéolaires produites sont conformes aux critères établis. Tout le processus de contrôle qualité a été transmis au fabricant où il est en service.

Bien que la masse du Higgs soit un paramètre libre du Modèle Standard et donc ne puisse être prévue, des arguments théoriques et des données expérimentales de mesures électrofaibles privilégient un boson de Higgs de masse intermédiaire. Dans le domaine de masses s'étendant d'environ 120 GeV jusqu'à m_Z, un des principaux canaux de recherche du Higgs est $H \rightarrow ZZ^* \rightarrow 4l^{\pm}$, où les leptons sont des électrons ou des muons. Dans cette thèse, nous avons étudié le canal avec 4 électrons dans l'état final. Les sections efficaces et rapports de branchement du signal ont été calculés grâce à des programmes appliquant les calculs théoriques les plus récents, incluant les corrections QCD et QED suivant le terme dominant. Les particules de l'état final ont été produites par le programme de Monte Carlo PYTHIA, avec des sections efficaces calculées à l'ordre dominant. La normalisation de la section efficace obtenue par la méthode de Monte Carlo à celle calculée par des modèles théoriques plus rigoureux nécessite la concordance des variables cinématiques. Nous avons étudié la distribution du

moment transverse du Higgs en comparant les prédictions de deux modèles : l'un basé sur le formalisme des gerbes de partons introduit dans les générateurs de particules de Monte Carlo, et l'autre basé sur la resommation des gluons mous. Nous concluons que les deux méthodes sont en accord dans la région des p_T petits et intermédiaires, qui domine la distribution globale. Dans la région des grands p_T, le calcul de resommation correspond au calcul exact des éléments de matrice, tandis que le modèle de gerbe de partons peut soit être ajusté en permettant une plus grande activité de la gerbe partonique, soit nécessite l'addition de calculs pour s'ajuster mieux aux éléments de matrice. Un autre aspect important de l'étude du canal $H \rightarrow ZZ^* \rightarrow 4e^{\pm}$ fut l'évaluation du fond en $Zb\bar{b}$. Pour les calculs de section efficace et la génération d'événements, le programme de Monte Carlo CompHEP a été utilisé ; il traite correctement la génération d'espace de phase de ce processus. Nous avons étudié les processus de production par fusion de gluons et par annihilation de quarks, et nous avons trouvé que ce dernier contribue pour environ 16% à la section efficace totale. Vu la variation d'environ 20% de l'ordre dominant de la section efficace avec l'échelle de QCD, nous estimons que les corrections d'ordre plus élevées sont importantes. Pour les 2 sources de bruit de fond, $t\bar{t}$ et ZZ^*/γ^*, les calculs théoriques récents ont été examinés et ont servi à normaliser les sections efficaces du générateur de Monte Carlo. Nous avons étudié l'optimisation des coupures de l'analyse. Les coupures en p_T des deux premiers électrons ont été choisies à 20 GeV et à 15 GeV, pour avoir une acceptance du signal de plus de 99%. Le très petit nombre d 'événements de ce canal, en particulier pour les plus basses masses possibles, fait que des coupures en p_T aussi basses que 10 GeV et 7 GeV pour les 3ième et 4ième électrons respectivement sont optimales. Les fonds irréductibles, $t\bar{t}$ et $Zb\bar{b}$, peuvent être efficacement supprimés par les coupures d'isolation, demandant l'absence de traces chargées avec $p_T > 2{,}5$ GeV dans un cône $R = 0,2$ autour des quatre électrons.

Les résultats de l'analyse au niveau des particules du canal $H \rightarrow ZZ^* \rightarrow 4e^{\pm}$ conduit à des exigences très strictes pour la reconstruction des électrons. La validité du signal est, en gros, proportionnelle à la racine carrée de la largeur de la masse du Higgs reconstruite. De plus, le petit nombre d'événements de signal attendus, le faible moment transverse des deux électrons les plus légers et la prédominance de la résolution du détecteur dans la largeur du Higgs reconstruit demandent d'avoir de bonnes efficacité et précision de reconstruction des électrons. Ceci a été étudié grâce à une description détaillée du détecteur. Pour la reconstruction des traces, l'algorithme de recherche des traces est basé sur le filtre de Kalman. Pour la reconstruction des agrégats dans le calorimètre électromagnétique, un algorithme de recherche spécialement adapté a été développé ; il suit, événement par événement, les fluctuations du point d'impact et de la direction des particules. Le plus gros problème dans la reconstruction des électrons à CMS vient du bremsstrahlung dans la matière du trajectomètre. Dans ce travail, nous avons étudié un algorithme de récupération des photons de bremsstrahlung. Les agrégats de photons sont recherchés dans une région déterminée par l'énergie transverse des électrons mesurés, puis associés aux agrégats d'électrons. Les propriétés intrinsèques de cette méthode, testée avec les informations de Monte Carlo pour l'identification des traces d'électrons de 10 GeV d'impulsion transverse, lui donnent une efficacité de reconstruction supérieure d'environ 30% à celle de la méthode recherchant uniquement les agrégats d'électrons. Pour des électrons de 30 GeV de p_T, le gain avec la méthode de récupération est d'environ 15%. L'algorithme de récupération est aussi utilisé pour améliorer l'efficacité de l'identification des électrons. Au lieu d'utiliser le barycentre d'un simple agrégat pour correspondre à la trace extrapolée, l'ensemble de toutes les combinaisons possibles d'agrégats électrons-photons est d'abord déterminé, et leur barycentre est utilisé pour la détermination de la trace d'électron correspondante. Cet algorithme donne une efficacité meilleure d'environ 10% pour des élec-

trons de p_T 10 GeV, et d'environ 5% pour des électrons de p_T 30 GeV. De plus, nous avons étudié l'optimisation de l'estimateur de l'impulsion des électrons. En utilisant des prédictions de la répartition des dépôts d'énergie de l'électron dans le calorimètre électromagnétique, la résolution en énergie peut être améliorée de plus de 15% pour des électrons de p_T 10 GeV, pour environ 50% des événements. L'amélioration s'accroît avec la valeur du bruit par canal ainsi qu'avec le moment transverse de l'électron. Pour l' estimation finale du moment de l'électron, nous avons combiné l'estimateur du moment du trajectomètre et l'estimateur d'énergie du calorimètre électromagnétique. Des améliorations d'efficacité significatives ont été obtenues, la résolution étant donnée par celle du trajectomètre à basse énergie, et celle du calorimètre électromagnétique à haute énergie. Les algorithmes développés ont été appliqués à la reconstruction des événements $H \rightarrow ZZ^* \rightarrow 4e^{\pm}$. Les résultats obtenus pour la largeur de la masse du Higgs reconstruit sont de 1,3 GeV, 1,6 GeV et 1,8 GeV pour des masses du Higgs de respectivement 130 GeV, 150 GeV et 170 GeV, avec une efficacité dans la fenêtre $m_H \pm 2\sigma_{m_H}$ de 67%. En combinant les résultats de la reconstruction avec ceux de l'analyse au niveau des particules, nous concluons que le bosons de Higgs peut être trouvé par $H \rightarrow ZZ^* \rightarrow 4e^{\pm}$ dans le domaine de masse s'étendant de 127 GeV à 168 GeV et de 172 GeV à 2 m_Z, en un an de LHC fonctionnant à la luminosité nominale. Au voisinage de 150 GeV, le Higgs peut être trouvé plus rapidement, dés la première année de LHC fonctionnant à basse luminosité.

CMS discovery potential for the Higgs boson
in the $H \rightarrow ZZ^* \rightarrow 4e^{\pm}$ decay channel.
Contribution to the construction of the CMS electromagnetic calorimeter.

Contents

Introduction

Chapter 1 *Physics of the Higgs boson*

1.1 Introduction 55
1.2 The Standard Model and beyond 55
1.2.1 The electroweak sector 56
1.2.2 The Higgs mechanism 57
1.2.3 Limits on the Higgs mass 60
1.2.4 Beyond the Standard Model 62
1.3 Higgs boson production at the LHC 65
1.3.1 Gluon fusion: $gg \to H$ 65
1.3.2 W and Z fusion: $qq \to V^*V^*qq \to Hqq$ 66
1.3.3 Higgs-strahlung: $q\bar{q} \to V^* \to VH$ 67
1.3.4 Associated production with a pair $t\bar{t}$ 67
1.3.5 Cross sections for Higgs boson production at the LHC 68
1.4 Higgs decays 68
1.4.1 Decays to fermion pairs 69
1.4.2 Decays to gauge boson pairs 69
1.4.3 Total decay width and branching ratios 70

Chapter 2 *The Large Hadron Collider and the CMS detector*

2.1 Introduction 71
2.2 The Large Hadron Collider 71
2.3 The CMS detector 74
2.4 The tracking system 76
2.5 The electromagnetic calorimeter 78
2.5.1 Lead tungstate crystals 79
2.5.2 Photodetectors and readout electronics 80
2.5.3 Energy resolution 81
2.5.4 Properties measured in the test beam 81
2.6 The hadron calorimeter 86
2.7 The muon system 87
2.8 The trigger and data acquisition systems 88

Chapter 3 *Contribution to the construction of the electromagnetic calorimeter*

3.1 Introduction 91
3.2 The electromagnetic calorimeter structure 92
3.3 Light collection optimization 98
3.3.1 The light collection curve 98
3.3.2 Choice of the crystal surface 99
3.3.3 Choice of the alveolar structure material 100
3.4 Production of the alveolar structures 102
3.5 Optical quality control of the alveolar structures 106
3.5.1 MONICA 106
3.5.2 The optical control procedure 113
3.5.2.1 Reference measurement 113
3.5.2.2 Aluminum sample measurement 113
3.5.2.3 Alveolar structure measurement 116
3.5.3 Results on the Module 0 117
3.6 Conclusion 121

Chapter 4 *Study of the $H \to ZZ^* \to 4e^{\pm}$ signal and the backgrounds*

4.1 Introduction 123
4.2 Higgs transverse momentum 124
4.3 Study of the signal characteristics 132
4.3.1 Z boson kinematics 132
4.3.2 Electron kinematics 133
4.3.3 Internal bremsstrahlung 134
4.3.4 Generation and preselection 136
4.4 Study of the backgrounds 138
4.4.1 The ZZ^*/γ^* background 139
4.4.2 The $t\bar{t}$ background 141
4.4.3 The $Zb\bar{b}$ background 146
4.4.4 Summary of the backgrounds estimate 151
4.5 Trigger and detector geometrical acceptances 152
4.6 Analysis cuts 153
4.6.1 Electron cuts 153
4.6.2 Z mass cuts 156
4.6.3 Z* mass cuts 157
4.6.4 4-electrons invariant mass cut 158
4.7 Isolation 159
4.8 Additional cuts 161
4.8.1 Azimuthal distance between the Z's and pT4e cuts 161
4.8.2 Angular distributions and scaled electron energy in the Higgs frame 162
4.9 Results on signal visibility 164

Chapter 5 *Study of the $H \to ZZ^* \to 4e^{\pm}$ reconstruction*

5.1 Introduction 167
5.2 The bremsstrahlung problem 168
5.3 Track reconstruction 173
5.4 Cluster reconstruction 174
5.5 Bremsstrahlung photons recovery method 177
5.5.1 Electron kinematics 177
5.5.2 Method and results 180
5.5.3 Hard bremsstrahlung photons recovery 185
5.6 Electron momentum estimation 191
5.6.1 Weighting method 191
5.6.1.1 Method description 191
5.6.1.2 Shower model 194
5.6.1.3 Covariance matrix 199
5.6.1.4 Results 202
5.6.1.5 Summary and discussion 211
5.6.2 Electron momentum estimator 212
5.7 Results and discussion 217

Conclusion

Bibliography

Abstract

Résumé

Introduction

The central question of today's particle physics is the origin of the particle masses, or in the quantum field theory language the electroweak symmetry breaking mechanism. The most plausible electroweak symmetry breaking scenario is the so called Higgs mechanism. It allows to account for the quarks, leptons and vector bosons masses and predicts the existence of at least one scalar boson, the famous Higgs particle.

Direct searches for the Higgs bosons through its decays, performed at LEP and Tevatron accelerators, have not yet given positive results, setting therefore a lower limit on its mass to about 100 GeV. Theoretical arguments using a consistency of the Standard Model and indirect searches set a higher limit on the Higgs boson mass to several hundreds GeV. The resulting mass region will be efficiently explored by a new accelerator, the Large Hadron Collider (LHC). It is currently being built at the European laboratory for particle physics (CERN), near Geneva, and is expected to start in 2005. The Compact Muon Solenoid (CMS) detector, one of the two general purpose detectors, will be used to explore the physics reachable at the LHC.

The subject of this thesis is a study of the CMS potential for the Higgs boson search through the decay channel $H \rightarrow ZZ^* \rightarrow 4e^{\pm}$. This channel is expected to be used for Higgs search in the mass region of about 120 to 180 GeV. The electromagnetic calorimeter is essential for the electron detection. Our contribution to its construction is also presented in this thesis.

In the first chapter we give a short overview of the Standard Model Higgs sector, recent theoretical and experimental limits on the Higgs boson mass and an outline of the Higgs sector in the theories beyond the Standard Model. In somewhat more details we present recent theoretical calculations relevant for our study: main Higgs production mechanisms at the LHC and Higgs branching ratios.

A short description of the Large Hadron Collider and the Compact Muon Solenoid detector is given in the second chapter. The main CMS subdetector systems are introduced. An emphasis is given on the electromagnetic calorimeter performances, since it is one of the most important detectors involved in the electron detection.

In order to reach and maintain requested performances of the electromagnetic calorimeter it is important to control the characteristics of each of its component. In the third chapter we describe a system for the quality control of the alveolar containers, the supporting structures of the crystal towers. We insist on the description of the optical quality control system, where the developed instrument and procedure, as well as obtained results are presented.

Our study of the $H \rightarrow ZZ^* \rightarrow 4e^{\pm}$ sensitivity is presented in the fourth chapter. The study is based on a particle level analysis, using the most recent theoretical knowledge and the newest

version of the Monte Carlo particle generators. Emphasis is put on the Higgs transversal momentum and on the $Zb\bar{b}$ background studies, important aspects for which more detailed investigations were needed. The kinematical characteristics of the signal and background processes, the optimization of the kinematical and topological cuts, as well as some additional cuts will be presented, together with the results on expected Higgs visibility through this channel.

In the fifth chapter we study the detector effects in the $H \rightarrow ZZ^* \rightarrow 4e^{\pm}$ search in CMS. The recently proposed electron reconstructing algorithms are implemented and used in a detailed detector simulation. The emphasis is put on the bremsstrahlung in the tracker material, which is the main problem in the electron reconstruction. The algorithms developed for bremsstrahlung photon recovery are presented. In order to efficiently use these algorithms, sophisticated electron energy estimator was needed. We have developed a new method for electron energy estimation, using a shower model to predict an electron energy deposition pattern in the electromagnetic calorimeter. As a final electron momentum estimator a combination of the measurements from the electromagnetic calorimeter and the tracking system is used. The developed algorithms are then applied on the signal events reconstruction, and the results compared with those obtained using particle level analysis.

Chapter 1

Physics of the Higgs boson

1.1 Introduction

Since the discovery of the top quark in 1995 [1] at the Fermilab Tevatron collider the Higgs boson remains the last missing piece of the Standard Model. This particle, aimed to provide an understanding of the masses of gauge bosons and fermions, has been searched for extensively at LEP and Tevatron colliders. Since its mass is not predicted by the theory, a machine dedicated to the Higgs search should cover a wide range of accessible mass. The LHC has been designed for the Higgs search in particular. In this chapter, we recall how the Higgs boson is introduced in the Standard Model, give the latest results for the Higgs mass limits from the theory and the experiments, and review a possible extension of the Higgs sector. We also present the processes for Higgs production at LHC and its decays.

1.2 The Standard Model and beyond

The Standard Model (SM) is our theory for the quantitative descriptions of all interactions of fundamental particles except quantum gravity effects. It is a renormalizable relativistic quantum field theory based on a non-Abelian gauge symmetry of the gauge group $SU(3) \times SU(2) \times U(1)$. The Standard Model consists of two sectors: the Quantum Chromodynamics (QCD) and the Electroweak theory. Quantum Chromodynamics is a vector gauge theory which describes the SU(3) color interactions of quarks and gluons [2]. The Electroweak theory describes the electromagnetic and weak interactions of quarks and leptons as a chiral non-Abelian isospin and an Abelian hypercharge gauge symmetry $SU(2) \times U(1)$ [3].

The QCD sector of the Standard Model is described by the Lagrangian:

$$L_{SU(3)} = -\frac{1}{4}F^i_{\mu\nu}F^{i\mu\nu} + \sum_r \bar{q}_{r\alpha} i\gamma^\mu D^\alpha_{\mu\beta} q^\beta_r . \qquad \text{(EQ 1)}$$

The $F^i_{\mu\nu}$ are the tensors of the gluon field G^i_μ , $i = 1, \ldots, 8$:

$$F^i_{\mu\nu} = \partial_\mu G^i_\nu - g_s f_{ijk} G^j_\mu G^k_\nu . \qquad \text{(EQ 2)}$$

g_s is the strong coupling constant, and f_{ijk} $(i, j, k = 1, \ldots, 8)$ are the *SU(3)* group structure constants. In the second term of the $L_{SU(3)}$ q_r is the quark spinor of the rth flavor, $\alpha, \beta = 1, 2, 3$ are color indices, and the covariant derivative can be written in the form:

$$D^\alpha_{\mu\beta} = (D_\mu)_{\alpha\beta} = \partial\delta_{\alpha\beta} + ig_s G^i_\mu \lambda^i_{\alpha\beta}/2 , \qquad \text{(EQ 3)}$$

where λ^i are *SU(3)* matrices. We can remark that $L_{SU(3)}$ does not contain quark mass terms $m_q \bar{q} q$. Although allowed by QCD alone, they are forbidden by the chiral symmetry in the electroweak sector of the theory. In the following sections we will show how quark masses can be introduced in the theory through the spontaneous symmetry breaking mechanism.

The electroweak sector of the theory contains the Higgs sector and, therefore, we will describe it in more details.

1.2.1 The electroweak sector

A phenomenological basis for the formulation of the electroweak sector of the Standard Model is given by the following empirical facts:

- *The $SU(2) \times U(1)$ family structure of the fermions*

  The gauge group $SU(2)$ corresponds to the weak isospin symmetry (I) while $U(1)$ represent a weak hypercharge symmetry (Y). The fermions are organized in isospin multiplets: doublets with $I = 1/2$ and singlets with $I = 0$:

$$\begin{pmatrix} \nu_e \\ e \end{pmatrix}_L \begin{pmatrix} \nu_\mu \\ \mu \end{pmatrix}_L \begin{pmatrix} \nu_\tau \\ \tau \end{pmatrix}_L \qquad e_R, \mu_R, \tau_R$$
$$\begin{pmatrix} u \\ d \end{pmatrix}_L \begin{pmatrix} c \\ s \end{pmatrix}_L \begin{pmatrix} t \\ b \end{pmatrix}_L \quad u_R, d_R, c_R, s_R, t_R, b_R \qquad \text{(EQ 4)}$$

  The members of the same multiplet have the same value of the weak hypercharge. Indices L and R denote chiral projections of the Dirac spinors, i.e. left and right projections.

- *The Gell-Mann-Nishijima relation:*

$$Q = I_3 + \frac{Y}{2}, \qquad \text{(EQ 5)}$$

  where Q is the particle charge.

- *The existence of vector bosons*

  There are four vectors bosons, mediators of the electroweak force: γ, W^+, W^-, Z. The photon is massless, while the masses of $W^\pm$ and Z are about 80 GeV and about 90 GeV, respectively.

This empirical structure can be unified in a theory of electromagnetic and weak interactions by interpreting $SU(2) \times U(1)$ as the group of local gauge transformations under which the Langrangian is invariant. Since this symmetry forbids mass terms in the langrangian, but we know that the fermions and the vector bosons (except the photon) have a mass, this symmetry must be broken spontaneously [4], preserving the renormalizability [5] of the theory. The most plausible mechanism for such a symmetry breaking is called the Higgs mechanism [6], exploring the idea that the lowest energy (vacuum) state does not respect the gauge symmetry and induces effective masses for particles propagating through it. It, therefore, can account for the particle masses and predicts the existence of at least one scalar particle, the Higgs boson.

According to a general principle for the construction of a gauge invariant field theory with a spontaneous symmetry breaking, the electroweak Lagrangian can be written as a sum of a gauge, fermion, Higgs and Yukawa terms:

$$L_{SU(2)\times U(1)} = L_G + L_f + L_H + L_Y. \qquad \text{(EQ 6)}$$

$SU(2)\times U(1)$ is a non-Abelian group with weak isospin I_1, I_2, I_3 and weak hypercharge Y operators as generators. Each of these generators is associated with a vector field: the isospin with the isotriplet of vector gauge fields $W_\mu^{1,2,3}$ and the hypercharge with the vector gauge field B_μ. The corresponding fields tensors are:

$$\begin{aligned} W_{\mu\nu}^a &= \partial_\mu W_\nu^a - \partial_\nu W_\mu^a - g\varepsilon_{abc} W_\mu^b W_\nu^c \\ B_{\mu\nu} &= \partial_\mu B_\nu - \partial_\nu B_\mu \end{aligned}, \qquad \text{(EQ 7)}$$

where g is the $SU(2)$ coupling constant. With the above tensors the gauge term of the electroweak lagrangian can be written as

$$L_G = -\frac{1}{4} W_{\mu\nu}^a W^{a\mu\nu} - \frac{1}{4} B_{\mu\nu} B^{\mu\nu}. \qquad \text{(EQ 8)}$$

One can notice the absence of vectors bosons mass terms $\sim V^\mu V_\mu m_V$, where m_V represents a mass and V^μ the vector field, since it would not be invariant under the $SU(2)\times U(1)$ transformations of the vector fields.

The Fermion sector of the electroweak langrangian can be written in the form:

$$L_f = \sum_j \bar{l}_L^j i\gamma^\mu D_\mu l_L^j + \sum_j \bar{l}_R^j i\gamma^\mu D_\mu l_R^j + \sum_j \bar{q}_L^j i\gamma^\mu D_\mu q_L^j + \sum_j \bar{q}_R^j i\gamma^\mu D_\mu q_R^j, \qquad \text{(EQ 9)}$$

where j is the family index, l_L (l_R) are left (right) leptons fields, and q_L (q_R) are left (right) quarks fields. The interactions between fermions and gauge bosons are induced through the covariant derivative:

$$D_\mu = \partial_\mu + igI_a W_\mu^a + ig'\frac{Y}{2} B_\mu, \qquad \text{(EQ 10)}$$

where g' is the $U(1)$ coupling constant. Here again, one can notice the absence of fermion mass terms since they are forbidden by the gauge symmetry.

1.2.2 The Higgs mechanism

The simplest choice of the scalar field needed for the electroweak symmetry breaking is an isodoublet of complex fields with hypercharge $Y = 1$:

$$\Phi = \begin{pmatrix} \Phi^+ \\ \Phi^0 \end{pmatrix} = \begin{pmatrix} (\Phi_1 + i\Phi_2)/\sqrt{2} \\ (\Phi_3 + i\Phi_4)/\sqrt{2} \end{pmatrix}, \qquad \text{(EQ 11)}$$

where Φ_i, $i = 1, \ldots, 4$ are real scalar fields.

The langrangian of these scalar fields is:

$$L_H = (D_\mu \Phi)^\dagger (D^\mu \Phi) - V(\Phi), \tag{EQ 12}$$

where the potential is given by the relation:

$$V(\Phi) = \mu^2 \Phi^\dagger \Phi + \lambda (\Phi^\dagger \Phi)^2. \tag{EQ 13}$$

The choice of this potential is based on the requirements to have a local gauge invariance, non-zero vacuum expectation value of neutral components and renormalizability of the interactions in the langrangian.

The scalar potential depends on two parameters μ and λ. For $\lambda < 0$ it does not have a lower limit and the theory does not have a physical meaning. In the case $\lambda > 0$ and $\mu^2 > 0$, the potential has a minimum at $\Phi = 0$ and there is no symmetry breaking possibility. The interesting case is when $\lambda > 0$ and $\mu^2 < 0$, where the scalar potential has a minimum for

$$\Phi^\dagger \Phi = \frac{1}{2}(\Phi_1^2 + \Phi_2^2 + \Phi_3^2 + \Phi_4^2) = -\frac{\mu^2}{2\lambda} \equiv \frac{v^2}{2}, \tag{EQ 14}$$

The vacuum, which is the lowest energy state, corresponds to one of these minima.

So far all the expressions respect the symmetry under the $SU(2) \times U(1)$ transformations. Because of the complex nature of the scalar field, the above relation has an infinite number of solutions which transforms under the $SU(2) \times U(1)$ group. The perturbative theory demands the expansion of Φ near its vacuum expectation value. Therefore, when choosing one solution as the vacuum expectation value, the above equations are no more symmetric. Every choice of the minima will generate a mass for the boson associated with the group whose symmetry becomes broken. Therefore, to have three massive bosons and one massless photon, we choose the minimum which remains invariant under the symmetry having the charge as the generator. That is obtained with the vacuum expectation value having the weak isospin $I = 1/2$, $I_3 = -1/2$ and weak hypercharge $Y = 1$:

$$\Phi_0 = \frac{1}{\sqrt{2}} \begin{pmatrix} 0 \\ v \end{pmatrix}. \tag{EQ 15}$$

One can now rewrite the scalar field in the form:

$$\Phi(x) = \frac{1}{\sqrt{2}} e^{i\lambda^a(x) I^a} \begin{pmatrix} 0 \\ v + H(x) \end{pmatrix}, \tag{EQ 16}$$

where the fields $\lambda^a(x)$, $(a = 1, 2, 3)$ and $H(x)$ have zero vacuum expectation values. Since L_H is invariant under the local $SU(2)$ transformations one can choose a so called unitary gauge, in which the particle content becomes visible:

$$\Phi(x) \rightarrow \Phi'(x) = e^{-i\lambda^a(x) I^a} \Phi(x) = \frac{1}{\sqrt{2}} \begin{pmatrix} 0 \\ v + H(x) \end{pmatrix}. \tag{EQ 17}$$

By putting this field into the kinematical term of L_H and identifying the gauge bosons as:

$$W_\mu^\pm = \frac{W_\mu^1 \mp iW_\mu^2}{\sqrt{2}}$$
$$Z_\mu = \cos\theta_W W_\mu^3 - \sin\theta_W B_\mu \qquad \text{(EQ 18)}$$
$$A_\mu = \sin\theta_W W_\mu^3 + \cos\theta_W B_\mu$$

where θ_W is so the called Weinberg mixing angle, Z_μ is the neutral vector boson field and A_μ is the photon field. From quadratic terms in the relations:

$$(D_\mu\Phi')^\dagger(D^\mu\Phi') = \left(\frac{g^2v^2}{4}\right)W_\mu^+W^{-\mu} + \frac{1}{2}\left(\frac{(g^2+g'^2)v^2}{4}\right)Z_\mu Z^\mu + \ldots$$
$$V(\Phi') = \frac{1}{2}(2\mu^2)H^2 + \ldots \qquad \text{(EQ 19)}$$

we can read the following masses:

$$M_W = \frac{gv}{2}$$
$$M_Z = \frac{\sqrt{g^2+g'^2}}{2}v \qquad \text{(EQ 20)}$$
$$M_H = \sqrt{2}\mu = \sqrt{2\lambda}v$$

The parameter v can be determined from muon decay experiments and is estimated to $v = 246$ GeV.

The fermion sector of the Standard Model is described by the Yukawa Langrangian:

$$L_Y = -g_e\bar{l}_L\Phi e_R - g_u\bar{q}_L\Phi^c u_R - g_d\bar{q}_L\Phi d_R - \ldots \qquad \text{(EQ 21)}$$

where g_i are Yukawa coupling constants and

$$\Phi^c = \begin{pmatrix} \Phi^{0*} \\ -\Phi^- \end{pmatrix}. \qquad \text{(EQ 22)}$$

By substituting the Higgs field in the unitary gauge, L_Y becomes:

$$L_Y = -\sum_f m_f\bar{\Psi}_f\Psi_f - \sum_f \frac{m_f}{v}\bar{\Psi}_f\Psi_f H, \qquad \text{(EQ 23)}$$

where ψ_f represents a fermion field. The fermion masses are given by:

$$m_f = g_f\frac{v}{\sqrt{2}}. \qquad \text{(EQ 24)}$$

As an outcome of the mass generation mechanism, the Yukawa interactions between massive fermions and the Higgs field are proportional to the fermions masses:

$$g_f = \frac{m_f}{v}. \qquad \text{(EQ 25)}$$

1.2.3 Limits on the Higgs mass

As we can see from the relation 20, the Higgs mass depends on the unknown coupling λ, and therefore cannot be predicted. Nevertheless, consistency arguments for the Standard Model give us informations about the allowed mass range. As all the couplings in the gauge theory, the quartic coupling λ evolves with the energy scale, and consistency requires it to be finite and positive so that we can deduce bounds for the Higgs mass.

A first bound can be derived through the requirement that spontaneous symmetry breaking actually occurs [7], that is,

$$V(v) < V(0). \qquad \text{(EQ 26)}$$

It is essentially equivalent to the requirements that λ remains positive at all energy scales, since for the negative quartic coupling the potential is unbounded from below and has no state of minimum energy. Close to this limit, i.e. for small λ, corresponding to light Higgs, radiative corrections from the top quark and gauge couplings become important and the above requirement yields a lower bound on the Higgs boson mass [8][9]:

$$M_H > \frac{3v}{32\pi^2}(16g_t^4 - g^4 - 2g^2g'^2 - 3g'^4)\log\left(\frac{\Lambda}{M_H}\right). \qquad \text{(EQ 27)}$$

Λ is an energy scale at which the Standard Model in no longer valid and new physics should arise. This bound corresponds to the lower shaded region in figure 1.

If λ is large, which corresponds to a heavy Higgs boson, the requirements that it remains finite up to some large scale (Λ) gives an upper bound on the Higgs mass [8]:

$$M_H^2 < \frac{8\pi^2 v^2}{3\log(\Lambda/v^2)}. \qquad \text{(EQ 28)}$$

This is an approximate relation since the effects of gauge couplings and the top quark are neglected. A more sophisticated analysis, including the running of all gauge and Yukawa couplings yield a similar upper bound and is shown as the upper shaded region in figure 1 [9]. This bound is often called the 'triviality bound'.

A phenomenological bound on the Higgs mass comes from precision electroweak measurements. The Higgs boson enters into one loop radiative corrections in the Standard Model and a global fit to the electroweak data, taking the Higgs mass as a variable to be fitted, gives mass limits. The latest results of such fit constrain the Higgs mass to [10]:

$$M_H = 62^{+53}_{-30}\ \text{GeV}, \qquad \text{(EQ 29)}$$

with

$$M_H < 170\ \text{GeV at 95\% confidence level.} \qquad \text{(EQ 30)}$$

However, the limits derived from this method are relatively weak since the radiative corrections dependence on the Higgs mass is only logarithmic.

Although the Higgs mass remains a free parameter, the combination of limits from the triviality bound and from fits to the electroweak data suggests that the Higgs boson may be relatively light, in the few hundreds GeV range.

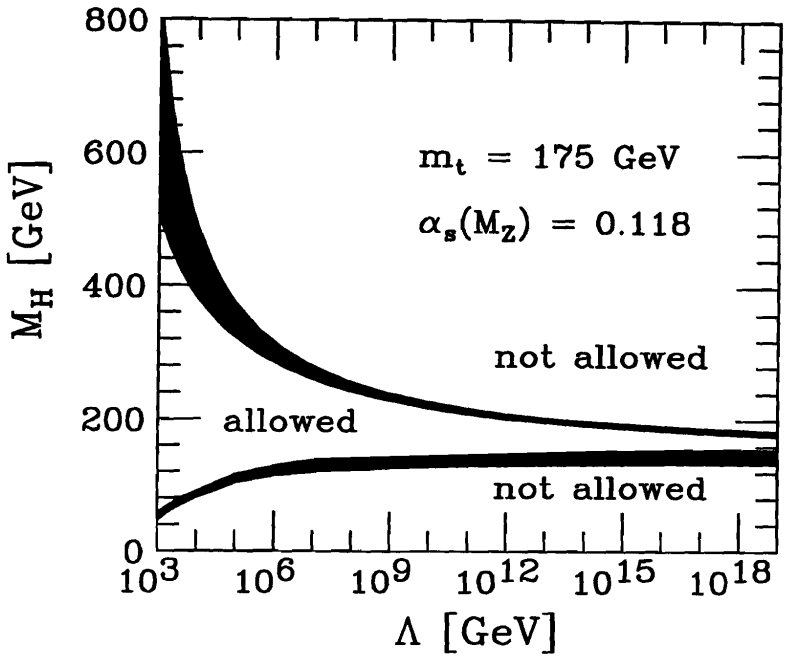

FIGURE 1. The lower and upper Higgs mass theoretical bounds as a function of the energy scale Λ at which the Standard Model breaks down. The shaded areas reflect the theoretical uncertainties in the calculation of the Higgs mass bound [9].

Up to spring 2000, the direct searches performed by the four LEP experiments did not show any evidence for the Higgs boson. From the data collected in 2000 at center of mass energies between 200 and 210 GeV, a lower bound of

$$M_H > 112.3 \text{ GeV at } 95\% \text{ confidence level,} \qquad \text{(EQ 31)}$$

has been obtained [11].

Very recently, a number of events compatible with a Higgs boson production with mass around 114-115 GeV was reported in the combined results of the four LEP experiments [11]. However, the topology of these events is also compatible with originating from other known standard model processes. Consequently, the LEP's experimental program is extended until beginning of November 2000, in order to better test the possible Higgs boson signal at 114-115 GeV.

If the Higgs boson is not discovered at LEP II, the next place to look for will be the Tevatron collider at Fermilab. It is a proton-antiproton collider, currently being upgraded to the center of mass energy of 2 TeV. Data taking for the Run II will start in March 2001, with two experiment, CDF and D0. With expected machine and detectors performances the LEP II Higgs sensitivity will start to be extended a few months before the start of the LHC [12].

1.2.4 Beyond the Standard Model

Despite the remarkable agreement between the precision measurements of electroweak observables and Standard Model predictions, there are strong theoretical arguments that the Standard Model is not the ultimate theory of the fundamental particles and their interactions. It has about 20 arbitrary parameters, which may seem too many for a fundamental theory and leaves several unanswered questions. Some of them concerns the problems of unification of interactions, number of fermions families, neutrino mass, hierarchy (or naturalness) etc. Therefore, the Standard Model is generally considered as an effective field theory, valid up to some energy scale Λ.

Among these problems, the hierarchy problem [13] is considered to be one of the most serious theoretical drawbacks of the Standard Model. Most of the attempts to build theories beyond the Standard Model have concentrated on its solution. The hierarchy problem comes from the difficulty in the theory to keep fundamental scalar particles much lighter than the maximum energy scale up to which the theory remains valid. From figure 1 we see the Higgs mass bounds suggesting that the consistency of the Standard Model is broken unless $M_H < O(1\ \text{TeV})$. But, already at one loop there are quadraticaly divergent contributions to the Higgs mass. These terms could be canceled by mass counterterms, but they should be fine tuned at each order in the perturbation theory, with a precision of roughly 1 part in 10^{15}. Although formally there is nothing wrong with such tuning it is regarded as unnatural.

One solution to this problem comes from the supersymmetric theory. Such a theory relates fermions and scalars in the same multiplets. The loop contributions from fermions and scalars have opposite sign and therefore cancel in the corrections to the Higgs mass. The supersymmetry langrangian contains scalars and fermions with the same masses. Since, for example, there is no scalar particle with the mass of the known particles, such a symmetry must be broken.

The simplest solution for the symmetry breaking is to introduce two complex SU(2) Higgs doublets:

$$H_1 = \begin{pmatrix} H_1^+ \\ H_1^0 \end{pmatrix}, H_2 = \begin{pmatrix} H_2^0 \\ H_2^- \end{pmatrix}, \qquad \text{(EQ 32)}$$

with therefore 8 degrees of freedom. This model is called the Minimal Supersymmetric Standard Model (MSSM). The symmetry is broken when the neutral components of the Higgs doublets get the vacuum expectation values:

$$\langle H_1 \rangle = \begin{pmatrix} 0 \\ v_1 \end{pmatrix}, \langle H_2 \rangle = \begin{pmatrix} 0 \\ v_2 \end{pmatrix}. \qquad \text{(EQ 33)}$$

As in the Standard Model, the *W's* and *Z* get masses by absorbing three degrees of freedom. Five degrees of freedom remain, and therefore there are 5 Higgs bosons, denoted by: charged Higgs bosons $H^{\pm}$, a CP-odd neutral A, and 2 CP-even neutral, h and H. At the tree level, the Higgs sector of MSSM is described by two parameters. The usual choice is:

$$\tan\beta \equiv \frac{v_2}{v_1} \text{ and } m_A. \qquad \text{(EQ 34)}$$

The MSSM Higgs boson masses versus m_A for different values of $\tan\beta$ are shown on the figure 2. It is interesting to note that $H^{\pm}$, A and H are almost degenerated for high values of m_A.

One of the important predictions of the MSSM is the existence of a neutral Higgs boson with a mass less than around 130 GeV. Such a scale is accessible already by LEP II and will be explored by the upgraded Tevatron and the LHC, providing a definite test of the MSSM.

In more complicated supersymmetric models the upper bound on the lightest Higgs boson mass is changed. The absolute upper limit is about 205 GeV, for any model with arbitrary matter content compatible with gauge coupling unification at about 10^{17} GeV scale [14].

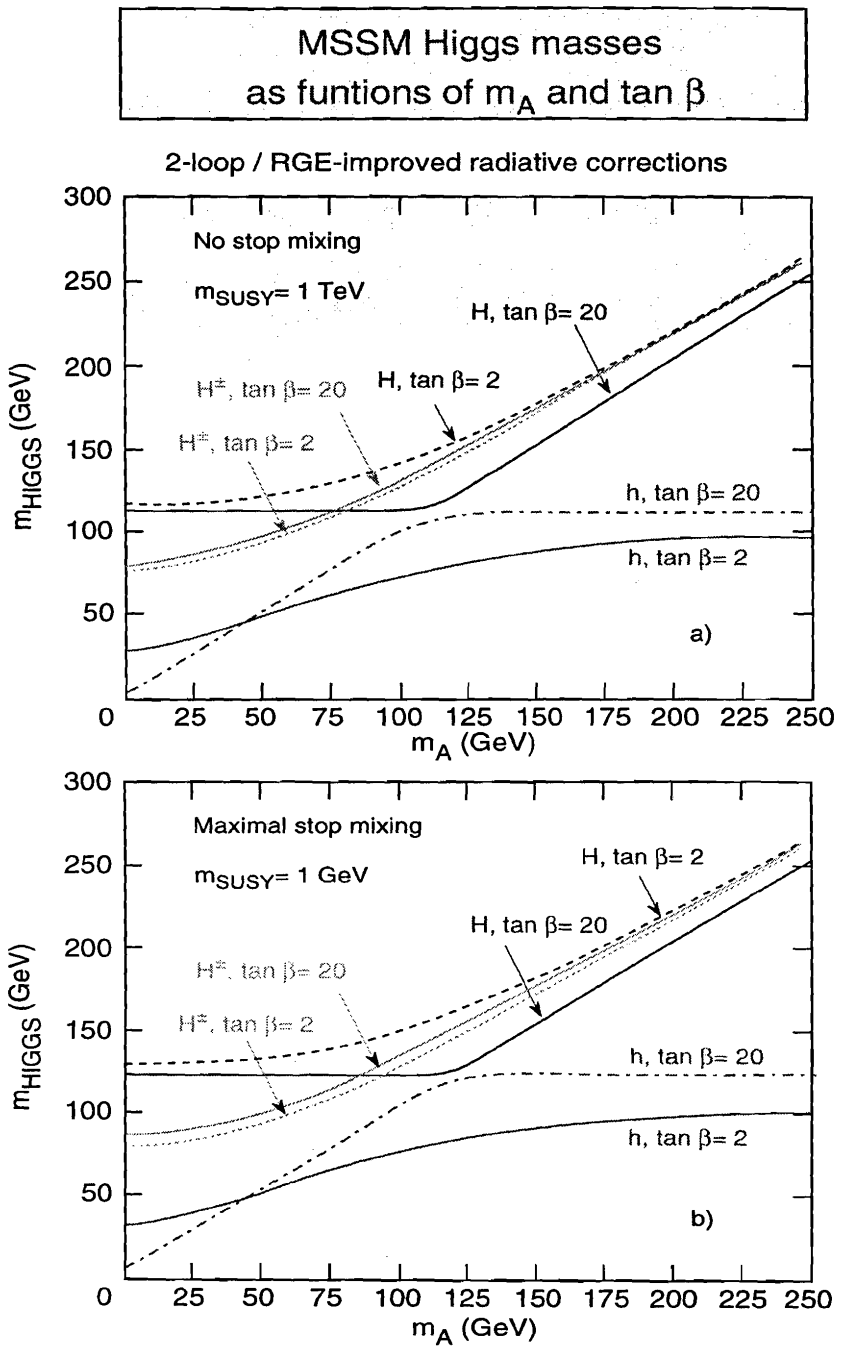

FIGURE 2. MSSM Higgs bosons masses versus m_A for various $\tan\beta$ values, including 2-loop RGE-improved radiative corrections. The results are given for two scenarii concerning the stop mixing [15].

1.3 Higgs boson production at the LHC

In this section, we shall review the most important Higgs boson production modes at the LHC. Because of its importance, a particular attention will be given to the gluon fusion process.

1.3.1 Gluon fusion: $gg \rightarrow H$

The gluon fusion process, $gg \rightarrow H$, is the dominant Higgs production mode at the LHC over the entire mass range, that is up to about 1 TeV. The coupling of the Higgs to the gluons goes through a quark triangle loop, with a dominant contribution from the heavy quarks top and bottom. The diagram at leading order is presented on the figure on the right, and the complete calculations are given in the reference [16].

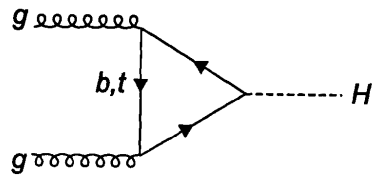

QCD corrections

In order to obtain realistic gluon fusion cross section predictions, it is necessary to calculate the 2-loop QCD radiative corrections. The cross section at this next to leading order (σ_{NLO}) can be written as a sum of virtual corrections and real corrections associated with additional partons in the final state ($gg \rightarrow Hg$, $gq \rightarrow Hq$, $q\bar{q} \rightarrow Hg$):

$$\sigma_{NLO} = \sigma_{LO} + \Delta_{virt} + \Delta_{gg} + \Delta_{qg} + \Delta_{q\bar{q}} \qquad \text{(EQ 35)}$$

The full (σ_{NLO}) calculations can be found in the reference [17].

The amount of higher order corrections is commonly expressed through the so called *'K factor'*, defined as a ratio of higher order and leading order cross sections. When considering only NLO, it is defined as:

$$K = \frac{\sigma_{NLO}}{\sigma_{LO}} \qquad \text{(EQ 36)}$$

The K factors for virtual (K_{virt}) and real ($K_{gg}, K_{qg}, K_{q\bar{q}}$) corrections are presented in figure 3. The factors K_{virt} and K_{gg} have about the same values, around 50%, while K_{qg} and $K_{q\bar{q}}$ are smaller. The total correction (K_{tot}) is positive and large, and increases the cross section for the Higgs production at LHC from gluon fusion by 60% to 90%.

The most important theoretical uncertainties in this cross section come from the parametrization of the partons distribution functions, especially the gluon ones, and from the contributions of higher orders, still unknown. An insight to partons density functions uncertainties can be obtained by calculating the cross section with different structure functions. In the reference [18], using recent proton structure functions (CTEQ4M, MRS(R1), GRV('92)), variations of about 10% of the cross section over the entire mass range were found. The variations of the σ_{NLO} with the renormalisation and factorization scales are small with respect to the variations of σ_{LO} and contribute to less than 15% [18].

A calculation of the cross section at NNLO is not yet available and needs the proton structure functions at this order, which are not yet known.

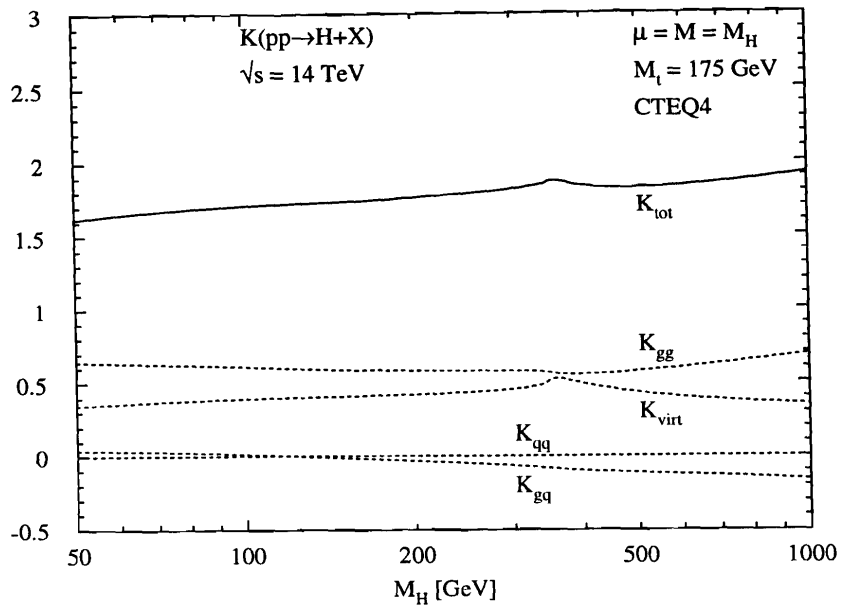

FIGURE 3. K factors for the Higgs production at LHC through gluon fusion [18].

1.3.2 W and Z fusion: $qq \to V^*V^*qq \to Hqq$

The production cross section of the Higgs boson through the fusion of W or Z bosons is one order of magnitude smaller than the production through gluon fusion in the intermediate mass range, and becomes competitive around $M_H \approx 1$ TeV [19][20]. The process at leading order is shown on the figure on the right.

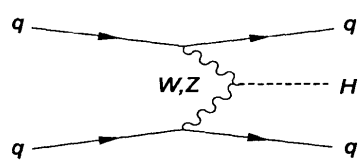

The QCD corrections are introduced by corrections to the structure functions, which are well known [20]. The K factors for these processes are presented in figure 4. We can see that the QCD corrections for the Higgs production through the vector bosons fusion are about 8-10%.

The most important characteristics of these production processes are the presence of two forward jets, a high invariant mass of these jets and a suppression of the hadronic production in the central region. An analysis at the parton level shows that these characteristics can be used for an efficient rejection of the background in the $H \to \gamma\gamma$ and $H \to \tau\tau$ decay channels. These decay channels could be used for the search of an intermediate mass Higgs already in the low luminosity running of LHC [21].

1.3.3 Higgs-strahlung: $q\bar{q} \rightarrow V^* \rightarrow VH$

The Higgs production through the Higgs-strahlung processes may be important in the intermediate mass range due to the possibility to observe the associated W or Z vector bosons. The cross section for these processes is about one to two orders of magnitude smaller than the cross section for the gluon fusion process for a Higgs mass $M_H < 200$ GeV. The Higgs-strahlung process at leading order is presented on the figure on the right, and the cross section calculation are given in the reference [22].

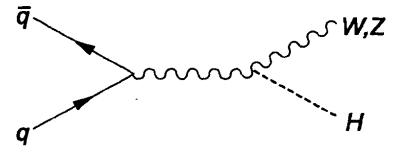

The QCD corrections are identical to the one for the Drell-Yan process [23], and therefore large. The K factor for this process is presented in figure 4. The QCD corrections to the cross section for Higgs production through the Higgs-strahlung process are about 25-40%.

1.3.4 Associated production with a $t\bar{t}$ pair

In the intermediate mass range, the cross section for the Higgs production in association with top quarks becomes similar to the Higgs-strahlung cross section. With the detection of the associated $t\bar{t}$ pair and in the $H \rightarrow \gamma\gamma$ decay channel, this process gives an additional possibility to search for the Higgs for a mass $M_H < 130$ GeV [24]. The process at leading order is presented on the diagrams below, and the cross section calculations can be found in the references [24][25]. The QCD corrections for this process are still unknown.

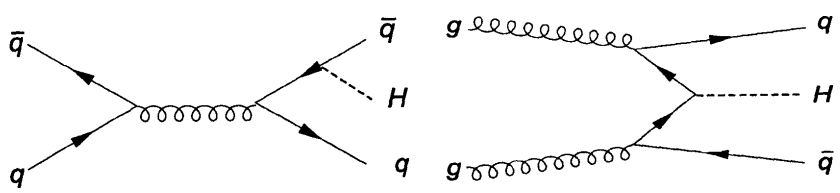

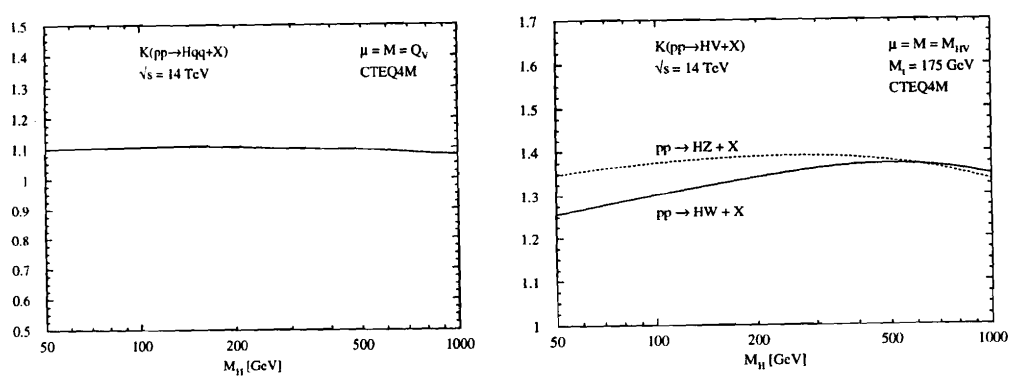

FIGURE 4. K factors for the Higgs production at LHC through vector boson fusion (left) and Higgs-strahlung (right) [18].

1.3.5 Cross sections for Higgs boson production at the LHC

The cross sections of the various Higgs production mechanisms at the LHC are presented in figure 5 as a function of the Higgs mass [18]. All known QCD and QED corrections are included in the calculations.

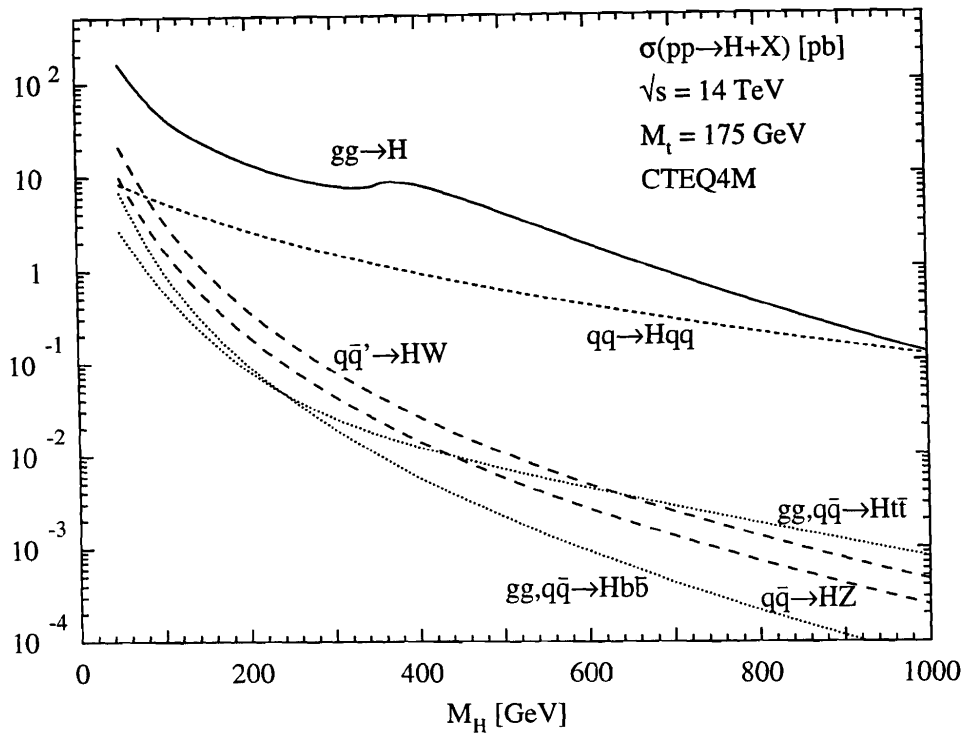

FIGURE 5. Higgs production cross sections at the LHC as a function of the Higgs mass [18].

In the entire mass range shown, the gluon fusion is the dominant production mode, and the vector boson fusion becomes competitive for $M_H \geq 800$ GeV. In the intermediate mass range, $100 \leq M_H \leq 200$ GeV, several combinations of the production and decay channels could be accessible at the LHC, thus providing the possibility to measure the Higgs couplings [26].

In the mass region of about 130 GeV to 180 GeV, the total cross section for the Higgs production is of the order of 20 pb, implying that one could expect about 2×10^5 Higgs events for first year of the LHC running.

1.4 Higgs decays

The Higgs couplings to the gauge bosons ($V = W, Z$) are proportional to their mass (M_V) squared and the Higgs coupling to the fermions is proportional to their mass (m_f):

$$g_{VVH} = 2\sqrt{\sqrt{2}G_F}M_V^2 \ , \ g_{f\bar{f}H} = \sqrt{\sqrt{2}G_F}m_f. \qquad \text{(EQ 37)}$$

Therefore, the Higgs tends to decay in pairs of the heaviest particles kinematically allowed. If possible, the measurement of different decay channels would allow to distinguish between a Standard Model Higgs and a more complex Higgs sector.

1.4.1 Decays to fermion pairs

In the lowest order the partial width for the Higgs decay into a lepton pair is given by [27]:

$$\Gamma(H \to l\bar{l}) = \frac{G_F M_l^2}{4\sqrt{2}\pi} M_H \beta^3 \qquad \text{(EQ 38)}$$

where $\beta = \sqrt{1 - 4M_l^2/M_H^2}$ is the lepton velocity. The branching ratio of decays into τ leptons is about 10% in the intermediate mass range. Muonic decay reach a level of a few 10^{-4}, and all other leptonic decay modes are phenomenologically unimportant.

The partial width for the decay into quark pairs has an additional color factor ($N_c = 3$), as well as important QCD corrections [8]

$$\Gamma(H \to q\bar{q}) = \frac{3G_F M_q^2}{4\sqrt{2}\pi} M_H \beta^3 \left(1 + \frac{4\alpha_s}{3\pi}\Delta_H^{QCD}\right). \qquad \text{(EQ 39)}$$

The QCD corrections factor, Δ_H^{QCD}, can be found in the reference [28]. To illustrate the importance of these corrections, let us mention that, for the Higgs of about 100 GeV, the branching ratio for the decay into a pair of b quarks decrease by a factor 2 when including the QCD corrections to the order α_s. The large portion of the corrections can be absorbed into a 'running' quark mass $m_q(\mu)$, evaluated at the energy scale $\mu = M_H$ [29].

The electroweak corrections for the Higgs decay into heavy quarks and into leptons are small and can be neglected [29].

1.4.2 Decays to gauge boson pairs

Above the *WW* and *ZZ* decay thresholds the decay of the Higgs boson into pairs of massive gauge bosons becomes the dominant mode. The partial widths for this decay are given by [30]:

$$\Gamma(H \to VV) = \delta_V \frac{G_F M_H^3}{16\sqrt{2}\pi}\sqrt{1-4x}(1 - 4x + 12x^2), \qquad x = \frac{M_V^2}{M_H^2}, \qquad \text{(EQ 40)}$$

with $\delta_W = 2$ and $\delta_Z = 1$. Electroweak corrections are small in the intermediate mass range [29] and thus can be neglected.

Below the *WW* and *ZZ* thresholds, the decays into off-shell gauge bosons are important. The partial widths for decays in one real and one off-shell gauge boson, $\Gamma(H \to VV^*)$, can be found in the reference [31]. For a Higgs mass slightly larger than the corresponding gauge bosons mass the decay branching ratio to a pair of off-shell gauge bosons W^*W^* and Z^*Z^*

becomes important [32]. They reach the per cent level for Higgs mass above about 100 (110) GeV for W^* (Z^*) pairs.

1.4.3 Total decay width and branching ratios

The total decay width and the branching ratios of the Higgs boson are shown in figure 6 as a function of the Higgs mass. For masses below around 120 GeV, the decay into a $b\bar{b}$ pair is largely dominant, but will be very hard to exploit at LHC due to an overwhelming QCD background. For intermediate and high masses, the dominant modes are WW and ZZ (real or off-shell), with a fall-off of the ZZ* at the opening of the WW decay channel, where both W are real. Given the fact that the gauge bosons are not directly detectable particles, final branching ratios are multiplied by the branching ratios corresponding to the decay of the gauge bosons to observable particles (for instance $BR(ZZ \rightarrow e^+e^-e^+e^-) = 0.03366^2 = 1.13\times10^{-3}$). In this way, although the two photons branching ratio is small, the fact that the photons are directly detectable will allow the use of this channel in a mass range from about 110 to 150 GeV.

The total Higgs decay width plays an important role in the design of the detectors. Up to around 200 GeV, the total Higgs width is below 1 GeV, and therefore the width of the reconstructed Higgs mass distribution will be dominated by the detector resolution. For masses above 200 GeV, the relation $\Gamma(H) = 0.5$ TeV $\times M_H^3$ (M_H in TeV) is approximately satisfied.

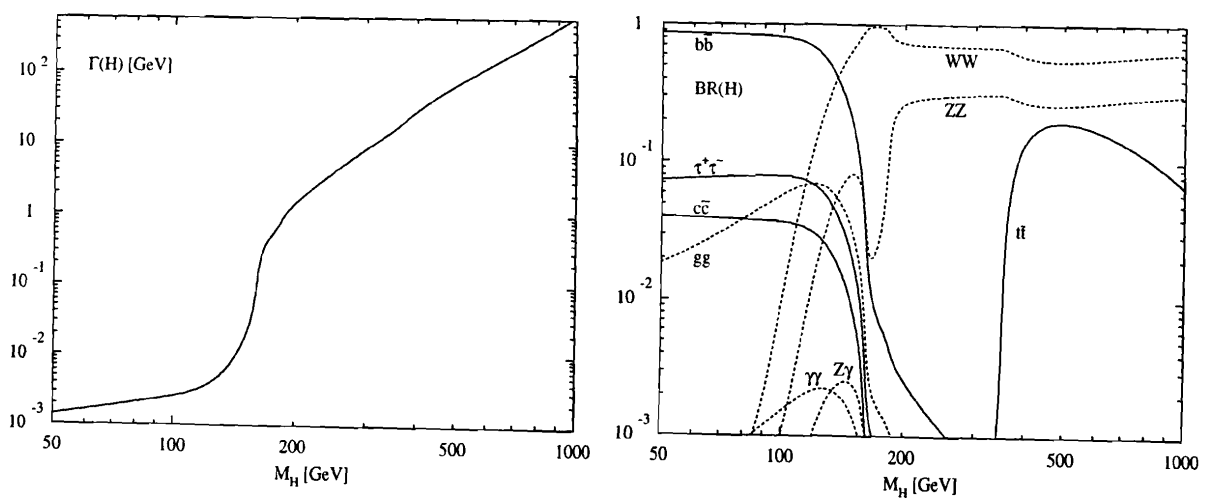

FIGURE 6. The Higgs natural width as a function of its mass (left). The Higgs branching ratio in its main decay modes as a function of the Higgs mass (right). The QCD and electroweak corrections are included [33].

Chapter 2

The Large Hadron Collider and the CMS detector

2.1 Introduction

In this chapter we will present the main characteristics of the Large Hadron Collider (LHC). In the second part the Compact Muon Solenoid (CMS) detector will be briefly described through a short overview of the subdetector systems. The electromagnetic calorimeter will be presented in more details, since its properties are important for the chapters which follow.

2.2 The Large Hadron Collider

The LHC will produce proton-proton collisions with a center of mass energy of 14 TeV. Since the proton is not an elementary particle, the energy available in the collisions between its constituents (the quarks and gluons) will be smaller but nevertheless will reach the TeV range, which is about 10 times that of CERN Large Electron Positron (LEP) collider and Fermilab Tevatron collider. Figure 7 shows the cross sections and the event rates in proton-proton and proton-antiproton collisions as a function of the center of mass energy. Comparing the LHC and the Tevatron one can see that the LHC cross sections for all of the shown processes is at least one order of magnitude higher than at Tevatron. It is also interesting to remark several orders of magnitude difference between the expected Higgs rates and those of potentially background processes ($t\bar{t}$, $b\bar{b}$), which makes the Higgs search a real challenge.

The LHC will also collide heavy ions beams such as lead with a total collision energy in excess of 1150 TeV, about 30 times higher than at the Relativistic Heavy Ion Collider (RHIC) at the Brookhaven National Laboratory in USA.

Because of the highest energy ever reached, close to the possible limits of validity of the Standard Model, the LHC will be the source of very interesting physics. The most important goal is the search for the mechanism responsible for the electroweak symmetry breaking, through the search for SM and MSSM Higgs bosons. Among many other interesting subjects are the search for supersymmetric particles, Standard Model tests, CP violation and the study of the quark-gluon plasma.

The LHC will be installed in the 26.7 km long LEP tunnel and will start in 2005. The proton beams will be accelerated in several steps using the existing CERN accelerator complex, shown in figure 8.

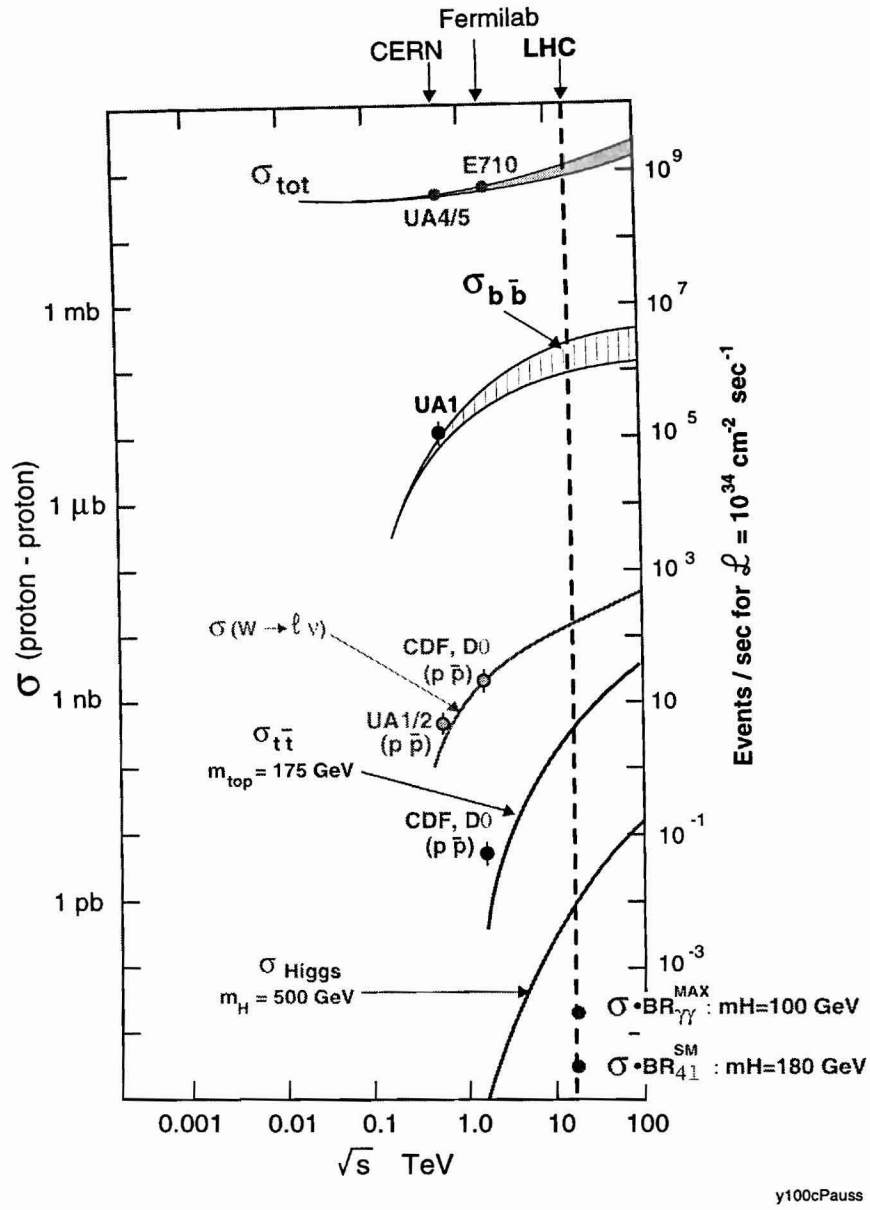

FIGURE 7. Cross sections in proton-proton collisions as a function of center-of-mass energy [35].

The LHC machine will use the most advanced superconducting magnets and accelerator technologies ever employed. The main LHC operational parameters are listed in table 1. More details can be found in [36]. The two most important parameters, which define the experimental environment around the collision point where the detectors will be installed, are its high luminosity and short bunch crossing interval. During an initial period, the LHC will work at a luminosity of 10^{33} $cm^{-2}s^{-1}$ before reaching the nominal luminosity[1] of 10^{34} $cm^{-2}s^{-1}$. In one

calendar year, the average LHC working period can be estimated to about 100 days ($\sim 10^7$ s) at the peak luminosity. At the nominal luminosity, this period will correspond to an integrated luminosity of 10^5 pb^{-1}.

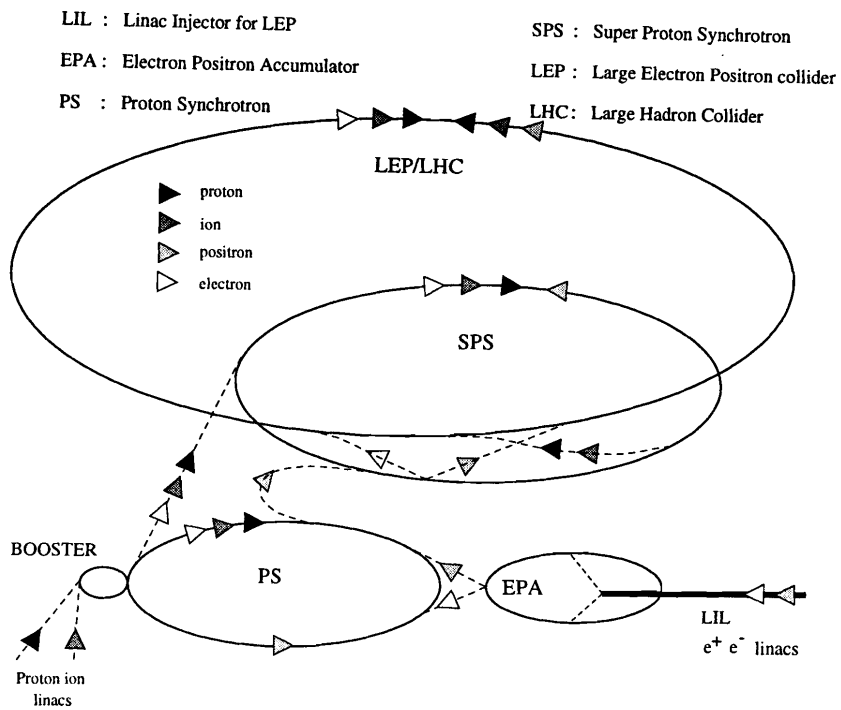

FIGURE 8. The layout of the CERN accelerator complex.

Collision energy	14 TeV
Energy at injection	450 GeV
Dipole magnetic field	8.33 T
Nominal luminosity	10^{34} $cm^{-2}s^{-1}$
Bunch spacing	7.48 m
Bunch time separation	24.95 ns
Number of bunches	2835
Number of particle per bunch	1.1×10^{11}
Luminosity lifetime	10 h

TABLE 1. The main LHC parameters

1. The nominal luminosity is often referred as high luminosity, while initial one as low luminosity.

The expected value of the inelastic proton-proton cross section at the LHC is σ_{in} = 60 mb [37], while the total proton-proton cross section is estimated to σ_{tot} = 100 mb. With the LHC nominal parameters, this means that an average of about 19 proton-proton interactions is expected per bunch crossing. This will result in a large track multiplicity of both charged and neutral particles. Together with the short bunch crossing interval of 25 ns this imposes the following requirements on the detector design:

- a fine granularity to be able to separate the large number of particles,
- a fast response to minimize the pile up effects,
- a fast and efficient trigger and data acquisition system,
- a good radiation resistance for all detector components, especially in the forward part.

Four detectors will be installed to study the collisions produced at the LHC. Two general purpose detectors, CMS [38] and ATLAS (A Toroidal LHC ApparatuS) [39], a B physics dedicated detector (LHCb) [40] and a heavy ions physics detector ALICE (A Large Ion Collider Experiment) [41].

2.3 The CMS detector

The CMS detector has been particularly designed to detect the Higgs boson, even at low luminosity, as well as possible signatures from new physics at the LHC. To achieve this goal the specific CMS objectives are:

1. to have a very good and redundant muon detection system. This has lead to the choice of a high-field superconducting solenoid with 4T magnetic field, and consequently to a compact design for the muon spectrometer,
2. to have the best possible electromagnetic calorimeter consistent with the choice of the magnet,
3. to have a high quality central tracking system able to reconstruct all high p_T muons and isolated electrons at high luminosities, as well as hadrons down to $p_T \sim 1$ GeV,
4. to have a hadron calorimeter of adequate performances and a highly hermetic overall system of calorimeters for good missing E_T measurements.

The detector will be built by an international collaboration consisting of about 1800 physicists, from 141 institutions from 31 country.

A general view of the CMS detector is shown in figure 9 and one quadrant of its longitudinal cross section is presented in figure 10. It is subdivided into a barrel region and two identical endcap regions. The central part of the detector is a 13 m long superconducting solenoid of 6 m diameter. The overall length and width of the detector are approximately 22 m and 14.6 m respectively, and the total weight will be about 14500 tons. The basic detector elements are, from inside out: a inner tracking system to measure the momenta of charged particles in the magnetic field, an electromagnetic calorimeter to measure the energies and locations of photons and electrons, a hadron calorimeter to measure jets, a forward calorimeter to complement the measure of the missing energy and to tag forward jets, and a muon system to identify and measure muons.

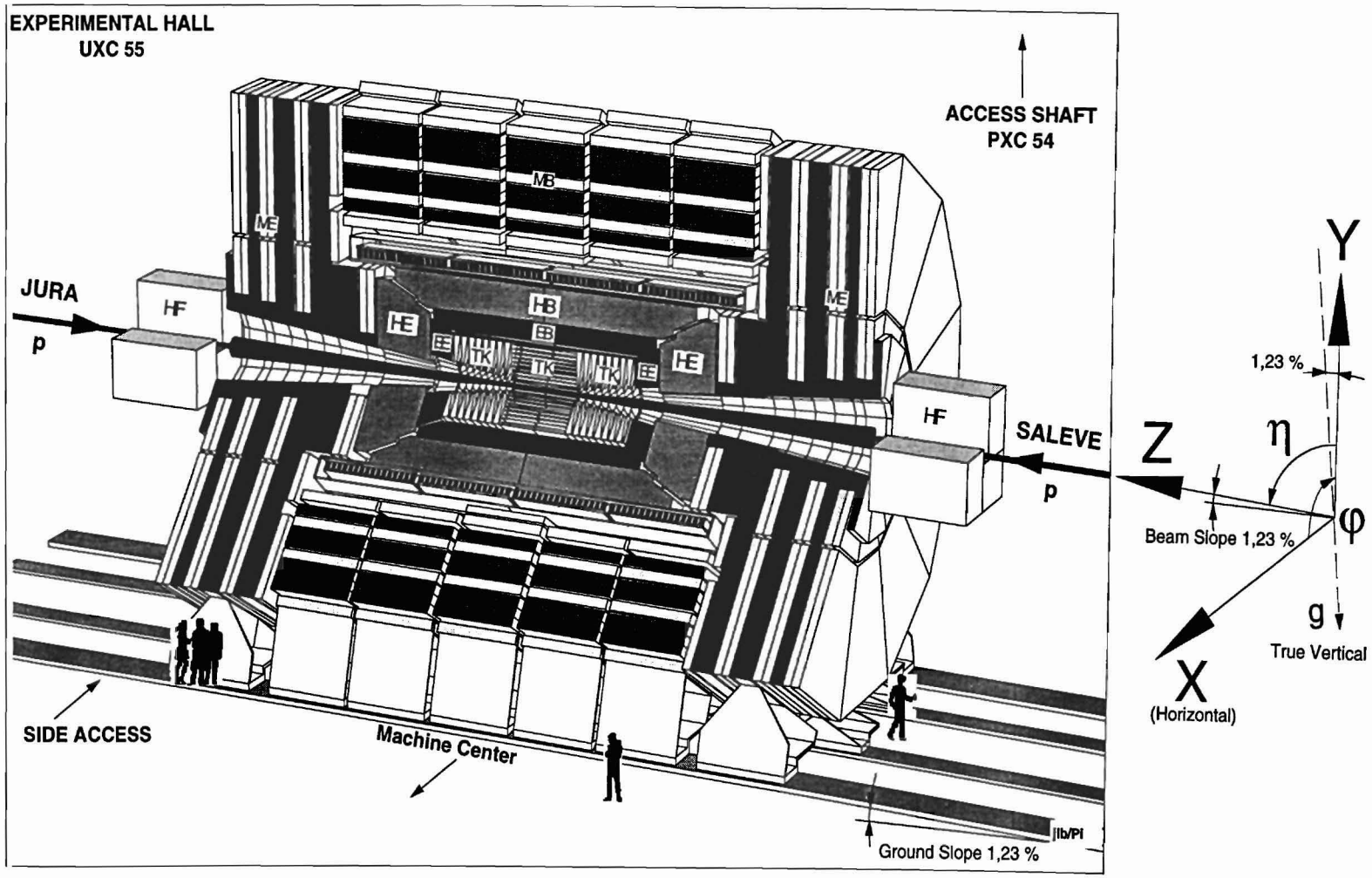

FIGURE 9. General view of the CMS detector.

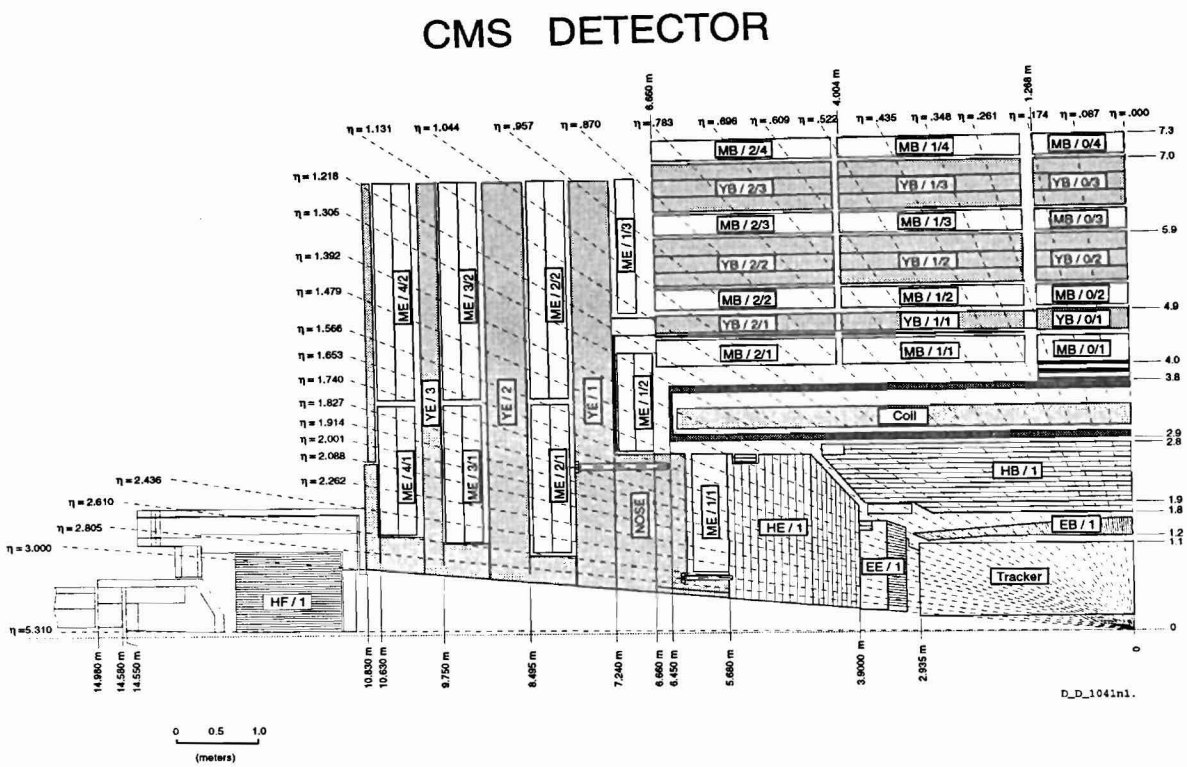

FIGURE 10. Longitudinal cross section of one quadrant of CMS.

2.4 The tracking system

The design goal of the central tracking system [42][43] is to reconstruct isolated high p_T electrons and muons with an efficiency better than 95%, and high p_T tracks within jets with an efficiency better than 90% over the pseudorapidity range $|\eta| < 2.5$. This has to be achieved in a high track density and hostile radiation environment. The momentum resolution required for isolated charged leptons in the central rapidity region is $\Delta p_T / p_T \approx 0.15 p_T$ (p_T in TeV).

Important discoveries may depend on the ability of the tracking system to perform efficient tagging of b quarks even at the highest luminosities. This has led to the choice of silicon pixel detectors close to the interaction vertex. The design goal is to achieve an impact parameter resolution at high p_T of the order of about 20 μm in the transverse plane and 100 μm in the beam direction. The pixel detectors are organized into three barrel layers (at radii of about 4 cm, 7 cm and 11 cm) and two endcap disks (covering radii from 6 cm to 15 cm). The granularity in the pixel detectors is 150 μm by 150 μm. In the high luminosity configuration, the pixel detector will have an active surface close to one square meter, instrumented with approximately 40×10^6 channels.

In addition to pixel detectors the tracker will use silicon micro-strip detectors. They are organized into inner and outer barrel and endcap. The barrel parts consist of cylindrical layers, the

inner barrel having 4 layers and outer barrel having 6 layers. Some of micro-strip detectors are double-sided, providing a measurement of the z coordinate in addition to the $r-\phi$ coordinate measured by single-sided detectors. The endcaps are organized in disks, which are themselves made of rings. The inner endcaps consist of 3 small disks closing the inner barrel, while the outer endcaps have 9 big disks. As in the barrel part some of detectors are double-sided providing a measurement of the radial coordinate. A shematic view of one quarter of the silicon micro-strip detectors layout is given in figure 11.

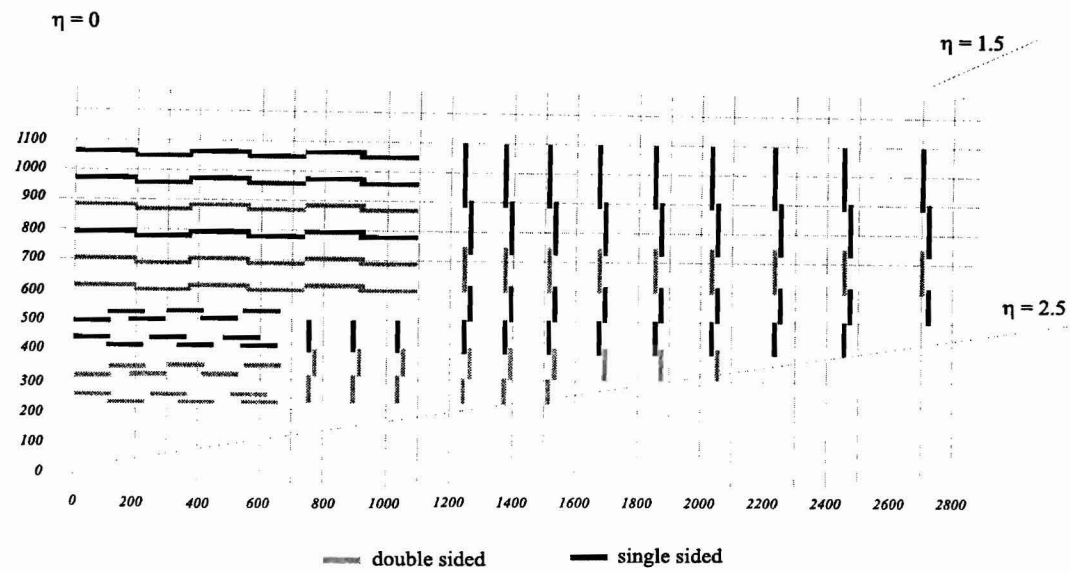

FIGURE 11. Longitudinal view of one quarter of the silicon strip tracker.

The overall design tracker performances can be summarized as follows:

- resolution for high p_T isolated tracks better than

$$\left(\frac{\delta p_T}{p_T}\right)^2 \approx (0.15 \cdot p_T)^2 + 0.005^2, \qquad \text{(EQ 41)}$$

  with p_T in TeV, in the central region $|\eta| \leq 1.6$, gradually degrading to

$$\left(\frac{\delta p_T}{p_T}\right)^2 \approx (0.60 \cdot p_T)^2 + 0.005^2, \qquad \text{(EQ 42)}$$

  as $|\eta|$ approaches 2.5.
- In combination with the outer muon chamber system, the muon momentum resolution above approximately 100 GeV can be parametrized as $\delta p/p \approx (4.5 \cdot \sqrt{p})\%$, with p in TeV, for pseudorapidities extended up to at least $|\eta| = 2$.
- In dense jet environments, charged hadrons with p_T above 10 GeV are reconstructed with an efficiency approaching 95%, and even hadrons with p_T as low as 1 GeV are reconstructed with an efficiency better than 85%. The reconstruction efficiency for muons is bet-

ter than 98% over the full pseudorapidity range. The efficiency of the electron reconstruction will be discussed in section 5.3.

- The impact parameter resolution in the transverse plane better than 35 μm, and in the longitudinal plane better than 75 μm.
- In the central pseudorapidity region tagging efficiency of 50% or better can be obtained for b jets ranging from 50 GeV to 200 GeV E_T, with a mistagging probability of around 1% to 2%. In the forward regions, for equal mistagging probability, the tagging efficiency is around 40%.

In this thesis we use the CMS tracker design proposed in the Tracker TDR [42]. The difference with respect to the current design consisted in proposing to use the Microstrip Gas Chambers (MSGC) as detectors in the outer barrel layers and in the part of the outer endcap layers. The silicon detectors were covering the intermediate radial region, from 22 cm to 60 cm, while for larger radii the MSGCs were used. This tracker design had one more barrel layer and two more endcap disks, and consequently slightly larger average number of measurement planes per track. The tracker material budget was about the same, with a somewhat different radial distribution. Simulation studies have shown that the physics performances of the current (all silicon) tracker with respect to the previous version should remain at the same level, which was a strong supporting argument for the change of design.

2.5 The electromagnetic calorimeter

The task of the electromagnetic calorimeter is to measure the energy and location of electromagnetic particles and to contribute to the hadronic particle measurement in combination with the hadron calorimeter. It should also allow for an efficient distinction between the electromagnetic showers created by electrons and charged pions[2], or photons and neutral pions[3].

The electromagnetic calorimeter is an essential piece of the CMS detector in the search for Higgs boson, in particular through the $H \rightarrow \gamma\gamma$ and $H \rightarrow ZZ^* \rightarrow 4e^{\pm}$ decay channels. As we have seen in the previous chapter, in the mass range where the Higgs could be searched for through these channels, the natural Higgs width is very small and the detector resolution dominates the Higgs reconstructed mass width. It is therefore essential to have an excellent energy resolution. Because of the intrinsically high resolution of homogeneous media, CMS has chosen to build the electromagnetic calorimeter using scintillating crystals.

The electromagnetic calorimeter will consist of about 80000 towers of lead tungstate ($PbWO_4$) crystals, organized in barrel and two endcap regions. In the following sections we will describe the most important characteristics of the electromagnetic calorimeter. The emphasis will be put on the properties of the lead tungstate crystals and on the measurements of prototypes in the beam tests. The mechanical structure of the calorimeter will be described in the next chapter.

2. Charge pions dissipate their energy through a hadronic shower whose shape differs from the electromagnetic shower one.
3. In the tracker cavity π° decays into two photons which enter the ECAL separated by typically few centimeters.

2.5.1 Lead tungstate crystals

The lead tungstate crystal has been chosen because of its compacity, fast response and radiation hardness. The compactness of this material is expressed through its high density of 8.28 g/cm^3, short radiation length[4] of 0.89 cm and small Molière radius[5] of 2.19 cm. The typical crystal light response has three time constants: 5 ns, 15 ns and 100 ns with amplitudes of 39%, 60% and 1% respectively. Therefore, about all the light can be collected in 100 ns. A disadvantage of the lead tungstate crystal is its relatively small light yield of about 10 photoelectrons/MeV and a strong light yield temperature dependence (-2%/°C). The small light yield imposes the use of photodetectors with an internal gain. Avalanche photodiodes (APDs) have been chosen for the barrel region, while vacuum phototriodes (VPTs) will be used in the endcaps. The light yield temperature dependence implies the construction of a temperature stabilization and monitoring system.

The typical emission spectrum of the PbWO4 crystals is shown in figure 12. The maximum of emission is at about 440 nm, with 140 nm FWHM and a range from 360 nm to 570 nm at 10% of the maximum. APDs and VPTs have been tuned to have a good quantum efficiency in this region.

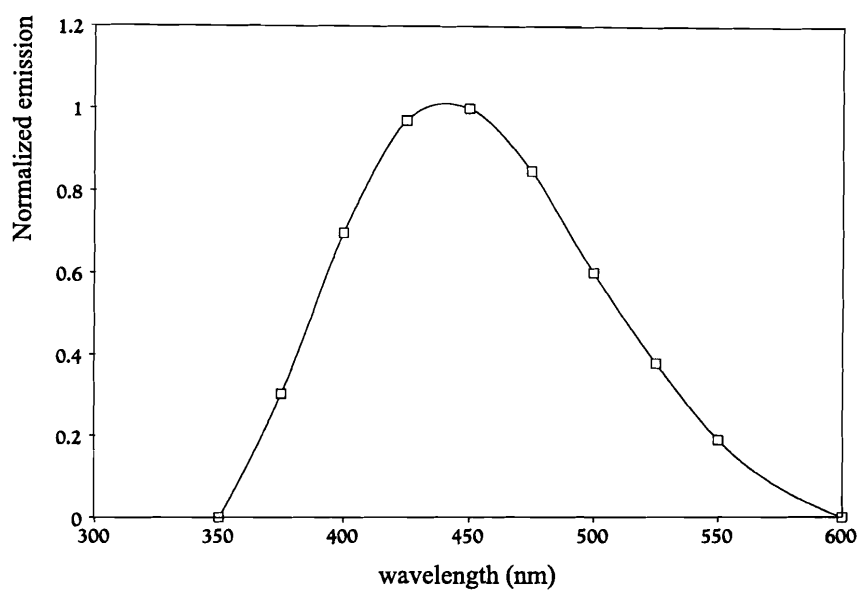

FIGURE 12. The typical scintillation light spectrum of $PbWO_4$ crystals.

The radiation hardness of $PbWO_4$ crystals has been studied in the conditions expected at the LHC, for different luminosities and different pseudorapidities. Extensive studies have shown that the radiation damage does not affect the crystal scintillation mechanism. It rather

4. The radiation length (X_0) is defined as the distance over which the electron energy is reduced by a factor $1/e$ due to radiation losses only.

5. The Molière (R_M) radius is a measure of the lateral spread of electromagnetic showers. About 95% of the total deposited energy is contained in a cylinder with a radius of $2R_M$.

decreases the transparency of the crystals by the formation of color centers and therefore results in a loss in the amount of collected light. The color centers are formed in the existing crystal lattice defects and thus the damage can be reduced by controlling the growth process or by introducing dopants. Because of the self-anealing the light loss rate depends on the dose rate. For the dose rates expected at LHC, the loss saturates at the level of few percents after several days. Keeping the loses at the level $< 10\%$ ensures that changes can be followed by a light monitoring system. Doing so the radiation is expected to not significantly deteriorate the energy resolution.

2.5.2 Photodetectors and readout electronics

The low light yield of the crystals, the strong magnetic field of 4 T and the hostile radiation environment impose strong constraints on the choice of the photodetectors. In addition, to reduce the influence of the rear shower leakage on the energy resolution, the photodetectors are requested to have a small response to charged particles that may come from the shower tail. All of these requirements cannot be met by a single type device. The choice has been made for the use of APDs in the barrel part (2 APDs per crystal) and VPTs in the endcaps, since the high level of radiation preclude the use of the APDs in endcaps. Although being a vacuum device, the VPTs can be employed in endcaps because of the smaller angles between the magnetic field direction and the device axis. The main characteristics of APD and VPT photodetectors are shown in table 2.

	APD	VPT
Active area	2×25 mm^2	~ 300 mm^2
Quantum efficiency (at 420 nm)	70%	18%
Capacitance	2×70 pF	A few pF
Operating gain (M)	50	8 (at 4T)
Excess noise factor	2.0 (at M=50)	2.5 - 3.0
dM/dV (M=50)	3.3%/V	<0.1%/V
dM/dT (M=50)	-2.2%/^{o}C	<1%/^{o}C

TABLE 2. Main parameters of the photodetectors.

An important parameter of photodetectors with gain is the so called 'excess noise factor', characterizing the fluctuations in the avalanche multiplication process. The r.m.s. of these fluctuations, for a signal of N electrons, is given by $\sqrt{F/N}$. At a gain of about 50, the excess noise factor is about 2. For the VPT, at nominal gain, the excess noise factor is about 2.5-3.0.

The high neutron flux in the region where the APDs will be installed will create defects in the silicon lattice and induce additional (leackage) current, which will increase the electronic noise. Extensive studies of the leakage current evolution over the lifetime of the experiment have allowed to estimate a noise contribution at the level of about 6 MeV/channel during the first year of the LHC operation at low luminosity and about 22 MeV/channel during the first year at high luminosity.

2.5.3 Energy resolution

The energy resolution of the $PbWO_4$ calorimeter can be parametrized as:

$$\left(\frac{\sigma}{E}\right)^2 = \left(\frac{a}{\sqrt{E}}\right)^2 + \left(\frac{b}{E}\right)^2 + c^2, \qquad \text{(EQ 43)}$$

where a, b and c are the stochastic, noise and constant term respectively. The stochastic term comes from the fluctuations in the number of elementary physical processes by which the particle releases its energy in the calorimetric media and from the photostatistics fluctuations. The noise term comes from pileup and electronic noise. The constant term comes from different sources: rear shower leakage, nonuniformities in the light collection, crystal-to-crystal intercalibration errors and residual geometrical imperfections.

The expected gaussian contributions to the energy resolution are given in table 3. The noise values include contributions from both the electronic noise and the pileup.

	Barrel	Endcaps
Stochastic term	$2.7\%/\sqrt{E}$ (E in GeV)	$(5.7\%)/\sqrt{E}$ (E in GeV)
Constant term	0.55%	0.55%
Low luminosity noise	155 MeV	770 MeV
High luminosity noise	210 MeV	915 MeV

TABLE 3. Expected contributions to the CMS ECAL energy resolution, when the electron/photon energy is estimated with the 5×5 crystal matrix.

2.5.4 Properties measured in the test beam

Prototypes of all ECAL components have been tested, during several years of R&D, in conditions as close as possible to the ones expected in the experiment. Considerable improvements in prototypes characteristics have been obtained since first tests [45] and the latest results demonstrate that most of the given milestones have been reached. Many experimental setups have been used to measure the characteristics of the crystals, photodetectors, electronic chain, mechanical structure etc. Here, we will describe the tests of energy resolution, radiation hardness and reproducibility of the crystals.

Tests with high energy electrons from 10 to 280 GeV have been performed at the SPS (Super Proton Synchrotron) H4 and X3 lines at CERN. The experimental setup consists of a crystal matrix with its electronic chain[6], a set of beam chambers for the determination of the electron impact position, scintillation counters for events triggering and a data acquisition system.

In figure 13, the results on the energy resolution for one typical crystal are shown [46]. The electron energy have been reconstructed as the sum of the deposited energy in a 3×3 crystal

6. The electronics used in the test beam up to now was not the final one.

matrix centered on the electron impact crystal. Electrons enter the crystal with a 3° angle in both directions with respect to its axis, and events with impact point in a region of 4×4 mm^2 around the crystal center are selected. Every point in the figure represents the normalized sigma for the gaussian fit of the energy distribution. The noise term, extracted as the pedestal width, have been subtracted and stochastic and constant term fitted on the obtained points. In figure on the right are shown the values of the three terms in the resolution, determined by the above procedure for 11 different crystals. Comparing with the values shown in table 3, we can see that the requested values for stochastic and constant terms are reached. The noise value per channel is still somewhat larger than requested and further studies for possible improvements are under way (in the table, the noise estimation assumed a sum of 25 crystals to reconstruct the energy).

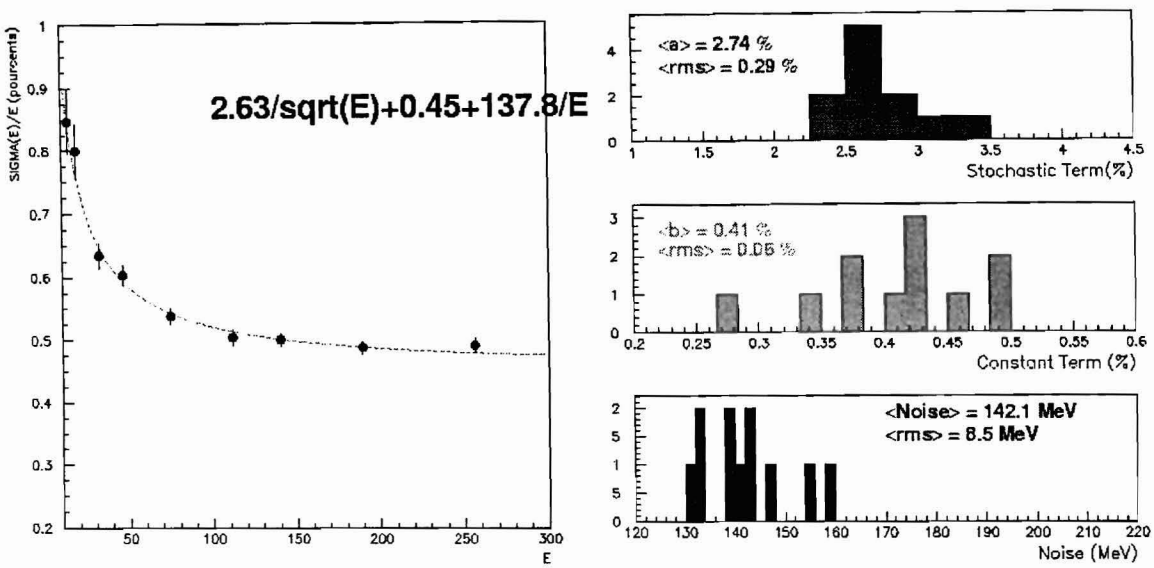

FIGURE 13. Energy resolution for one crystal (left) and stochastic (a), constant (b) and noise term for 11 crystals (right) [46]. In the expression on the left figure, '+' denotes quadratic sum.

From equation 43 we can see that the constant term dominates the resolution at high energies. A possible contribution to the constant term may come from rear shower leakage. Particles produced at the shower tail enter directly the photodetector, leaving a signal equivalent to those from higher energy electromagnetic particle entering the crystal. This effects should manifest itself as a high energy tail in the energy distribution. In figure 14 the energy distribution for 280 GeV electrons is shown. The energy has been reconstructed as the sum of signals from 3×3 crystal matrix. The absence of a high energy tail demonstrates the negligible influence of the rear leakage on the energy resolution. The measured resolution of 0.45% includes a contribution from the beam momentum spread of about 0.24%.

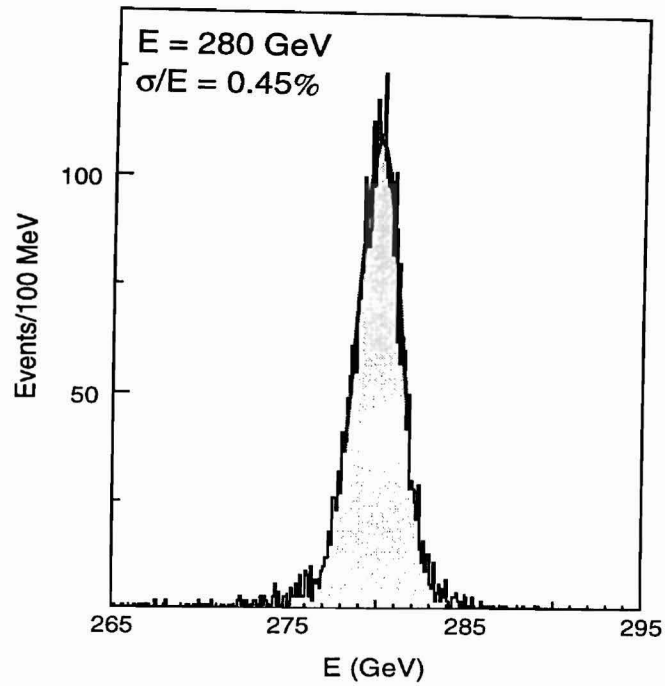

FIGURE 14. Energy distribution for 280 GeV electrons measured in the test beam.

Another important aspect is the monitoring of the light yield changes induced by the radiation damage. The light monitoring system has been studied in the test beam. A laser light of 523 nm (green) and 660 nm (red) has been injected from the crystal front side and then measured on the back side in the period between two electrons impacts. The normalized response to electrons versus normalized response for 523 nm light injection is shown in figure 15, for 9 different non-radiation-hard crystals[7]. As we can see there is a strong correlation between the two responses, with a slope dispersion of about 10%. This allows to correct for the radiation damage induced changes without deteriorating the energy resolution, as long as the light yield decrease remains below $\approx 10\,\%$ and the slope of the monitoring versus shower response remains within 10% for all crystals sharing the same light monitoring system. The first condition is already satisfied with the radiation-hard crystals and efforts are currently under way to find a reliable procedure for producing a large number of crystals with a uniform behavior under the radiation.

7. These crystals are old prototypes, having a too big light yield decrease and will not be used in the experiment.

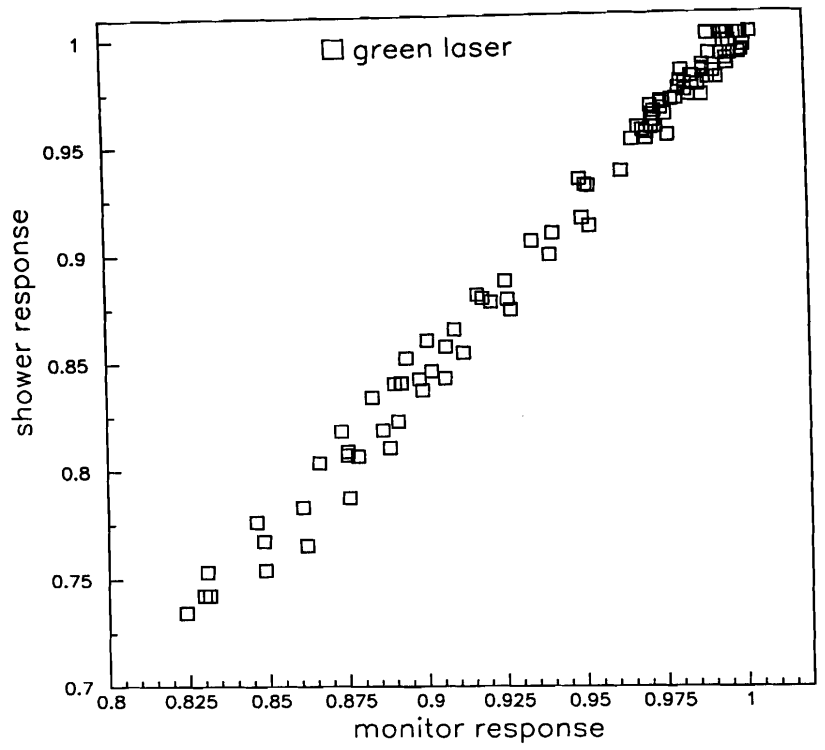

FIGURE 15. Normalized shower response versus monitoring response for 9 different crystals. The monitoring system has used 523 nm (green) laser signal.

Tests on a large sample of crystals have been performed to test their reproducibility regarding different crystal characteristics. In figure 16, the response to a 50 GeV electron beam for 30 crystals arranged in the 5×6 matrix is shown. Electrons entered the crystals perpendicular to the front face with $3°$ tilt in both directions with respect to its axis. The impact points were uniformly distributed along two perpendicular axis in the middle of the crystal and parallel to its sides. We can remark a very small dispersion between the crystal responses, demonstrating a good crystal reproducibility regarding the uniformity of the transversal crystal response. The deviation for two crystals in the 'y beam' profile is due to shower development in the copper cooling shielding at the edge of the crystal matrix.

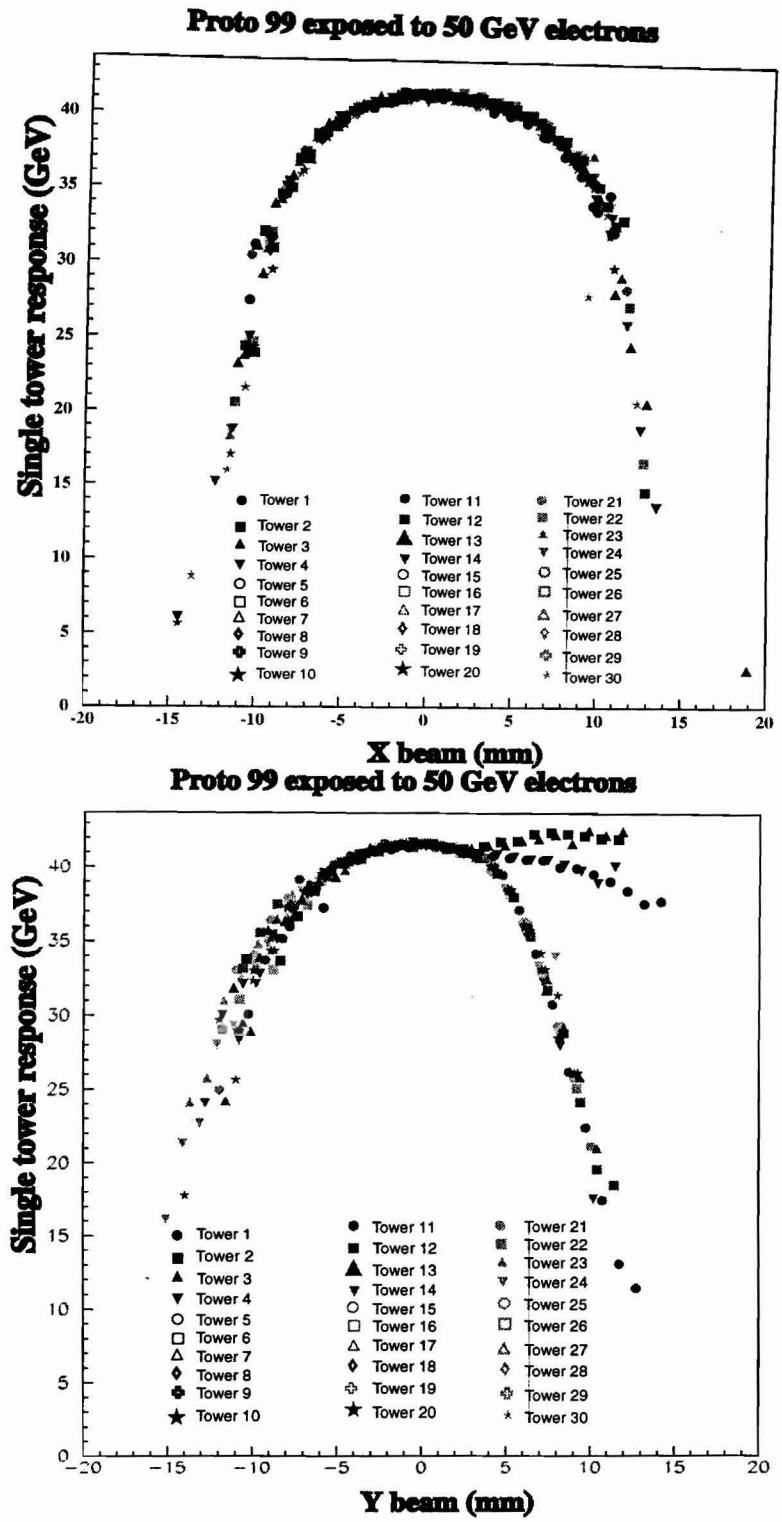

FIGURE 16. Transverse response uniformity for 30 crystals measured in the test beam. The deviation for two crystals in the y beam profile is due to shower development in the copper cooling shielding at the edge of the matrix.

2.6 The hadron calorimeter

The role of the hadron calorimeter (HCAL) [47] is to measure the energies and directions of particle jets as well as the missing transverse energy flow, together with the electromagnetic calorimeter. It will also help in the identification of electrons, photons and muons in conjunction with the electromagnetic calorimeter and the muon system.

The design of the hadron calorimeter is governed by the requirements of a good hermicity, good transverse granularity, moderate energy resolution and sufficient depth for hadron shower containment. A lateral granularity of $\Delta\eta \times \Delta\phi = 0.087 \times 0.087$ is chosen to match the one of the electromagnetic calorimeter trigger towers and the muon chambers, and is sufficient for a good di-jet separation and mass resolution.

The hadron calorimeter consists of two systems: a central calorimeter ($|\eta| < 3.0$) with excellent jet identification and moderate single particle and jet resolution and a forward calorimeter ($3.0 < |\eta| < 5.0$) with modest hadron energy resolution but with good jet identification capability. The central calorimeter consists of a barrel ($|\eta| < 1.3$) and two endcaps ($1.3 < |\eta| < 3.0$), all located inside the magnet cryostat. It is made of brass absorber plates interleaved with scintillator tiles. Because of the 4 T magnetic field, the readout is done with hybrid photodetectors. The tiles are grouped in towers, whose structure is given in figure 17.

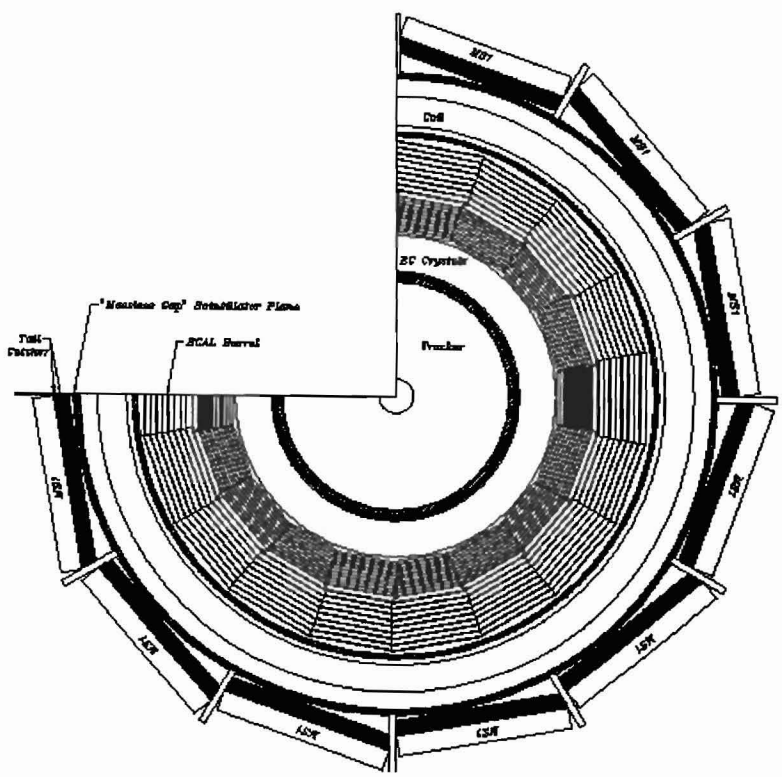

FIGURE 17. The tower structure of the HCAL barrel.

The barrel hadron calorimeter has a thickness of about 6.5 nuclear interaction lengths[8] (λ_I) which is not enough for a total hadronic shower containment. This would results in a low-energy tail in the response to hadrons and deteriorate the missing transversal energy measure-

ments. Therefore, an additional hadron calorimeter (a so called tail-catcher) will be embedded in the first muon absorber layer and will cover a pseudorapidity range of $|\eta| < 1.5$. The inclusion of the tail catcher increases the total hadron calorimeter depth to at least 10 λ_I over the entire pseudorapidity range.

The forward calorimeter, located in a very high radiation and a very high rate environment, is made of iron and quartz fibers. As the photodetectors, the forward calorimeter will use conventional photomultiplier tubes.

The test beam results of hadron calorimeter prototypes indicate that an energy resolution of $(\sigma/E)^2 = (100\%/\sqrt{E})^2 + (4.5\%)^2$ is achievable for hadrons between 30 GeV and 1 TeV.

2.7 The muon system

The role of the muon system [48] is the identification, triggering and momentum measurements of muons. The presence of muons in the final states is characteristics of many interesting physical processes. The most stringent requirements on the performance of the muons system comes from the $H \rightarrow ZZ^* \rightarrow 4\mu$ decay channel.

The muon system will be located outside the solenoidal magnet and will cover the pseudorapidity region of $|\eta| < 2.4$. It consists of barrel and endcap detectors using different technologies. Both barrel and endcap detectors have four muons stations interleaved with the iron of the magnet yoke. The barrel region $|\eta| < 1.3$ is made of drift tubes (DT) layers, a choice that was possible due to the low expected rate and due to the relatively low intensity of the local magnetic field. For the endcaps, $0.9 < |\eta| < 2.4$, the cathode strip chambers (CSCs) are chosen since they are capable of providing precise space and time information in the presence of a high magnetic field and high particle rate. CSCs are multiwire proportional chambers with the cathode plane segmented into strips. They are organized into modules containing six layers, thus providing a robust pattern recognition.

In addition resistive plate chambers (RPCs) in both the barrel and endcaps are added to provide an additional, complementary trigger with an excellent time resolution for the bunch crossing identification. RPCs are gaseous parallel-plate chambers that combine a reasonable level of spatial resolution with excellent time resolution (3 ns), comparable to that of scintillators. RPCs constitute a fast dedicated trigger system which can identify candidate muon tracks and assign the bunch crossing with high efficiency.

The muon track reconstruction efficiency with the stand-alone muons system is better than 90% for track momenta below 100 GeV. The momentum resolution, shown in figure 18, is about 6-30% for $p_T \approx 100$ GeV depending on pseudorapidity. Combining muon with the tracker measurement these resolutions improve to about 1-6% for muons with $p_T \approx 100$ GeV, as shown on the same figure.

8. Nuclear interaction length is defined as the mean free path between inelastic interactions of particle and nuclei.

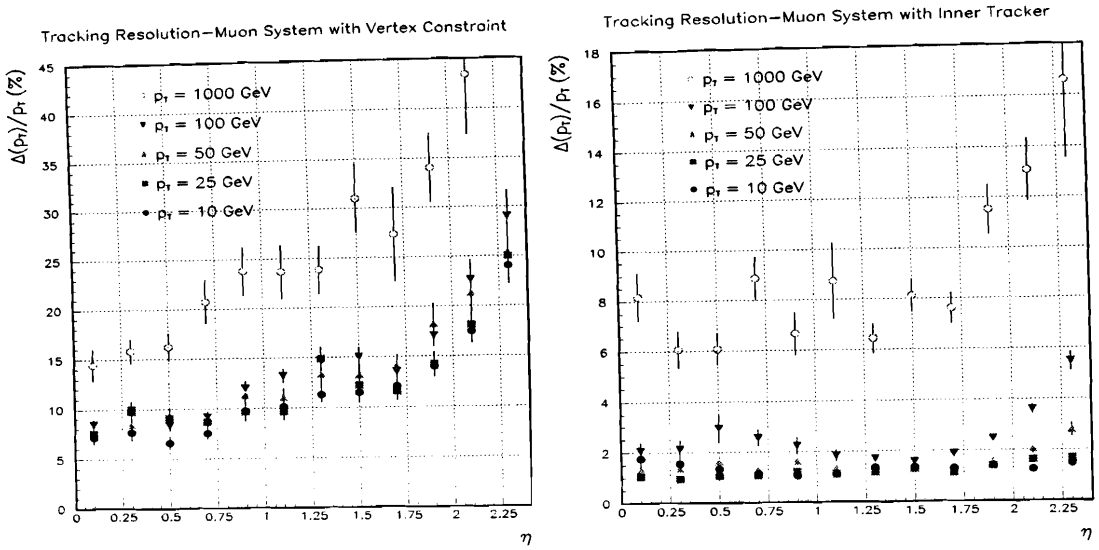

FIGURE 18. Momentum resolution for muon tracks using hits from the muon system with a vertex constraint (left) and combining hits from muon system and central tracker (right).

2.8 The trigger and data acquisition systems

At the nominal LHC design luminosity of 10^{34} cm^{-2} s^{-1}, an average of 20 events occurs at the beam crossing frequency of 25 ns. This event rate of about 10^9 Hz has to be reduced to at most 100 Hz, the upper limit that can be archived for off-line analysis. CMS has chosen to reduce this rate in two steps:

- The Level-1 trigger

  Using the coarsely segmented data from calorimetry and muon system, the Level-1 trigger searches for "trigger objects" such as photons, electrons, muons, jets, missing transversal energy (E_T) and total E_T, and retains only the events passing a predefined set of criteria. At this level the input rate of 1 GHz is reduced to about 100 kHz.
- The Higher level triggers system

  Events passing the Level-1 trigger are forwarded to the Higher level trigger system. It has an access to all the subdetectors data, including the tracker and the full granularity of the calorimeters. Using all the data and a more complete event analysis, the final decision whether to keep an event is made. On this level, the requested rate of ≤ 100 events per second for the mass storage is reached.

A shematic view of the CMS trigger and the data acquisition system is shown in figure 19. At the first level, all the information about an event is preserved, with the Level-1 trigger using only a subset of all data. Made at a fixed time after the interaction has occurred, a first level decision is issued every 25 ns. The full data are stored in the pipelines, with a storage time of 3.2 μs. If the first level trigger generates an accept, the event data are moved or assigned to a buffer for readout and processing by the Higher level triggers.

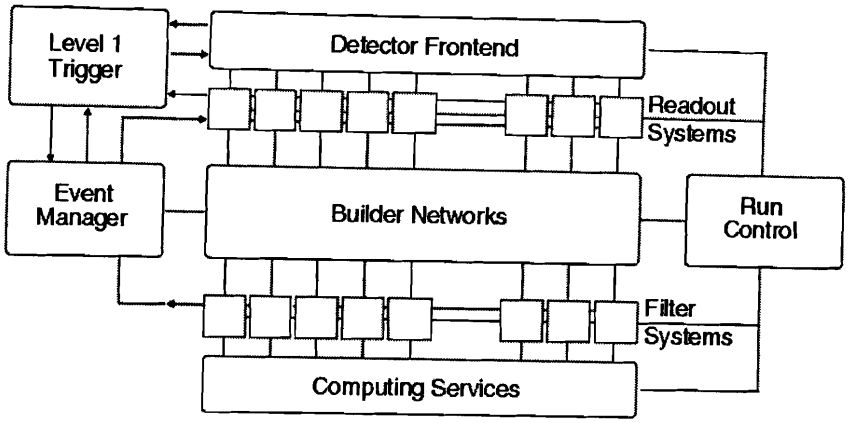

FIGURE 19. CMS trigger and data acquisition system.

The Level-1 trigger is organized into three major subsystems: the Level-1 calorimeter trigger, the Level-1 muon trigger and the Level-1 global trigger. The global trigger accepts muon and calorimeter trigger informations, and by using the logical combinations of these data with corresponding thresholds makes a global trigger decision. The Higher level trigger system is organized as a series of filters, progressively using more informations to reduce the event rate.

The electron/photon Level-1 trigger is based on the recognition of a large and isolated energy deposit in the electromagnetic calorimeter. The electromagnetic calorimeter is subdivided into trigger towers, with a granularity of $\Delta\eta \times \Delta\phi = 0.087 \times 0.087$ in the barrel. The electron/photon trigger algorithm [49] is based on 3×3 trigger tower sliding window technique and is illustrated in figure 20. This algorithm involves the eight nearest neighbors around the central 'hit' trigger tower and is applied sliding over the entire (η,ϕ) plane. The electron/photon candidate E_T is determined by summing the E_T in the hit tower with the maximum E_T tower of its four broad side neighbors. In each 4×4 trigger towers region the highest E_T non-isolated and isolated electron/photon candidates are separately found. The non-isolated candidate requires passing of two shower profile vetos, the first of which is based on the fine-grain ECAL crystal energy profile (FG veto) and the second is based on HCAL to ECAL energy comparison, e.g. H/E less than 5% (HAC veto). The isolated electron/photon candidate requires passing of two additional vetoes, the first of which is based on the passing of FG and HAC vetoes for all eight nearest neighbors, and the second is based on there being at least one quiet corner, i.e. one of the four five-tower corners has all towers below a programmable threshold, e.g. 1.5 GeV. The four highest E_T non-isolated and the four highest E_T isolated electron/photon candidates are transferred to the global calorimeter trigger where the top four candidates of each type are retained for processing by the CMS global trigger.

As an illustration of the electron/photon trigger algorithm performance, we show in figure 21 an efficiency for triggering on top to electron decay events $(t \rightarrow e + X)$ versus the p_T and η of the electron for various cuts. All efficiencies are over 90% about 10 GeV above 25 GeV trigger E_T cutoff.

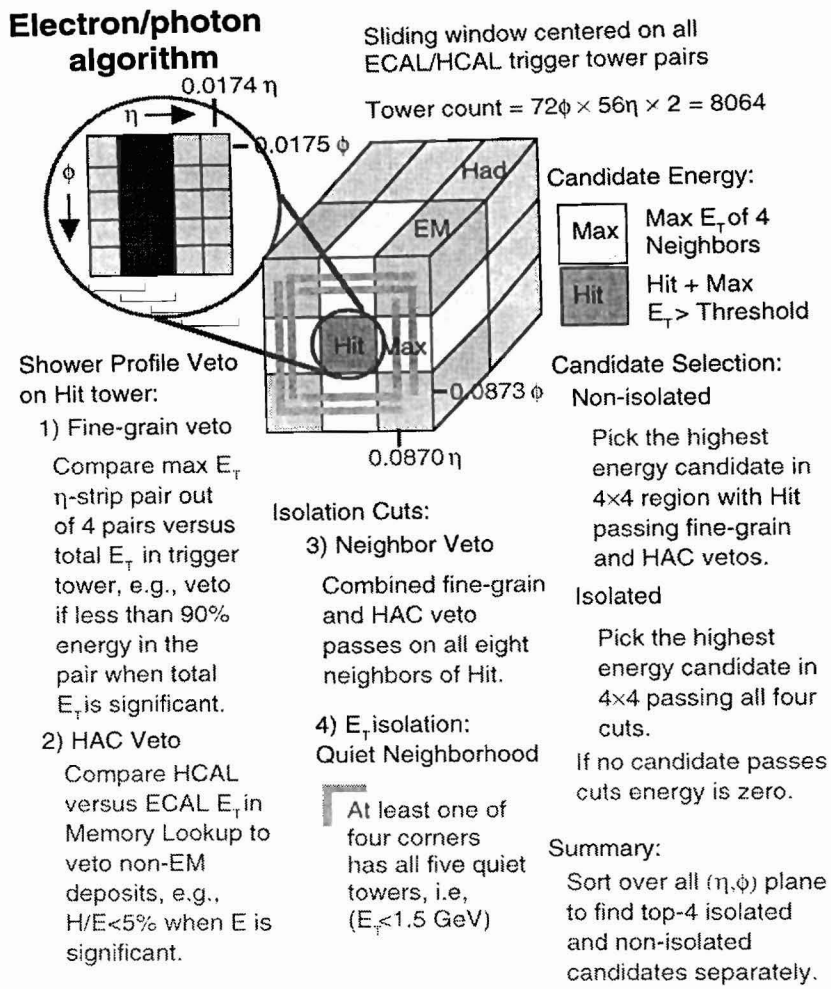

FIGURE 20. Illustration of the electron/photon trigger algorithm [49].

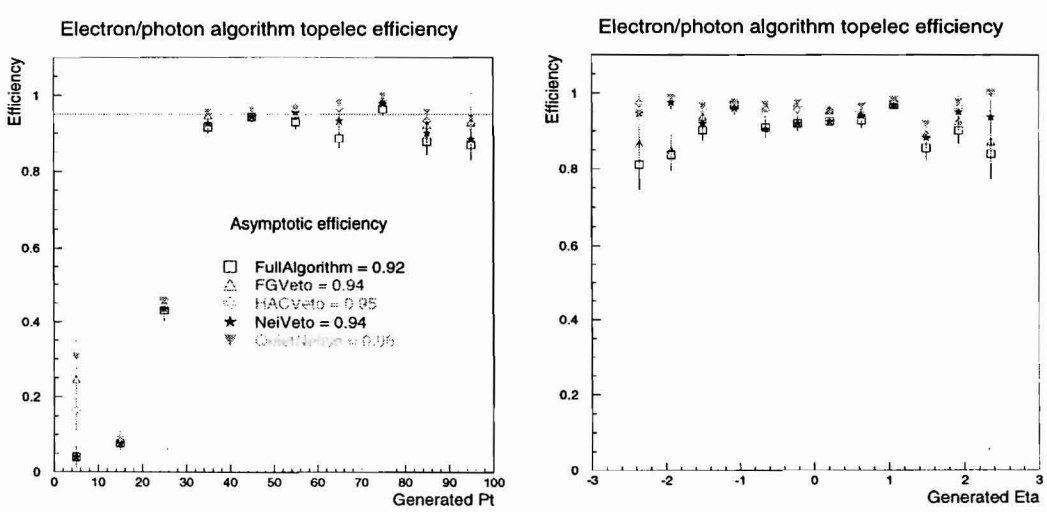

FIGURE 21. Efficiency of the single electron trigger for various trigger cuts versus the generated p_T and η of the electrons in top decay events [49].

Chapter 3 *Contribution to the construction of the electromagnetic calorimeter*

3.1 Introduction

One of the main CMS design objective is to construct a high performance electromagnetic calorimeter. It has been carefully designed and optimized for the precise reconstruction of high energy electrons and photons by combining their energy measurement with informations from other subdetectors. In the electron reconstruction process, the energy deposited in the electromagnetic calorimeter will be used for:

- an electron trigger, since a high energy deposit in the ECAL indicates potential importance of the physical event, which will eventually be kept for a further analysis,
- an electron identification, by matching the energy deposits in ECAL with the tracks measured by tracker,
- a precise electron energy estimation.

To fulfill these tasks, at the level required by physics studies, the CMS electromagnetic calorimeter is designed as a very complex system. It will consist of about 80 000 $PbWO_4$ crystals, each placed in a supporting structure, an alveolar container. The optical signal from crystals will be read-out by photodetectors, avalanche photodiodes in the barrel (two per crystal) and vacuum phototriodes in the endcaps, followed by the associated electronics. Together with the temperature sensors and the monitoring system, the complete electromagnetic calorimeter will consist of more than a million pieces. The production of such large number of elements is difficult to be carried out in scientific laboratories, and the CMS collaboration has decided to give it entirely to the factories, chosen by a procedure of public offer.

During several years of R&D, the prototypes of every detector component have been carefully studied and their properties optimized in order that the entire system fulfill the requirements fixed by detailed physics simulations. With these properties being defined, one of the main tasks is to keep all the pieces produced inside corresponding tolerances. Therefore, quality control of the detector components is an important step in the detector construction.

In the first part of this chapter we will describe the electromagnetic calorimeter mechanical structure, with a special attention on the alveolar containers mechanical design. We will also discuss the crystal light collection optimization and the choice of the inner coating material of the alveolar container.

The most important characteristics of an alveolar container are its mechanical and optical properties. They depend very strongly on an exact production procedure and it is therefore

important to monitor the entire production process. We will describe the alveolar structures production process and the system developed for its monitoring.

The inner coating of the alveolar structure has been specially optimized to keep the crystal light yield and the longitudinal response uniformity at a level not significantly deteriorating the energy resolution. To ensure this for all the structure produced, we have developed an optical quality control system. As the main content of this chapter we will describe the instrument developed for the optical properties measurements, as well as the methodology used for the optical quality control. The developed control process have been tested by measuring the optical properties of the alveolar structures produced in the laboratory.

3.2 The electromagnetic calorimeter structure

The general ECAL design requirements, coming from the physics to be studied in CMS, can be summarized as follows:

- Pseudorapidity coverage

  The geometrical crystal coverage extends to $|\eta| \leq 3$, while the energy measurements will be carried up to $|\eta| \leq 2.6$. These limits have been determined by considering the radiation doses, the amount of pileup energy and the matching with the geometrical coverage of the tracking system.
- Transverse granularity

  One of the biggest advantage of the $PbWO_4$ is its compacity, expressed by the smallness of its Molière radius of 21.9 mm. In the barrel, a crystal transverse granularity of about 22×22 mm^2, corresponding to $\Delta\eta \times \Delta\varphi = 0.0175 \times 0.0175$ has been chosen. It matches the Molière radius and therefore allows to reduce the effect of the pileup on the energy measurement by reducing the area to be used for the energy estimation. Such a fine crystal granularity allows for precise identification of electromagnetic objects, and makes possible the development of sophisticated algorithms to correct effects like bremsstrahlung and conversions in the tracker material. In the endcaps, the granularity will decrease progresively with increasing η to a maximum value of $\Delta\eta \times \Delta\varphi = 0.5 \times 0.5$, keeping a constant crystal front cross section of 28.6×28.6 mm^2.
- Longitudinal thickness (depth)

  In order to limit the backward leackage of high-energy electromagnetic showers to an acceptable level, whilst keeping the crystal volume and cost at an acceptable level too, a total thickness of about 26 radiation lengths at $\eta = 0$ is required, corresponding to a crystal length of about 23 cm. In the endcaps, the presence of a preshower detector, and therefore of 3 X_0 of material in front of the ECAL, allows for the use of slightly shorter crystals of about 22 cm.

In addition to these requirements, the engineering design should ensure the best possible hermeticity by minimizing the gaps between crystals, and optimizing the barrel-endcap transition region, as well as minimizing the material in front of the ECAL and between the ECAL and the hadron calorimeter. It is also necessary to stabilize the temperature of the whole calorimeter (crystals, APDs) to ≤ 0.1 °C.

In figure 22, the longitudinal view of one ECAL quadrant is shown. The barrel part covers the pseudorapidity range $|\eta| < 1.479$, with the crystals starting at a radius of 1.29 m, while endcaps covers the pseudorapidity range $1.479 < |\eta| < 3$, with the crystals front face starting at $z = 3.17$ m. In front of the endcaps, the preshower detector, covering a pseudorapidity range from $|\eta| = 1.65$ to 2.61, will be present from the start of the experiment.

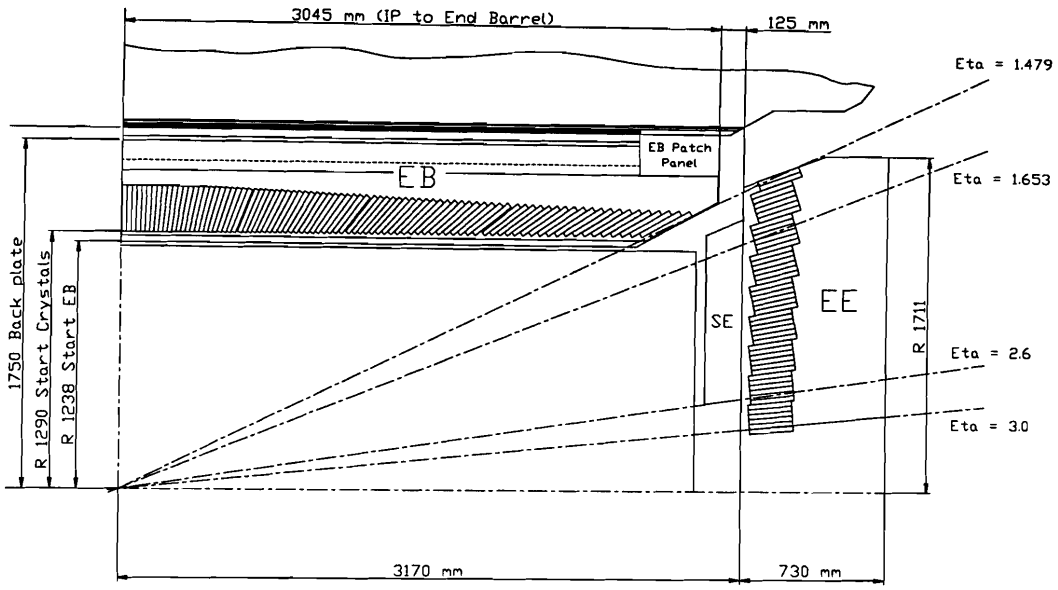

FIGURE 22. Shematic view of one quadrant of the electromagnetic calorimeter.

The crystals are organized into modular structures, with the two $\pm z$ half-barrels having the same structure, as well as the two endcaps. In the barrel, the basic structure is a submodule, containing 2 crystals in ϕ and 5 crystals in η. Submodules are assembled in modules, with module type 1 consisting of 50 submodules (10 in ϕ and 5 in η) and module type 2, 3 and 4 of 40 submodules (10 in ϕ and 4 in η). Finally, modules will be grouped in supermodules, each consisting of four modules, one of each type (i.e. 1 module in ϕ and 4 modules in η). Therefore, each half-barrel will have 18 supermodules. The endcap crystals are organized in supercrystals, each containing 25 crystals. In one endcap there will be 268 full and 64 partly filled supercrystals to complete the inner and outer perimeter. The supercrystals are grouped in dees, with 2 dees per endcap. In figure 23 the shematic view of the ECAL geometrical structure is given, and in table 4 the main geometrical parameters are listed.

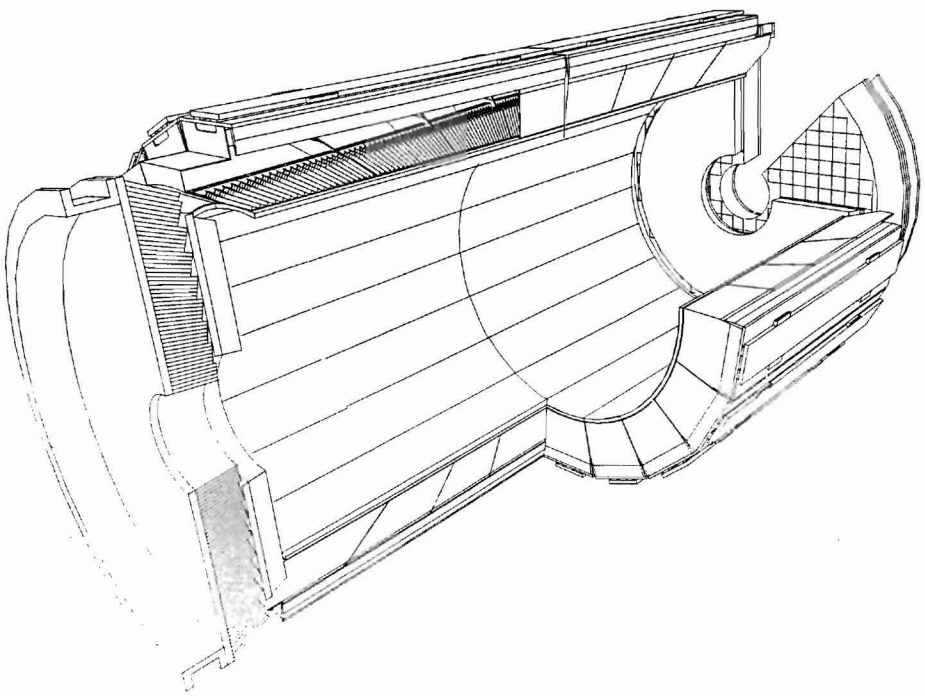

FIGURE 23. Shematic view of the ECAL structure.

Parameter	Barrel	Endcap
Pseudorapidity coverage	$\|\eta\| < 1.479$	$1.479 < \|\eta\| < 3.0$
ECAL envelope: r_{inner}, r_{outer} (mm)	1238, 1750	316, 1711
ECAL envelope: z_{inner}, z_{outer} (mm)	0, ±3045	±3170 , ±3900
Granularity: $\Delta\eta \times \Delta\phi$	0.0175×0.0175	0.0175×0.0175 to 0.05×0.05
Crystal dimensions (mm^3)	typical: $21.8 \times 21.8 \times 230$	$28.6 \times 28.6 \times 220$
Depth in X_0	25.8	24.7
Number of crystals	61 200	16000
Total crystal volume (m^3)	8.14	3.04
Total crystal weight (t)	67.4	25.2
Modularity	36 supermodules	4 Dees
1 supermodule/Dee	1700 crystals (20 ϕ , 85 η)	4000 crystals
1 supercrystal unit	-	25 crystals

TABLE 4. Summary of the main ECAL design parameters.

To avoid that photons originating from the interaction vertex pass directly through the cracks between crystals, the crystal axis are tilted by about 3° with respect to the line connecting the

origin of the coordinate system (which coincides with the mean proton-proton interaction point) and the crystal front face barycenter [50]. For the endcaps, the tapered geometry of the crystals ensures that most of the crystals are effectively tilted from 2° to 8°.

For reason of construction and assembly ease, crystals in the barrel have been grouped in the so-called flat-pack configuration (figure 24), with a left-right symmetry. The crystals have a truncated pyramidal shape, with parallel front and back faces (small and large base of a truncated pyramid).

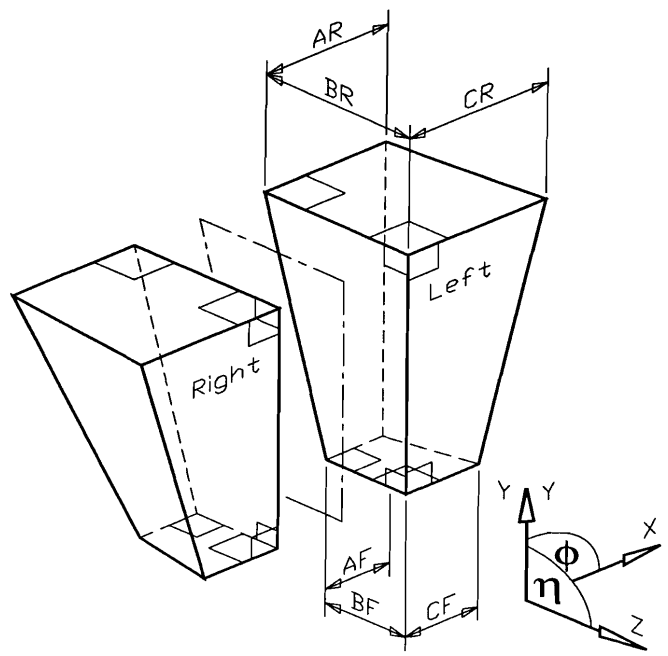

FIGURE 24. Flat-pack geometry principle.

The geometry of the endcaps is based on a right-sided crystals with two tapering sides. The taper is defined by a line from a point 1300 mm from the far side of the intersection point, to the rear corner of the crystal. In this way the off pointing of the crystals is obtained, ensuring also a maximum path length through the crystals.

The chosen granularity of crystals implies that one half barrel consists of $85(\text{in } \eta) \times 360(\text{in } \phi)$ crystals. The group of 10 $(5(\eta) \times 2(\phi))$ crystals is contained in a separate alveolar structure, and with the associated mechanical pieces forms one submodule. In order to reduce the number of geometrically different crystals, in each submodule all five alveolas in η are filled by crystals of the same size, taken from the smallest (the one in the furthermost $|\eta|$ alveola). This reduces the number of crystal types from 85 to 17, as shown in figure 25 with each crystal being characterized by the parameters defined on the figure 24. There is, therefore, 17 different alveolar structure types, with 360 submodules of each type. Figure 26 shows the definition drawing of two alveolar structures types.

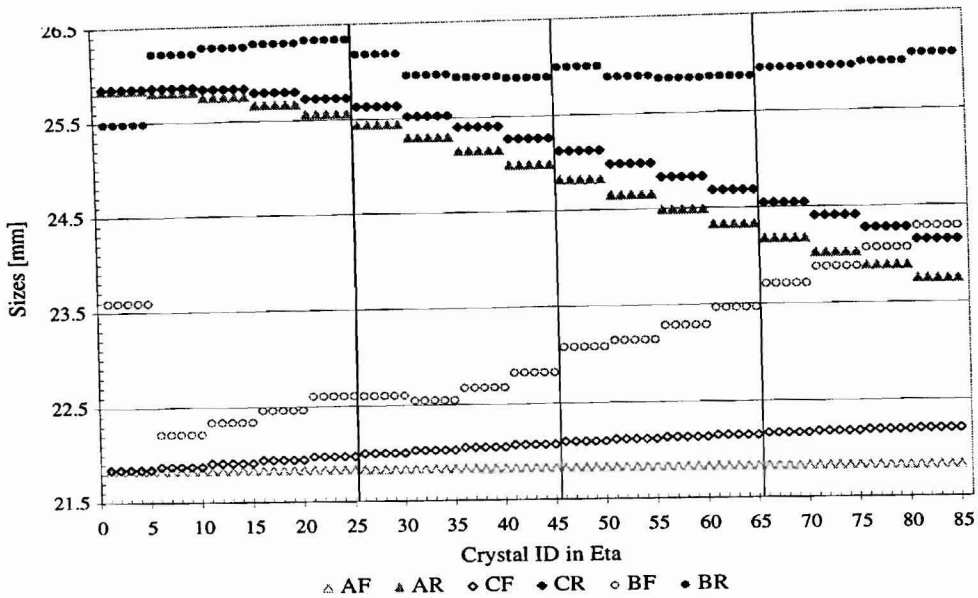

FIGURE 25. Shapes of the 17 crystal types.

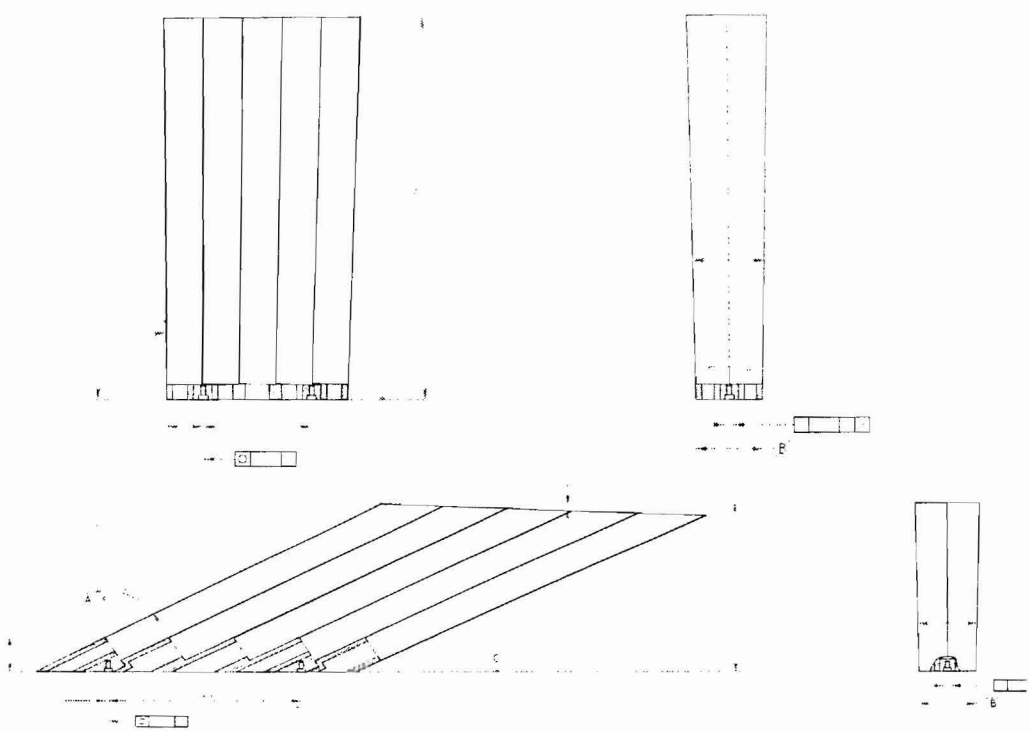

FIGURE 26. Definition drawing for the alveolar structures of type 1 and 17.

The use of an alveolar structure to hold the crystals has been chosen because of the PbWO4 crystal fragility and in order to facilitate the assembly process. The rigidity of the structure is such that no load is transferred to a crystal from any of its neighbors. Once the 10 crystals are inserted, the alveolar structure is closed with an aluminum tablet (figure 27). The tablet is a 20 mm thick prismatic plate bored with 4 slots corresponding to the position of the capsules and provides an outlet for the electronics. The tablet weights 150 g and is riveted on the outer periphery. The pressure exerted by the tablet on each crystal subunit is taken by a foam piece which closes the cell bottom. The overall weight of an assembled submodule is about 12 kg.

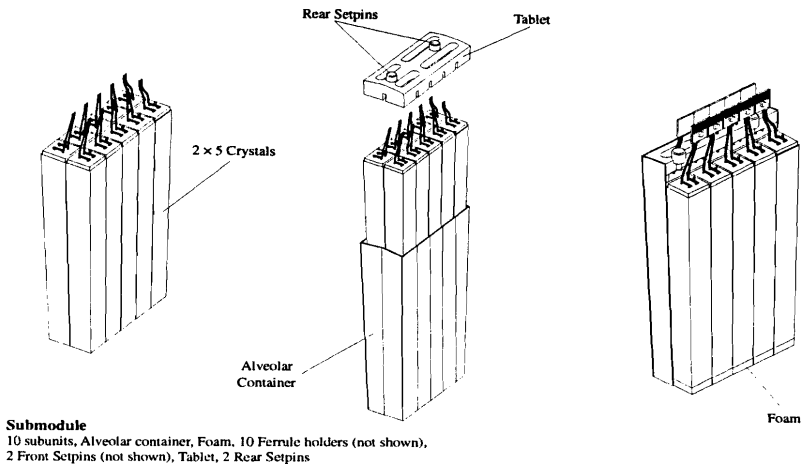

FIGURE 27. Assembly of one submodule.

The submodule is positioned on the grid at the back. The set of modules forming the supermodule is covered by a basket. Both the grid and the basket are made of an aluminum alloy. The structure is held by two pins at the front and at the back precisely located as shown in figure 28. The two front pins are integrated to the structure, while the two back pins are contained in the tablet.

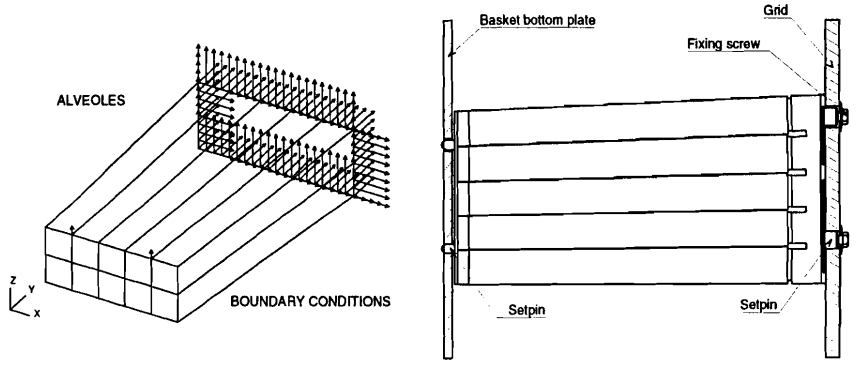

FIGURE 28. Boundary conditions of the submodules and attaching to the grid.

In order to obtain the desired energy resolution, the gap between crystals has to be at most equal to 0.5 millimeters. The alveolar unit nominal wall thickness is 0.2 mm, with the manufacturing tolerances of ±20 μm. In the alveolar structure, the crystals are free with an air gap of about 0.1 mm. Including the crystal processing tolerance, from 0 to 0.1 mm, the chosen design guaranties a maximum distance of 0.4 mm between crystals inside a submodule, and of 0.6 mm between two submodules, in ϕ and in η.

3.3 Light collection optimization

The most important property of the CMS electromagnetic calorimeter is energy resolution, i.e. the precision of the electrons and photons energy measurements. As we have seen in section 2.5.3, the ECAL energy resolution can be parametrized with three terms, the so called stochastic, constant and noise terms.

The main contribution to the stochastic term comes from the photostatistics fluctuations. It is inversely proportional to the squared root of the collected light yield, that is to the number of secondary photoelectrons after amplification in the photodetector per unit of incident particle energy. It is thus very important to have both an intrinsic light yield of crystals as high as possible and an optimal light extraction system. The light extraction from the crystal depends on the crystal geometry, the state of the crystal surface, the crystal wrapping, the optical coupling between the crystal and the photodetector, and on the quantum efficiency of the photodetector. The design goal is to have a contribution from the stochastic term coming from photostatistics at the level of 2.3%. With an excess noise factor of the avalanche photodiodes of about 2, this gives a light yield requirement of more than 4000 photoelectrons per GeV for a particle in the barrel. In the endcaps, the lower quantum efficiency of the vacuum phototriodes is compensated by their bigger area, in comparison with APDs.

3.3.1 The light collection curve

One of the most important contribution to the constant term comes from the light yield collection non uniformity. Two effects contribute to this non uniformity:

- A "focusing effect" produced by the crystal pyramidal shape. The photons, produced by the crystal scintillation mechanism, can enter the photodetector on the back side if they have, at the rear face, an angle within the extraction cone. Because of the crystal pyramidal shape, the photons produced far from the photodetector have a higher probability to enter the photodetector. This effect is responsible for the increase of the light collection curve with the distance to the photodetector.
- Because of the optical attenuation in the crystal, the collected light yield decreases with the distance between the photodetector and the source of photons.

The influence of the longitudinal light collection non uniformity on the energy resolution has been studied with detailed Monte Carlo simulations [51]. It was found that the size of the constant term induced by the non uniformity in the region of the e/γ shower maximum is linearly related to the response slope in this region. If we want this contribution to be less than

0.3%, we can tolerate a maximal slope for the longitudinal non uniformity in the region of the shower maximum of $0.35\%/X_0$ for electrons and $0.25\%/X_0$ for photons[1]. In addition, the energy resolution is insensitive to the response slope in the region from the beginning (front face) of the crystal to about 3 cm, as long as that slope is less that ±20 %. It was also found that an increase in the response toward the back of the crystal can compensate for the rear leakage of high-energy showers. An optimal compensation is achieved when the response at the back of the crystal increases towards the rear face by 10% over the last 10 cm. The optimal curve of the longitudinal response is shown in figure 29.

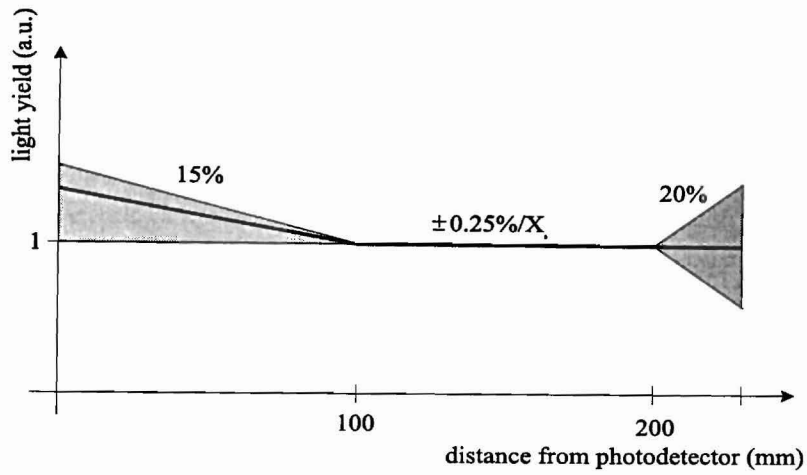

FIGURE 29. The Optimal light collection curve (thick line) with tolerances (shaded regions), obtained from Monte Carlo simulations [51].

3.3.2 Choice of the crystal surface

The amount of light collected as well as the shape of the longitudinal collection curve depends on geometry, on the absorption length of the crystals, on the optical properties of the crystal sides and of the wrapping material. As the geometry is fixed by the physics considerations cited in previous sections and the absorption length by the crystal production, to obtain the requested longitudinal response uniformity several methods have been studied, combining changes in optical properties of the crystal sides and in the wrapping materials. For example, in the first tests, the $PbWO_4$ crystals were uniformized with black scotch or black paint in the region at the crystal beginning. Although giving a good uniformity, these methods have as a drawback a significant reduction of the overall light yield.

From the point of view of the overall light collection efficiency, it was found that a wrapping with tyvek gives the best results [52]. However, this method has been found very difficult to implement because of the large natural spread of the tyvek thickness.

1. The difference between electrons and photons comes from the higher fluctuations of the longitudinal shower average in the case of the photons.

From the light collection uniformity point of view, an optimal light collection curve, with a tolerable 10% light yield loss, was achieved by depolishing one lateral side of each crystal. Therefore, crystals will be delivered by the producer having one side depolished.

3.3.3 Choice of the alveolar structure material

Taking into account the requirements for the mechanical and the optical properties, two types of material have been chosen for the alveolar structure production: a glass fiber epoxy resin prepreg (reference Hexcel 2125/ES70/40%) and an optically treated aluminum. The glass fiber epoxy resin prepreg has been chosen thanks to its capacity to produce walls thin enough to maintain the nominal gap between the crystals.

For what concerns the optical properties the alveolar containers have been optimized in order to keep the longitudinal uniformity inside the requested tolerances with an acceptable light yield loss. This is achieved by choosing the treated aluminum foil, with the structure shown in figure 30. It is made of a 25 μm aluminum coating, ensuring the rigidity of the structure as well as electromagnetic shielding, and by polyester coating, glue, chrome, aluminum and silicium oxide to enhance surface reflexivity and to protect against oxidation.

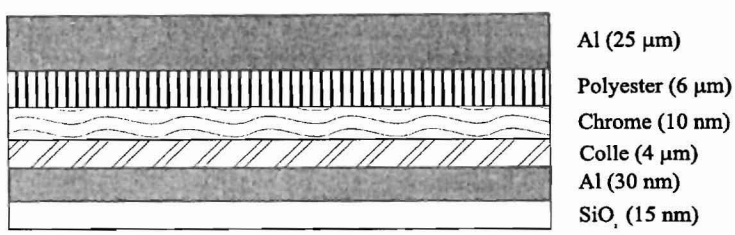

FIGURE 30. The components of the treated aluminum foils used for the production of the alveolar structures.

The optical properties of four samples of treated aluminum, expressed through the hemispheric reflexivity and the diffused reflexivity ($R_{hemispheric} - R_{specular}$) are shown in figure 31 [53]. The samples 1, 2 and 3 have been produced at the Fraunhofer Institute (FEP) in Dresden, except for the optical coating of sample 3, deposited at CERN. The sample 4 has been entirely produced at CERN. The sample 2 has a Rexor substrate, while the others have a Teknek substrate. The samples produced at CERN have the hemispheric reflexivity slightly higher (5% in average) than those produced at the FEP. The mean values, in a region corresponding to the $PbWO_4$ scintillation spectrum (350 nm to 550 nm), are about 85% for the samples 1 and 2 and about 90% for the samples 3 and 4. The mean diffused reflexivity is at the level of 1-2%, except for the sample produced with the Rexor.

As we have already seen, the stochastic term in the energy resolution is inversely proportional to the squared root of the collected light yield. Eventual deterioration of the alveolar structure

optical properties implies a loss of the collected light yield. In order to keep the influence of the alveolar structure optical properties to the stochastic term in the energy resolution on the level of less than 10%, the collected light yield decrease should be smaller than about 20%.

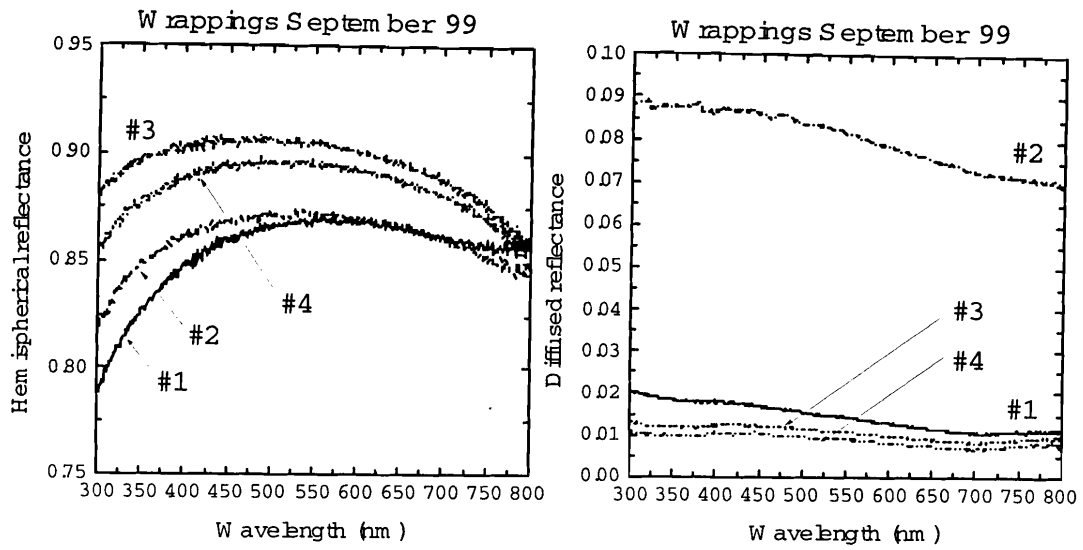

FIGURE 31. The optical characteristics of the 4 samples (see text), measured with a Perkin Elmer lambda 19 spectrophotometer equipped with an integrating sphere of 15 cm [53].

As an illustration of the alveolar structure influence on the crystal light collection, in figure 32 we show the light yield measurements for the same crystal with different wrappings: tyvek, two types of aluminized mylar and two alveolar containers, one produced with treated aluminum and one with non-treated aluminum. From the light collection curves shape, we can see that the alveolas do not change significantly the longitudinal uniformity (the crystal has a slightly higher slope than requested since it was not completely optimized at the shower maximum region). The total light yield is about 10-12% lower with the good alveolas with respect to the tyvek. The non-optimized alveolar container has in addition about 18-20% lower total light yield.

We conclude that the technology of producing the alveolar containers with the treated aluminum allows to keep the optical properties at the requested level. In order to guarantee this properties for the alveolar containers produced on an industrial scale, an efficient quality control system has to be established. This has been the subject of our contribution and will be presented in next sections, after a short overview of the alveolar structures production process.

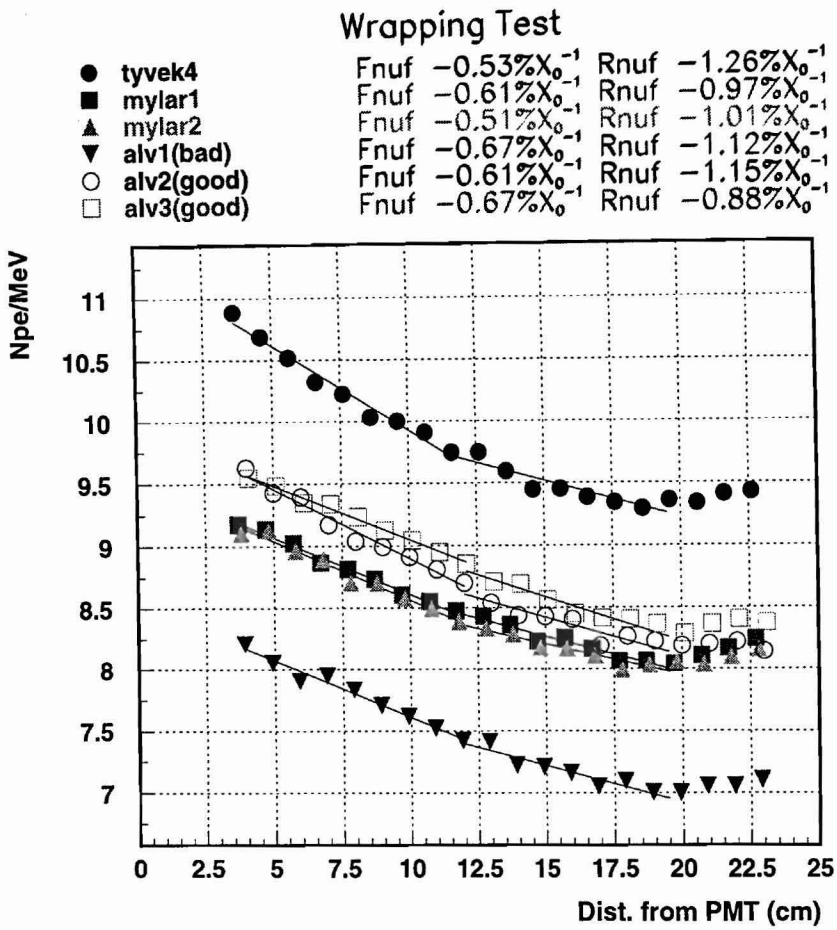

FIGURE 32. Measurements of the distribution of the collected light as a function of the source position and for different crystal wrappings.

3.4 Production of the alveolar structures

The alveolar structures production process has been studied in the preproduction process optimization on a set of structures in the laboratory. It has been optimized in a way of minimizing the material usage, the duration of the process and the number of rejected pieces, while keeping the quality at the requested level, both in terms of mechanical and optical properties. The experience acquired during the development phase has allowed to extend the production to the industrial scale. The alveolar structures will be produced by the firm MOC Composite.

The production procedure proceeds through the following steps:

- quality control of the aluminum foils and of the prepreg,
- cutting up of the foils and wrapping on the mandrels,
- positioning inside the moulds,
- thermal treatment,
- extraction from the moulds and visual inspection,
- cutting to the specified dimensions,
- final geometrical control,
- optical validation,
- packaging and delivery.

Figure 33 shows the process of cutting out of the aluminum foils and the prepreg, their wrapping on the mandrels and the mandrels positioning in the moulds. In figure 34 the photography of the moulding tools is shown. Figure 35 presents a photography of several types of alveolar structures produced in the laboratory.

In order to maximize the alveolar structure production efficiency, a system for controlling each task in the production process has been designed and set up. It consists of 17 electronic boards, one for each structure type. An optical switch is used for the identification of the alveolar type which is being produced, and one button is dedicated for each production task. It will be pressed by the operator after the task completion. All the 17 posts are connected to a data acquisition system. This system sends periodically identifying signals, sequentially for each active post, in order to read their current status. Then, comparing it with the previous state, the operator's action can be determined. A dedicated software program analyzes the sequence of performed tasks and issues warnings in case of eventual non-conformity. Therefore, the production control system monitors the production process and effectively reduces the number of rejected pieces. It also helps in optimizing the whole process in terms of timing, quality and efficiency. The shematic view of the whole system is shown in figure 36.

One of the most important requirements on the alveolar structure is to have very accurate dimensions. The modularity of the ECAL design, with the precise positioning of the structures to the grid and the basket, as well as the closure of the structure with the tablet, request very accurate outer dimensions. Insertion of the crystals demands very accurate internal dimensions. The internal dimensions of the alveolar structures are defined by the mandrels dimensions and the thickness of the alveolar structure walls is controlled by the exact production procedure (the care in the materials wrapping on the mandrels and in the mould closure). The main concern remains for the planarity of the alveolar walls and the alveolar cutting accuracy to the specified dimensions. It is therefore necessary to control the final dimensions of the alveolar structures. Every alveolar structure produced will be precisely measured following the fixed procedure and the results checked to be inside the predefined tolerances. Only the structures passing this dimensional tests will be accepted.

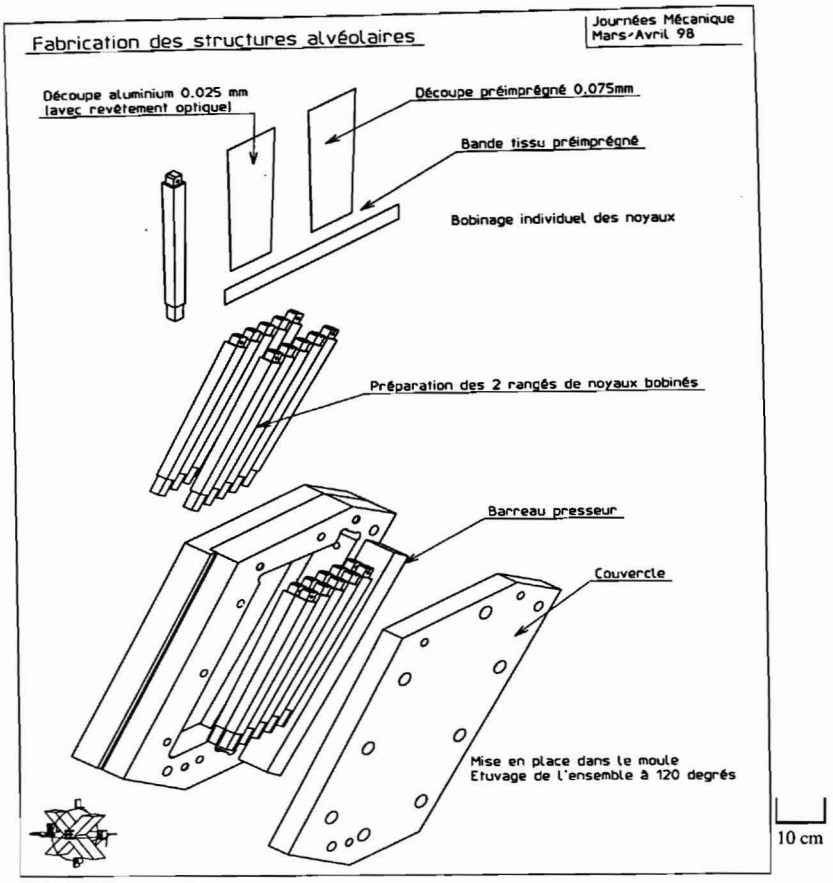

FIGURE 33. A few steps in the alveolar structure production process.

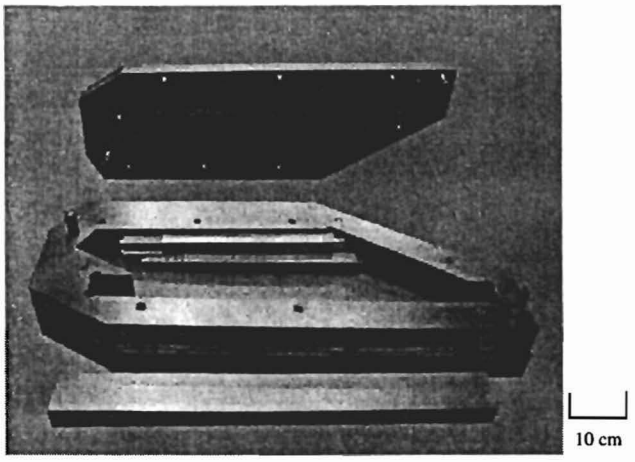

FIGURE 34. Photography of the moulding tools.

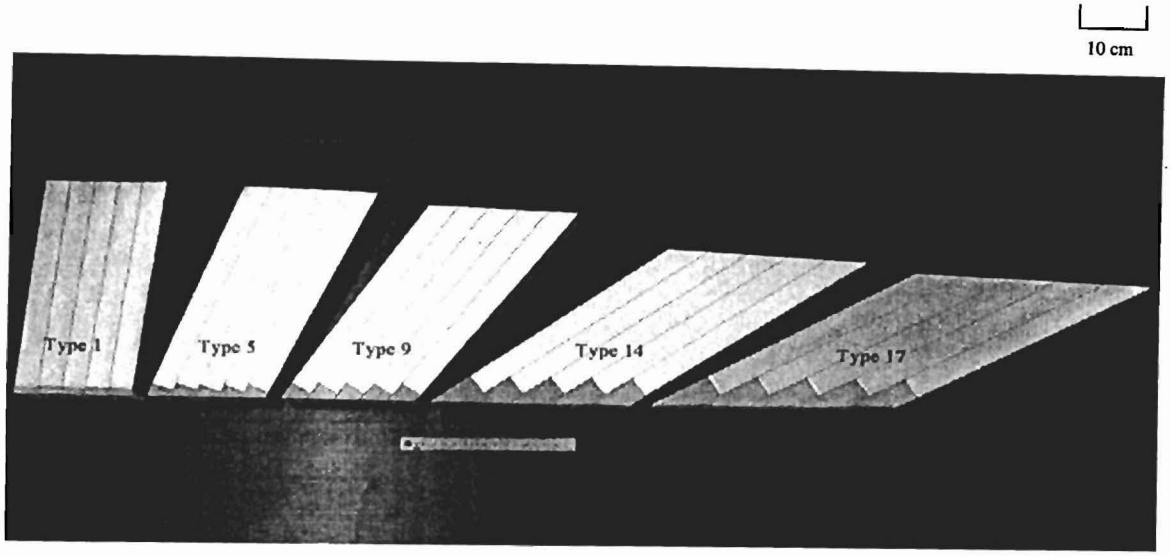

FIGURE 35. Photography of alveolar structures of 5 different types.

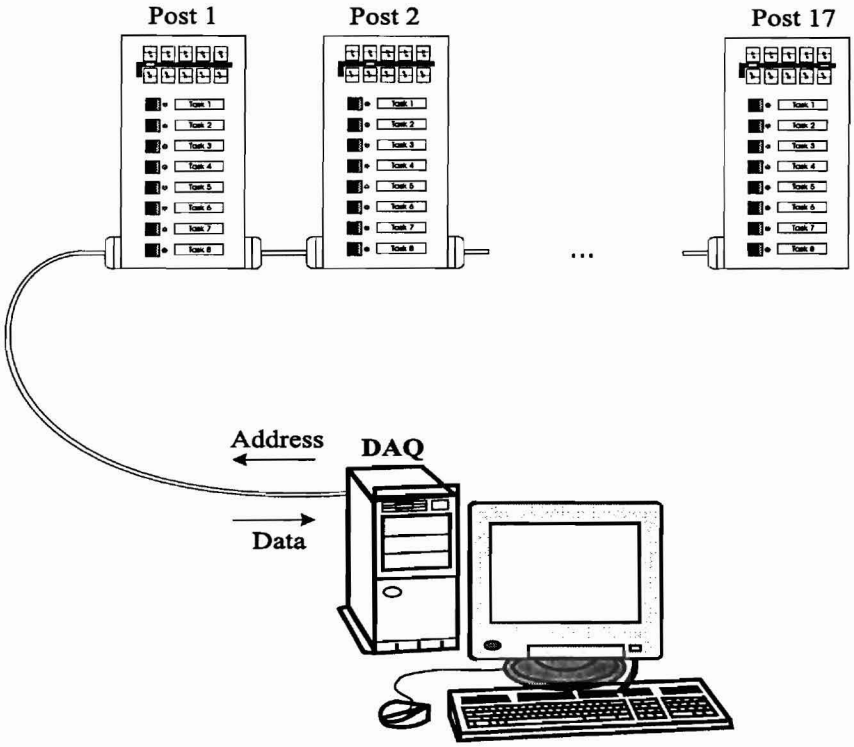

FIGURE 36. Shematic view of the production process monitoring system.

3.5 Optical quality control of the alveolar structures

The optical properties of the alveolar container should remain on the same level for all the structure produced. To ensure this we have developed a control process, consisting of measuring the treated aluminum sample before the alveolar structure production and the structure produced from that sample after the full production process. In this section we present the instrument developed for optical properties measurements, the quality control procedure and the results for the alveolar structures produced in the laboratory.

3.5.1 MONICA

In order to control the optical properties of the alveolar containers, we have developed a dedicated instrument, named MONICA[2]. The design of the instrument is governed by the following requirements:

- measurements of the relevant optical characteristics in a short period of time (a few minutes, i.e. at least one order of magnitude smaller than the time needed for a structure production),
- simple to use for the operator in the factory and in the laboratory,
- dimensions suitable for an insertion into an alveolar structure,
- a short term stability (during the structure measuring period).

The MONICA instrument measures the specular and the diffused reflexivity of a given surface, and its shematic view is presented in figure 37. The most important elements of the instrument are: an electroluminescent diode (LED) as the light source, two PIN photodiodes as the photodetectors, signal amplifiers, a data acquisition system and user interface. The photodiodes are located inside a metallic piece fixed to a shank which holds the cables. The piece has its lateral dimensions slightly smaller than the alveolas nominal ones, so to be able to be inserted inside an alveola. The system is insulated from the noise coming from the 50 Hz lamps. In order to obtain reproducible measurements, the metallic piece has to be well fixed to the measured surface. This is obtained by means of a vacuum pump which, when the piece is well fixed, starts the measurement thanks to a vacuum switch.

The measuring principle is based on the detection of the light reflected and diffused by the measured surface. The continuous light emitted by the LED propagates to the measured surface at an angle of 45°. Part of this light is reflected at a 45° angle, while the other part is diffused in a 2π solid angle. The photodiode positioned at a 90° angle with respect to the surface measures the fraction of the total light diffused (D) in the solid angle $d\Omega_1$ covered by the photodiode ($D \cdot d\Omega_1/2\pi$). We shall call this component *the diffusion*. The second photodiode, located at 45° angle, measures about the same fraction of the diffused light and in addition the fraction of the reflected light (R) with an angle of 45° ($(D+R) \cdot d\Omega_2/2\pi$). We shall call these components *the reflexion*.

2. Apparatus for the 'Mesures Optiques de Nature Industrielle pour le Contrôle des Alvéoles' in French.

The main characteristics of the LED light source are given in table 5. The wavelength of the emitted light well matches the emission spectrum of the $PbWO_4$ crystals which peaks between 440 and 500 nm, with 10% of the peak signal in a window between 360 and 570 nm.

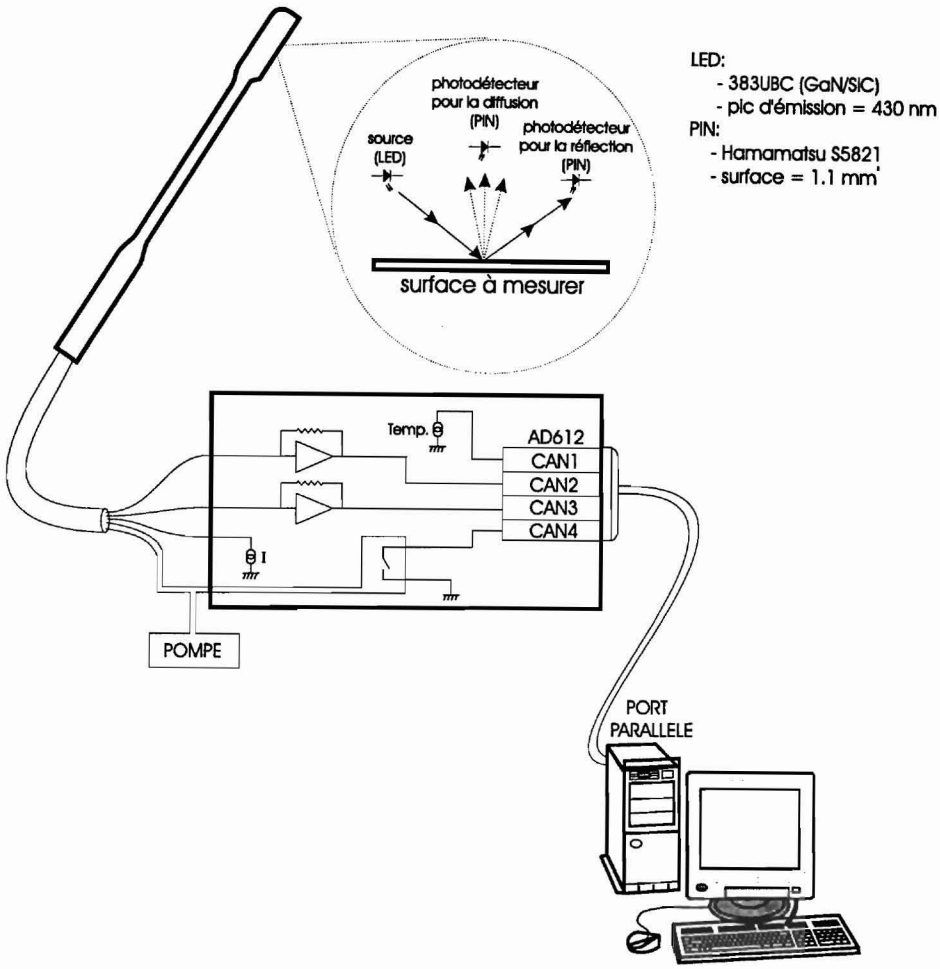

FIGURE 37. The shematic view of the MONICA apparatus.

Material	GaN/SiC
Emission peak	430 nm
V_f, typical	4.9 V
V_f, maximal	5.5 V
Typical current	20 mA
Emission angle	24°

TABLE 5. Characteristics of the 383 UBC LED.

The PIN photodiode produced by Hamamatsu is of type S5821 and has a surface of 1.1 mm^2. Its spectral response has a maximum around 1000 nm, and at 430 nm the 30% of the maximum response is reached.

As the data acquisition system, we have used an analog to digital converter AD612 (from Keithley Instruments, Inc.) which is connected to the parallel port of a computer. It has 6 analog input and 3 digital input/output channels. The converter has a resolution of 12 bits and an input dynamical range from 0 to 4.096 V. The maximal allowed acquisition rate is 15 Hz. A temperature sensor AD590 is located inside the electronic box. It is used to study the variations of the instrument response with respect to the temperature.

We have developed an user interface to drive the use of the apparatus. It allows to choose the working mode (manual or control procedure), as well as the number of measurements. All the measurements results are written into a file for a later analysis.

After the data acquisition triggered by the vacuum switch, the program computes the mean value of 5 consecutive measurements in the same conditions and takes this value as the measurement result. In order to avoid any bias from spurious measurements, the N measurement values are sorted and the final results are obtained by computing the median and the effective RMS defined as:

$$\text{median}=\begin{cases} x_{\frac{N+1}{2}}, & \text{for odd N} \\ \frac{1}{2}\left(x_{\frac{N}{2}}+x_{\frac{N}{2}+1}\right), & \text{for even N} \end{cases} \qquad \text{(EQ 44)}$$

$$RMS_{eff} = \frac{1}{2}\{(w \cdot x_l + (1-w) \cdot x_{l+1}) - ((1-w) \cdot x_k + w \cdot x_{k+1})\} \qquad \text{(EQ 45)}$$

where:

$w = mod(\frac{N \cdot (1-0,683)}{2},1)$,

$k = int\left(\frac{N \cdot (1-0,683)}{2}\right)$,

$l = N-k$.

The general performances of the apparatus have been studied by measuring the optical characteristics of several surfaces. The results are shown on the figure 38. The chosen surfaces correspond to samples of a treated aluminum foil used for the alveolar structures production, white paper (XEROX), black paper and tyvek. One can easily notice the differences between a highly reflective material like the treated aluminum foil and the diffusive material like the white paper. The tyvek has the reflexivity about twice the diffusivity and for the black paper both components are at the level of the instrument offset.

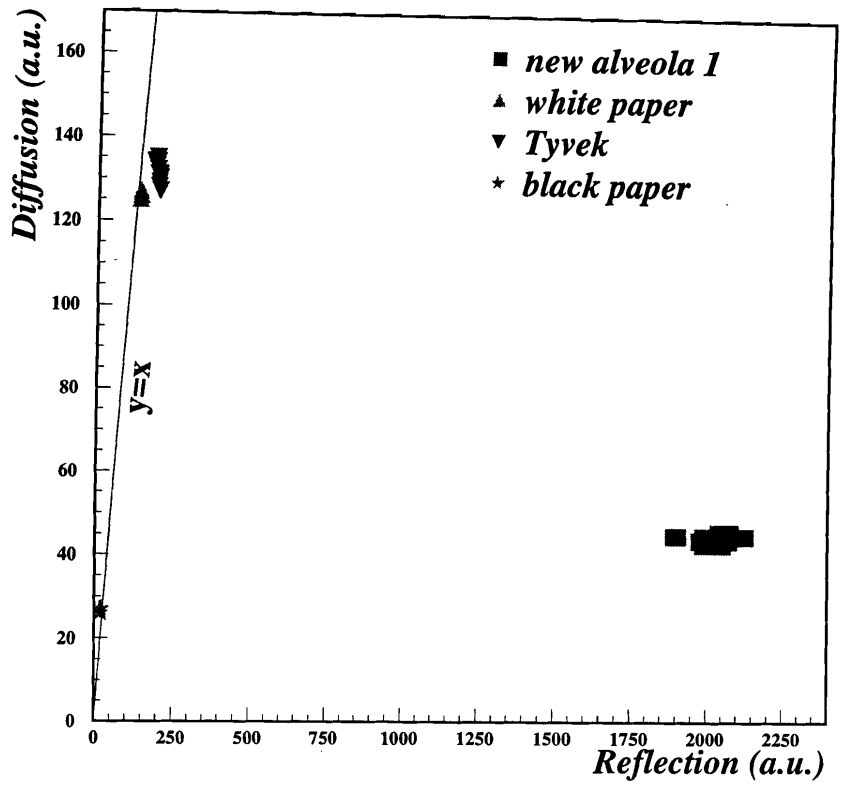

FIGURE 38. Reflexivity and diffusivity measurements on several materials.

One of the most important characteristics of the MONICA instrument is a stability of its response. The main source of variations are the LED aging and the temperature dependence of the emitted LED light intensity. The first effect is responsible for the long term instabilities. The typical lifetime of the LED being used is about 2000 hours, a few order of magnitude larger than the typical alveolar structure measuring period. Nevertheless, a large number of structures to be produced over a period of about 3 years implies that this long term instabilities are not negligible.

Short term variations of the LED response are caused by the temperature dependence of the emitted LED light. The LED is power supplied with the constant voltage and for the typical voltage the current and therefore the intensity of the emitted light increase with the temperature. To study the short term variations of the whole instrument we have measured the optical characteristics of a mirror, in a period of about 1.5 days. The results are shown in figure 39. In order to decouple the characteristics of the instrument from an eventual non uniformity of the measuring surface, all the measurements have been taken at the same point. From the figure, one can see that the responses of both PIN diodes, the one measuring the reflexivity and the one measuring the diffusivity, follow well the temperature variations. The temperature coefficients have been extracted from a linear fit of the correlations shown in figure 40. They are: 1.7%/^{o}C for the reflexivity and 1.5%/^{o}C for the diffusivity. The small histograms on the figure 39 show the deviation for each measurement with respect to the mean value of 4 consecutive measurements ($<>_{loc}$ in the distributions). The variations of the diffusivity are at the

level of the ADC sensitivity and the variations of the reflexivity are negligible with respect to the signal amplitude.

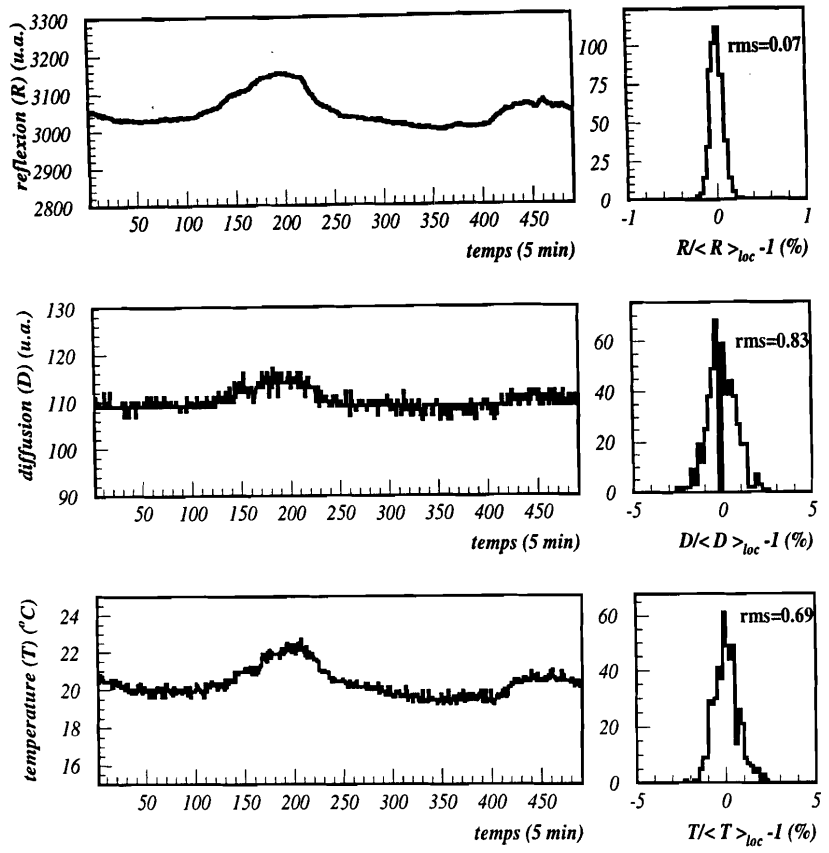

FIGURE 39. Test of the MONICA apparatus short term stability.

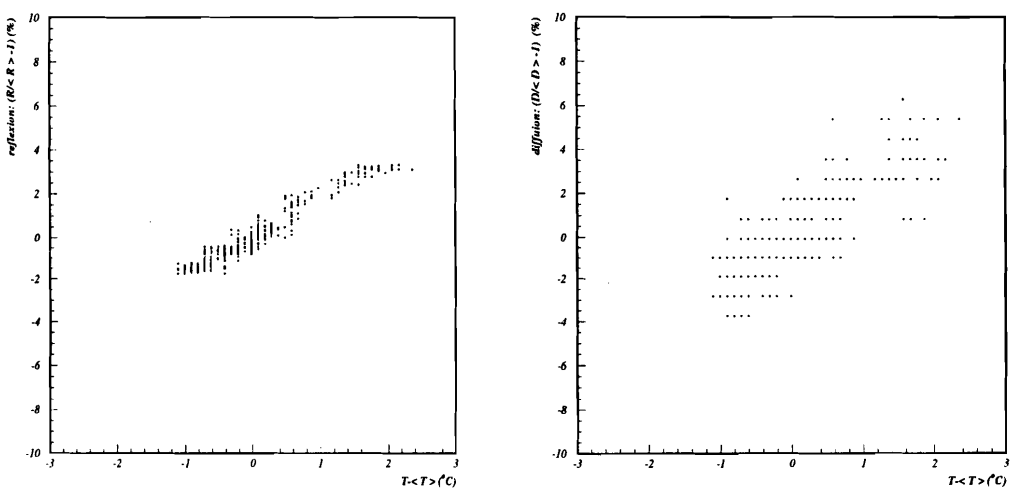

FIGURE 40. Correlations of the reflexivity and of the diffusivity measurements with the temperature. The temperature coefficients are 1.7%/°C for the reflexivity and 1.5%/°C for the diffusivity.

We can therefore conclude that the stability of the measurement apparatus is satisfactory in a few minutes period. This matches the period needed for the measurement of one alveolar structure. If one wants to compare measurements separated by a bigger time interval, it is necessary to normalize them to the results for the corresponding reference surface measured just before. The optical properties of the reference surface have to be stable over a large period of time, at least one order of magnitude larger than the lifetime of the LED.

The light emitted by the LED depends on the applied voltage. It is thus necessary to find a working point in agreement with the constraint of the PIN/amplifier/ADC system saturation on one side, and of the precision on the another side. In order to determine this point, we have measured the reflexivity of a treated aluminum sample, of three alveolar structures made out of the same treated aluminum, one of which had traces on its optical coating (denoted as 'old alveola') and of one structure produced with non-treated aluminum (denoted as 'very old alveola'). The results are presented on the figure 41. The mean values follow the characteristic behavior $I=f(U)$ of the diode. Above around 3.35 V, the separation between the different surfaces becomes visible. As the working point we have chosen a LED voltage between 3.4 and 3.45 V[3].

In order to better compare the optical characteristics of the measured surfaces, the measurements of the reflexivity and of the diffusivity for the LED voltage of 3.42 V are shown in figure 42. On can see a difference of about 5-10% between the treated aluminum sample and the structures produced with the same aluminum. The structure having traces on its optical coating presents an additional decrease of reflexivity of about 10%, with a higher dispersion. The structure produced with the non-treated aluminum, which therefore had started to oxidize, is characterized by a still smaller reflexivity, between 10% and 15%, and a higher diffusivity of about 30%. Comparing these results with the measurements of the collected light, shown in figure 32, we can see that there is approximately the same correspondence between the total collected light with the tyvek wrapping and the alveolar structures when compared to the reflexivity measurements for the treated aluminum sample and the alveolar structures. This shows that, with the instrument developed, we can determine sufficiently small differences for our needs. We shall use the established correspondences in the process of optical quality control of the alveolar structures as described in the next section.

3. Since a few instruments have been produced in the laboratory, their nominal values are different and are determined by a calibration process.

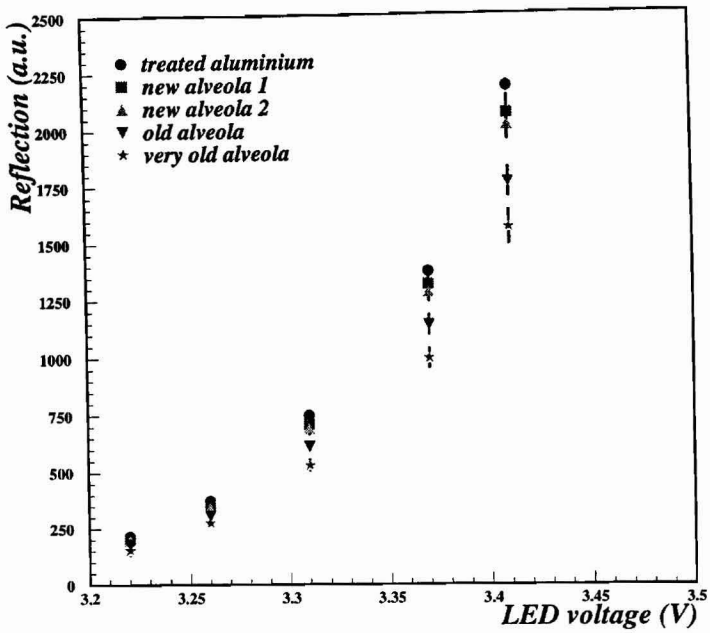

FIGURE 41. The reflexivity measurements of the treated aluminum sample and of different alveolar structures as a function of the voltage applied on the LED.

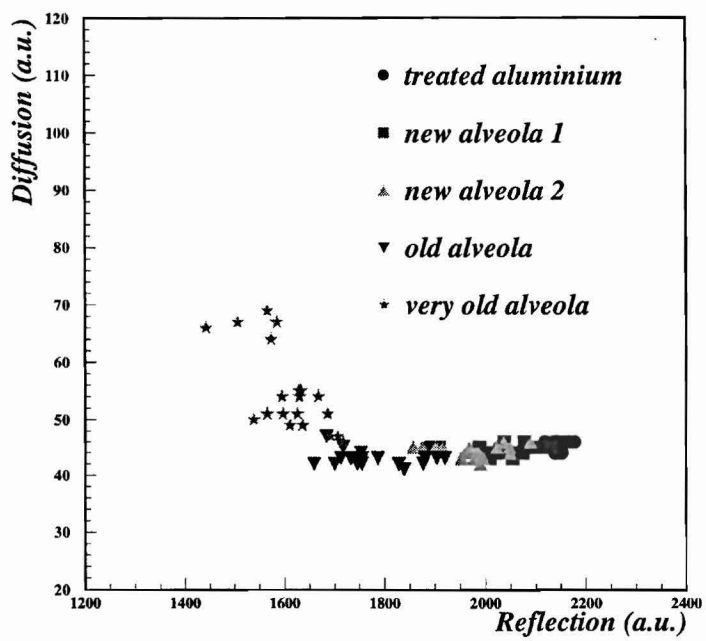

FIGURE 42. The reflexivity and the diffusivity measurements of the treated aluminum sample and of different alveolar structures for a LED voltage of 3.42 V.

3.5.2 The optical control procedure

The alveolar structure optical quality control will consist of two steps:

- Measurements of the aluminum foil samples before the structure production. Only the foil whose sample passes a predefined set of criteria will be used for the alveolar structures production.
- Measurements of the structure after the complete production process. The results for the structure are compared with those for aluminum foil sample from which this structure was produced, and in the case where predefined sets of criteria are not satisfied the structure will be studied more carefully and eventually rejected.

Before each sample and alveolar structure measurement, a reference surface will be measured as needed in order to decouple the optical characteristics of the measured surface from the variations due to the apparatus.

3.5.2.1 Reference measurement

As we have already concluded, the reference material has to have very stable optical properties over the long period of time. As reference candidates we have studied a white paper and several types of mirrors. The white paper has been used for the measurement of some alveolar structures produced in the laboratory, while for the industrial production we have chosen a mirror. It is an interferential mirror made out of PYREX, optimized for a reflexivity maximum of 98% at 45° angle and for wavelengths between 450 and 650 nm. The size of the reference is $130 \times 76 \times 3$ mm^3 and it is protected by a wooden box and identified by an authentication code and a bar code. The results of 40 sets of the reflexivity and the diffusivity measurements for this mirror are shown in figure 43. The measurements have been taken during a 2 hours period, on uniformly distributed points. Again, one can notice a very good stability over a short period of time. The RMS_{eff} values of less than 0.5% for the reflexivity and 1% for the diffusivity are largely sufficient for a normalization of the aluminum samples and the alveolar structures measurements. The long term stability is also expected to be sufficiently good, since the reference is chosen as to be very scratch resistive.

3.5.2.2 Aluminum sample measurement

The aluminum foil used for the alveolar structures is produced at the Fraunhofer Institute (FEP) in Dresden, and delivered in the form of rollers, with the approximate dimensions of $50\ cm \times 300\ m$. Before the production of the alveolar structures, the optical properties of the aluminum foil have to be verified. Every 10 or 20 meters of roller, 4 samples of $10\ cm \times 10\ cm$ will be cut out, one in order to be measured and the others in order to allow an eventual check in the laboratory. Because of the pressure in the MONICA instrument, the samples should be glued on a rigid and plane surface. After several tests on different surfaces, we have chosen an aluminized mylar because of its excellent planarity.

After the reference measurement, the sample will be measured at N randomly distributed points. Upon the measurement completion, a local and a global criteria will be applied. The local criterion checks that the values of one measurement are not too much dispersed by

requesting that the RMS_{eff} and the median ratio is lower than a given value. This value is determined by the calibration procedure of the apparatus measuring the sample etalon in the laboratory.

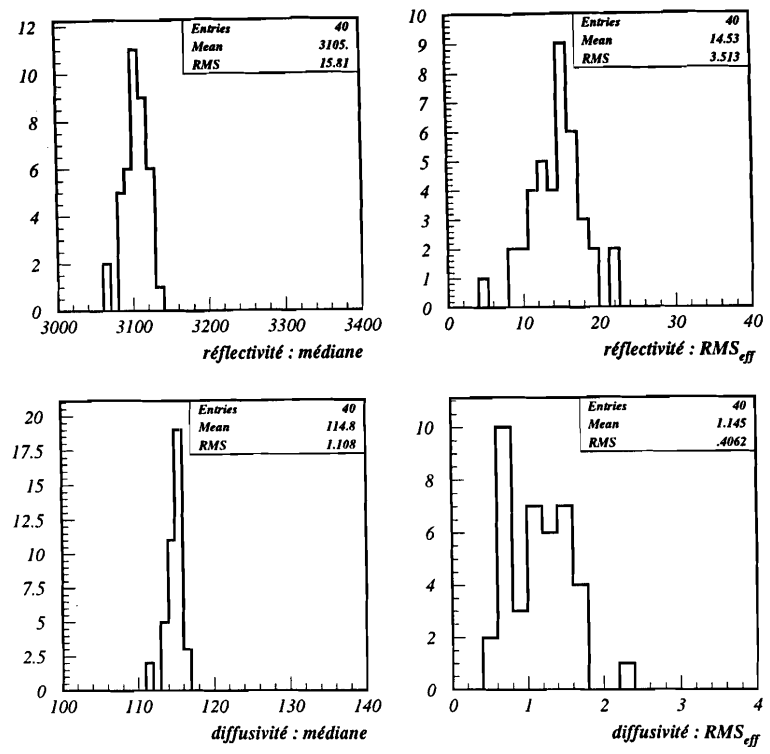

FIGURE 43. Measurement of the interferential mirror reference.

If the local criterion is satisfied, a global criterion is applied. It checks the mean values of the sample reflexivity and the diffusivity by requesting:

$$\frac{\left(\frac{M_{\text{sample}}}{M_{\text{ref}}}\right)}{R_{\text{fix}}} \in [A,B] \qquad \text{(EQ 46)}$$

where:
- M_{sample} is the median of the sample measurements,
- M_{ref} is the median of the reference measurements,
- $R_{\text{fix}} = M'_{\text{sample}}/M'_{\text{ref}}$ is the ratio of the medians obtained by the detailed measurements of the sample etalon and the reference in the laboratory,
- $[A,B]$ is the acceptance interval: [0.9,1.2] for the reflexivity and [0.8,1.2] for the diffusivity.

If the sample does not satisfy the local or the global criteria, the same procedure will be repeated with 2N measurements, to decouple an eventual influence of the small statistics to the results. If again at least one of the criteria is not satisfied, a new sample will be cut a few meters away and the same procedure repeated. If the new sample does not pass the criteria, the

whole procedure will be applied for the last time to a sample cut further away. If the problems do persist, this defines a major non-conformity implying a very detailed study of the aluminum foil.

Figure 44 presents the measurement results of four different samples in the same conditions. The sample on the top of the figure corresponds to the type 4, as defined in the section 3.3.3, and the two others correspond to the type 3. The sample on the bottom of the figure has parameters similar to type 4, but has been cut at the end of the roller where the optical characteristics were deteriorated. We can see that the measurements performed with the MONICA instrument are in agreement with the detailed optical measurements presented in the section 3.3.3.

In order to check the homogeneity of an aluminum roller, we have compared the measurements of several samples coming from the same roller. Figure 45 shows the results, normalized to the reference measured just before the sample. The reflexivity uniformity of the treated aluminum in the same roller is about $\pm 1\%$, and the diffusivity uniformity about $\pm 2\%$, with a degradation of the optical characteristics near the end of the roller which can be as high as 50%. This confirms the strong need for the optical control of the treated aluminum before the alveolar structures production.

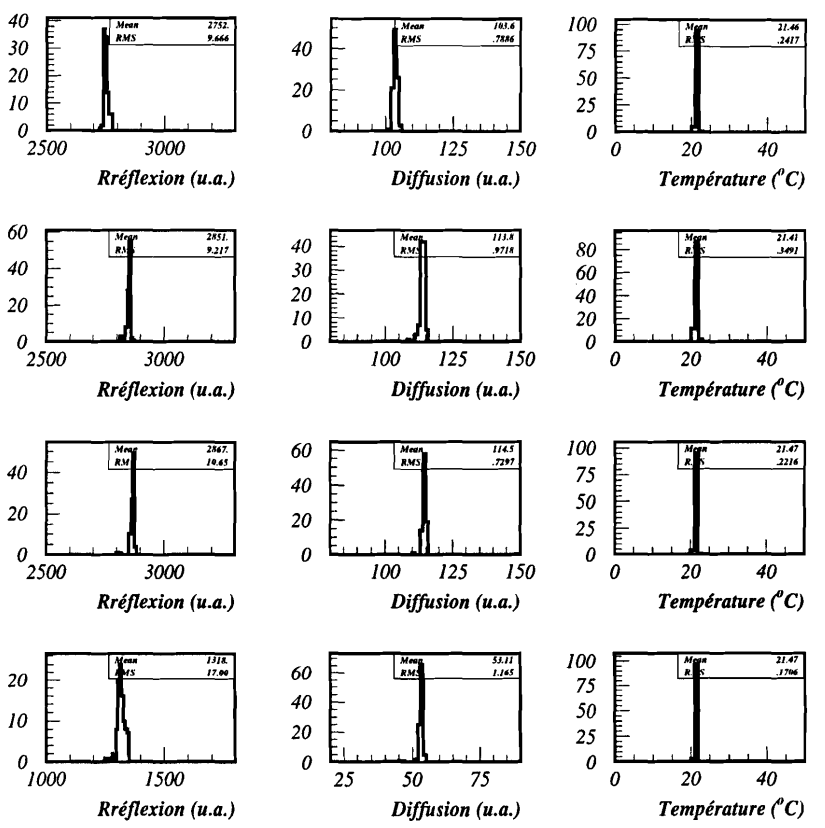

FIGURE 44. The optical properties measurements of samples coming from different rollers (note the change of scale for the last sample).

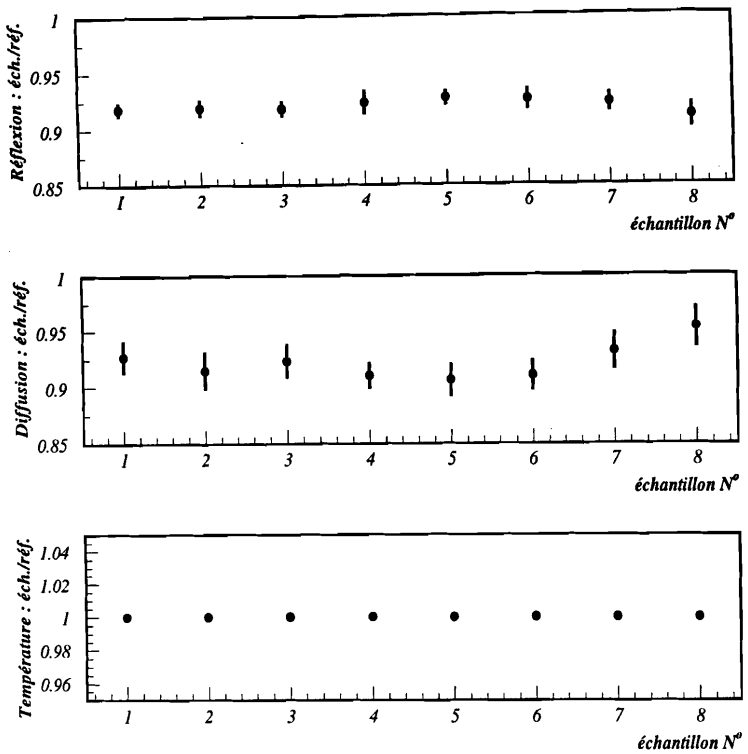

FIGURE 45. The optical properties of several samples from the same roller.

3.5.2.3 Alveolar structure measurement

At the end of the production process each alveolar structure will be measured and the results compared with those for the sample of the aluminum foil from which it was made out. In order to get a realistic insight of the structure optical properties, the measurements will be distributed uniformly in each alveola. The number of measurements is set to 50, that is 5 per alveola.

After the measurement of the reference and of the structure, the local and the global criteria are applied. The local criterion is the same as for the aluminum samples, with different limits determined by the detailed measurements in the laboratory. The global criterion compares the mean values of the alveolar structure and the corresponding sample, requesting their ratio to be inside a predefined acceptance interval:

$$\frac{\left(\dfrac{M_{\text{alv}}}{M_{\text{ref}}^{\text{alv}}}\right)}{\left(\dfrac{M_{\text{sample}}}{M_{\text{ref}}^{\text{sample}}}\right)} \in [A,B] \qquad \text{(EQ 47)}$$

where:

- M_{alv} is the median of the alveolar structure measurements,

- M_{ref}^{alv} is the median of the reference measurements, performed before the alveolar structure measurements,

- M_{sample} is the median of the sample measurements,

- M_{ref}^{sample} is the median of the reference measurements, performed before the sample measurements,

- $[A,B]$ is the acceptance interval: [0.85,1] for the reflexivity and [0.8,1.1] for the diffusivity.

If at least one of the criteria is not satisfied, the alveolar structure will be studied in details. The alveolar structures passing the criteria will be delivered to the laboratory together with the measurements data.

The complete control procedure has been implemented in a software program having the following characteristics:

- automatic gestion of the alveolar structures and samples identifiers,
- link between the structures and the sample from which they were produced with the knowledge of the roller and of the sample position in the roller,
- automatic treatment of all control tasks, with a warnings issued in cases of non-conformity,
- storage of all measurements data of the both references, of the sample, and of the alveolar structure, as well as all the criteria used during the control procedure. These data will be transferred to the CRISTAL database.
- gestion of the correspondence between the bar codes and the alveolar structures identifiers.

3.5.3 Results on the Module 0

The developed optical quality procedure has been tested on the alveolar structures of the ECAL Module 0 produced in the laboratory. The Module 0 is made of 4 different types of alveolar structures (types 6, 7, 8 and 9), with 10 sub-modules of each type.

As the reference surface we have used a white paper (XEROX). Figure 38, we can see the main characteristics of the white paper, with a reflexivity slightly higher than the diffusivity.

Because of the pressure in the apparatus and the alveolar structure walls flexibility, there was a difference of about 5% between the reflexivity values for the internal walls and the external walls. These measurements are presented in figure 46. In order to avoid an influence of these dispersions to the results, we have decided to measure only the external walls.

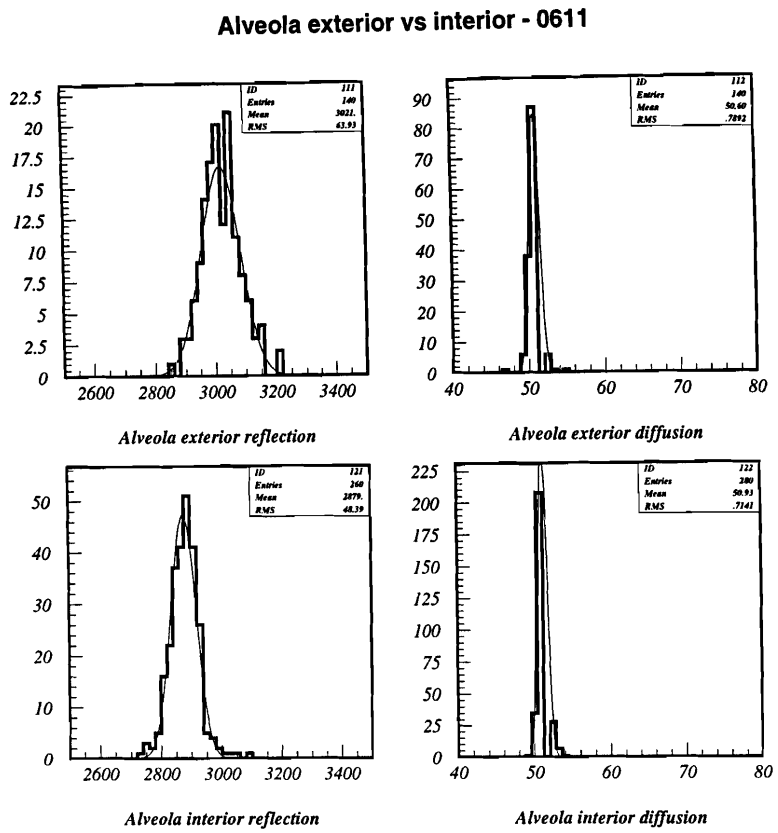

FIGURE 46. Measurements of the reflexivity and the diffusivity of internal and external walls of the alveolar structure 06011.

Figure 47 presents the ratio of the RMS_{eff} to the median value for all the references, the samples and the alveolar structures. We can clearly see differences between the surfaces. For the samples and the alveolar structures, the diffusivity values are dominated by the instrument noise. As the local criterion, we have taken the following values: 2% for the reference, 3% for the samples and 4% for the structures, both for the reflexivity and the diffusivity.

We have also used these measurements of the optical properties of the aluminum samples and of the alveolar structures to extract following informations:

- The optical uniformity of the alveolar structure, by looking at the measurements dispersion inside the structure. Figure 48 shows the measurements results of each alveola of three structures (10 distributed measurement points per alveola), and the values of the median and of the RMS_{eff} for all the measurements together. We can notice some differences between the three structures, with the reflexivity RMS_{eff} values of 1.5%, 2.5% and 4% and the diffusivity of 1%, 2% and 1%. All these values satisfy the local criterion for the alveolar structures.

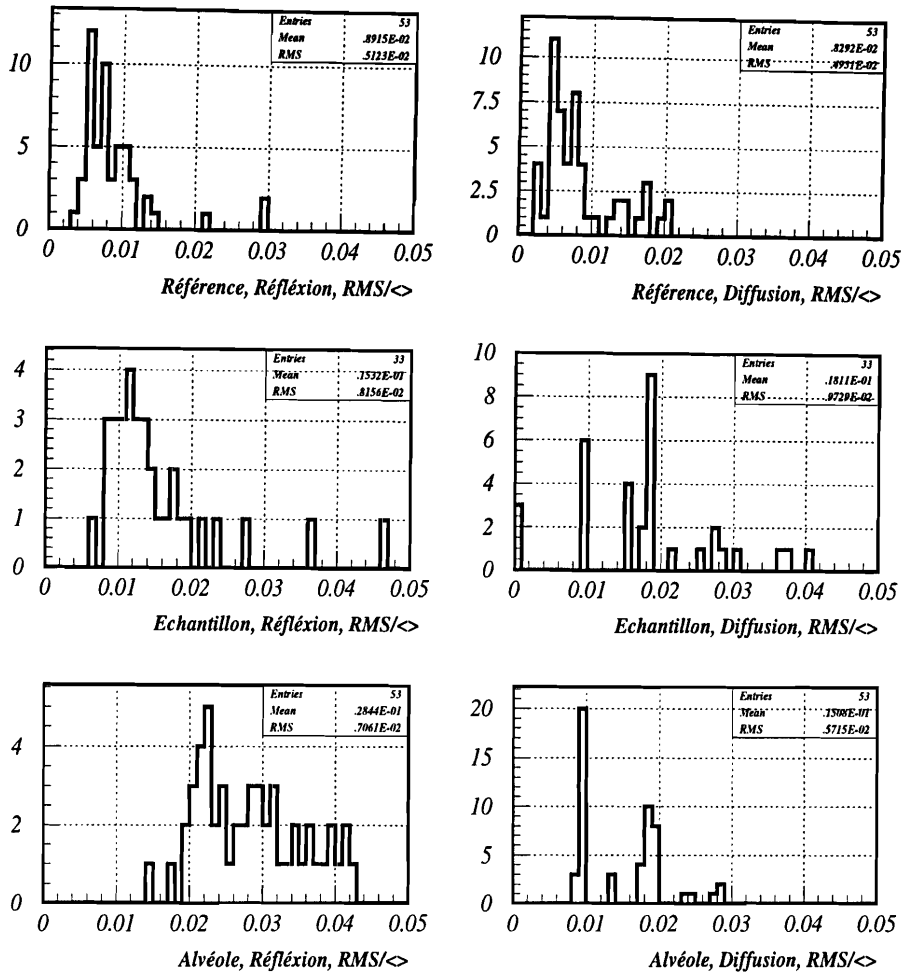

FIGURE 47. The ratio of the effective RMS to the median for the references, the samples and the alveolar structures.

- The uniformity between the structures, by comparing the measurement results normalized to the corresponding references (figure 49). The main difference between the structures comes from different aluminum foils used for these structures. In the production of these structures, two different rollers were used with about 4% difference in reflexivity and about 9% difference in diffusivity. They correspond to the first two rollers from which the samples presented in figure 44 were cut out.
- The difference between the values obtained for the structure with respect to those for the samples of the aluminum foil from which the structure was made. The results of these measurements are shown in figure 50. The notation 'relative' stands for the ratio defined by equation 47. The difference between the structure and the sample is in average 7% for the reflexivity and about 5% for the diffusivity.

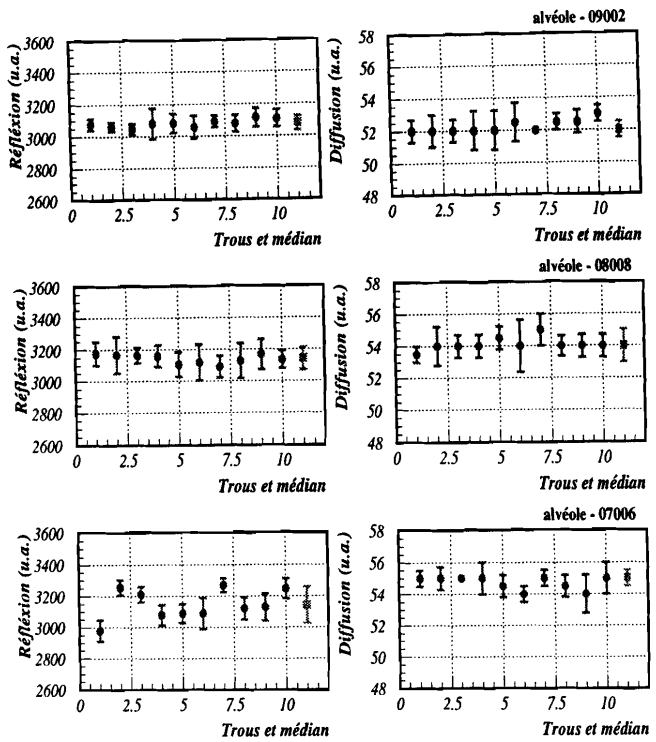

FIGURE 48. The reflexivity and the diffusivity uniformity of three alveolar structures. The values for one alveola are obtained as the median and the RMS_{eff} of 10 measurements, and the median and RMS_{eff} at the end of the histograms correspond to all the measurements taken together.

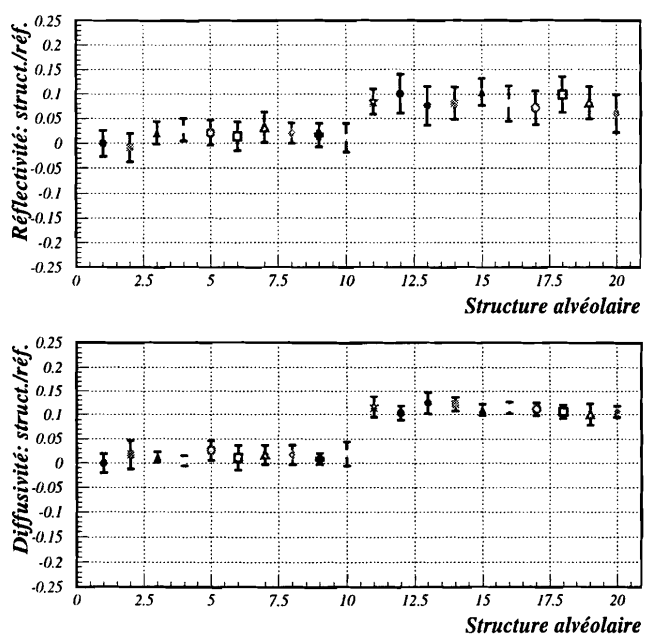

FIGURE 49. Results for the alveolar structures produced from two different rollers of aluminum.

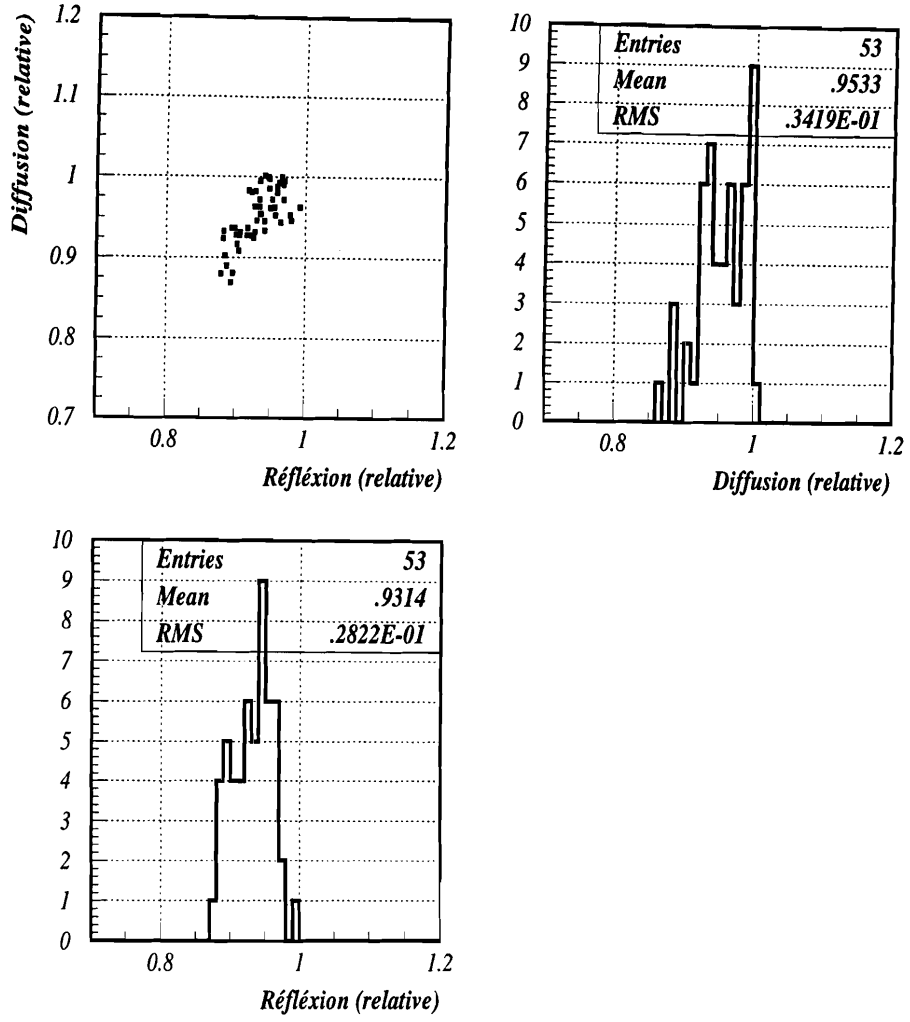

FIGURE 50. Ratio of the alveolar structures and the aluminum samples: diffusivity versus reflexivity. All the values are normalized to the corresponding references.

3.6 Conclusion

The quality control of the detector components is an important step in the detector construction process. For the alveolar structures quality control we have developed a control process consisting of three steps: the production process monitoring, the geometrical (3D) measurements and the optical quality control.

In the production monitoring process each sub-operation in the alveolar structure production is registered by the developed electronic system. The tasks sequence is analyzed to verify an exact production procedure. The 3D measurements are necessary to verify the alveolar struc-

ture dimensions and consist of a predefined set of measurements. Finally, the optical quality control is needed in order to keep the contribution of the alveolar structure optical properties to the stochastic and the constant terms in the energy resolution at an acceptable level. By the specially developed instrument, the reflexivity and the diffusivity of the alveolar structure is measured and the results verified to be inside the predefined tolerances with respect to the results obtained for the aluminum foil from which the structure has been made out.

Following the developed control process, the alveolar structure production is optimized from the points of view of efficiency and quality. The control procedure and the developed instruments have been optimized and verified on the alveolar structures produced in the laboratory and then the whole system has been installed in the factory.

The output of every quality control step is a set of data, consisting of the sub-operation results, date and time, as well as the operator informations and eventual comments. The production, geometrical and optical measurements data will be transmitted to the LPNHE, together with the alveolar structures. Then, the data will be verified by the operator and, after eventual completion of the missing data, transmitted to a local CRISTAL[4] database. For some of the alveolar structures the geometrical and the optical measurements will be performed again in order to cross check the results obtained in the factory. Then, the alveolar structures will be sent to the regional centers for assembly. The data will be sent to the central CRISTAL database, where they could be consulted by the assembly operator in the regional center and by any other physicist of the collaboration.

4. The CMS collaboration have developed the CRISTAL system (Concurrent Repository and Information System for Tracking Assembly and production Lifecycles) [54], aimed to monitor and control the quality of the production and assembly process.

Chapter 4 *Study of the $H \rightarrow ZZ^* \rightarrow 4e^{\pm}$ signal and the backgrounds*

4.1 Introduction

As we have seen in the first chapter, many decay channels can be exploited to search for the Higgs boson in the intermediate mass region, from ~ 110 GeV to $\sim 2M_Z$. One of the most important channel is Higgs 4 leptons decay through a ZZ^* intermediate state. In this channel, the explorable final states can be divided into three classes: $e^+e^-e^+e^-$, $e^+e^-\mu^+\mu^-$ and $\mu^+\mu^-\mu^+\mu^-$. As a subject of this thesis, we have chosen to study the $H \rightarrow ZZ^* \rightarrow 4e^{\pm}$ channel. As we shall see, it gives very strong requirements on the electron reconstruction.

The higher order effects will play an important role at the LHC. Many processes have a significant increase of the cross section at the next to leading (NLO) order with an important influence of the higher order processes on the event kinematics. One example is the gluon fusion process for the Higgs production, having an about 70% increase of the cross section at the next to leading order in the intermediate Higgs mass range. On the other hand, the Monte Carlo event generators allows for cross section evaluations at the leading order (LO). The higher order contributions are generated through initial and final state QCD and QED showering processes. A simple scaling of the LO cross sections to the NLO ones, obtained from more rigorous theoretical models, is justified only if the corresponding kinematical variables agree. A dedicated study of the Higgs transverse momentum distribution has been performed and will be described in this chapter. We will compare the predictions from Monte Carlo generators and theoretical calculations based on the soft gluon resummation technique.

In order to extract the signal from the backgrounds, we will analyze the kinematical distributions of the particles in the final state as well as in the intermediate state. In such an analysis, a detailed study of the Monte Carlo generators is important. We shall insist in particular on the main characteristics of the Z* mass spectrum, as well as on the transverse momentum of the four electrons in the final state.

Then, we will evaluate the main background processes: ZZ^*/γ^*, $t\bar{t}$ and $Zb\bar{b}$. For the first two processes, we will give an update of the recent theoretical results as well as new results from Monte Carlo generators. The $Zb\bar{b}$ process which was not satisfactorely described in the existing generators, has been therefore the subject of a detailed study.

Finally, we will address the question of the kinematical cuts optimization. Because of the small number of expected signal events there is a strong interest to lower as much as possible the transverse momentum cuts, especially at the lower Higgs mass reachable with this channel. We have studied an optimization of the kinematical cuts with the emphasis on the p_T

electrons cuts. In this study, we show how the $t\bar{t}$ and $Zb\bar{b}$ backgrounds can be effectively suppressed to an acceptable level by isolation cuts, and how some additional cuts may help in a further rejection of the ZZ* background.

4.2 Higgs transverse momentum

There are several reasons why it is important to study the p_T distribution of the Higgs boson:

- For a complete event generation, existing Monte Carlo programs use a parton showering model. The most relevant theoretical approach for the p_T distribution prediction is based on the soft gluon resummation. Comparing this two methods is useful in order to understand their strenght and weakness and to test their reliability.
- As we have already mentioned, Monte Carlo event generators compute the cross sections at the leading order. The Higgs production processes, particularly the gluon fusion mechanism, have important NLO contributions. In order to take them into account as a simple normalization factor to the Monte Carlo generated events, it is essential to have an agreement between the kinematical variables of the generated events and theoretical higher order calculations. A sensible variable is the Higgs boson transverse momentum.
- In the Higgs decay modes $H \rightarrow \gamma\gamma$ and $H \rightarrow ZZ^*$ the shapes of the signal and the corresponding background p_T distributions are different, with the signal being harder. This difference can be used to enhance the statistical significance of the signal over the background. It is, therefore, important to understand the reliability of the predicted p_T distributions.
- The p_T of the Higgs will have an influence on the vertex determination in Higgs events in CMS, specifically in the $H \rightarrow \gamma\gamma$ channel in the presence of pile-up events.

The dominant mode for the Higgs production at LHC is the gluon fusion process. At the leading order, it is a $2 \rightarrow 1$ process and the Higgs is produced with a very small transverse momentum, of the order of the gluon transverse momentum inside the protons, around 0.5 GeV [55]. The Higgs with a sizeable transverse momentum is generated by the higher order processes, where the Higgs is associated with one or several partons in the final state. Some of these processes, $gg \rightarrow gH$, $gq \rightarrow qH$, $q\bar{q} \rightarrow gH$ are shown in figure 51. In the other production channels, the Higgs transverse momentum is balanced by the partons already present in the final state (for instance the two quarks in the W and Z boson fusion), and the higher order processes have a smaller effect on the p_T distribution. A comparison of the Higgs p_T distributions in the gluon fusion and vector boson fusion processes is shown in figure 52. Both distributions are normalized to the same area. We can observe the expected difference, the Higgs produced through the vector boson fusion having a distribution with mean a value of the order of the W and Z masses, and therefore harder than the distribution corresponding to the gluon fusion process.

Giving the fact that the gluon fusion process is the main Higgs production mode, we shall concentrate on this process.

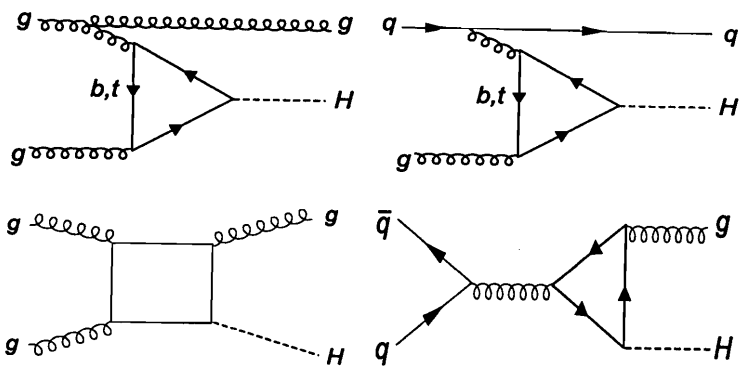

FIGURE 51. Some parton-level processes producing the Higgs boson with sizeable p_T.

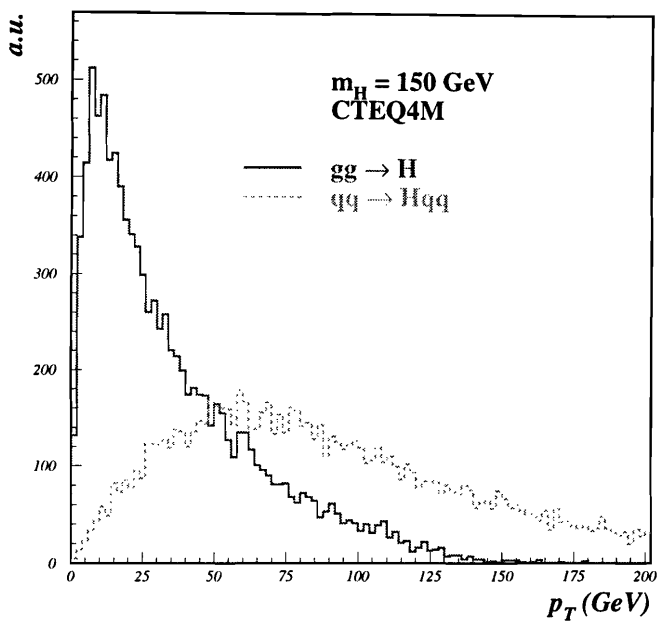

FIGURE 52. Transverse momentum of the Higgs produced through the gluon fusion process and the W and Z boson fusion, normalized to the same area.

In existing Monte Carlo generators, there are two ways to describe the Higgs transverse momentum in the gluon fusion process: by a process $2 \to 1$ with the parton showers or by a process $2 \to 2$ using explicit matrix elements at NLO[1]. The latter method succeeds better in the exclusive cross section description, but fails to describe events with one soft parton or two colinear partons. The first method allows to generate full events with an arbitrary number of partons in the final state, but hardly describes exclusive cross sections. This method is used in the inclusive studies of the Higgs boson and we will use it in the further comparison. The most relevant analytic calculation is a soft gluon resummation at all orders, based on the CCS (Collins, Soper, Sterman) formalism [56]. This method allows to predict the differential cross sections, but does not provide a full event generation. These analytical calculations are

1. In this process, the parton showers contribution to the transverse momentum is smaller.

implemented in the ResBos simulation program [58]. We will now go into a detailed comparison of the Higgs transverse momentum predictions obtained using both methods. Both models, the parton shower and the resummation, have been compared and tested with the Tevatron experimental data for the p_T distribution of the Z boson. A very good agreement of both models with the data has been observed [59]. The agreement of PYTHIA with the data in the high p_T region is a consequence of the implementation of explicit matrix element corrections (from the subprocesses $q\bar{q} \to Zg$ and $gq \to Zq$) to the Z process [57]. These corrections are implemented for all s-channel colorless gauge boson productions, but are not valid for Higgs production because of a quite different nature of the production process.

The Higgs p_T distribution obtained with ResBos and two versions of PYTHIA are shown in figure 53, for a Higgs mass of 150 GeV. In each case, the structure function CTEQ4M [60] is used. All the distributions are normalized to the same total cross section obtained with ResBos, so as to be able to better compare their shapes.

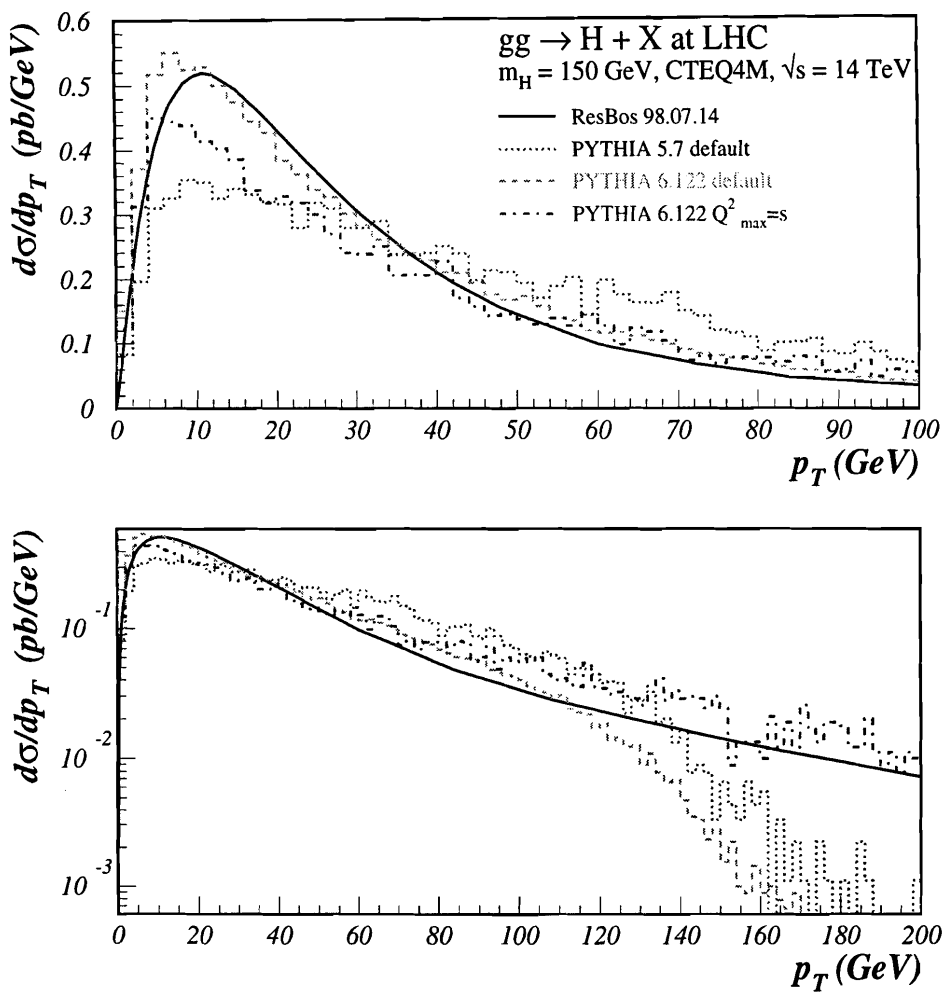

FIGURE 53. Higgs transverse momentum distributions for the gluon fusion production process, as predicted by ResBos and two versions of PYTHIA, in a linear scale (top) and in a logarithmic scale and up to 200 GeV (bottom).

There are several important characteristics to be observed for these distributions:

- a very significant difference between the PYTHIA versions 5.7 [61] and 6.122 [62] in the region of low and intermediate p_T ($p_T < 100$ GeV),
- a very good agreement between ResBos and PYTHIA 6.122 in the region $p_T < 120$ GeV,
- a disagreement between ResBos and PYTHIA in the region $p_T > 140$ GeV. A better agreement is obtained by allowing in PYTHIA the momentum of the partons in showers to reach the maximum energy in the proton-proton center of mass, that is $Q^2_{max} = s$, instead of $Q^2_{max} = m_H$.

The discrepancies between the two PYTHIA versions comes from a change in the modeling of the parton showers generation[2]. Two modifications have been incorporated in the 6.122 version. The first one is a condition $\hat{u} = Q^2 - \hat{s}(1-z) < 0$. Q^2 is related to the mass or transverse momentum scale of the shower branching and z is the momentum fraction taken by one of the daughter particles in the branching. $\hat{s}$ refers to the subsystem of the hard scattering plus the shower partons considered to that point. The association of these variables with $\hat{u}$ is relevant if the branching is interpreted as a $2 \rightarrow 2$ process [62]. The condition $\hat{u} < 0$ induces a considerable reduction of parton radiation, as can be seen from the figure 54, where the distributions for several changes of the relevant parameters in PYTHIA are shown. The second modification involves the parameter controlling the minimum energy that a gluon can carry in a shower. It allows more radiation and therefore, goes against the first modification. However, the condition on $\hat{u}$ appears to be the dominating one, as it can be seen from figure 54.

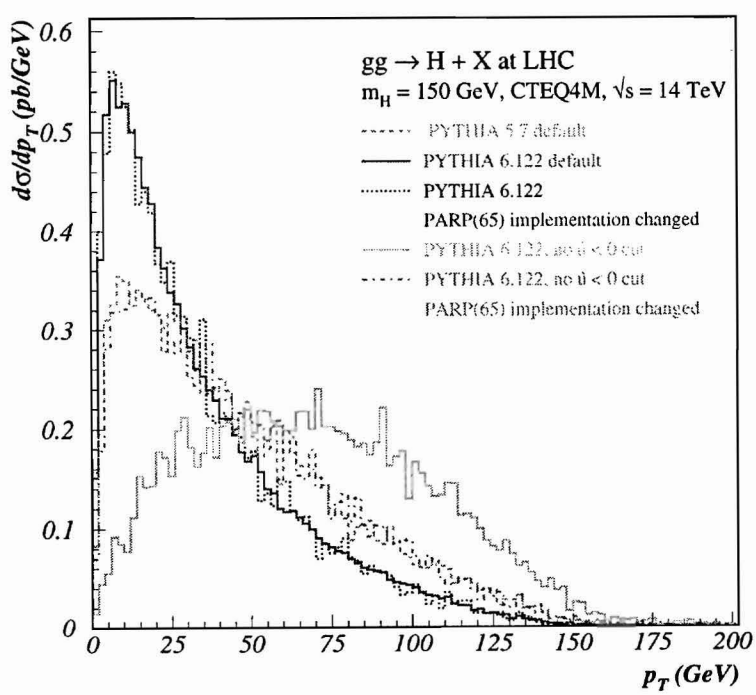

FIGURE 54. Transverse momentum distributions for different parameter values in PYTHIA. The parameter PARP(65) is related to the minimum energy that a gluon can carry in a parton shower.

2. The parton shower can be described as a sequence of $1 \rightarrow 2$ branchings $a \rightarrow bc$. Here a is called mother and b and c are two daughters.

In the high transverse momentum region, $p_T > 140$ GeV, there is an important discrepancy between both versions of PYTHIA and ResBos. In this region, ResBos switches to the NLO Higgs plus jet matrix elements and we take it as a reference. In the default PYTHIA version, the condition for the maximum virtuality in the shower development $Q^2_{max} = m^2_H$ induces a drop in the p_T distribution when p_T reaches the value of about one Higgs mass. The change $Q^2_{max} = s$, that can be introduced in PYTHIA 6.122, increases the available phase space for partons radiation and therefore induces the tail in the distribution. As a consequence of more radiation there is a considerable event reduction in the peak region. We, therefore, conclude that the optimum value for Q^2_{max} that has to be introduced in PYTHIA depends on the region of transverse momentum to be studied.

The differences between both PYTHIA versions give us indications on the uncertainties due to the choice of the parameters in Monte Carlo programs. It is thus interesting to compare with another Monte Carlo generator. In figure 55, a comparison between PYTHIA 6.122, Herwig 5.6 [63] and ResBos is shown. We can observe similar effects as the ones already mentioned, with a slightly better agreement between Herwig and ResBos distributions in the region at low p_T.

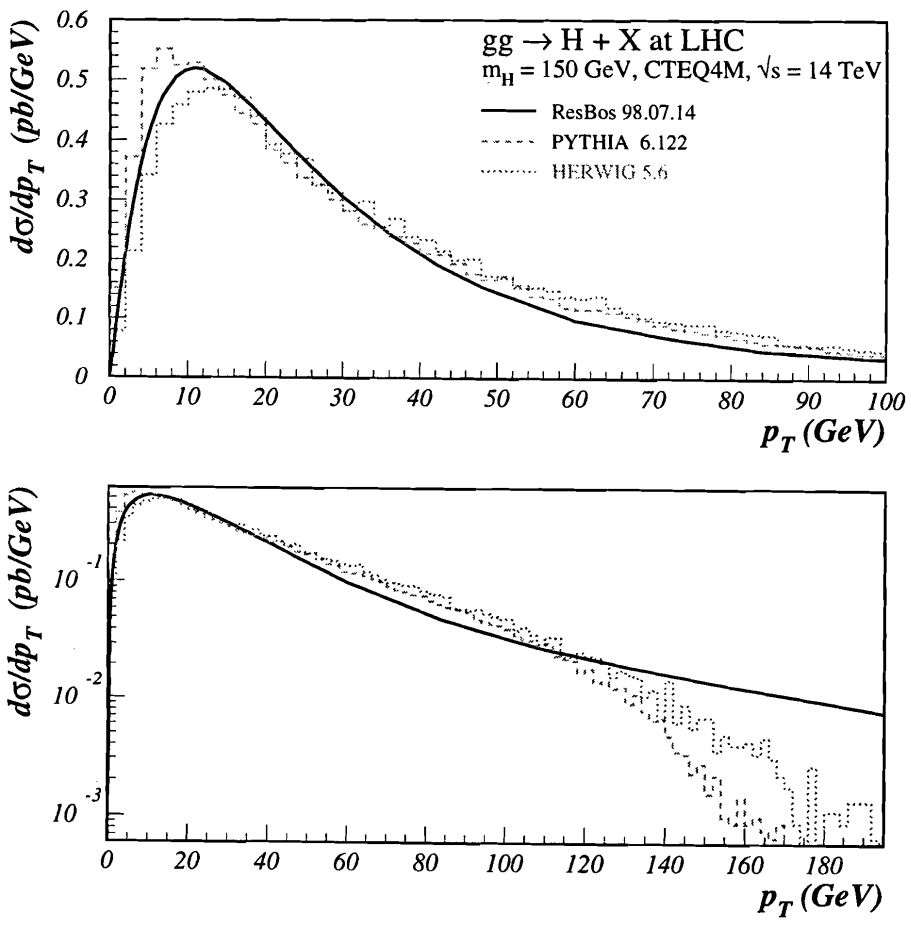

FIGURE 55. Higgs transverse momentum distributions as obtained from Pythia 6.122, Herwig 5.6 and ResBos.

As we have already underlined, the cross sections obtained by the Monte Carlo generators are at leading order while the one obtain with ResBos is at the next to leading order. The presented distributions up to now were normalized to the cross section obtained with ResBos. In order to illustrate the differences, the distributions normalized to the total cross sections predicted by the same model are shown ib figure 56.

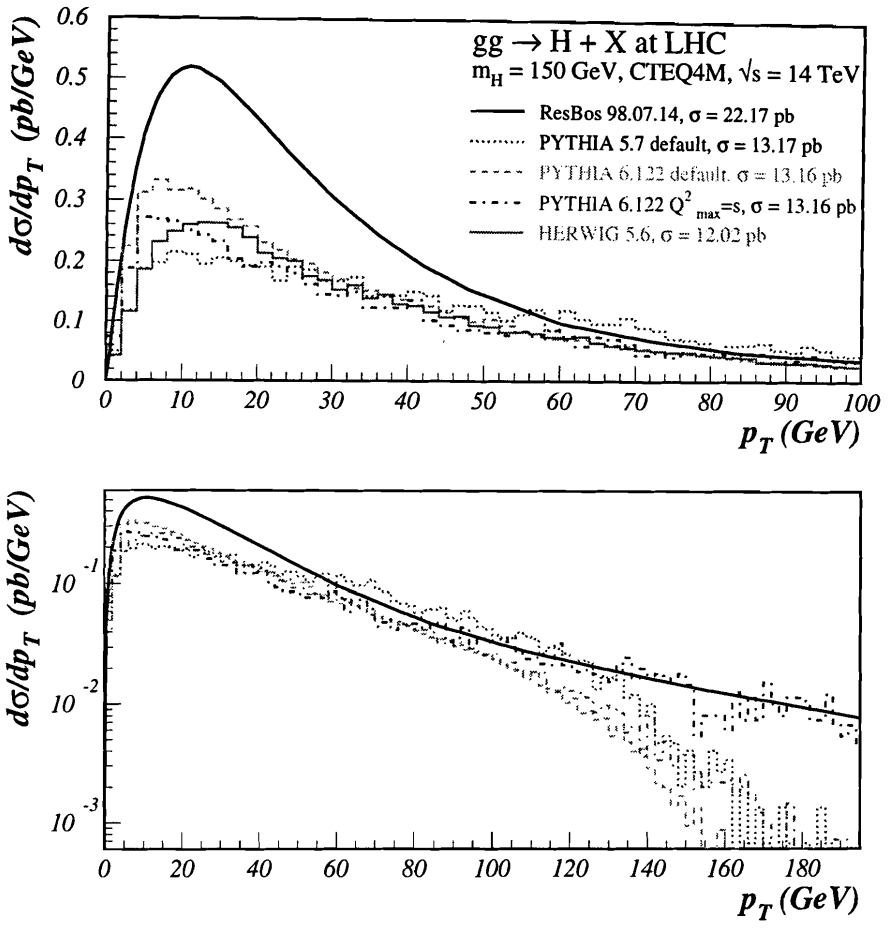

FIGURE 56. Higgs transverse momentum distributions normalized to the corresponding cross-sections.

The primordial k_T effect

The experimental data of the Z and W bosons p_T distributions at the Tevatron have shown that, for a better agreement with the data, it is necessary to introduce a primordial k_T of 2.15 GeV per initial parton[3] in the Monte Carlo generators [59]. This value is very close to a corresponding value in the soft gluons resummation formalism. It does not mean that there is something wrong in the k_T distribution of the partons in the nucleon, but rather that it is necessary to correct the defects in parton showers generation due to the cut-off (Q_0) introduced in this process. We have studied the effect of the k_T distribution width changes[4] on the Higgs p_T

3. The k_T value which corresponds to the proton size is about 0.5 GeV.

distribution. The results are shown in figure 57, for two values of the k_T distribution width, and compared with the ResBos prediction.

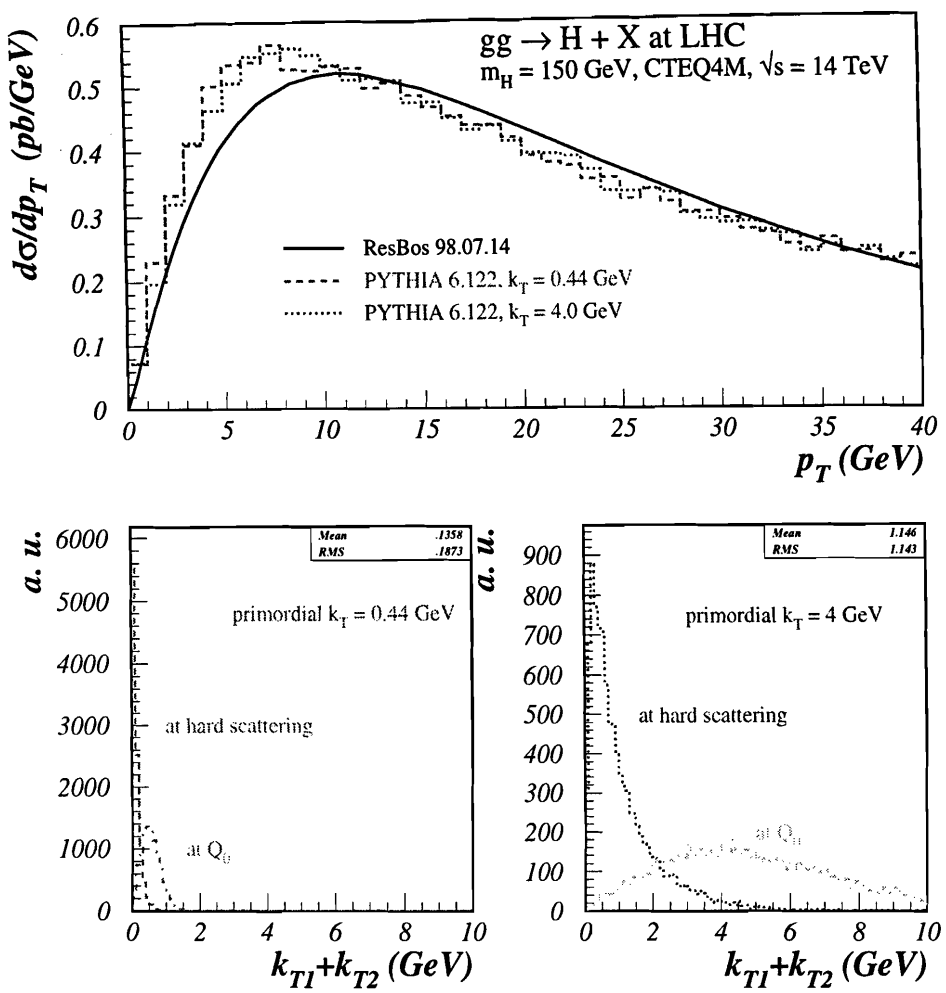

FIGURE 57. Higgs transverse momentum distribution for two values of the width of the partons k_T distribution of the partons, compared with the distribution obtained with ResBos (top). The distributions of the two partons k_T vectorial sum at the shower initial scale and at the scale of the hard process (bottom).

We can see from the figure that there is no sizeable difference between the distributions obtained with different k_T. This is due to the higher activity of the parton shower at LHC, in comparison with the Tevatron, because of the bigger phase space allowed for parton radiation. The amount of shower activity is visible on the lower plots, comparing the distributions of the partons k_T vectorial sum at two different scales, the one corresponding to partons momentum before radiation (Q_0) and the one corresponding to the partons momentum in the hard process.

4. The k_T distribution in the proton, in our case, has a gaussian shape, that is $\exp(-k_T^2/\sigma^2)k_T dk_T$ and the change of width corresponds to a change of σ.

For reason of completeness, in figure 58, we give the prediction of the Higgs p_T distributions from the gluon fusion production process for several masses and structure functions. The decrease of the mean p_T expected with a decrease of the mass is attenuated by the increase of α_S [55]. There is no significant difference with the change of structure functions.

We conclude that, for the inclusive Higgs studies, the recent Monte Carlo generators provide a transverse momentum distribution in agreement with the analytical calculations. It is therefore justified to use them to generate Higgs events. For the cross section, one has to use the results from the higher order calculation, which could be introduced as a simple K factor. For what concerns exclusive processes (for example the Higgs production at high transverse momentum), it is necessary either to use exact matrix elements or to introduce merging of the parton showers and the matrix elements as it has been done in the case of the gauge bosons production [57][64].

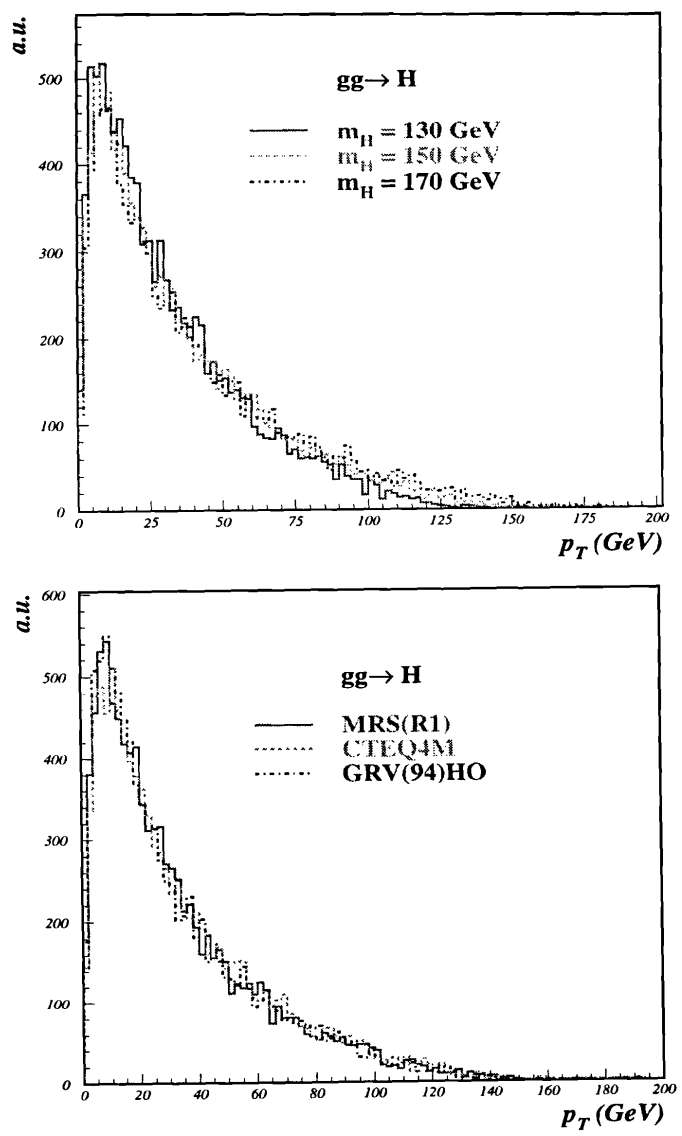

FIGURE 58. Higgs p_T distributions in the gluon fusion production process for several Higgs masses and structure functions.

4.3 Study of the signal characteristics

The distinction between the signal and the background events is based on their kinematical differences. In this section we will study the main kinematical characteristics of the signal events and give the cross section and the branching ratios obtained using the most recent theoretical calculations.

4.3.1 Z boson kinematics

One of the important characteristics of the signal events is the presence of two Z bosons in the intermediate state, which could be either real or off-mass-shell. In the Higgs mass region we are interested in, from ~ 120 GeV to $\sim 2M_Z$, at least one Z boson is off-mass-shell. The fraction of events with both Z off-mass-shell is decreasing with increasing Higgs mass. This is illustrated in figure 59, showing the mass distribution of the Z closer to the nominal Z boson mass, for three different Higgs masses, as well as the fraction of events having both Z bosons with the mass smaller than 85 GeV. There are about 22%, 13% and 8% of such events for Higgs mass of 130 GeV, 150 GeV and 170 GeV, respectively. In the further analysis the vector boson closer the nominal Z mass we referred as Z boson, and the other one as Z*.

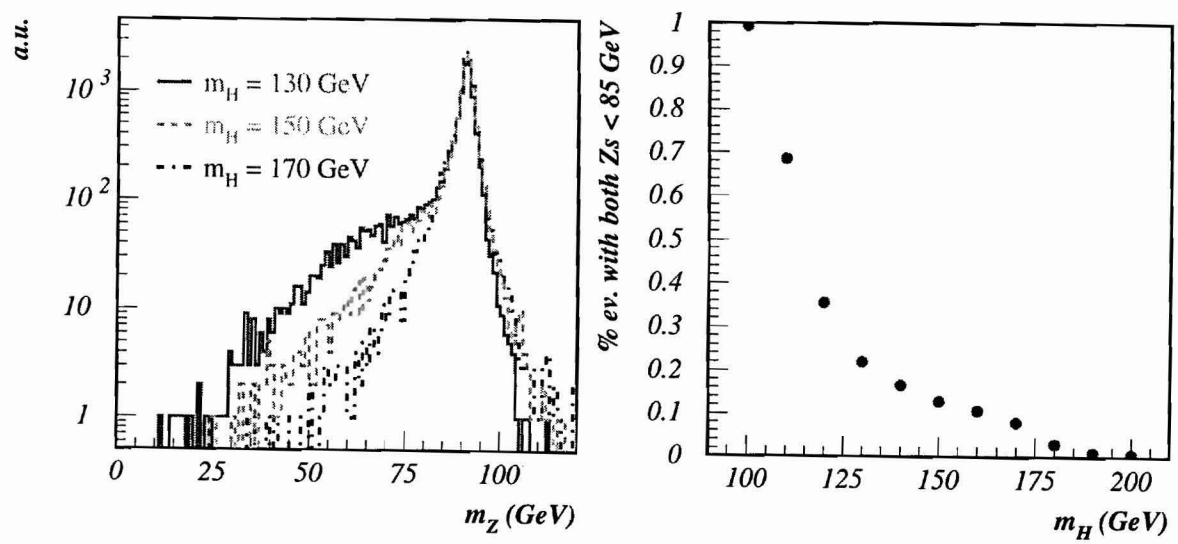

FIGURE 59. Mass distribution of the Z boson closer to the nominal Z mass (left) and a fraction of events with both Z bosons having the mass smaller than 85 GeV (right).

The Z* mass distribution is shown in figure 60, together with the transverse momentum distributions of both Z's for three Higgs masses. We can notice a m_{Z^*} characteristic upper edge, at the position $m_H - m_Z$, becoming more pronounced as the Higgs mass increases. The Z p_T distribution is slightly harder than the Z* one, the difference becoming smaller with increasing Higgs mass.

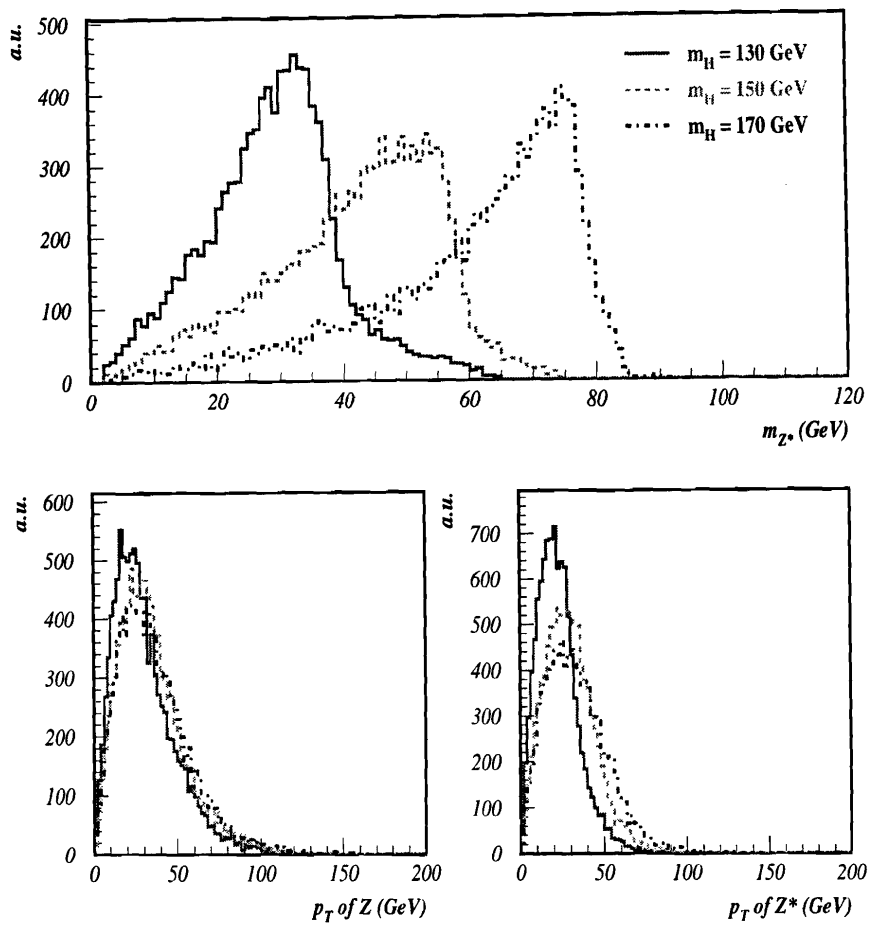

FIGURE 60. Mass distributions of the Z* and transverse momentum distributions of both Z's separately.

4.3.2 Electron kinematics

The main characteristic of the studied physics channel is the presence of 4 relatively isolated and high p_T electrons in the final state. These electrons properties will be used to effectively reduce the backgrounds. As an illustration, in figure 61 we show the transverse momentum distribution of the 4 electrons from the Z and Z* decays, sorted by decreasing p_T, for three values of the Higgs mass. Events have been preselected with the following conditions: at least 2 e^- and 2 e^+, with $|\eta| < 2.7$ and $p_T > 5$ GeV. The difference between the distributions for different Higgs masses becomes visible on the third electron, with almost all of the electrons having a p_T higher than 10 GeV, even for the smaller Higgs masses. From the softest p_T electron distribution, for which the peak at M_H = 130 GeV is around 10 GeV, we can foresee that the signal acceptance will be very sensitive to the minimum p_T cut chosen. In this mass region, the number of expected signal events is small and it will be very important to maximize the acceptance together with the reconstruction efficiency to optimize the low mass reach.

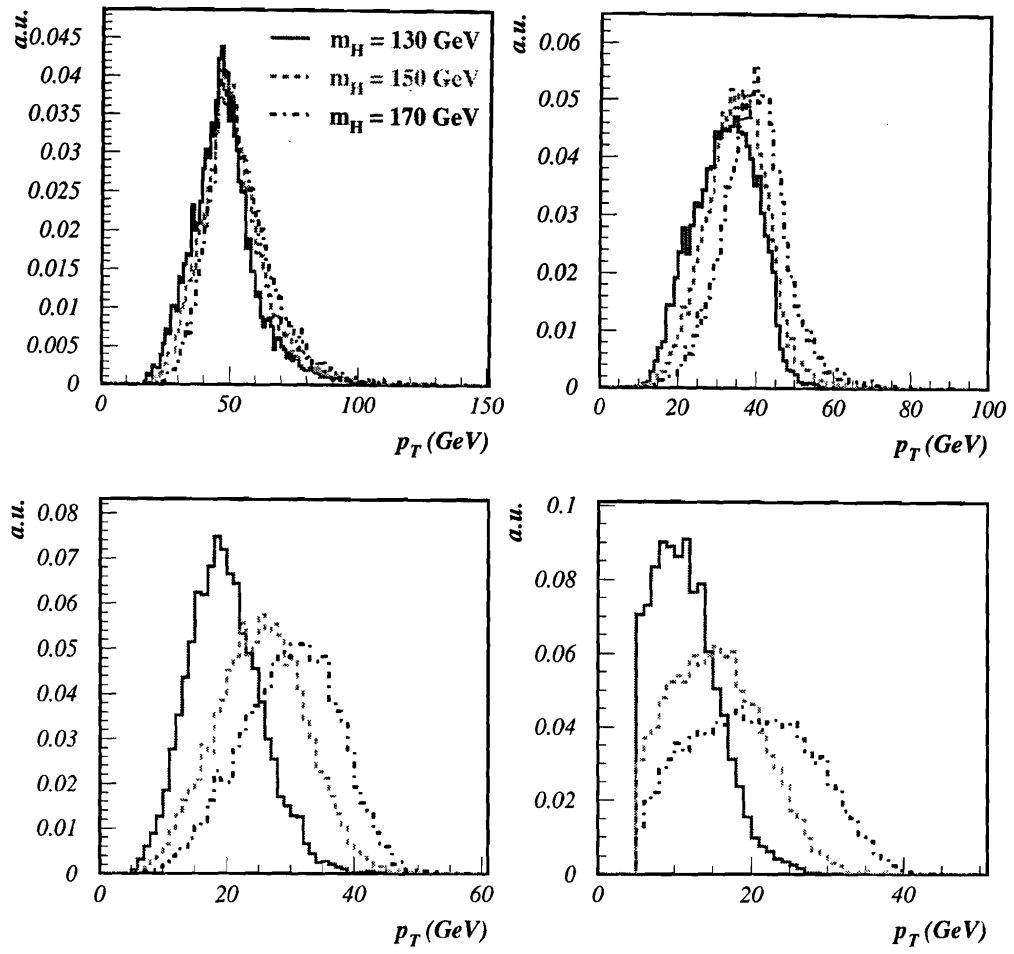

FIGURE 61. Momentum distributions of the 4 electrons coming from the Z and Z* decays. The generation cut is $p_T > 5$ GeV.

4.3.3 Internal bremsstrahlung

Another specificity of this channel is the radiation of photons in the Z decays, which is called internal bremsstrahlung. This process is taken into account using the program PHOTOS [65], which implements an algorithm for single and double photon emission in these decays. Figure 62 presents the distribution of the angular distance between the emitted photon and the electron, as well as the photon p_T. About 25% of the photons are radiated within a cone defined by $\Delta R < 0.05$ and will be, in most of the cases, reconstructed together with the electrons. However, an important fraction of the photons are clearly separated from the electrons with a non-negligible p_T. The importance of these photons reconstruction is shown in figure 63, which presents the Z and Z* mass distributions with and without taking into account the emitted photons in the mass calculation.

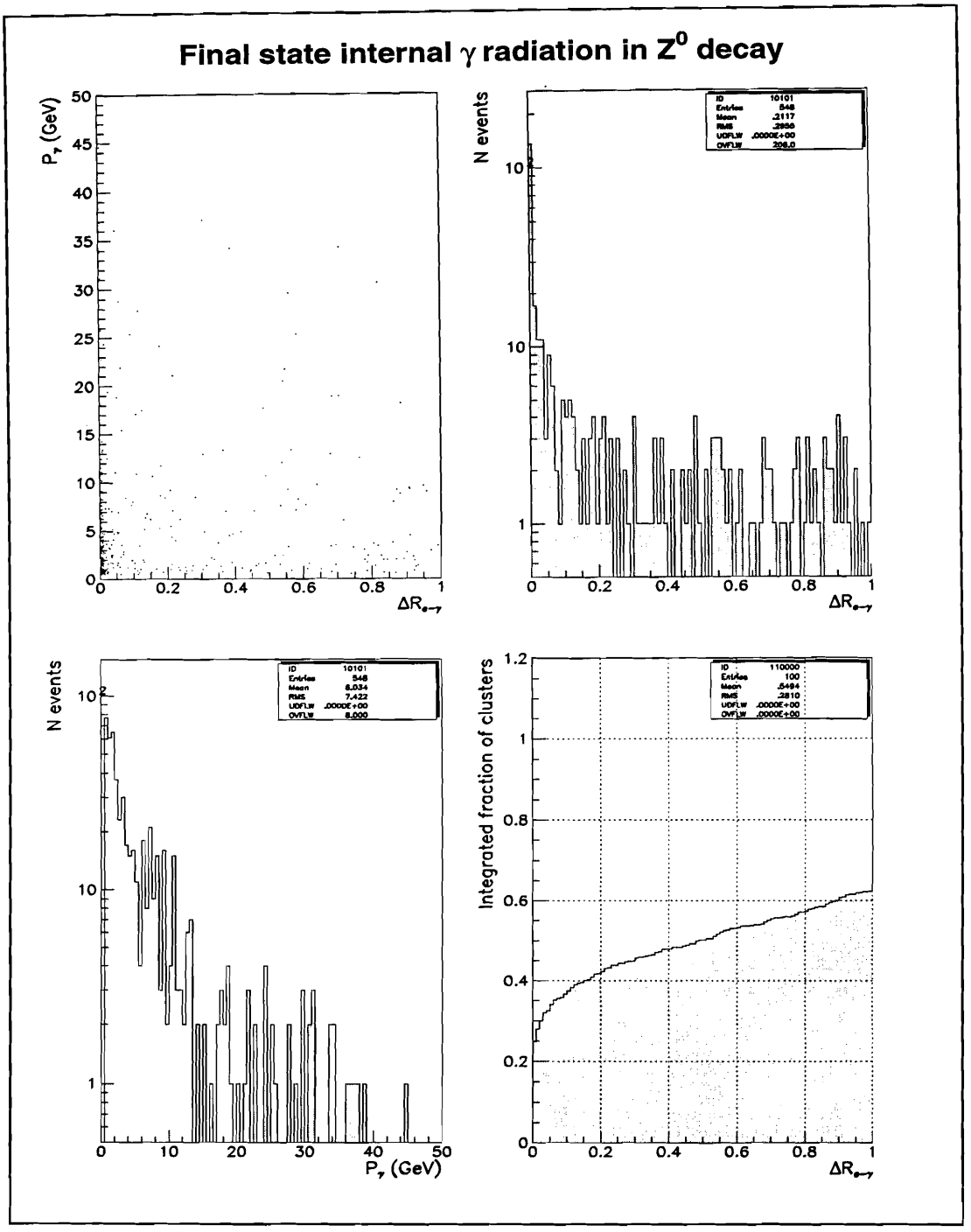

FIGURE 62. Angular distance between the electron and the photons from internal bremsstrahlung. The transverse momentum of the photons is also shown.

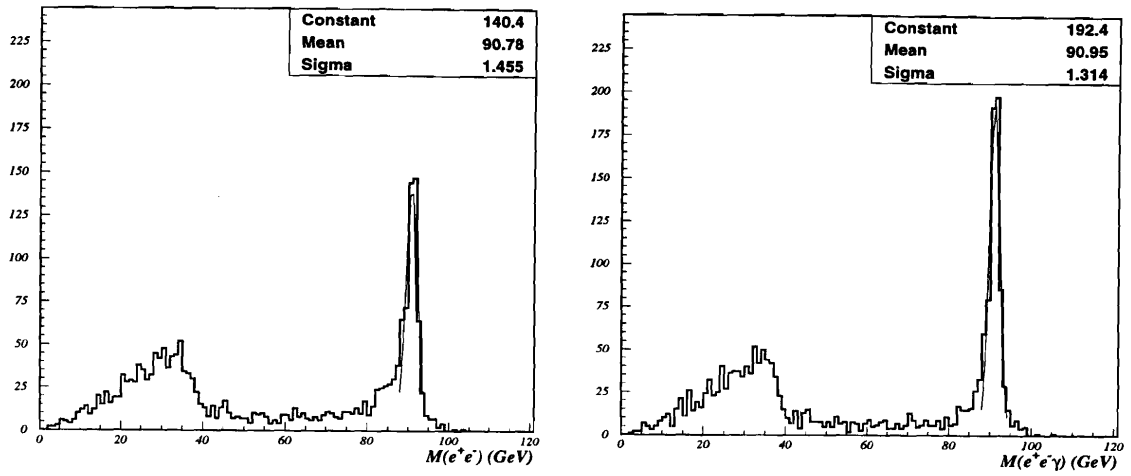

FIGURE 63. Z and Z* mass distributions, with and without accounting for the emitted photons in the mass calculation, for m_H = 130 GeV.

4.3.4 Generation and preselection

The cross sections numerical values for the main Higgs production modes, as well as the branching ratio for $H \rightarrow ZZ^*$ and the acceptances of the generation cuts are summarized in table 6. For the cross section calculations, we have used the programs of reference [66]. The gluon fusion and Higgs-strahlung processes are calculated at next-to-leading order, while the vector boson fusion is calculated at the leading order and corrected by the K factor presented in chapter 1. The associated production with $t\bar{t}$ and $b\bar{b}$ pairs is calculated at the leading order only, since the QCD corrections are not known. For the calculations at leading order, we have used the CTEQ4L structure functions [60], while at the next-to-leading order, we have used the CTEQ4M ones. The branching ratio for $H \rightarrow ZZ^*$ are computed using the program of reference [34], and for the 2 electrons Z decay, we have taken $BR(Z \rightarrow e^+e^-)$ = 0.03366 [67]. Final state particles have been simulated with PYTHIA, and PHOTOS has been used for the internal bremsstrahlung. In order to have a reasonable sample of events, without biasing the analysis, we have introduced cuts at the generation level by requesting at least 2 e^- and 2 e^+, within $|\eta| < 2.5$ and $p_T > 6.5$ GeV.

From the last column of the table 6, we underline once again the small number of events expected in this channel. At the generation level, with the preselection cuts and for an integrated LHC luminosity of 100 fb^{-1}, we can expect about 69, 146 and 35 events for Higgs masses of 130, 150 and 170 GeV respectively. These small number of events imposes strong requirements on the electron reconstruction efficiency, as well as on optimisation of cuts which will be used to suppress the backgrounds. These cuts will be studied in details in the following sections.

The number of expected events for an integrated luminosity of $10^5 pb^{-1}$ is shown in figure 64. The number of events including μ decays of the Z bosons is also shown.

m	$\sigma(gg \to H)$	$\sigma(qq \to Hqq)$	$\sigma(q\bar{q} \to VH)$	$\sigma(gg, q\bar{q} \to Hq\bar{q})$	$BR(H \to ZZ^*)$	$\sigma_{tot} \times BR$ $(H \to 4e)$	η(gen.acc.)	$\sigma_{tot} \times BR \times \eta$
GeV	**pb**	**pb**	**pb**	**pb**		**fb**		**fb**
120	33.22	4.73	2.79	0.95	0.013	0.61	0.40	0.24
130	28.90	4.46	2.17	0.75	0.034	1.40	0.49	0.69
140	25.43	4.09	1.72	0.60	0.063	2.27	0.54	1.23
150	22.56	3.80	1.37	0.47	0.080	2.56	0.57	1.46
160	20.18	3.51	1.11	0.39	0.043	1.26	0.59	0.74
170	18.17	3.31	0.90	0.32	0.022	0.57	0.62	0.35
180	16.49	3.07	0.74	0.26	0.057	1.33	0.64	0.85

TABLE 6. Numerical results for the main Higgs production modes cross sections, $H \to ZZ^*$ branching ratios and preselection cuts aceptances. Preselection cuts are: at least 2 e^- and 2 e^+, with $|\eta| < 2.5$ and $p_T > 6.5$ GeV.

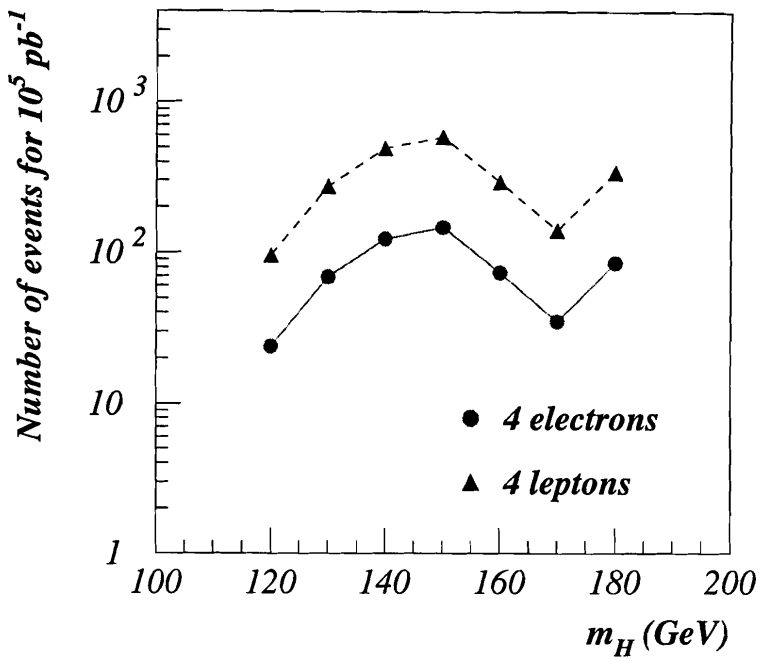

FIGURE 64. Number of events in 4 electrons and 4 leptons Higgs decay channels, after preselections cuts, for one year at high luminosity running of LHC. The numbers for 4 leptons (i.e. $4e+2e2\mu+4\mu$) are obtained by a simple scaling.

4.4 Study of the backgrounds

For the physics channel we are studying, the background processes are all processes with 4 electrons in the final state. There are two basic classes of such processes, called reducible and irreducible backgrounds. The reducible backgrounds have very pronounced kinematical and topological differences with respect to the signal, both in the final states as well as in the 2 and 4 electrons combinations. Therefore, by appropriate kinematical and topological cuts, these backgrounds can be effectively suppressed. The main reducible background processes are $Zb\bar{b} \rightarrow 4e$ and $t\bar{t} \rightarrow 4e$. The only irreducible background is $ZZ^*/\gamma^* \rightarrow 4e$, with very similar final and intermediate states kinematics when compared to the signal events. Nevertheless, adjusting properly the kinematical cuts, and using some additional cuts like the four-electrons transverse momentum or the angular separations, this background can also be suppressed to some extent.

In this section, we will study the main properties of the background events, with a special attention on the distributions of the kinematical variables important for background discrimination.

4.4.1 The ZZ^*/γ^* background

At hadron colliders there are two processes for the ZZ^*/γ^* production: $q\bar{q} \rightarrow ZZ^*/\gamma^*$ and $gg \rightarrow ZZ^*/\gamma^*$, with the following Feynman diagrams at the leading order:

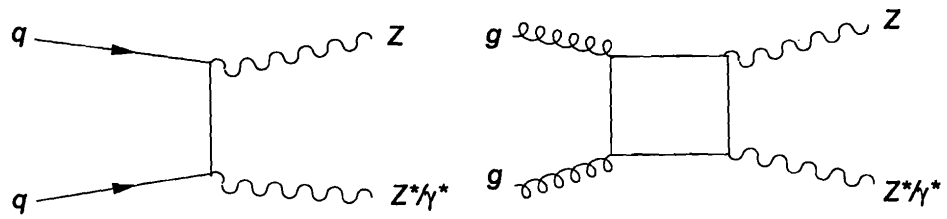

Only the first process is implemented in PYTHIA, with a cross section calculated at the leading order. The higher order corrections for this process have not yet been calculated. The next-to-leading order calculations for real vector bosons pairs production give a K factor of 1.33 [68][69]. For the same process calculated in the reference [70], using the extended CSS formalism to resum the large logarithmic terms due to soft gluons, the K factor is estimated to about 1.44. The application of the K factor on the events generated with PYTHIA depends on the corresponding kinematical variables predictions agreement. Again, only analytical calculations for the two real boson production have been performed [71], and comparing with PYHTIA results, one reaches the conclusion that PYTHIA significantly underestimates the rates for $p_T(ZZ) > 100$ GeV, but this region contains a very small fraction of events. This is to be expected, since this transverse momentum region is dominated by the higher order processes with one or more associated hard jets in the final state, which are not properly modeled in PYTHIA.

As an illustration of the PYTHIA generated Z's kinematics, in figure 65 we show the $p_T(ZZ^*)$, $m(ZZ^*)$, $p_T(Z)$ and $p_T(Z^*)$ distributions for the $q\bar{q} \rightarrow ZZ^*/\gamma^*$ background process. In order to obtain a statistically significant sample of events, we have imposed preselection cuts of $10 < m_{Z^*} < 80$ GeV, $76 < m_Z < 106$ GeV, with at least two electrons and two positrons in $|\eta| < 2.5$ and with $p_T > 6.5$ GeV. The acceptance of electrons $|\eta|$ and p_T cuts is 0.22 giving a $q\bar{q} \rightarrow ZZ^*/\gamma^* \rightarrow 4e^{\pm}$ cross section of 1.49 fb. It is interesting to notice very similar Z and Z* p_T distributions and a very soft $p_T(ZZ^*)$ distribution. The later could eventually be used to separate this background process from the signal. The sharp cuts on the m_{Z^*} distribution are the preselections cuts. One can also notice the maximum of the $m(ZZ^*)$ spectrum at about 120 GeV, making this background especially important for Higgs of low mass.

The second production process, $gg \rightarrow ZZ^*/\gamma^*$, is not implemented in PYTHIA. Although being a loop process of higher order in α_s, it is important since the gluon-gluon luminosity is much higher than the quark-antiquark luminosity for small x at hadron colliders. At the leading order, it has been calculated in reference [72], for the case of two real Z production. A ratio of $\sigma(gg \rightarrow ZZ)/\sigma(q\bar{q} \rightarrow ZZ) \approx 0.35 - 0.45$ has been found, for a center of mass energy $\sqrt{s} = 16$ TeV. It was also shown that the gluon fusion process produces Z's more centrally than the $q\bar{q}$ process. The next-to-leading order corrections for this process have not been calculated yet, but could be important.

The p_T distributions of the 4 electrons from the Z and Z^*/γ^* decays are shown in figure 66, sorted in decreasing p_T order. It is important to notice an almost exponential fall off of the softest electron p_T distribution, giving a potentially high rejection power by increasing the p_T threshold.

In conclusion, since we are interested in the inclusive ZZ^*/γ^* production and since the contribution of the region $p_T(ZZ) > 100$ GeV, where PYTHIA underestimate the rate is a small fraction of the overall cross section, we will take a K factor of 1.44 for $q\bar{q} \to ZZ^*/\gamma^*$. For the gluon fusion contribution, we will take $\sigma(gg \to ZZ^*/\gamma^*)/\sigma(q\bar{q} \to ZZ^*/\gamma^*) = 0.35$, neglecting the kinematical differences between these two production processes.

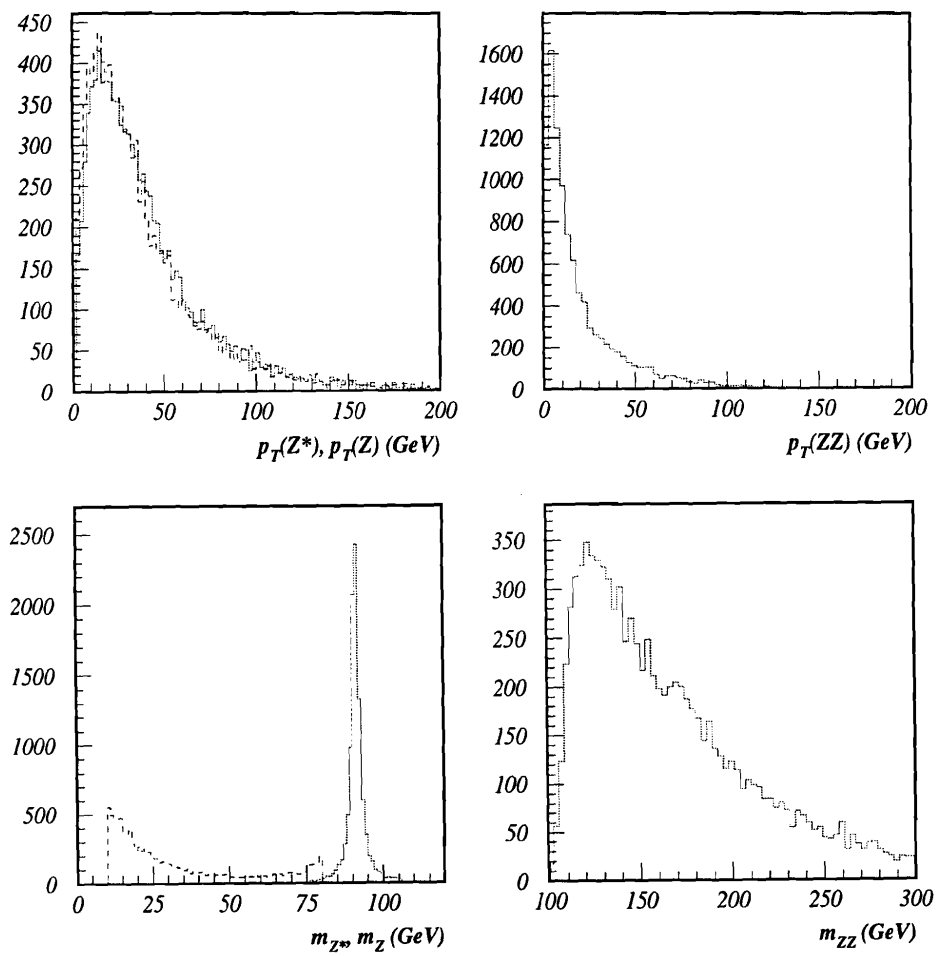

FIGURE 65. Transverse momentum and mass distributions of the Z and Z* separately, and of their combination, in the $q\bar{q} \to ZZ^*/\gamma^* \to 4e^{\pm}$ background process, using the electrons generation cuts described in the text.

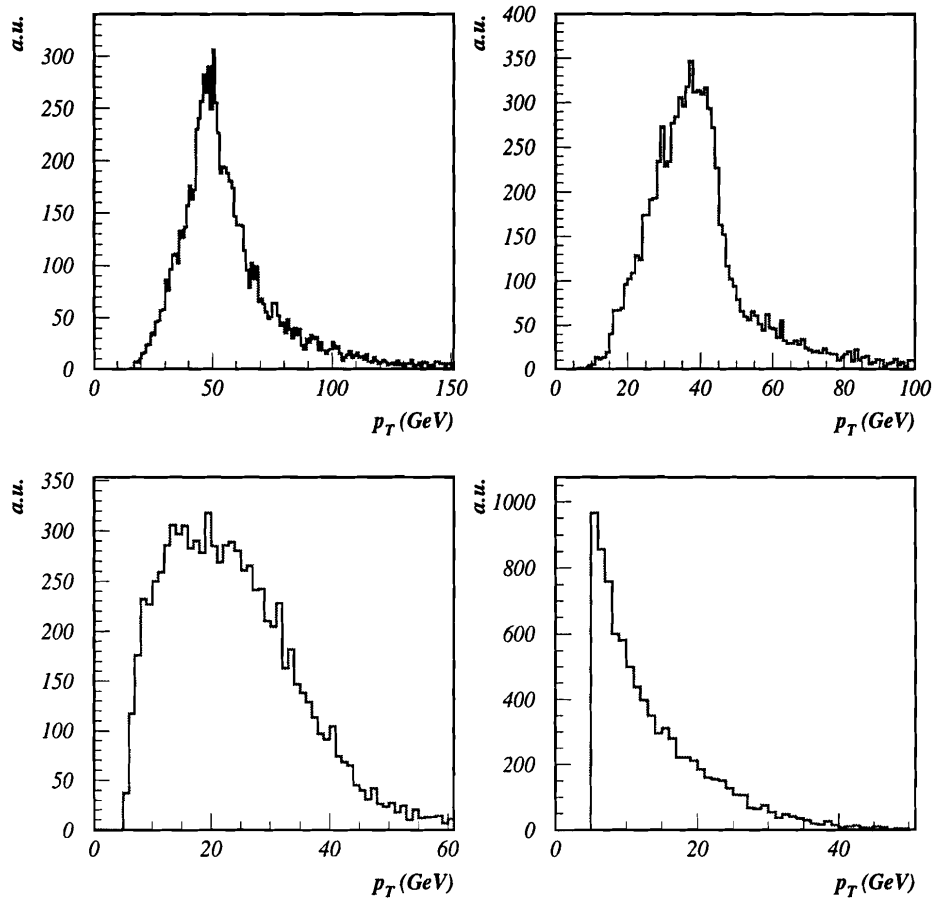

FIGURE 66. Transverse momentum distributions of the 4 electrons from the Z and Z^*/γ^* decays in the $q\bar{q} \rightarrow ZZ^*/\gamma^*$ background, sorted in decreasing p_T order.

4.4.2 The $t\bar{t}$ background

In the $t\bar{t}$ decay chain electrons could come from several sources: directly from the W boson decays, from leptonic decay of a τ lepton coming from the W's, or from semi-leptonic decay of mesons produced in the fragmentation process of either b-quarks and their decay products or in hadronic decays of the W's. The top decay chain is shematically shown in figure 67 and the relevant branching ratios are listed in the table 7. The most probable scenario is to have 2 electrons from direct W decays and 2 other coming from semi-leptonic decays of B hadrons. Although the electrons coming from τ or charm and light-quarks mesons will have, in general, a softer p_T spectrum than direct leptons, their contribution, as we shell see, is not negligible.

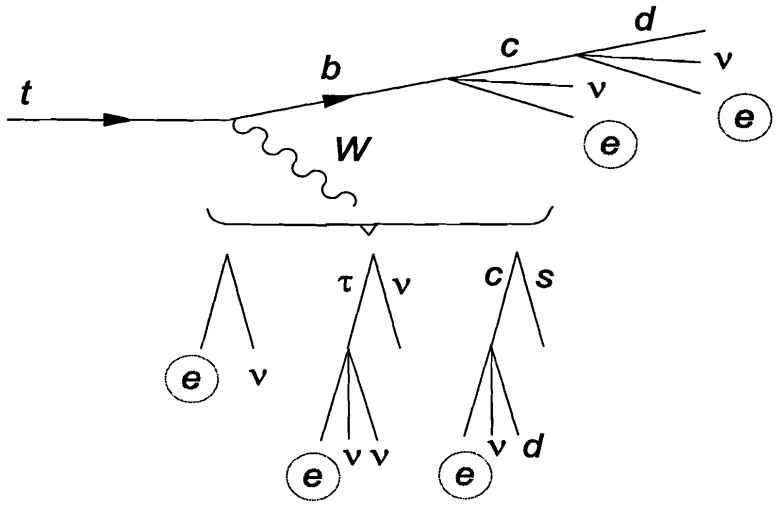

FIGURE 67. Possible sources of electrons in a top decay chain.

$BR(t \to Wb) = 99.8\%$	$BR(B^0 \to l\nu X) = 10.5\%$
$BR(W \to e\nu) = 10.9\%$	$BR(B^+ \to l\nu X) = 10.3\%$
$BR(W \to \tau\nu) = 11.3\%$	$BR(D^0 \to e\nu X) = 6.8\%$
$BR(\tau \to e\nu\nu) = 17.8\%$	$BR(D^+ \to e\nu X) = 17.2\%$
$BR(W \to hadrons) = 67.2\%$	$BR(\pi^0 \to ee\gamma) = 1.2\%$

TABLE 7. The relevant branching ratios in the top decay chain [61][67].

At hadron colliders there are two processes for the $t\bar{t}$ production: the gluon fusion $g + g \to t + \bar{t}$ and the quark annihilation $q + \bar{q} \to t + \bar{t}$, with the following Feynman diagrams at the leading order:

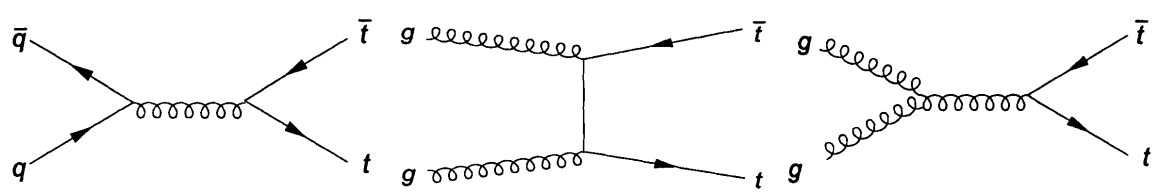

The NLO cross sections have been calculated in [73] and the results at the LHC center of mass energy are given in [74]:

$$\sigma_{LO}(t\bar{t}) = (515\ ^{+128}_{-95})\ \text{pb}, \qquad \sigma_{NLO}(t\bar{t}) = (758.8\pm75)\ \text{pb} \quad . \qquad \text{(EQ 48)}$$

The errors come from an uncertainty in the choice of the renormalisation scales in the proton structure functions and in the parton-level cross section calculations. About the same order of errors is obtained from varying the top quark mass. The central value is given for $m_t = 175.6$ GeV. From the errors size, we can conclude that the K factor uncertainties are large. As the nominal cross section we have taken the central NLO value given in equation 48. Due to the large gluon-gluon luminosity at the LHC, the gluon fusion production mechanism has about 6 times higher cross section than the quark annihilation process (according to PYTHIA's calculations). The parton distributions functions uncertainty at the NLO is about ±7 % [75].

Looking at the branching ratios listed in table 7 and given the fact that the electrons p_T distribution is softer for electrons originating later in the cascade, the generation of the 4 electrons passing loose kinematical cuts of, for example, $|\eta| < 2.5$ and $p_T > 6.5$ is very CPU time consuming. Therefore, to speed up the generation we have forced the $W \rightarrow e\nu$ decays and imposed loose preselection cuts by demanding at least 2 electrons and 2 positrons in $|\eta| < 2.5$ with a transverse momentum $p_T > 6.5$ GeV and with at least one electron-positron pair with an invariant mass within ±15 GeV around the Z boson mass. The last cut suppresses a large amount of this background, since the distribution of electron-positron pairs invariant mass has an almost flat shape around the Z mass.

Figure 68 shows the p_T distribution of electrons from direct W decays and semi-leptonic decays of hadrons, grouped according to the heaviest quark in the hadrons, together with the average number of electrons per event (ε). From the figure we can see that approximately one electron comes from light-quark hadrons, although with a significantly softer p_T spectrum. In our analysis the light-quarks producing these electrons come mainly from the B mesons cascade decays. Additional light-quarks could come from the W decays, and forcing W to electron decay underestimate this contributions. It will, therefore, remain as a source of systematic uncertainties.

Some of interesting 2-electrons and 4-electrons invariant masses and p_T distributions are shown in figure 69. The first electron-positron pair is chosen as the one with the invariant mass closest to the nominal Z mass. Among the remaining combinations, the second pair is chosen as the one with the highest invariant mass (in about 10% of events more than 4 electrons satisfy the kinematical cuts). From the 2 electrons invariant mass distribution we can see the power of a possible Z mass cut, i.e. requesting one electron-positron pair to have a mass in some region around the Z mass. Moreover, it is interesting to note a low mass peak in the second electron-positron invariant mass distribution which is due to electrons originating from the same cascade. This peak will be effectively suppressed by the lower Z* mass cut. The 4 electrons p_T distribution with the mean value of about 70 GeV is significantly harder than the one for the signal and the ZZ^*/γ^* background.The 4 electron invariant mass has a wide peak at about 150 GeV, slightly higher than the corresponding one for the ZZ^*/γ^* background.

At the end of this section, in figure 70, we show the p_T distributions of the 4 hardest electrons, sorted by decreasing p_T. As in the ZZ^*/γ^* background the lightest electron has an

"exponential-like" distribution, thus giving the possibility of a large background rejection by increasing the p_T threshold on the softest.

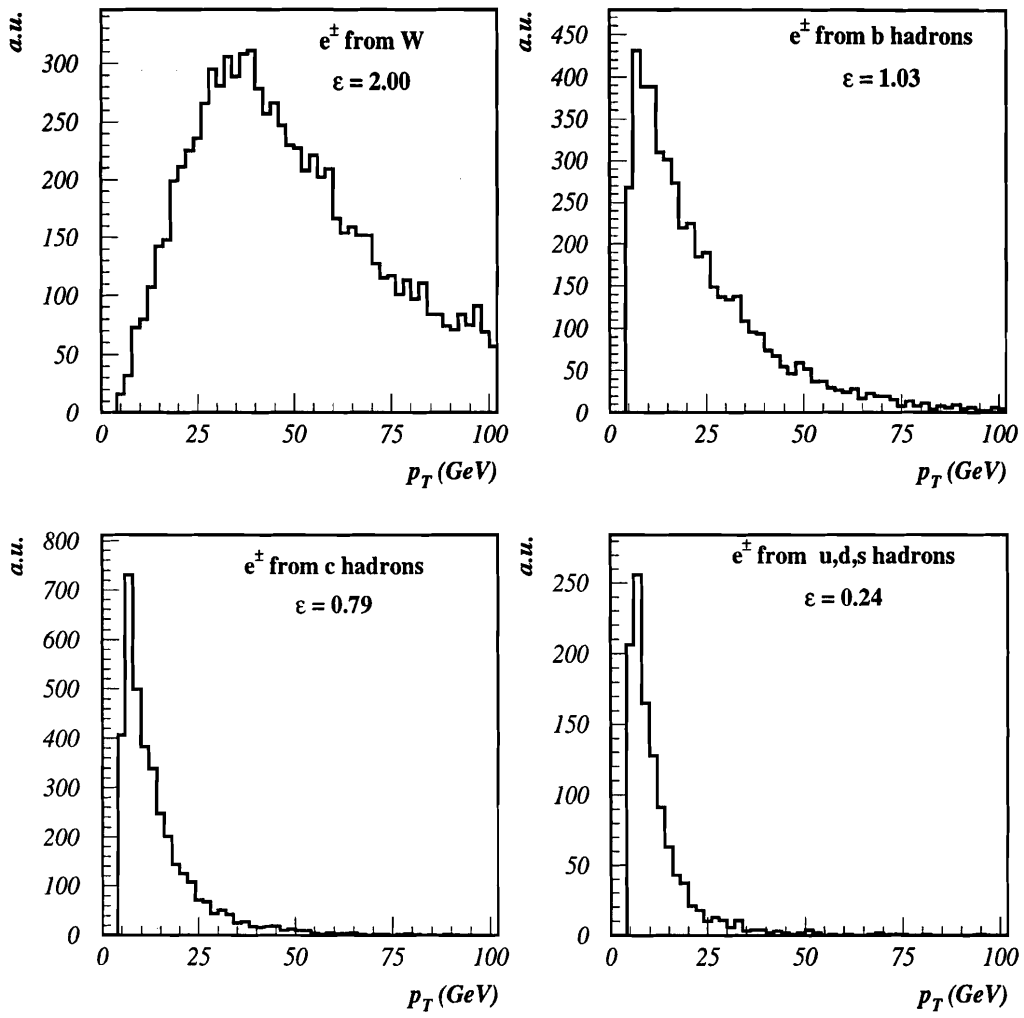

FIGURE 68. p_T distributions of electrons from $t\bar{t}$, sorted according to their parent particle. There is in addition a small contribution of electrons coming from τ decay with $\varepsilon = 0.04$.

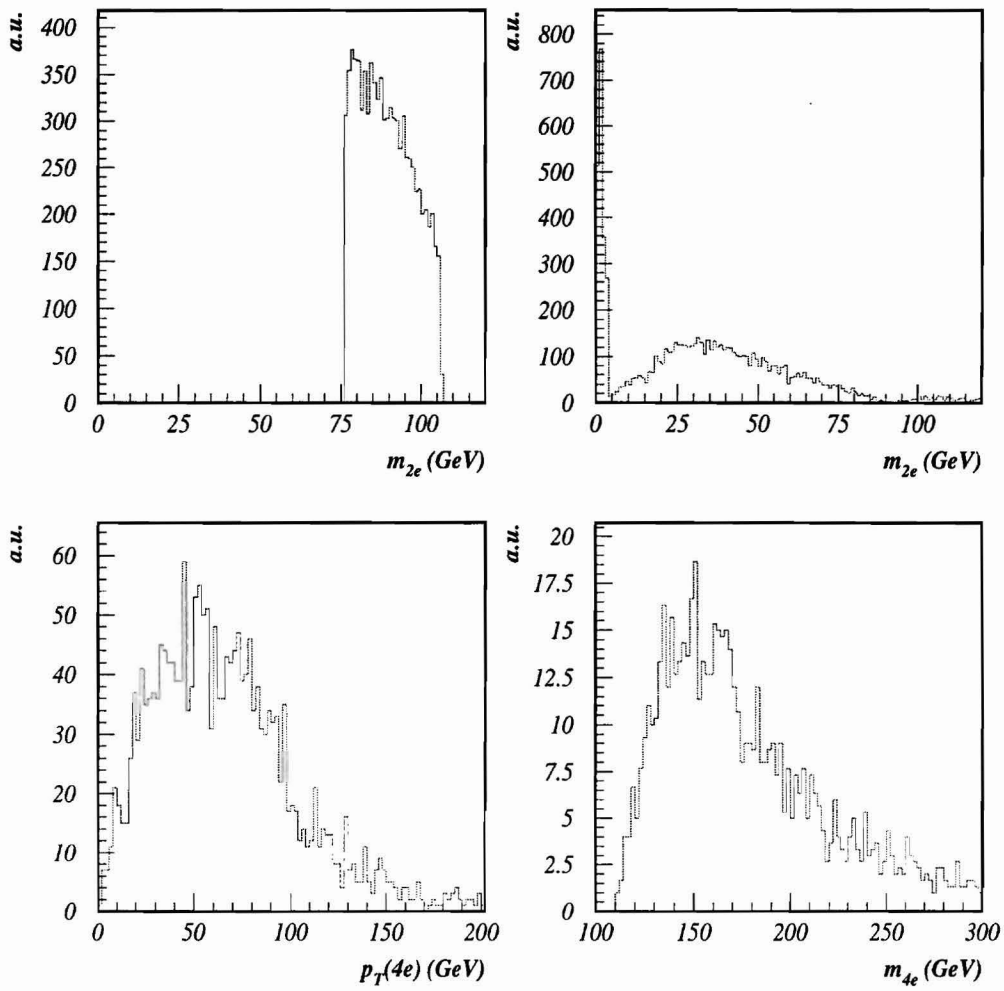

FIGURE 69. 2 electrons invariant mass distributions and 4 electrons p_T and mass distribution for the $t\bar{t}$ background.

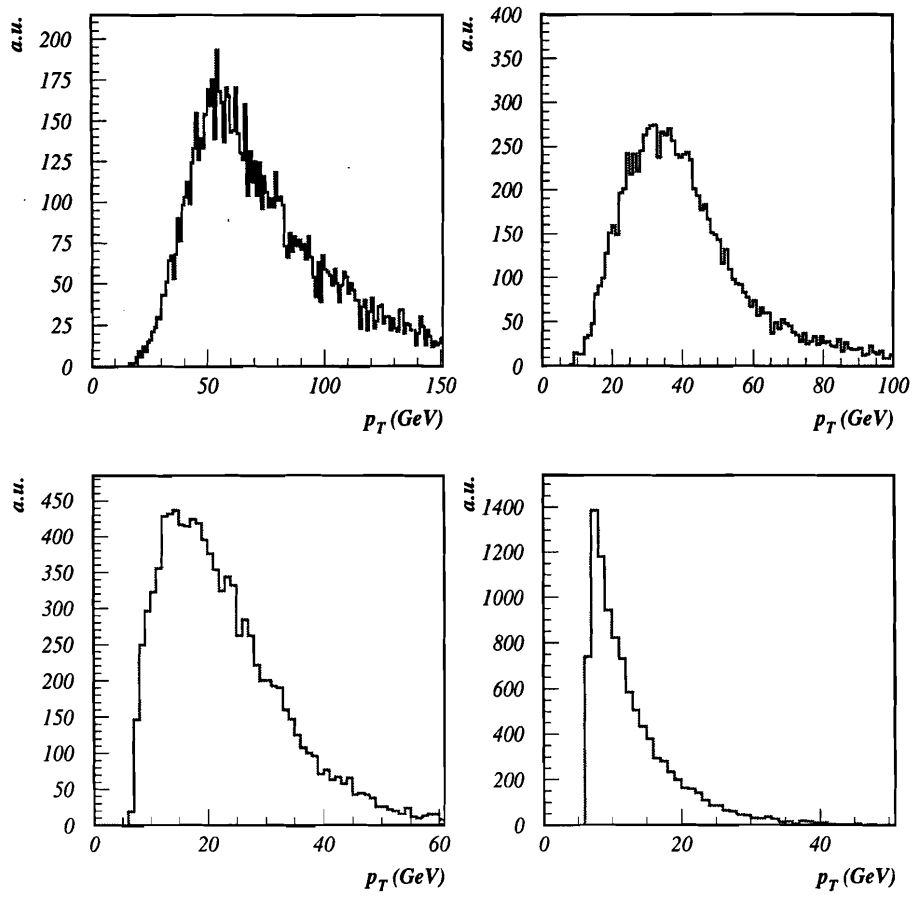

FIGURE 70. p_T distributions of 4 hardest electrons in the $t\bar{t}$ background.

4.4.3 The $Zb\bar{b}$ background

The third important source of background are 4 electrons coming from $Zb\bar{b}$ production and decay. In most of the cases, two electrons come from the Z decay while the other two originate from cascade decays of mesons produced in the b quarks hadronisation. The presence of a real Z boson makes this background insensitive to a Z mass cut (besides the internal radiation effects), on the contrary to the $t\bar{t}$ background. As in the $t\bar{t}$ background and contrary to the signal, this background is characterized by the presence of 2 non-isolated electrons, coming from the B meson cascade decays.

At leading order, there are two processes for $Zb\bar{b}$ production at hadron colliders: $g + g \rightarrow Z + b + \bar{b}$ and $q + \bar{q} \rightarrow Z + b + \bar{b}$. The Feynman diagrams are shown in figure 71. Because of the b and $\bar{b}$ quarks in the final state, besides the common diagrams with other $q\bar{q}$ initial states, there are some additional diagrams with b quarks in the initial state, as shown on the bottom of the figure.

The $g + g \rightarrow Z + b + \bar{b}$ process has been calculated in reference [76] at the leading order, and a cross section of 758 pb was found, with a 50% uncertainty from the scale and structure functions choice. The implementation of this process in PYTHIA suffers from problems with the

phase space generation. Therefore, it has been excluded from recent versions of PYTHIA. An alternative way of generating $Zb\bar{b}$ final states is to start with $q+\bar{q} \rightarrow Z$, $q+\bar{q} \rightarrow Z+g$ and $g+q \rightarrow Z+q$ and to generate one or both b quarks with the parton showering. It has been shown that this approach significantly underestimates the final rates after selection cuts, since the b quarks generated by the parton shower backward evolution have a softer p_T spectrum than those generated using exact matrix elements [77].

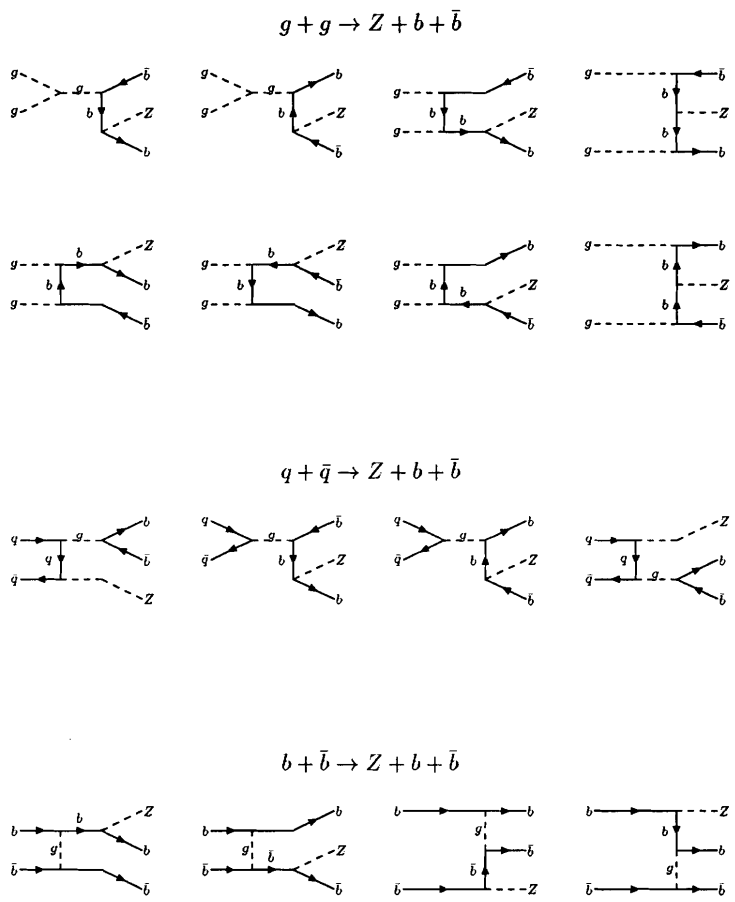

FIGURE 71. Leading order Feynman diagrams for the $Zb\bar{b}$ production at hadron colliders.

For the cross sections calculation and the $Zb\bar{b}$ events generation, we have used the CompHEP package [78]. In CompHEP, the multiparticle phase space is expressed in terms of the elementary parametrization of $1 \rightarrow 2$ phase space sequences, parametrized with the masses and the two-dimensional spherical angles. Then, by an appropriate transformation of these variables, the sharp peaks in the integrands are cancelled. Finally, the integrand is smoothed by a multi-channel Monte Carlo (branching) method, which in multi-peaks case performs a separate integration for each peak.

Using this program we have computed the cross sections for all the initial states shown in figure 71, using the CTEQ4L structure functions. A constant QCD scale equal to $m_Z = 91.2$ GeV and $\alpha_s^{LO}(m_Z) = 0.132$ have been used. The results are shown in table 8, separately for each initial state. The total cross section is 929.58 pb with a total $q\bar{q}$ initial state contribution of about 16%.

initial state	gg	$d\bar{d}$	$u\bar{u}$	$s\bar{s}$	$c\bar{c}$	$b\bar{b}$	$q\bar{q}_{tot}$
σ(pb)	780.79	53.38	60.83	16.32	5.78	12.48	148.79

TABLE 8. Cross sections for $Zb\bar{b}$ production at leading order computed with CompHEP.

In order to obtain an estimate of the NLO corrections size, we have calculated the $g + g \rightarrow Z + b + \bar{b}$ LO cross section dependence on QCD scale variations, from $Q = m_Z/4$ to $Q = 2m_Z$. The results are shown in figure 72. The importance of the higher-order corrections is obvious from the about ±20% variation of the cross sections with the QCD scale, around the nominal value $Q = m_Z$.

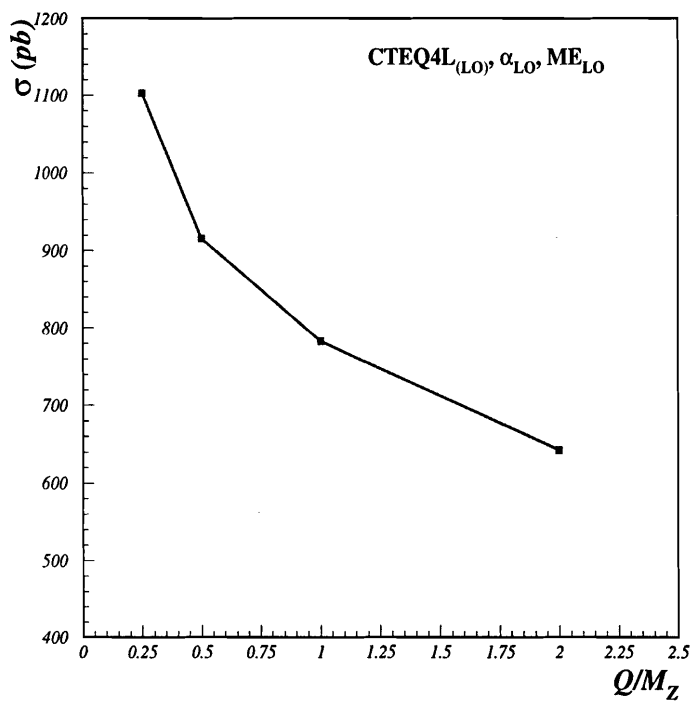

FIGURE 72. Evolution of the leading order cross section for the process $g + g \rightarrow Z + b + \bar{b}$ when changing the renormalization and fragmentation scales.

The transverse momentum and rapidity distributions of b quarks and Z boson separately for $g + g \rightarrow Z + b + \bar{b}$ and $q + \bar{q} \rightarrow Z + b + \bar{b}$ production processes are shown in figure 73. One can notice important differences in rapidity distributions, with the Z bosons being more centrally produced in the gluon fusion processes.

The partonic events generated by CompHEP are then passed through PYTHIA for the hadronisation and the initial and final state parton showers generation. The generation of internal photons in the Z decay is done using PHOTOS, as in the case of the signal and of the ZZ^*/γ^* background.

As for the signal and the other backgrounds, in order to obtain a sufficiently large statistical sample, we have imposed preselection cuts by demanding at least $2e^-$ and $2e^+$ with $|\eta| < 2.5$ and $p_T > 6.5$ GeV. The acceptance of this cut is 0.07%. The p_T and invariant mass distributions of 2 and 4 electrons combinations are shown in figure 74. The interesting property of the invariant mass distributions is a large near zero mass peak of the smaller 2-electrons combination mass, coming from the same cascade electrons, which will allow a considerable reduction of this background by an appropriate m_{ee} threshold. The four electrons mass distribution has a similar shape as for the $t\bar{t}$ and ZZ^*/γ^* background.

The transverse momentum distribution of the four electrons, sorted in decreasing order, is given in figure 75. In comparison with the signal and the other backgrounds, we can notice a somewhat softer distribution of the two lightest electrons, making this background particularly sensitive to the kinematical cuts.

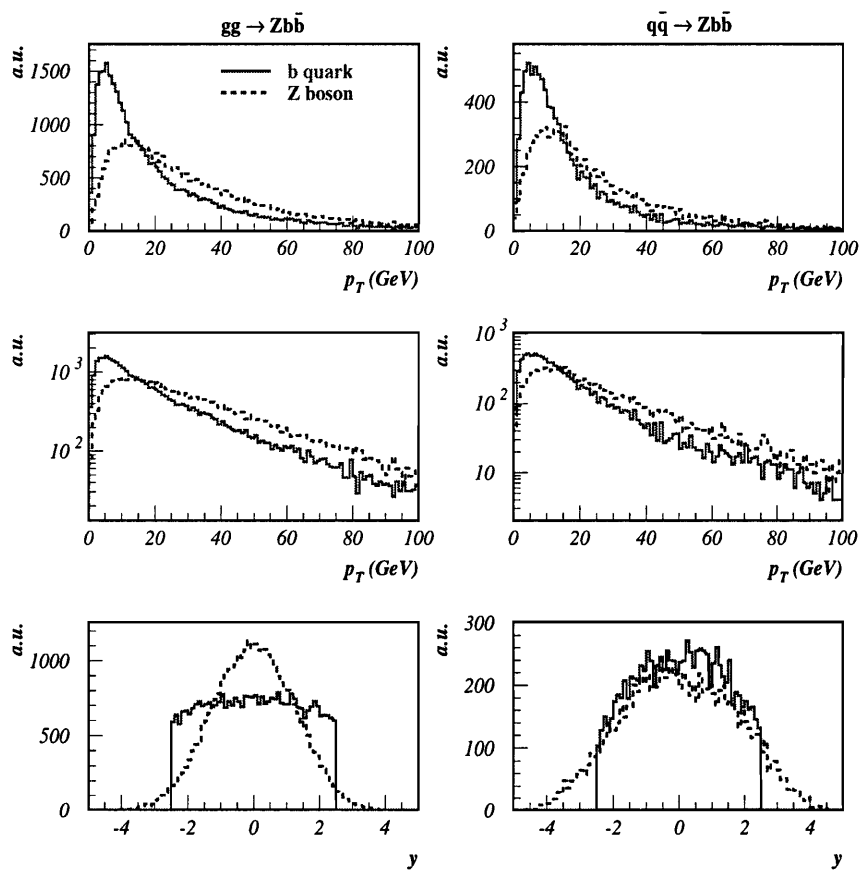

FIGURE 73. Transverse momentum (on linear and logarithmic scales) and rapidity distributions of b quarks and Z boson in the $Zb\bar{b}$ production, for both productions channels. A rapidity cut $|y_{b,\bar{b}}| < 2.5$ has been applied at the generation level.

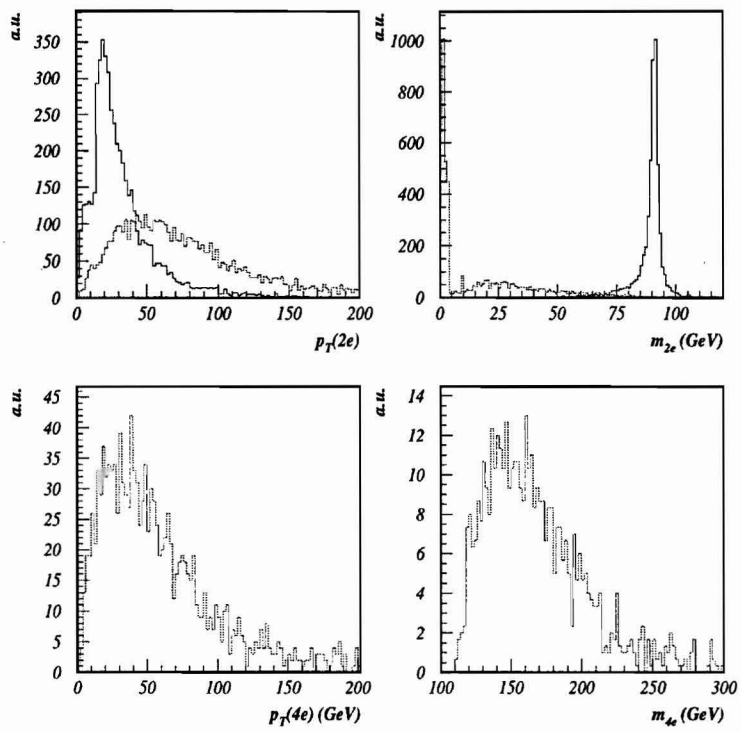

FIGURE 74. Two-electrons and four-electrons the transverse momentum and invariant mass distributions in the $Zb\bar{b}$ production.

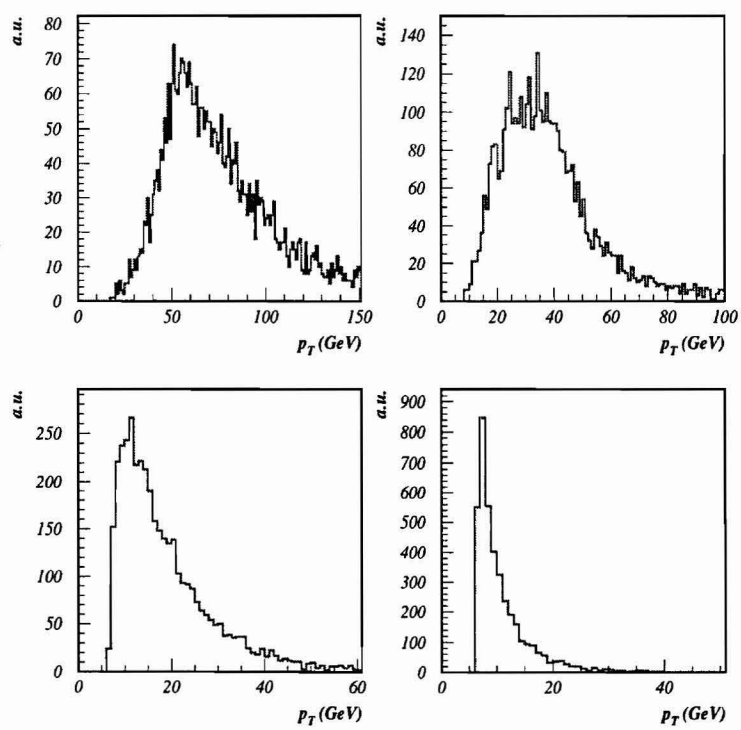

FIGURE 75. Transverse momentum distribution of the 4 electrons in the $Zb\bar{b}$ process, sorted by decreasing order.

4.4.4 Summary of the backgrounds estimate

In table 9, we summarize our study of the cross sections and preselection acceptances for the main background processes. For all the considered backgrounds, we have requested at least $2e^-$ and $2e^+$ with $|\eta| < 2.5$ and $p_T > 6.5$ GeV. In addition, for $ZZ^*/\gamma^* \to 4e$ the selection criterion $10 < m_{Z^*} < 80$ GeV and $76 < m_Z < 106$ GeV has been imposed on the production level. For $t\bar{t} \to 4e$, one electron-positron pair with an invariant mass around the Z mass, i.e. $|m_{ee} - m_Z| < 15$ GeV has also been required.

background (bgd)	$\sigma_{LO}(pp \to bgd)$	K factor		preselection acceptance (η)	$\eta \cdot \sigma$
ZZ^*/γ^*	7.95 pb	1.44	$\sigma(pp \to ZZ^*/\gamma^* \to 4e)$ 11.94 fb	22.27%	2.66 fb
$t\bar{t}$	515 pb	1.47	$\sigma(pp \to t\bar{t} \to WWb\bar{b} \to eeb\bar{b})$ 9.02 pb	0.30%	27.06 fb
$Zb\bar{b}$	929.58 pb	-	$\sigma(pp \to Zb\bar{b} \to eeb\bar{b})$ 31.29 pb	0.07%	20.65 fb

TABLE 9. Summary of the main backgrounds cross sections and preselection acceptances. K factor for the ZZ^*/γ^* background is applied only to the $q\bar{q} \to ZZ^*/\gamma^*$ production process.

4.5 Trigger and detector geometrical acceptances

The CMS electromagnetic calorimeter has a geometrical coverage of $|\eta| < 3$, while it can measure the energy up to $|\eta| < 2.6$. The acceptance of the tracker system is $|\eta| < 2.5$.

In figure 76 we show the fraction of events having all four electrons in a region smaller than a given $|\eta|$ value, and satisfying other generation cuts specified in the previous sections, normalized to the overall acceptance for $|\eta| < 2.5$. We can see that there is about 40% of events with all four electrons within the barrel ($|\eta| < 1.5$) acceptance.

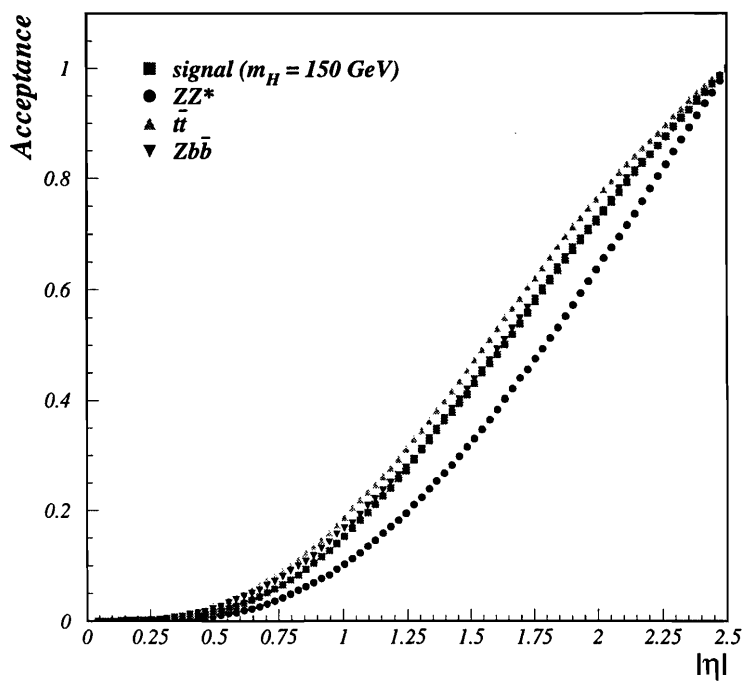

FIGURE 76. Angular acceptances of the signal and backgrounds normalized to the overall $|\eta| < 2.5$ acceptance.

At the trigger level, the $H \to ZZ^* \to 4e^{\pm}$ physics channel will be accepted for further analysis by single and double electrons triggers. The level 1 trigger algorithm, explained in the section 2.8, identifies electron candidates by finding large energy deposits in trigger towers and adds the energy leaking to the neighboring towers [49]. It vetoes candidates based on the profile of the energy deposited in both ECAL and associated HCAL towers. The single (double) electron trigger threshold is 20 (10) GeV for low luminosity running period and 30 (15) GeV for high luminosity. At the particle level, we have found that the signal and all backgrounds pass the trigger thresholds with an acceptance bigger than 99%. To account for eventual trigger reconstruction inefficiencies, we will assume a value of 98% efficiency for both signal and background events.

4.6 Analysis cuts

In the previous sections we have seen some kinematical differences between the signal and the backgrounds events: softer p_T distribution of the third and fourth electrons for the backgrounds than for the signal, flatter distribution of the electron-positron invariant mass around the Z mass in the $t\bar{t}$ background, a low mass peak in the electron-positron invariant mass for the $t\bar{t}$ and $Zb\bar{b}$ backgrounds, and, of course, a crucial difference between the 4 electron invariant mass distributions for the signal and the backgrounds. In this section we will present an optimization of these cuts in order to maximize the signal visibility.

4.6.1 Electron p_T cuts

In figure 77, the superimposed p_T distributions of the four electrons for the signal (m_H = 150 GeV) and the backgrounds are shown, sorted in decreasing order. The geometrical acceptance cuts and preselection cuts are included, visible on the lower side of the 2 lightest electrons distributions. All the distributions are normalized to the same area. We can clearly see a difference on the distribution of the 3rd electron, and particularly on the distribution of the 4th electron.

The effect of the p_T cuts on the signal and the backgrounds is presented in figure 78, where the rejection *(1-Acceptance)* is shown as a function of the cut. Since there is no considerable differences between the signal and the background distributions for the two hardest electrons, two first cuts of 20 and 15 GeV are chosen in order to have more the 99% acceptance for the signal. This results in a background acceptance of also more than 99%. The acceptances for different combinations of cuts on two lightest electrons is shown in table 10. The power of the cut on the third electron against the $Zb\bar{b}$ background is clearly visible. Changing it from 7 to 10 GeV allows to suppress additionally about 9% $Zb\bar{b}$ events, while retaining almost all the signal for higher masses, and loosing about 2% of signal for a 130 GeV Higgs mass. The cut on the fourth electron is even more powerful in suppressing the background, but results in a significant loss of signal events.

The p_T electron cuts have to be optimized in the way to loose as less signal as possible, while retaining enough power to reduce the backgrounds. As a strategy, we have chosen to open these cuts, because of the small number of events expected for low Higgs masses. We therefore take the following selection cuts: (20 GeV,15 GeV,10 GeV,7 GeV). Although the last cut seems small for high mass values, it is especially justified for the smaller mass of the Higgs reachable in this channel. If in a first analysis one gets a hint on the Higgs mass, these cuts could be tightened in a second pass of the analysis.

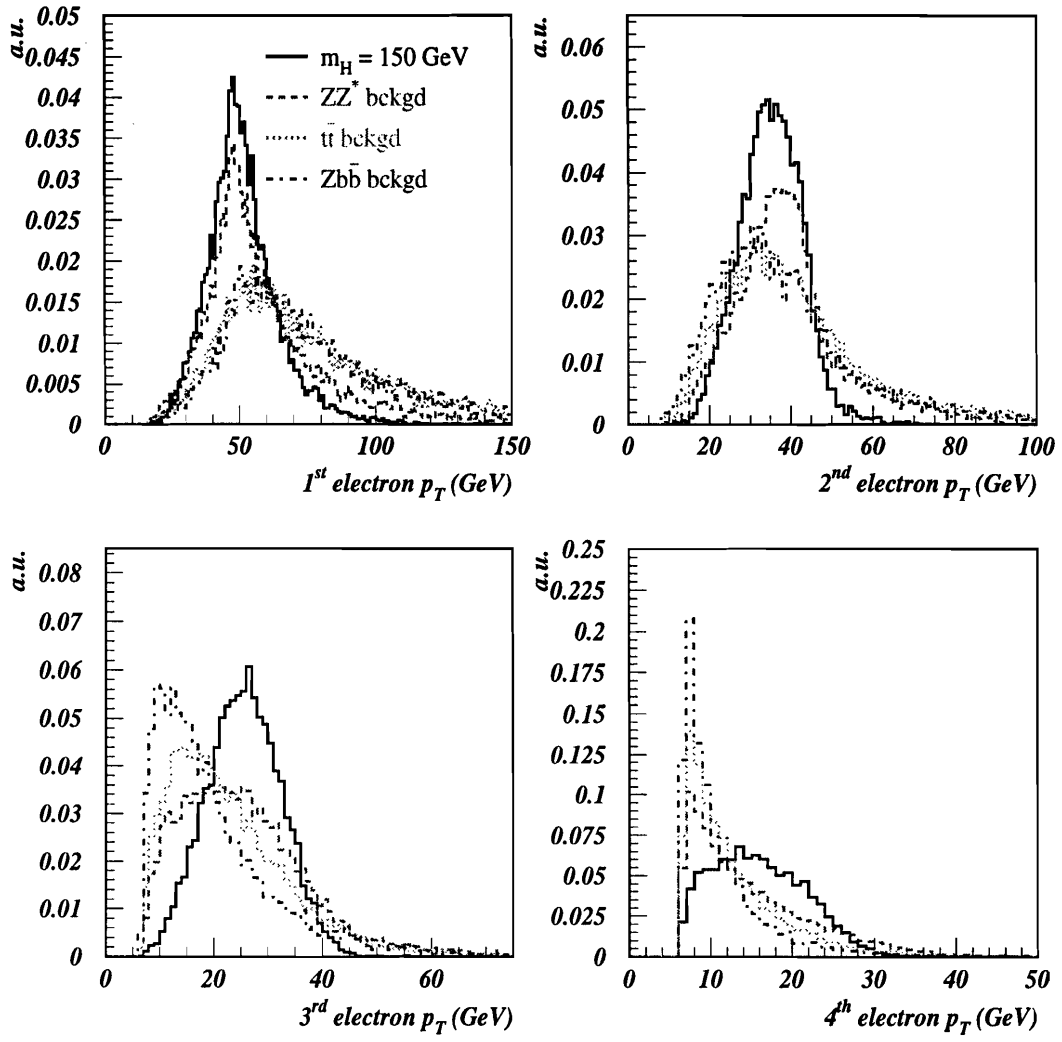

FIGURE 77. p_T distributions of the 4 electrons for the signal and the backgrounds.

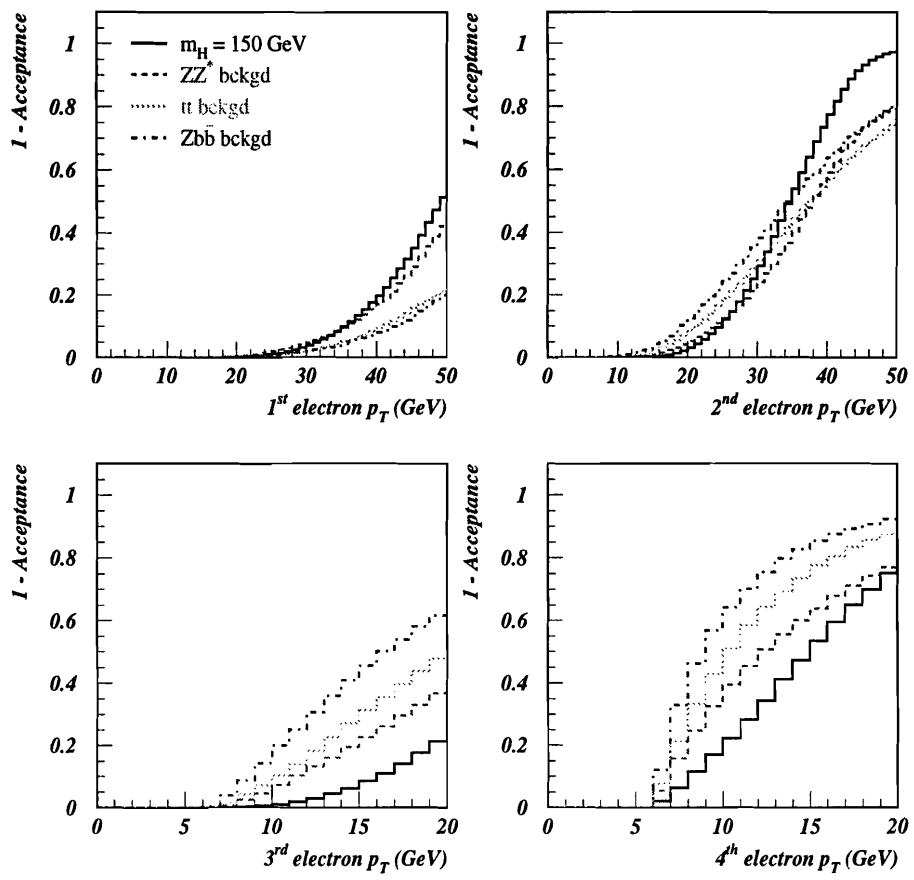

FIGURE 78. Rejection factors as a function of the p_T cuts on individual electrons for the signal and for the backgrounds.

	acc. for cuts (10,10) GeV (%)	acc. for cuts (10,7) GeV (%)	acc. for cuts (7,7) GeV (%)
m_H = 130 GeV	66.5	94.1	95.9
m_H = 150 GeV	83.1	97.4	97.9
m_H = 170 GeV	91.3	98.8	99.0
ZZ^*	67.2	90.8	93.9
$t\bar{t}$	56.9	86.5	91.2
$Zb\bar{b}$	42.9	76.5	85.4

TABLE 10. Acceptances, normalized to the preselection acceptance, for different sets of p_T cuts on the third and fourth electrons. The cuts on the first two electrons have been fixed to 20 and 15 GeV. Both the signal and backgrounds have the same preselection cuts: at least $2e^-$ and $2e^+$ with $p_T > 6.5$ GeV and $|\eta| < 2.5$.

4.6.2 Z mass cuts

The presence, in most of the cases, of one Z boson in our signal events allows, in the first place, to suppress non-resonant 4-electrons production or backgrounds with misidentified electrons. Among the backgrounds we are considering the $t\bar{t}$ does not have a real Z in the intermediate state, making it susceptible to an eventual Z mass cut. The invariant mass of the e^+e^- pair for the signal (m_H = 150 GeV) and the backgrounds, closest to the nominal Z mass is shown in figure 79, together with the acceptance for symmetrical ($\left|m_{e^+e^-} - m_Z\right| < \Delta_{symm}$) and asymmetrical cuts ($m_Z - \Delta_{asymm} < m_{e^+e^-} < m_Z + 6$ GeV).

The left tail on the invariant mass distribution, for the processes with a real Z, is caused by the internal bremsstrahlung in the Z decay, since the photons are not taken into account in the mass calculation. Some of these photons will be either separately identified or reconstructed together with the electrons, but part of the tail will still remain. In addition, because of the bremsstrahlung in the tracker material before the ECAL, the left tail on the reconstructed mass will be enhanced. Thus, it is necessary to open the cuts in order to keep as much signal events as possible. Because of the almost flat mass distribution for the $t\bar{t}$ background and of the asymmetrical shape of the Z mass distribution for the signal and the two other backgrounds, the asymmetrical cut is more justified. We have chosen the asymmetrical cut $m_Z - 13$ GeV $< m_{e^+e^-} < m_Z + 6$ GeV in order to keep 87% of signal events, for a 150 GeV Higgs. The acceptances for the backgrounds are 90%, 90% and 70% for ZZ^*, $Zb\bar{b}$ and $t\bar{t}$ respectively.

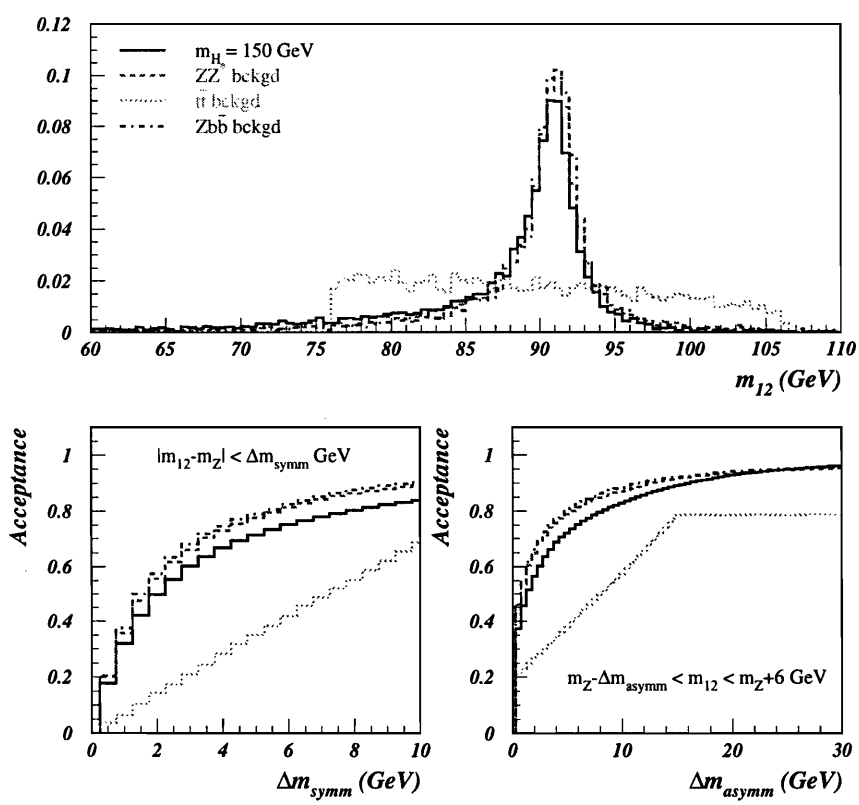

FIGURE 79. Distributions of the invariant mass of the electron-positron combination closest to the Z mass, for signal and background events, with the acceptance for symmetrical and asymmetrical cuts.

4.6.3 Z* mass cuts

In a large majority of cases, one electron-positron pair in the Higgs 4 electrons decay comes from one off mass shell Z boson. In figure 80, we show the invariant mass distribution of the electron-positron pair furthest away from the nominal Z mass (in the case of more than two electron-positron combinations, we first search for the pair with invariant mass closer to Z nominal mass and then, among the remaining combinations, we take the one with the highest invariant mass). All the distributions are normalized to the same area. We can notice a low mass peak for the $t\bar{t}$ and $Zb\bar{b}$ backgrounds coming from electrons originating from the same cascade. The acceptances with respect to a lower cut ($m_{ee} > m_{min}$) and an upper cut (15 GeV $< m_{ee} < m_{max}$) are also shown. We choose to open these cuts to accept at least 90% of events at small masses. Again, once one have a hint on the Higgs mass, these cuts could be adjusted. In table 11, we give a starting and optimal set of cuts, defined as the cuts giving a 90% acceptance for the signal, and the corresponding background acceptances.

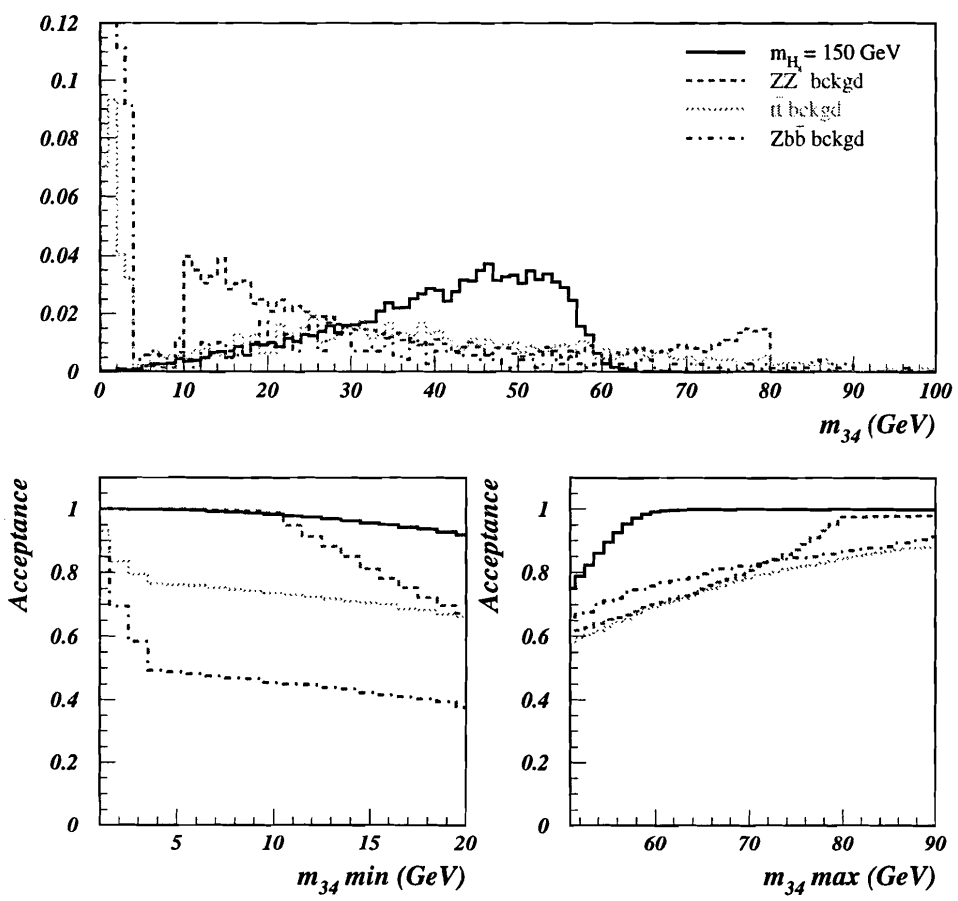

FIGURE 80. Invariant mass distribution for electron-positron pairs more distant to the nominal Z mass, for signal and backgrounds, and acceptances as a function of a lower and an upper cut.

	acc. for startup cuts (15, 80) GeV (%)	cuts for 90% acc. (min GeV, max GeV)	acc. for 90% cuts (%, %, %)
m_H = 130 GeV	90	(15, 60)	-
m_H = 150 GeV	95	(20, 65)	-
m_H = 170 GeV	96	(30, 80)	-
ZZ^*	81	-	(62, 52, 48)
$t\bar{t}$	64	-	(53, 53, 46)
$Zb\bar{b}$	38	-	(33, 31, 24)

TABLE 11. m_{Z^*} cuts: acceptances for start-up cuts, cuts for 90% signal acceptance and background acceptances of these cuts for three different Higgs masses, normalized to the Z mass cut acceptance.

4.6.4 4-electrons invariant mass cut

One of the biggest advantages of the Higgs search through this channel is the possibility to reconstruct its mass, as the 4-electrons invariant mass. In the relevant mass region, the natural Higgs width is small ($\Gamma_H << 1$ GeV) and the reconstructed mass width will be dominated by the detector resolution, which is a function of the combined tracker and electromagnetic calorimeter momentum resolution.

In the backgrounds study up to now, we have considered the 4 electrons inclusive production. For a given Higgs mass the effective background is only a fraction of the total background, contained in a limited region around the Higgs mass. In figure 81 we give the number of events for the signal and the backgrounds, in the area $m_H \pm 2\sigma_{m_H}$, for 10^5 pb^{-1} i.e. one year of the LHC running at high luminosity. All the cuts presented in the previous section have been applied. The expected energy resolution of the CMS electromagnetic calorimeter (given in the table 3) has been introduced as a smearing of the electron energy. The typical signal acceptance in the $m_H \pm 2\sigma_{m_H}$ window is about 80%. As we can see from the figure, at this stage, the number of events for the $t\bar{t}$ and $Zb\bar{b}$ backgrounds are of the order of the signal. It is therefore necessary to reduce them further, for at least one order of magnitude. This is possible by exploiting topological differences in these backgrounds with respect to the signal events. In the next section we will discuss the possibility of using isolation cuts.

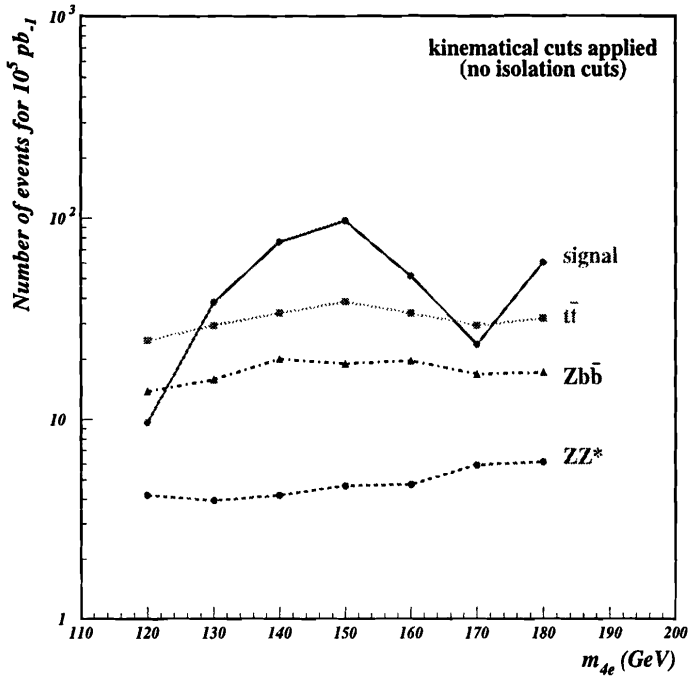

FIGURE 81. Number of events within $m_H \pm 2\sigma_{m_H}$ for an integrated luminosity of 10^5 pb^{-1} after the kinematical cuts optimized in the previous sections.

4.7 Isolation

The last important feature of the signal events is the presence of four isolated electrons in the final state. The same is true for the ZZ* background events. For the two other backgrounds, $t\bar{t}$ and $Zb\bar{b}$, it is not the case. They have in average two non-isolated electrons coming from cascade mesons decays. Therefore, by applying appropriate isolation algorithms, it should be possible to strongly suppress these backgrounds.

There are many possible isolation algorithms, which combine or use separately the informations from the tracker, electromagnetic and hadronic calorimeter. The tracker isolation demands the absence of any charged track with a p_T greater than some threshold p_{Tmax} in a cone $R = \sqrt{\Delta\eta^2 + \Delta\phi^2}$ around the electron. The calorimetric isolation is based on the difference between the energy deposited in a narrow and a wide region around the electron impact point. The tracker isolation require a good track reconstruction efficiency for low p_T tracks inside jets, while calorimetric isolation suffers from the internal radiation effects.

In this section, we present an isolation study based on the analysis of the charged tracks around the electrons. In figure 82, the acceptances for the signal (Higgs mass 150 GeV) and backgrounds for different choices of R and p_{Tmax} parameters are shown.

The power of isolation on the suppression of the $t\bar{t}$ and $Zb\bar{b}$ backgrounds is obvious. To have more than 90% (precisely 93%) signal acceptance we have chosen p_{Tmax} = 2.5 GeV and

$R = 0.2$, which give an acceptance for the ZZ^* background of 95% and a rejection factor of about 70 for the $t\bar{t}$ and about 15 for the $Zb\bar{b}$ background.

At high luminosity, where it is expected to have a pileup of about 20 minimum bias events per bunch crossing the isolation acceptances will change, lowering in particular the signal acceptance. To account for this effect we additionaly reduce the signal and ZZ* background acceptances for 15%, while keeping the same reducible background rejection factors. The level of rejection gives confidence that isolation criterion will allow for a reduction of these backgrounds well below the signal and the ZZ^* background, even at high luminosity.

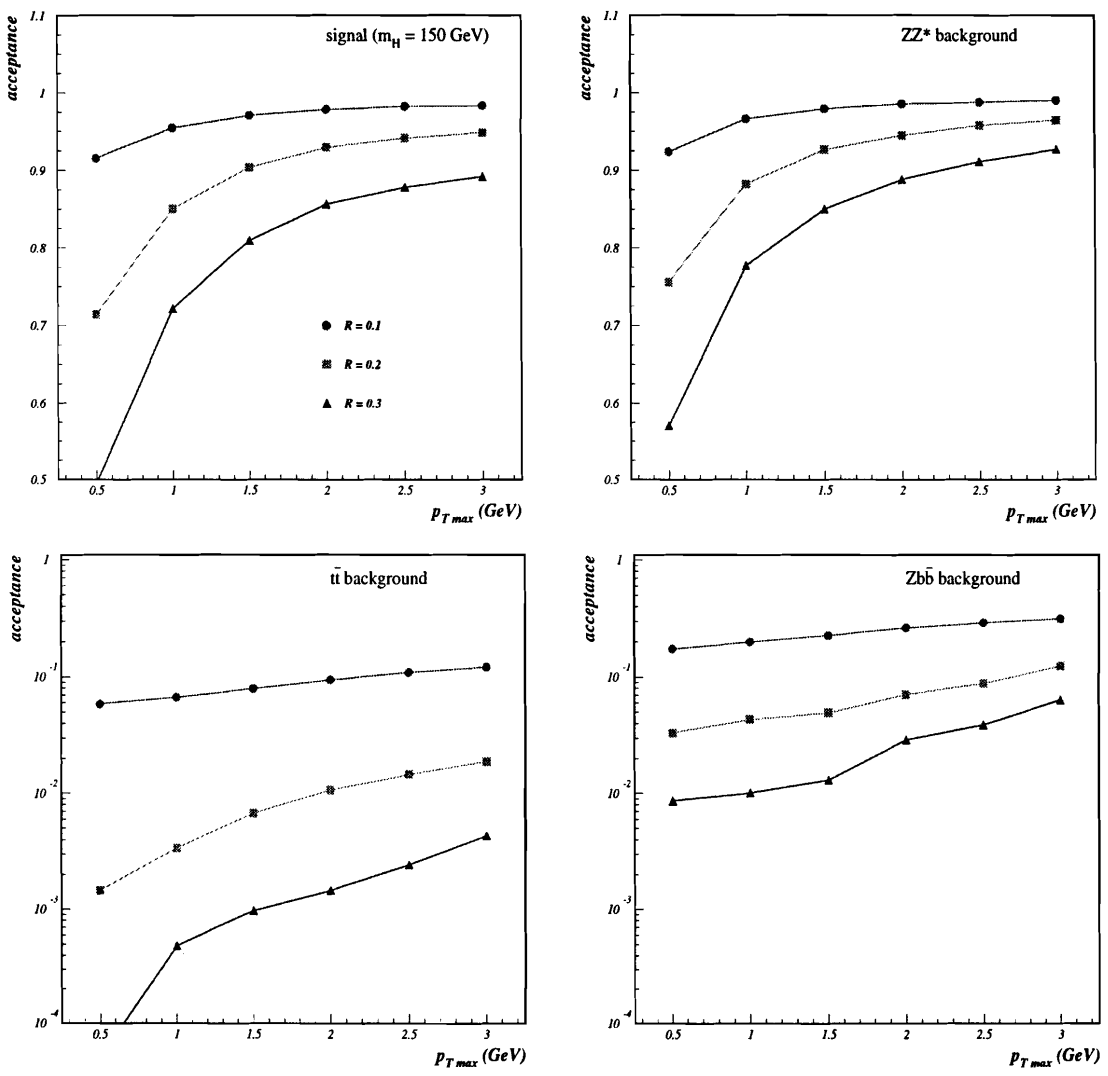

FIGURE 82. Acceptances for the isolation cuts, as a function of the maximal p_T of the tracks allowed in a cone, for three different values of the cone size, $R = 0{,}1\ ;\ 0{,}2\ ;\ 0{,}3$.

4.8 Additional cuts

As we have seen, isolation cuts allows to reduce the $t\bar{t}$ background by more than one order of magnitude below the signal level. To further reduce the $Zb\bar{b}$ background to about the same level, one could make use of the electron impact parameter. The previous studies [82] have shown that using the impact parameter cut, a rejection factor of about 3.5 for the $Zb\bar{b}$ background and about 4 for the $t\bar{t}$ background[5] can be obtained, with about 90% acceptance for the signal and the irreducible background. Therefore, in the end, the ZZ* background remains as the most important contribution. Besides the cuts used up to now in the analysis, there are some additional cuts which could further suppress the this background. They will be presented in this section.

4.8.1 *Azimuthal distance between the Z's* and p_{T4e} cuts

Since the main Higgs production process (gluon fusion) is a $2 \rightarrow 1$ process at the leading order, the transverse momentum of the Higgs boson is generated by higher order processes, i.e. in the language of Monte Carlo event generators, by the parton showers. In the irreducible background a p_T for the ZZ* system is also generated by the higher order processes. For the signal, about 90% of the cross section comes from the gluon-gluon initial state, while in the ZZ* background it is the quark-antiquark initial state which dominates, with about 70% of the total cross section. Because of the larger color factors and larger phase space for the parton showering for the gluon initial states, the p_T distribution of the Higgs bosons should be naturally harder than that of the di-boson system in the ZZ* background.

In figure 83, we show the distribution of the transverse momentum of the 4-electrons combination (p_{T4e}) for the signal and the ZZ* background and the rejection factor as a function of the p_{T4e} cut. All the kinematical cuts presented in the previous sections are applied. A cut at $p_{T4e} > 10$ GeV allows to reject about 40% of $q\bar{q} \rightarrow ZZ^*$ background, while keeping 85% of the signal, for a 150 GeV Higgs. To be conservative enough we assume that this cut does not remove any of the $gg \rightarrow ZZ^*$ background events, giving an overall ZZ* background rejection factor of 1.44.

Another variable which could be used for the background rejection, correlated with the p_{T4e}, is the azimuthal angular difference between the Z and the Z*:

$$\Delta\phi = \left|\pi - \left|\phi_Z - \phi_{Z^*}\right|\right| . \qquad \text{(EQ 49)}$$

In figure 83 the distributions of $\Delta\phi$ for both signal and background are shown, together with the rejection factor as a function of the $\Delta\phi$ cut. Choosing the same signal acceptance of 85% as for the p_{T4e} cut, we obtain a slightly better background rejection of 1.63, using the same assumption that gluon fusion background events entirely pass the cut. The cut value is $\Delta\phi < 0.2$.

In the section 4.2, where we have studied the p_T distribution of the Higgs boson, we have seen some of the limitations of the present PYTHIA Monte Carlo event generator. One should

5. Since the impact parameter cut is correlated with the isolation cut, the absolute impact parameter rejection factors are somewhat smaller.

be careful in using p_T cuts, or any other variable strongly correlated with it. The study described above should, therefore, be taken only as a possible additional selection which could be used after a detailed understanding of the variables used.

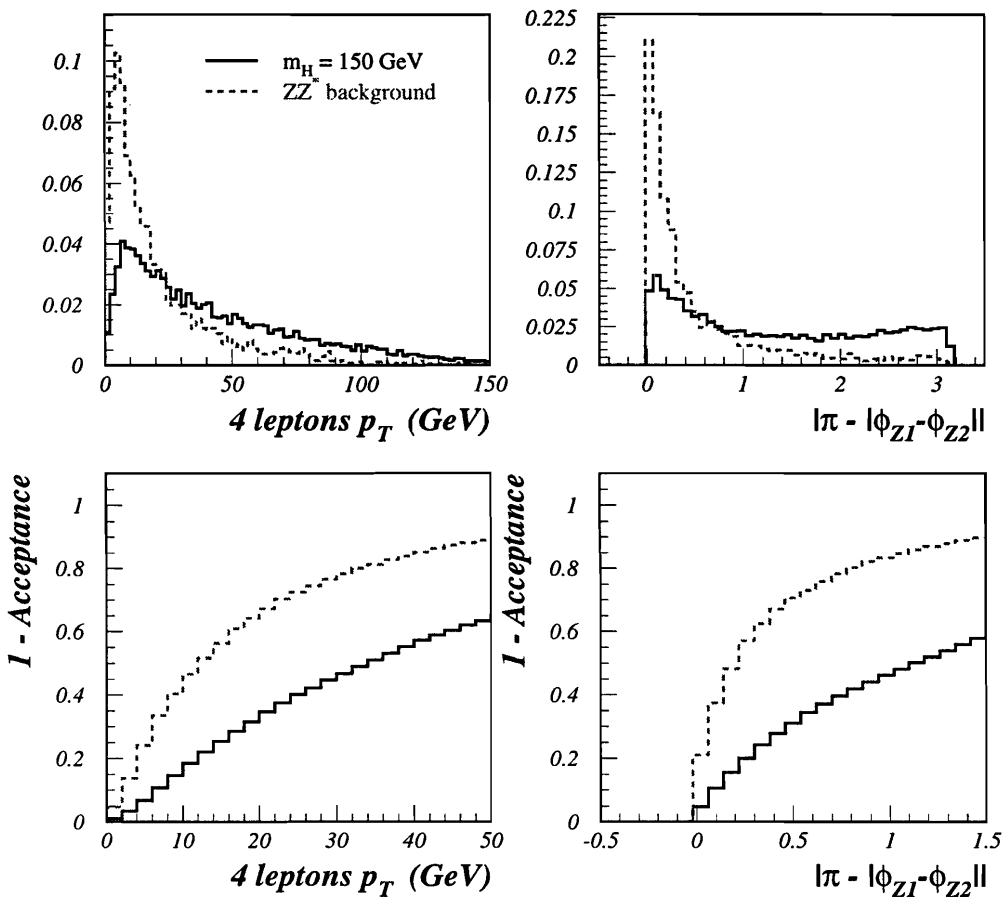

FIGURE 83. Distributions of the 4 electrons p_T and azimuthal angular difference (top) and corresponding rejection factors (bottom).

4.8.2 Angular distributions and scaled electron energy in the Higgs frame

In figure 84, we show several angular correlations between the electrons, Z bosons and 4-electron system. In the used version of PYTHIA (6.122), the angular correlations between the four electrons are correctly described. In older versions (5.7) they were treated as in the $H \rightarrow WW$ decay. From the figures we can see that there is no a considerable difference between these angular distributions and therefore we cannot use them in the signal versus background separation.

Another interesting variable for ZZ* discrimination is the scaled electron energy in the Higgs frame ($4E/m_H$). It is shown in figure 85, separately for Z and Z* electrons. We can see that these distributions could also be used to reject some of the irreducible background.

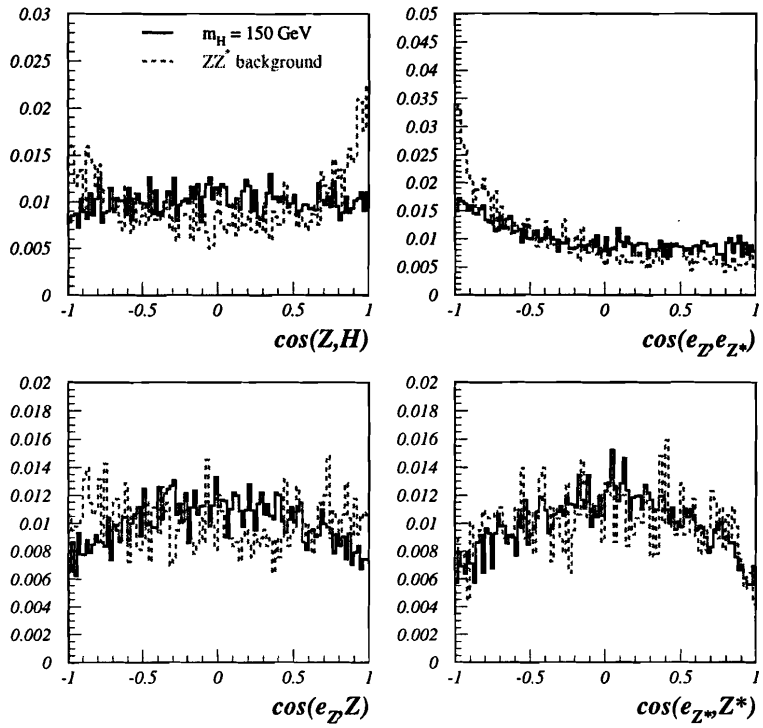

FIGURE 84. Several angular correlations between electrons, Z and 4-electron system for the signal and the irreducible background.

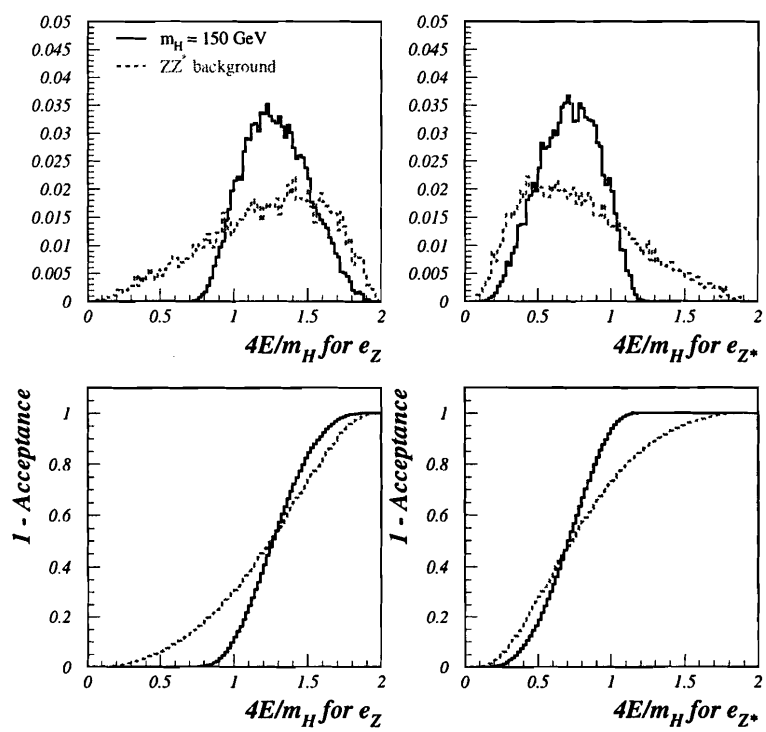

FIGURE 85. Scaled electron energies in the Higgs frame, separately for electrons from Z and Z*.

4.9 Results on signal visibility

At the end of this chapter we give the summary of the kinematical cuts and the results on the signal visibility, obtained with the particle level analysis. These results are aimed to point out the main requirements on the electron reconstruction in the detector and will be used as a reference for the reconstruction studies in the next chapter.

The first selection criterion for events to be accepted for a further analysis is to pass either single electron or double electron triggers. In addition, the charge constraint requests

$$\sum q_{e_i} = 0, \text{i=1,...,4}, \qquad \text{(EQ 50)}$$

i.e. 2 e^- and 2 e^+. In order to extract the signal over the backgrounds the following selection cuts have been found as optimum:

- p_T *cuts*:

$$p_T^{e_1} > 20 \text{ GeV}, p_T^{e_2} > 15 \text{ GeV}, p_T^{e_3} > 10 \text{ GeV}, p_T^{e_4} > 7 \text{ GeV}, \qquad \text{(EQ 51)}$$

- *Z mass constrain*:

$$m_Z - 13 \text{ GeV} < m_{e^+e^-} < m_Z + 6 \text{ GeV}, \qquad \text{(EQ 52)}$$

- *Z* mass constrain:*

$$15 \text{ GeV} < m'_{e^+e^-} < 80 \text{ GeV}, \qquad \text{(EQ 53)}$$

- *isolation:*

no charged tracks with $p_T > 2.5$ GeV in a cone $R = 0.2$ around each electron.

The electrons p_T cuts and Z bosons mass constrains could be refined after an eventual hint on the Higgs boson mass from a first analysis pass. The $t\bar{t}$ and $Zb\bar{b}$ backgrounds can additionally be suppressed using the impact parameter, and the ZZ^*/γ^* background can be further reduced to some extent by applying the cuts presented in the previous section.

The overall signal acceptance with these selection cuts is about 31%, 45% and 52% for the Higgs with masses of 130, 150 and 170 GeV respectively. The background rejection factors are about 70, 10^5 and 10^5 for the ZZ^*/γ^*, $t\bar{t}$ and $Zb\bar{b}$ backgrounds.

The 4-electrons invariant mass distributions, after the above selection criterion, are shown in figure 86 for three values of the Higgs mass (130, 150 and 170 GeV) superimposed to the backgrounds. The left tails on the Higgs mass distributions are caused by the internal bremsstrahlung, since the radiated photons are not taken into the mass calculations. As we can see, the $t\bar{t}$ background contribution is negligible, and the $Zb\bar{b}$ background contributes to a rather small extent. Therefore, the main background contribution is coming from the ZZ^*/γ^* background. A gaussian fit of the reconstructed Higgs mass distribution gives values of $\sigma_{m_H} = 0.74$ GeV for $m_H = 130$ GeV, $\sigma_{m_H} = 0.81$ GeV for $m_H = 150$ GeV and $\sigma_{m_H} = 0.97$ for $m_H = 170$ GeV. Detector effects, like the electron bremsstrahlung in the tracker material, and the electron reconstruction inefficiencies have not been taken into

account. Therefore, the obtained Higgs mass width is too optimistic but will be taken as a reference in the reconstruction studies presented in the next chapter.

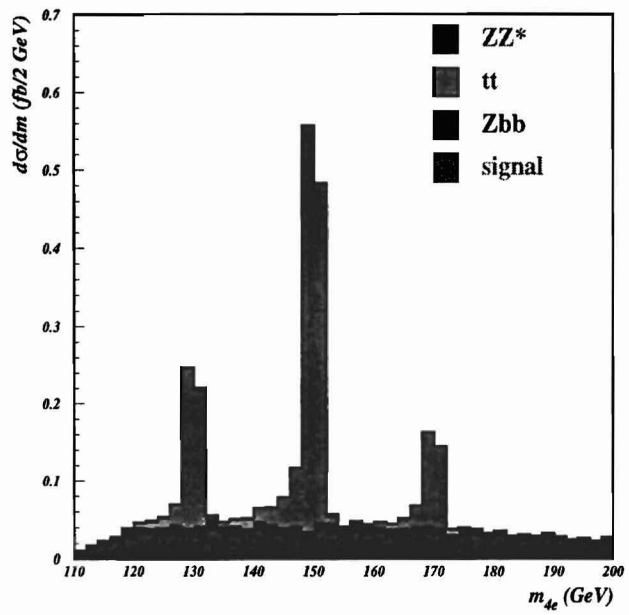

FIGURE 86. The 4-electrons invariant mass for 130, 150 and 170 GeV Higgs and the backgrounds, obtained with the particle level analysis. In the mass calculation the expected ECAL energy resolution is introduced as a gaussian smearing of the electron energy.

A criterion for the signal over background visibility is the requirement that the signal should be significantly greater than the background fluctuations. It is expressed through the so called *significance*, defined as the ratio of the number of signal events (N) and the squared root of the number of background events (B) in some window around the Higgs mass, $S = N/\sqrt{B}$. The usual criterion for a signal evidence is $S > 3$, and for a discovery is $S > 5$.

In first approximation the reconstructed Higgs mass has a gaussian shape, and the number of signal events in some window depends on the reconstructed mass distribution width (σ_{m_H}). For a smaller width, i.e. better resolution, the same number of events is contained in a smaller window. For the background, with the 4-electrons invariant mass spectrum shown in figure 86, the number of background events is roughly proportional to the mass window size. For the nearly gaussian shape of the signal and almost flat distribution of the background 4-electron invariant mass, the optimum window choice is $\pm 2\sigma_{m_H}$ around the reconstructed Higgs mass peak. Therefore, the signal significance is proportional to the $1/\sqrt{\sigma_{m_H}}$.

Both the number of signal events and the number of background events are proportional to the ε_e^4, where ε_e is the average electron reconstruction efficiency. Therefore, the signal significance is proportional to the ε_e^2.

The number of expected signal and background events in a mass window $m_H \pm 2\sigma_{m_H}$ for a 10^5 pb^{-1} integrated luminosity is shown in figure 87. As we can see, for one year of high luminosity running, we can expect from about 20 to 80 signal events in the mass range 130-

180 GeV. The signal significance is also shown in figure 87. As expected, its shape follows the $H \rightarrow ZZ^*$ branching ration shape with a maximum around 150 GeV and the minimum at about 170 GeV where the $H \rightarrow WW$ decay channel opens.

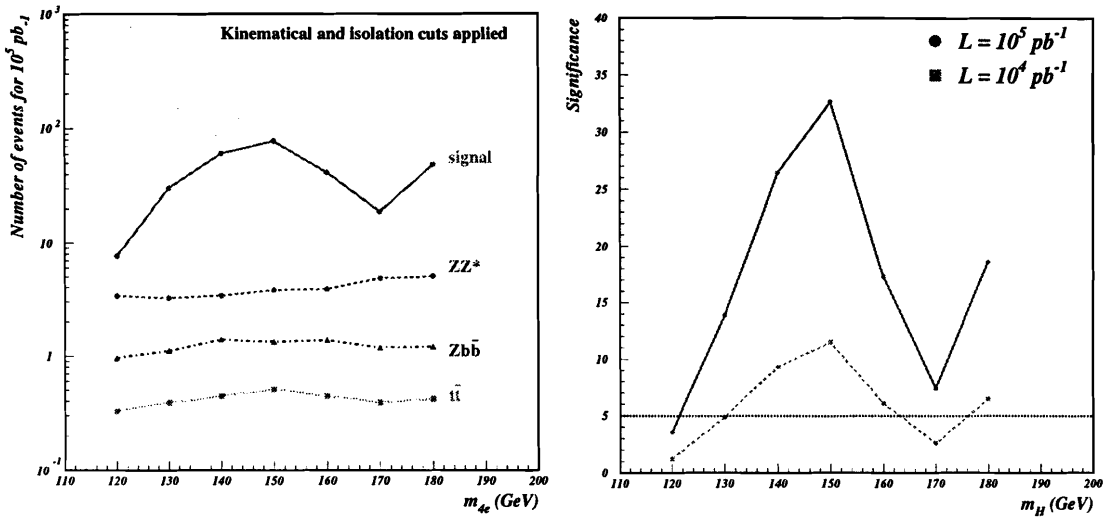

FIGURE 87. Number of events for one year of LHC running at high luminosity and significances for integrated luminosities 10^4 pb^{-1} and 10^5 pb^{-1}, obtained with the particle level analysis. Neither electron reconstruction inefficiencies nor specific detector effects influencing the electron reconstruction precision are taken into account.

From the particle level analysis, we conclude that the Higgs boson could be found through the $H \rightarrow ZZ^* \rightarrow 4e^{\pm}$ channel in a mass region from 122 to 180 GeV, for one year of high luminosity running at LHC. At low luminosity the discovery would be possible in the Higgs mass region from 130 to 164 GeV, and for the Higgs with 176 GeV mass and above.

Let us, at the end of this chapter, outline the two most important requirements on the electron reconstruction, coming from the particle level analysis results:

- The signal significance is proportional to the electron reconstruction efficiency squared, $S \sim \varepsilon_e^2$. In addition, the small number of events, particularly around 130 and 170 GeV Higgs masses, and the low momentum of the two lightest electrons gives strong requirements on the electron reconstruction efficiency.
- The signal significance is inversely proportional to the squared root of the Higgs reconstructed mass width(i.e. 4-electrons mass resolution), $S \sim 1/\sqrt{\sigma_{m_H}}$. Because of the detector resolution dominance in the Higgs reconstructed mass width, it is a direct and very strong requirement on the precision to be achieved on the electron momentum estimation.

Although the tracker and the electromagnetic calorimeter, the two most important detectors used in the electron reconstruction, have been designed in order to maximize the efficiency and the resolution, the electron reconstruction in the real detector is a rather sophisticated task. In the following chapter we will present our study of the $H \rightarrow ZZ^* \rightarrow 4e^{\pm}$ reconstruction, through the development of the electron reconstruction algorithms, taking into account the two above requirements.

Chapter 5 *Study of the $H \rightarrow ZZ^* \rightarrow 4e^{\pm}$ reconstruction*

5.1 Introduction

As we have seen in the previous chapter, the small number of events in the $H \rightarrow ZZ^* \rightarrow 4e^{\pm}$ process together with the multielectron final state demands an excellent reconstruction efficiency and low kinematical cuts on the electrons transverse momentum. In addition, the significance of the signal visibility is inversely proportional to the squared root of the reconstructed 4-electrons invariant mass width, requesting an excellent precision of the reconstructed electron momentum.

The electron reconstruction procedure which has been developed in CMS consists of tracks reconstruction in the tracker, clusters reconstruction in the electromagnetic calorimeter, tracks and clusters matching and refinement of electron momentum estimation combining the ECAL and tracker measurements. Therefore, the electron reconstruction quality relies on the performances of both the CMS tracker detector and the electromagnetic calorimeter.

A specific problem in CMS is the significant amount of tracker material before the electromagnetic calorimeter. Electron traversing the tracker cavity radiates photons thought the bremsstrahlung process, causing difficulties in the electron reconstruction, affecting both the reconstruction efficiency and the precision. In order to obtain a high reconstruction efficiency and precision in the $H \rightarrow ZZ^* \rightarrow 4e^{\pm}$ channel, sophisticated recovery algorithms from both the ECAL and the tracker are required.

In the first part of this chapter we first describe the bremsstrahlung problem. Then we give a short description of the track reconstruction algorithm used and the present track finding efficiency. Furthermore, the clustering in the ECAL and the method for the bremsstrahlung photons recovery is described, with a dedicated algorithm for hard photons recovery.

In the second part the developed method for the electron energy estimation is described. It makes use of a the shower model to predict the electron energy deposition in the electromagnetic calorimeter, which is then used in a weighting technique. The obtained energy estimator is combined with the tracker momentum estimator to construct a final electron momentum estimator.

At the end of the chapter, the developed electron reconstruction algorithms are applied to the $H \rightarrow ZZ^* \rightarrow 4e^{\pm}$ reconstruction and the results compared with those obtained from the particle level analysis described in the previous chapter.

For the reconstruction studies, we have used the detailed simulation of the CMS detector implemented in the CMSIM program [79]. The physical processes inside the detector have

been simulated with GEANT [80], with 100 keV cuts on the electromagnetic processes. We have used data samples of several thousands electrons, generated within the barrel geometrical acceptance ($|\eta| < 1.5$), for two representative transverse momenta of 10 and 30 GeV. The reconstruction algorithms have been used or developed within the CMS Reconstruction and Analysis (ORCA) framework [81]. The tracker used in this study corresponds to the Si-MSGC design. From the material budget point of view, the amount of material before the electromagnetic calorimeter with the recently chose all Si tracker design is expected to persist at about the same level, with a somewhat different transverse distribution.

5.2 The bremsstrahlung problem

The biggest problem in the electron reconstruction in CMS comes from the bremsstrahlung radiation in the tracker cavity. The material budget before the electromagnetic calorimeter, shown in figure 88, varies between 0.2 X_0 and 0.4 X_0 for $|\eta| < 1$ and grows to a rather flat maximum of about $0.8X_0$ in the region $1.5 < |\eta| < 2.0$. At larger pseudorapidities, tracks do not cross the outer tracker services and, therefore, in this region material budget decreases. The biggest contributions come from the silicon system, mainly due to the support structures, cables and cooling. The contribution from the detectors themselves is at a comparable level for both silicon and MSGC detectors.

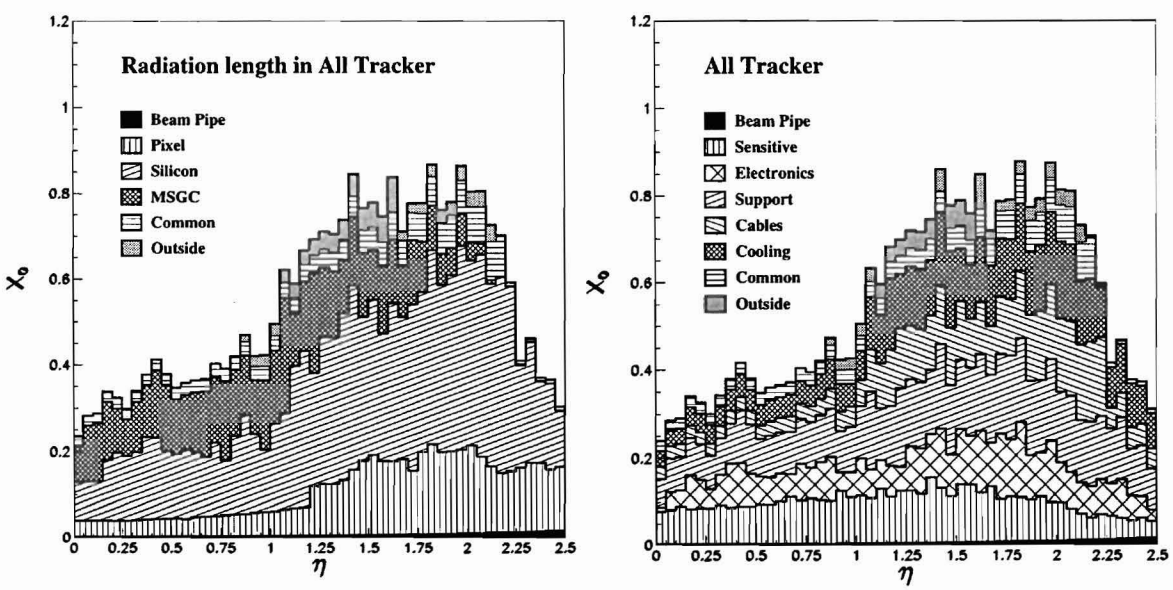

FIGURE 88. Material budget of silicon-MSGC version of the CMS tracker, together with the small contribution coming from the beam pipe. Left figure shows contributions from the tracker subsystems, and the right figure shows constributions broken down by functionality.

Importance of the bremsstrahlung process can be seen from figure 89 presenting the vertices of the secondary particles produced in the tracker cavity by electrons with 10 and 30 GeV

transverse momentum, generated in the barrel acceptance. Most of these vertices come from bremsstrahlung photons, but there is also a small contribution from e^+e^- pairs, coming from photon conversions. The biggest concentration of vertices is in the transition region between silicon and MSGC at a transverse radius of about 65 cm. This can be seen on the lower histograms showing the distribution of the number of vertices as a function of their transverse radius.

In order to quantify the bremsstrahlung emission, figure 90 shows the electron energies at ECAL entrance, normalized to the generated energy, for 10 GeV p_T electrons in the barrel. The integration of this distribution shows that 35.8% (80.8%) of electrons have lost more than 60% (10%) of their initial energies. Even more, in 11.7% of cases, electrons loose more than 90% of their initial energy. On the same figure, the energy distribution of the secondary particles is also given, together with the probability of having a secondary particle with energy bigger than a given value. We can see that 13.2% of the secondary particles have energy greater that 1 GeV. In figure 91 the corresponding distributions for 30 GeV p_T electrons in the barrel are given.

The bremsstrahlung radiation will affect both ECAL and tracker measurements. The kinematics of the process is such that the photons are radiated along the tangent to the electron trajectory. Afterwards their trajectory is a straight line, while electrons curve in the magnetic field. This means that the photon impact in the ECAL will be more distant to the electron impact in the case of an early radiation (i.e. photon emitted at the beginning of the electron trajectory).

In case of late radiation (i.e. photon emitted near the end of the electron trajectory), the photon cluster is expected to be at least partially merged with the electron one, and therefore the loss in the reconstructed energy by the calorimeter much less than the one suggested by figures 90 and 91. For what concerns the tracker, such a late radiation will also have a rather small effect on the reconstructed track parameters. On the contrary, an early radiation will lead to reconstructed track parameters moving away from the original electron momentum. From the ECAL point of view, in that case, part of the original energy will be lost in a separate photon cluster, which will have to be recovered in order to estimate the original electron momentum. All of these effects depend on the hardness of the radiated photon momentum, with increasing importance as the photon momentum increases.

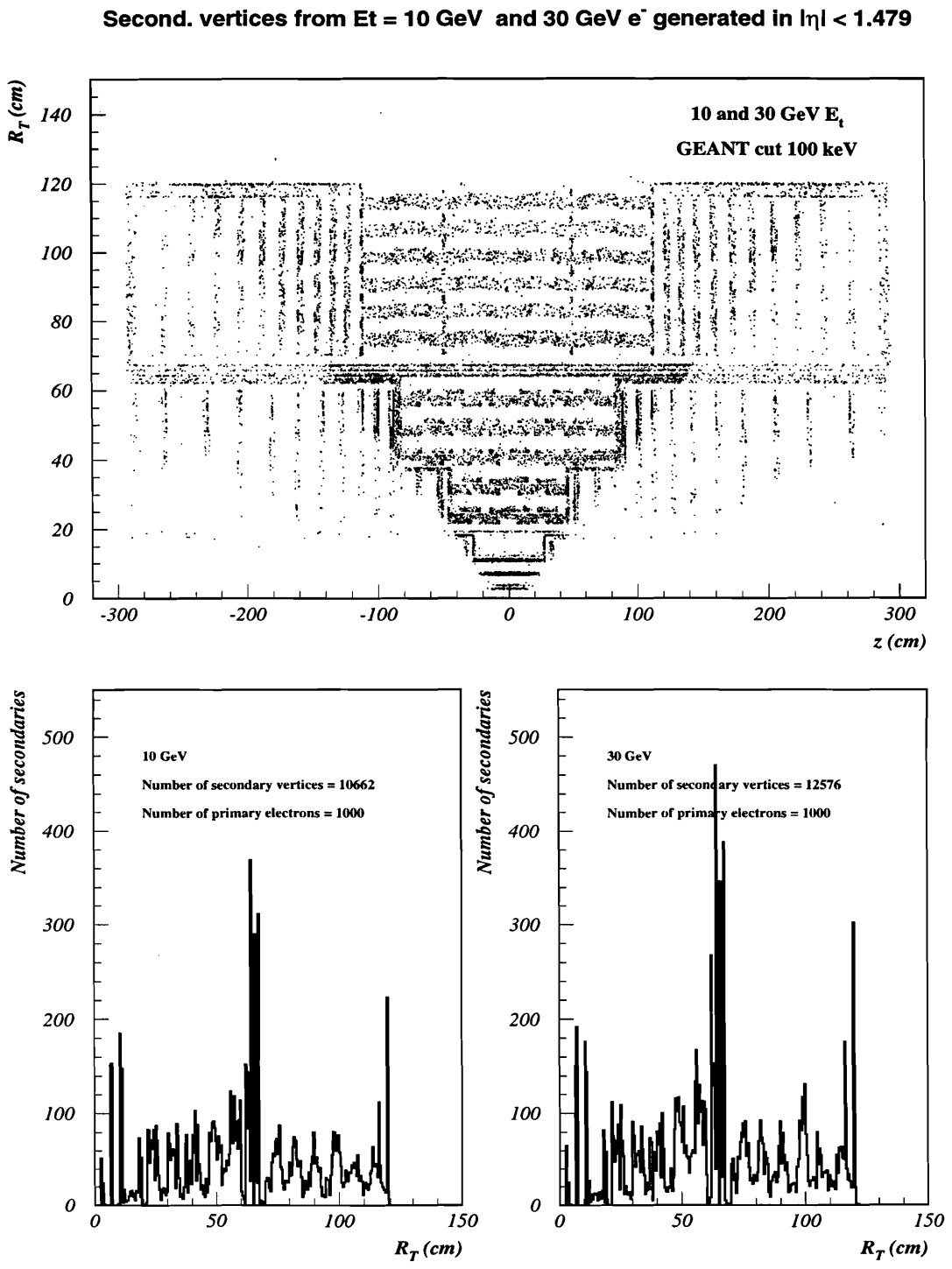

FIGURE 89. Secondary vertices in the tracker cavity from single primary electrons of 10 and 30 GeV p_T generated in the ECAL barrel acceptance (upper plot). Distribution of the number of secondary vertices with respect to their transverse radius (lower plots).

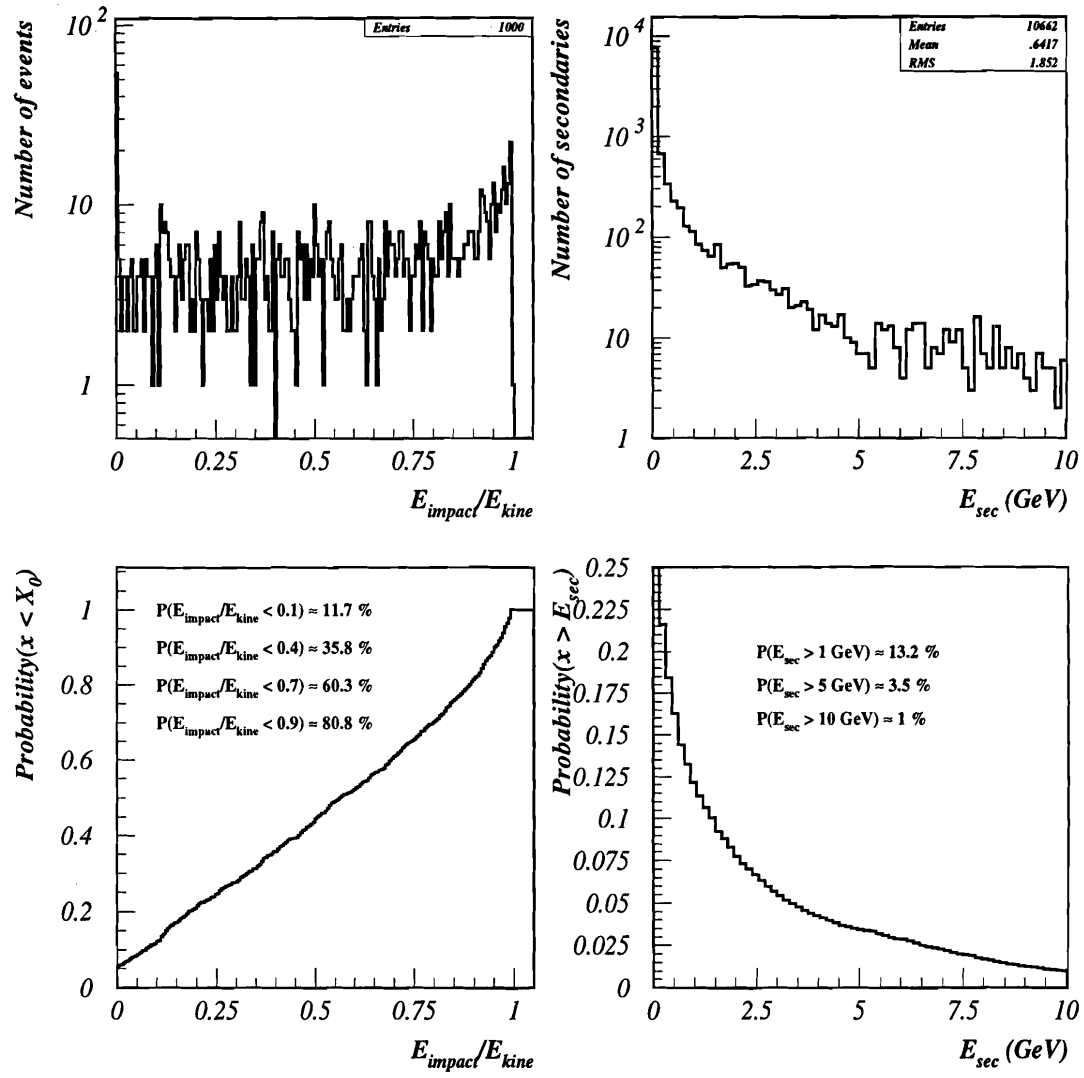

FIGURE 90. Distribution of electron energy at ECAL entrance normalized to the generated energy (top-left) and the integral of this distribution (bottom-left). Distribution of the energy of secondary particles (top-right) and corresponding probabilities (bottom-right), for 10 GeV p_T electrons in the barrel

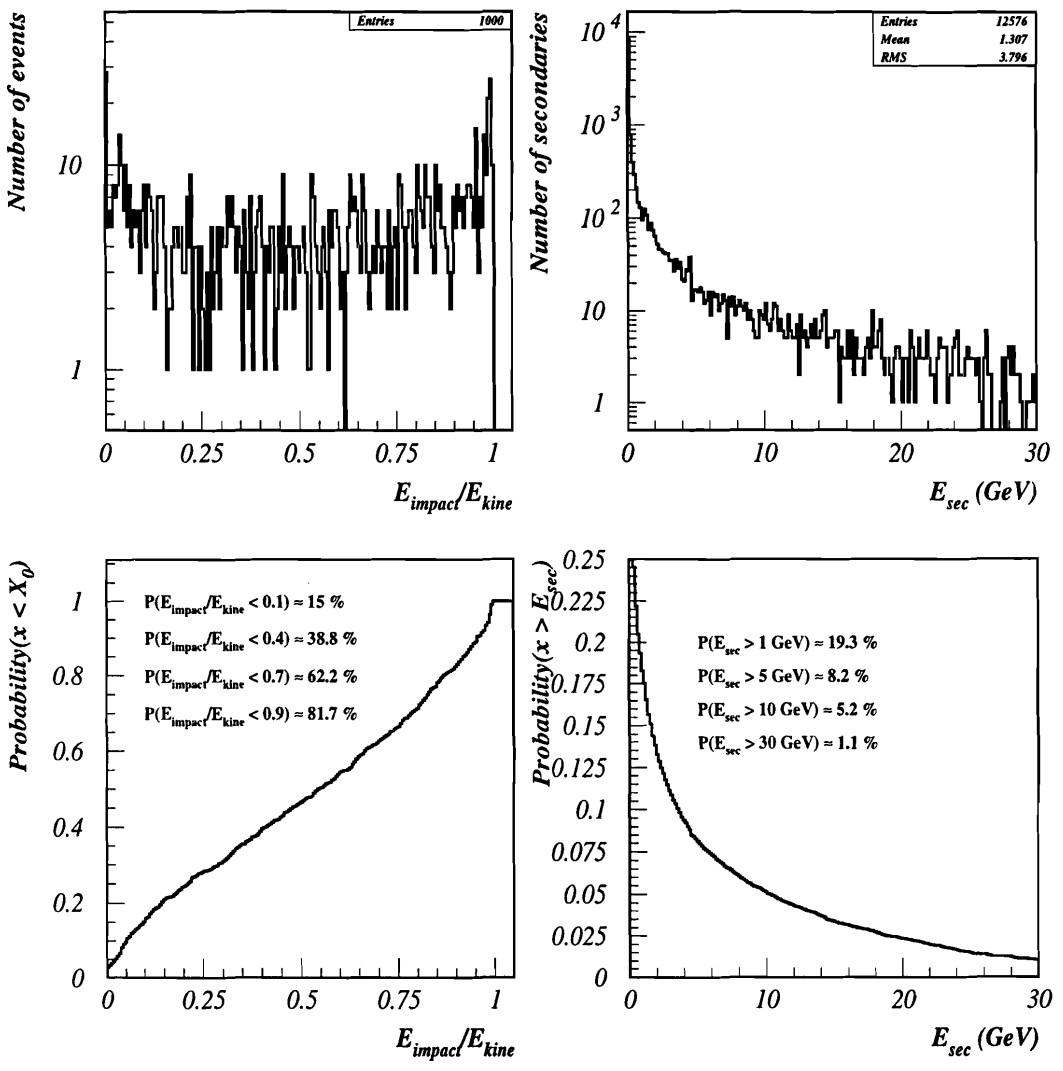

FIGURE 91. The same as figure 90 for 30 GeV p_T electrons in the barrel.

5.3 Track reconstruction

For electron tracks finding and reconstruction we have used the forward kalman filter (FKF) pattern recognition algorithm developed in CMS. This algorithm starts with searching the compatible hits in the two pixel layers, assuming a vertex at the nominal interaction point. When compatible hits are found, a track seed is constructed and the search for hits in outer layers is started. The track is extrapolated to the next layer where hits are searched for in the vicinity of the extrapolation point. When a compatible hit is found, the track parameters and corresponding errors are updated and the track is propagated to the next layer. The procedure is iterated until two consecutive layers without compatible hit are found. A minimum of 8 hits is required to build a track candidate. After that the track parameters are smoothed by refitting backward all the hits found. In figure 92 the electron track finding efficiency, defined as number of reconstructed electrons divided by number of generated electron in a given pseudorapidity interval, is shown. One can notice a regular drop of the efficiency as going toward higher rapidities, as expected from bremsstrahlung losses, since the tracker material budget increases with increasing rapidities. At a given rapidity, the efficiency increases with increasing transverse momentum of the track, since the track curvature is lower and hence the probability to miss the hit next to the bremsstrahlung emission is lower.

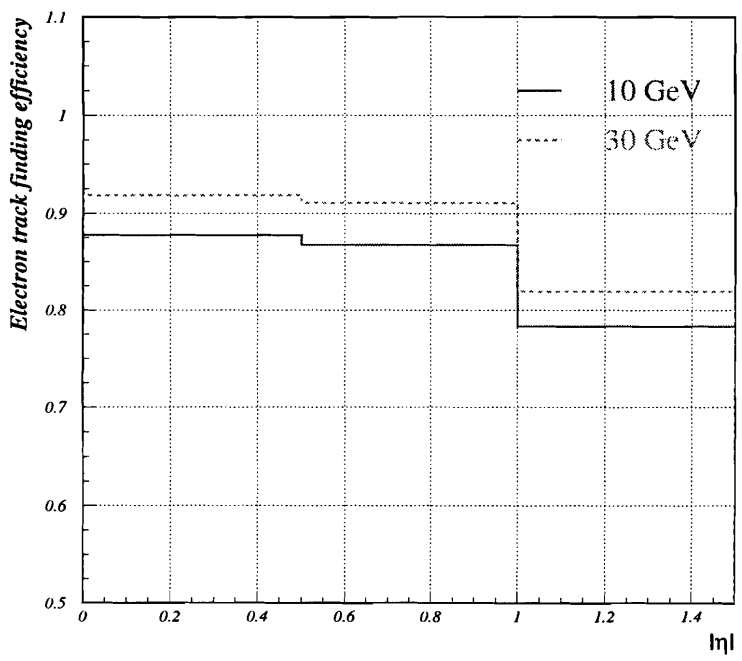

FIGURE 92. Electron tracks finding efficiency with FKF track finding algorithm for 10 and 30 GeV p_T electrons as a function of electron pseudorapidity.

The average track finding efficiencies are 84.3% for 10 and 88.3% for 30 GeV p_T electrons. There are several sources of track finding and reconstruction inefficiencies. A first one comes from the detector inefficiency. Furthermore, the forward track finding algorithm is currently not adapted to important changes of curvature which appears in case of hard bremsstrahlung. Alternative track finding algorithm, such as one starting from the outer layers, or even which is seeded by ECAL clusters should be studied. Third source of inefficiency is connected with the reconstruction track quality criteria. Loosed criteria means more reconstructed track.

Because of the possibility to combine ECAL and tracker measurements in the global electron reconstruction, we choose to loosen the tracker quality reconstruction criteria to accept more electron track candidates.

The reconstructed track momentum distributions for 10 and 30 GeV p_T electrons are shown in figure 93. One can notice low energy tails, coming from soft bremsstrahlung for which the track is reconstructed with slightly overestimated curvature. The low momentum tail also increases when going to higher momenta, as expected from radiation losses.

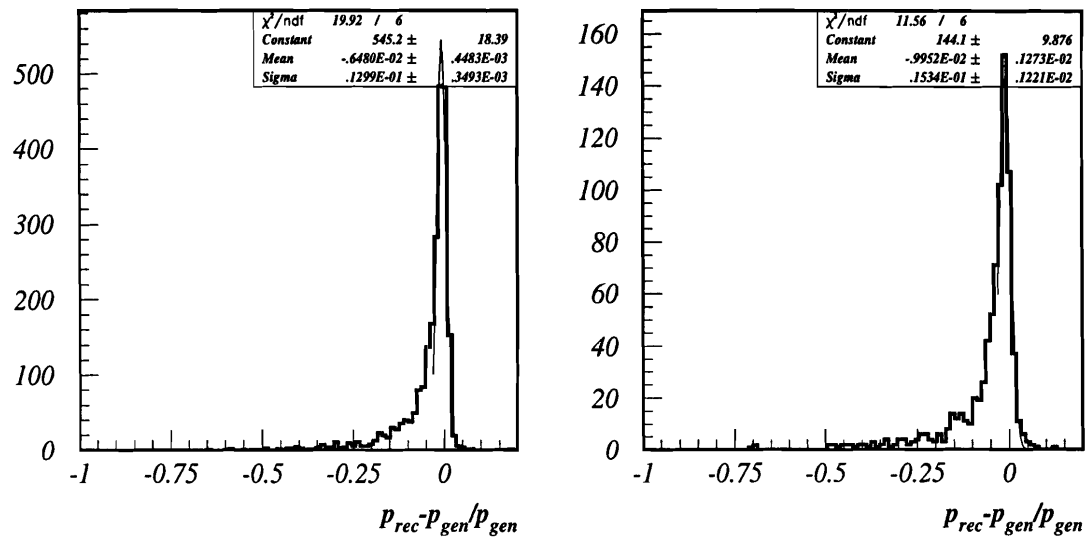

FIGURE 93. Reconstructed track momentum distributions, relative to the generated momentum, for 10 and 30 GeV p_T electrons.

5.4 Cluster reconstruction

In order estimate the electron energy it is necessary to consider a set of crystals, using thus a clustering algorithm. Several clustering algorithms have been proposed in CMS:

- *For photon reconstruction* [44].
  A cluster built from 5×5 crystals centered on the crystal with maximum energy has been used for the energy measurements of nonconverted photons. In the case of photon converted in the barrel tracking volume two algorithms have been used. For electron-positron pairs separated by $\Delta\phi < 0.045$ a $5(\text{in } \eta) \times 9(\text{in } \phi)$ window centered on the crystal with maximum energy deposit has been used. Otherwise a sum of fixed 3×3 (5×5) windows around every local maxima of 1 GeV (5 GeV) between the electron-positron impact points has been used. For the conversions in the endcaps, the 5×5 window has been used, because of the smaller average e^+e^- separation. The energy measurement obtained with these algorithms has been improved by leakage corrections, depending on either photon impact point or electron-positron separation in case of conversions.
- *For electron reconstruction.*
  For the calibration with $Z \rightarrow e^+e^-$ events [44] and in previous $H \rightarrow ZZ^{(*)} \rightarrow 4e$ studies

[82] an asymmetrical $5(\text{in } \eta) \times 7(\text{in } \phi)$ window surrounding the crystal with maximum deposited energy has been used. First the 5×5 was created around the crystal with maximal energy and then the window was extended in ϕ assuming direction of the eventually radiated photon. This algorithm has been selected as an optimal choice among several symmetrical and asymmetrical windows. For the calibration with $W \rightarrow e\nu_e$ events [44] a 3×3 matrix centered on the crystal with maximum signal was used.

All of these algorithms are based on the construction of fixed windows around the crystal with maximum energy deposit. Using fixed windows in electron reconstruction has several drawbacks. Being fixed it does not take properly into account event by event variations of the pattern due to of the particle impact point and direction variations. To overcome these problems the size of window should be extended. But, by increasing the window size the noise contribution increases, as well as the pile-up contribution, and at small electron energies these effects starts to significantly deteriorate the resolution. In addition to this problem, fixed window algorithms are not suitable for the reconstruction of very close showers, like it is the case with electron bremsstrahlung.

The algorithm which would be able to overcome these problems should therefore:

- construct a set of crystal well adapted to the shower shape to be able to follow event by event fluctuations of impact position and direction,
- be not too large in order to avoid too much noise contribution,
- be local as much as possible to separate close showers, like in case of electron bremsstrahlung or photon conversions.

An algorithm with these properties, so called dynamical clustering algorithm, has been developed [83]. It proceeds in two main steps:

1. *Search of a cluster seed.*
   Each crystal with local maximum energy deposit defines a cluster seed if its energy is above a threshold (E_{thr}^{seed}). We have used $E_{thr}^{seed} = 3.33 \cdot \sigma_s$, corresponding to 100 MeV in the barrel and 500 MeV in the endcaps. This threshold allows to suppress the clusters coming from noise, without significant loss of physical clusters.
2. *Construction of the cluster.*
   For each seed the algorithm loops over all the crystals still available and attaches to the cluster those who satisfy the criterion to be *adjacent by side and have smaller energy* than at least one crystal already belonging to the cluster. In this way the cluster stops when it encounters a crystal with higher energy deposit than its boundary crystals. This happens either in case of noise fluctuations or in case of a physical neighboring cluster.

In figure 94 few typical events, together with the reconstructed electromagnetic clusters using the dynamical clustering algorithm, are shown. For 10 (30) GeV p_T electrons the mean number of crystals in the electron cluster is about 25 (35). With the presented criteria for cluster construction two electromagnetic objects are reconstructed as separated clusters if they enter the electromagnetic calorimeter at impacts separated by at least one crystal.

Building the clusters this way, from the shower center outward, use the advantage of the nearly axial symmetry of the shower transverse profile. The cluster shape changes from event

to event following the variations of the impact position and direction. Because of its property to stop developing when it reaches the noise level the cluster would not pick up too much noise.

The energy and position of the cluster are, in a first iteration, estimated as:

$$E = \sum_i e_i , \qquad X = \frac{\sum_i x_i e_i}{E} , \tag{EQ 54}$$

where e_i and x_i are energy and position of the crystal i, and where the sum runs over all the crystals in the cluster. These simple estimators, as we will se, are appropriate for the electron identification. A more precise estimator of the electron energy will be studied in next sections.

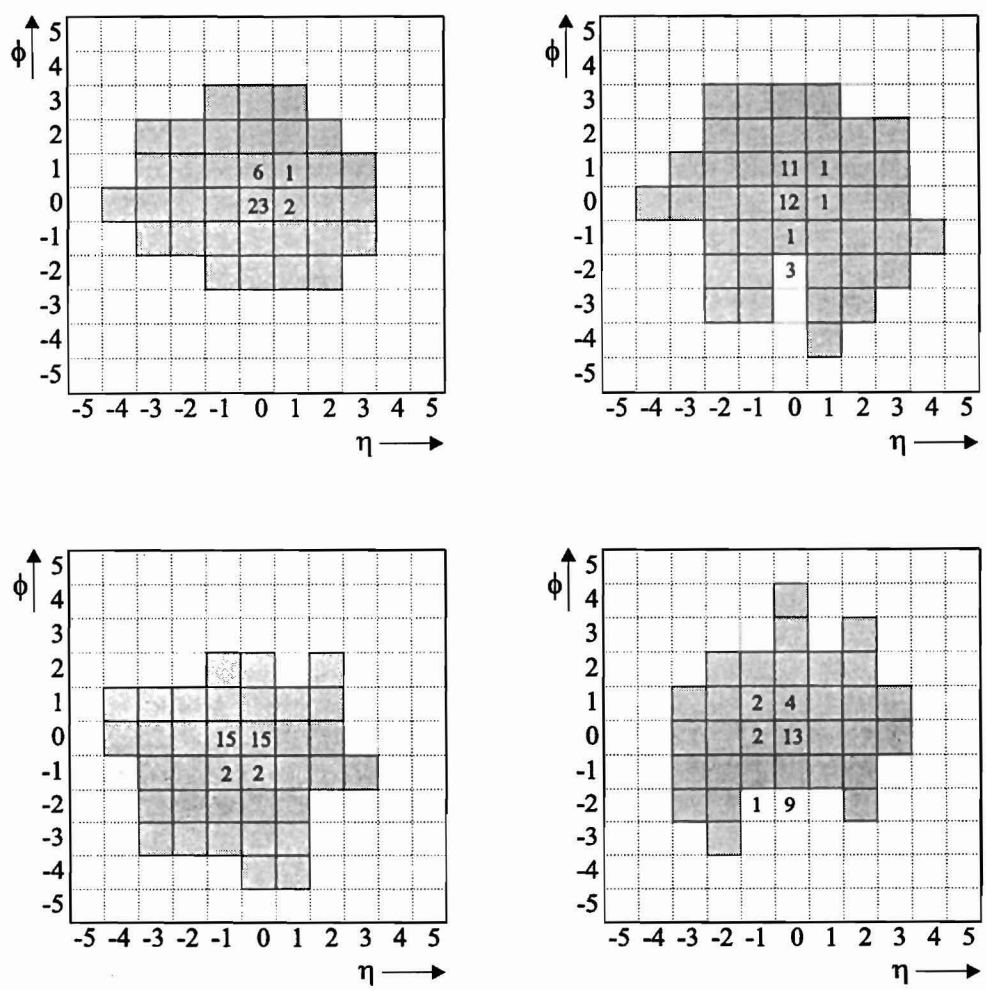

FIGURE 94. A few typical events with reconstructed electromagnetic clusters using the dynamical clustering algorithm. Numbers represents energy deposit for crystals with $E > 1$ GeV.

5.5 Bremsstrahlung photons recovery method

5.5.1 Electron kinematics

The bremsstrahlung recovery algorithm will exploit kinematical characteristics of the bremsstrahlung process.

Neglecting the multiple scattering and ionization losses[1], the charged particle trajectory in a uniform magnetic field $\vec{B} = (0, 0, B_z)$ is a helix, with the equations of motion given by

$$\begin{aligned} x(t) &= x_0 + \frac{\sin(kt + \varphi_0) - \sin\varphi_0}{k} \\ y(t) &= y_0 - \frac{\cos(kt + \varphi_0) - \cos\varphi_0}{k}, \\ z(t) &= z_0 + ct \end{aligned} \qquad \text{(EQ 55)}$$

where (x_0, y_0, z_0) is the vertex, t is the radial trajectory length measured from vertex, φ_0 is the tangent angle in the transverse plane at $t = 0$, $c = p_z/p_T$ and $k = 1/\rho$. ρ is the curvature radius in the transverse plane given by

$$\rho(\text{cm}) = \frac{p_T}{0.003 \cdot B_z}, \qquad \text{(EQ 56)}$$

with p_T in GeV and B in Tesla. In the CMS tracker cavity, in the uniform approximation one has $B_z = 4$ Tesla.

In the transverse plane, the trajectory is an arc of circle. For an electron coming from the origin of the coordinates system, with direction along the x axis, one has

$$\begin{aligned} (x_0, y_0, z_0) &= (0, 0, 0) \\ \varphi_0 &= 0 \end{aligned} \qquad \text{(EQ 57)}$$

and the circle can be written as

$$r^2 = x^2 + y^2 = 2y\rho. \qquad \text{(EQ 58)}$$

In absence of the bremsstrahlung, an electron would reach the electromagnetic calorimeter at

$$y^e_{\text{no brem}} = \frac{R^2_{\text{ECAL}}}{2\rho}, \qquad \text{(EQ 59)}$$

where R_{ECAL} is the transverse radius of the crystals front face ($R_{\text{ECAL}} \approx 129$ cm in the barrel). A bremsstrahlung photon emitted at a transverse radius $r = r_\gamma$ and taking a fraction $1 - \alpha$ of the electron momentum propagates along the tangent to the electron trajectory and reaches the calorimeter at

1. Which is a quite adequate approximation in the presented study.

$$y_\gamma = \frac{r_\gamma^2 + 2r_\gamma(R_{\mathrm{ECAL}} - r_\gamma)}{2\rho} = \frac{R_{\mathrm{ECAL}}^2 - (R_{\mathrm{ECAL}} - r_\gamma)^2}{2\rho}. \qquad \text{(EQ 60)}$$

The electron trajectory after the bremsstrahlung photon emission is given by

$$y = \frac{1}{2\rho\alpha} r^2 + br + c. \qquad \text{(EQ 61)}$$

At $r = r_\gamma$ the electron direction is unchanged, yielding

$$b = \frac{r_\gamma}{\rho}\left(1 - \frac{1}{\alpha}\right), \qquad c = -\frac{r_\gamma^2}{2\rho}\left(1 - \frac{1}{\alpha}\right), \qquad \text{(EQ 62)}$$

and the electron having emitted a bremsstrahlung photon reaches the calorimeter at

$$y^e_{\text{with brem}} = \frac{R_{\mathrm{ECAL}}^2 - \left(1 - \frac{1}{\alpha}\right)(R_{\mathrm{ECAL}} - r_\gamma)^2}{2\rho}. \qquad \text{(EQ 63)}$$

From the above equations we can deduce

$$y^e_{\text{no brem}} = (1 - \alpha) \cdot y_\gamma + \alpha \cdot y^e_{\text{with brem}} = y_{\text{barycenter}}, \qquad \text{(EQ 64)}$$

showing that the barycenter of the electron and bremsstrahlung photon positions is the position the electron would have reached if it had not emitted a bremsstrahlung, and

$$\alpha = \frac{y_\gamma - y_{\text{barycenter}}}{y_\gamma - y^e_{\text{with brem}}}, \qquad \text{(EQ 65)}$$

showing that the fraction of energy remaining to the electron is given by the fractional distance between the bremsstrahlung photon and the barycenter position. These two important properties will be used in section 5.5.3 to improve the electron identification in presence of bremsstrahlung radiation.

The kinematics of the bremsstrahlung process is illustrated in figure 95.

Another important kinematical aspects is the distribution of electrons impact angles at the electromagnetic calorimeter. Indeed to reduce the influence of the intercrystal cracks in calorimetric measurements, the design of the calorimeter is such that photons and infinite momentum electrons originating from the interaction point enter the crystals with an angle of about 3° with respect to the crystal axis, both in η an ϕ directions.

The interaction vertex smearing of about 5.3 cm in z direction at LHC gives an RMS of the distribution of this angles in η plane of about 1.6^o, for electrons in the barrel. In the ϕ plane the vertex uncertainty is about 15 μm, resulting in a negligible width of the impact angle distribution. But, because of the curvature of the electron trajectory in the magnetic field, electrons impact angles in the ϕ plane depend on the transverse momentum. In absence of bremsstrahlung, the angle between the electron at ECAL impact point and the line connecting the vertex and that point is given by:

$$\delta = \operatorname{asin}\left(\frac{R_{\mathrm{ECAL}}}{2\rho}\right). \qquad \text{(EQ 66)}$$

In the case of bremsstrahlung this angle is always bigger. Figure 96 shows the impact angles, in the ϕ plane, at ECAL entrance for electrons and positrons as a function of their transverse energy.

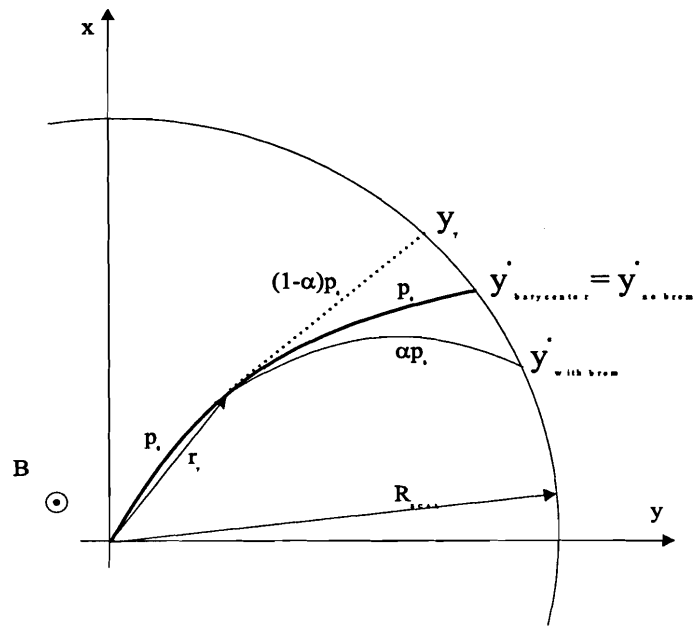

FIGURE 95. Kinematics of the electron bremsstrahlung process in the uniform magnetic field.

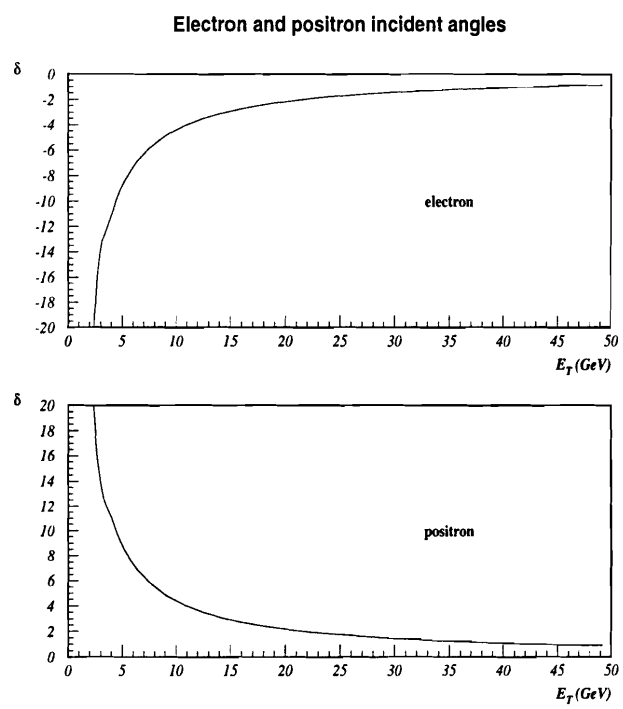

FIGURE 96. Angles between electrons (positrons) direction at the ECAL impact point and the vertex line as a function of their transverse energy.

In addition, the mechanical design of the ECAL barrel is such that the two half barrels (positive and negative z) are rotationaly symmetric with respect to the y axis. Hence, there is a 6° difference in the ϕ plane angles between the axis of the crystals at opposite η positions. An electron of about 15 GeV p_T and $\eta > 0$, and a positrons with the same transverse momentum and negative pseudorapidity, will enter the electromagnetic calorimeter in a direction about parallel to the crystal axis, therefore parallel to the cracks, resulting in a possible deterioration of the electron energy measurement [84].

5.5.2 Method and results

As we have seen, the kinematics of the bremsstrahlung process allows to predict where to search for radiated photon clusters, starting from an electron cluster. If the photon is separated enough and has enough energy to create a separate cluster it is possible to associate them to the electron one. In this section we will show a generic performances of the bremsstrahlung photon recovery algorithm, and in section 5.5.3 we will extend it to increase its efficiency in case of hard bremsstrahlung emission.

The presented results corresponds to $p_T = 10$ GeV and $p_T = 30$ GeV electrons generated in the ECAL barrel acceptance. The electron clusters have been identified in what follows using the true Monte Carlo information, in order to extract intrinsic properties of the bremsstrahlung photon recovery method.

The recovery algorithm consists of two main steps [83]:

1. From the reconstructed transverse energy of the electron electromagnetic cluster (E_T^e) one can define the maximum azimuthal distance between the electron and the radiated photon, given by

$$\Delta\phi_{max} = \mathrm{atan}\left(\frac{-\frac{R_{\mathrm{ECAL}}}{2q\rho}}{\sqrt{1-\left(\frac{R_{\mathrm{ECAL}}}{2q\rho}\right)^2}}\right), \qquad \text{(EQ 67)}$$

where

$$\rho(\mathrm{cm}) = \frac{E_T^e}{0.003B}, \qquad \text{(EQ 68)}$$

is the radius of the electron trajectory in the transverse plane, with E_T^e in GeV. R_{ECAL} is the transverse radius of the crystal front face, and q is the electron charge. $\Delta\phi_{max}$ corresponds to the azimuthal distance between the electron and a photon radiated at transverse radius $r = 0$ cm. It therefore represents the maximal distance between the electron and a radiated photon. For the calculation of $\Delta\phi_{max}$ we use the ECAL energy measurement, which provides a better estimate of the electron momentum at ECAL impact than the reconstructed track. For photons emitted at non zero transverse radius, the impact points have to be searched for in a ϕ road between 0 and $\Delta\phi_{max}$. In figure 97 the $\Delta\phi_{max}$ is plotted as a function of the measured electron transverse energy. One can see that for $E_T^e = 10$ GeV, the maximal azimuthal distance is of the order of 5 crystals, going down to

about 1 crystals at $E_T^e = 50$ GeV. The kinematics of the bremsstrahlung process is such that the pseudorapidity distance of the electron and photon at ECAL entrance is equal to 0.

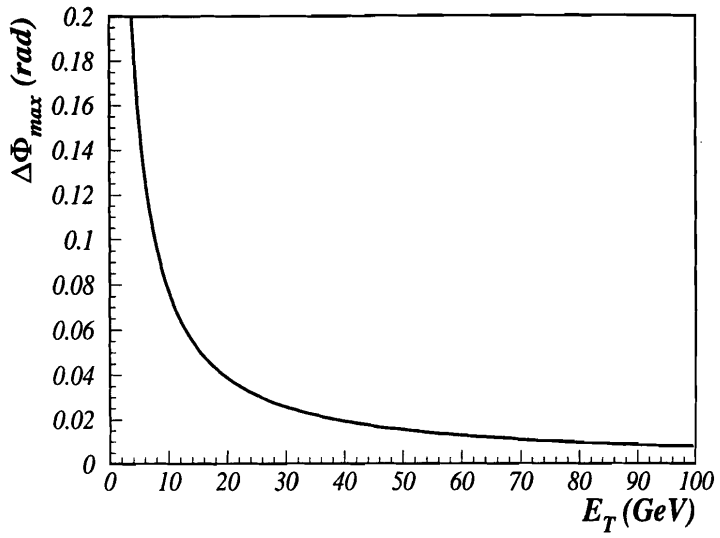

FIGURE 97. Maximal azimuthal distance between an electron and a radiated photon cluster, corresponding to the case of a photon radiated at zero transverse radius.

2. Having determined $\Delta\phi_{max}$, the search for photon clusters is performed. The clusters, with reconstructed values $(E^\gamma, \eta^\gamma, \phi^\gamma, M^\gamma)$ for energy, pseudorapidity, azimuthal angle and cluster multiplicity, respectively, are attached to the electron cluster if they satisfy the following criterion:

$$\begin{aligned} \eta^\gamma &\in [\eta^e - \Delta\eta, \eta^e + \Delta\eta] \\ \phi^\gamma &\in [\phi^e - \Delta\phi, \phi^e + \Delta\phi_{max} + \Delta\phi], \\ M^\gamma &> M_{thr} \end{aligned} \qquad \text{(EQ 69)}$$

where (η^e, ϕ^e) are the pseudorapidity and azimuthal angle of the electron cluster and M_{thr} is a cluster multiplicity threshold. $\Delta\eta$ and $\Delta\phi$ are tolerances aimed to account for the use of simple barycenter as cluster position estimate, without corrections. We have used a value of 0.0175, corresponding to one crystal width, for both $\Delta\eta$ and $\Delta\phi$. To minimize the noise contribution we have used $M_{thr} = 1$.

The figure 98 shows the position in $\eta - \phi$ plane of secondary clusters with respect to the electron cluster for 10 GeV p_T electrons. The localization of bremsstrahlung impact in pseudorapidity is clear. The central hole where no secondary clusters can be separated is the consequence of the extension of the electron clusters. The distributions on the right show the clusters recovered using the described procedure. The mean multiplicity of electron plus recovered clusters is about 35. The same results for 30 GeV p_T electrons are presented in figure 99. One can notice a higher bremsstrahlung activity with increasing electron energy, but with smaller distance between electron and photon clusters, as expected. The mean multiplicities of electron plus photon clusters, for 30 GeV p_T electrons, is about 43.

The results of the recovery algorithm, in terms of energy of the reconstructed electron clusters only and of the electron plus photons, normalized to the generated electron energy, are shown in figure 100, for both 10 and 30 GeV p_T electrons. In order to compare these distribution we define an effective RMS as the half width around maximum containing 68.3% of the distribution. It is illustrated in figure 101. The gain with the recovery method is clearly visible and expressed in terms of effective RMS as well as 2σ and 3σ efficiencies are shown in table 7.

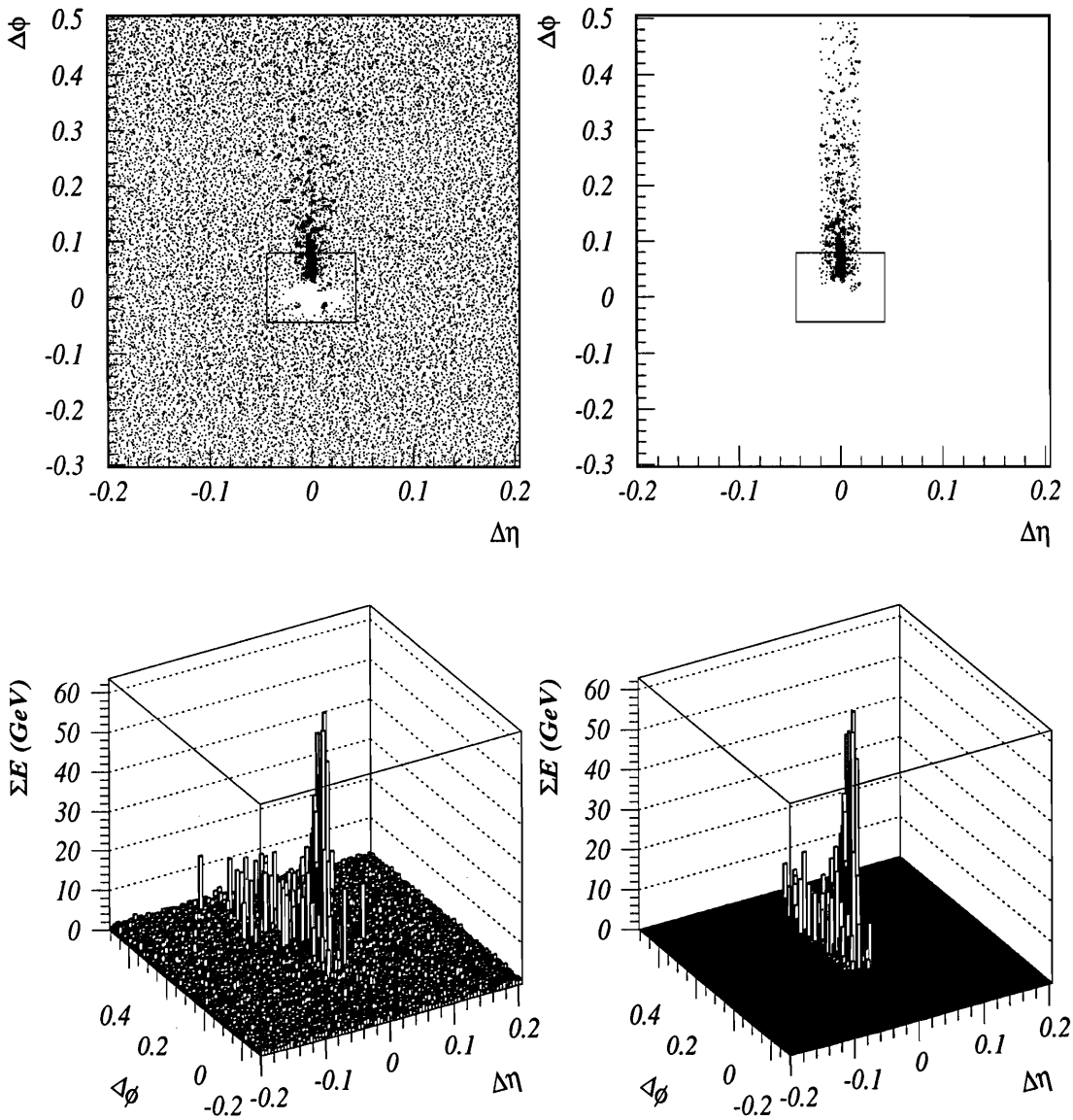

FIGURE 98. Position of the secondary clusters in $\eta - \phi$ plane reconstructed using dynamical clustering algorithm (left). Position of recovered cluster using bremsstrahlung photon recovery method (right). The figures corresponds to 10 GeV p_T electrons in barrel and cumulate 1000 generated electrons.

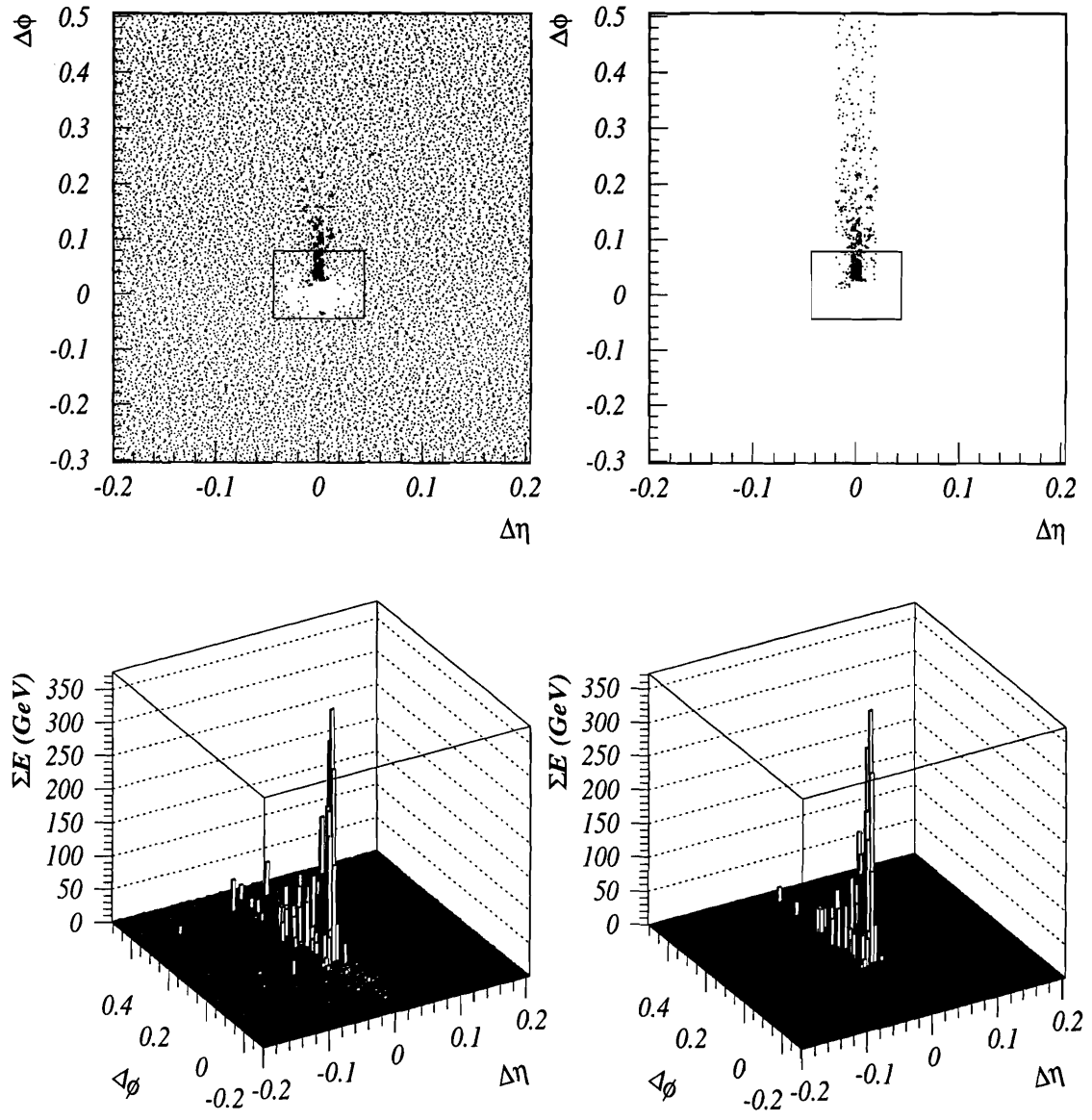

FIGURE 99. The same as figure 98 for 30 GeV p_T electrons in barrel.

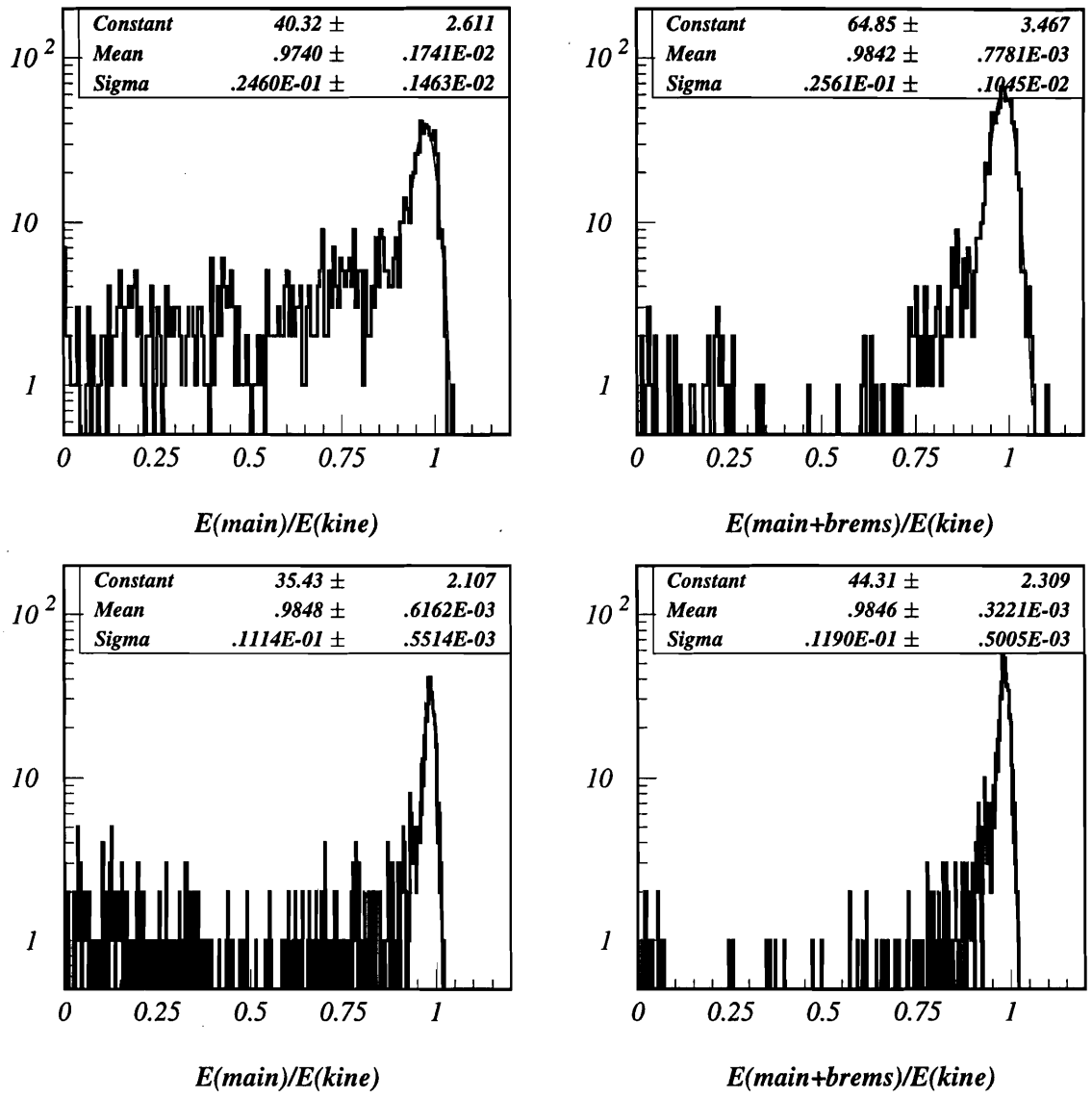

FIGURE 100. Reconstructed energy distribution for 10 GeV (up) and 30 GeV (down) p_T electrons without (left) and with (right) bremsstrahlung photon recovery. The energy is estimated as the crystals energy sum. The few events with $E \approx 0$ correspond to cases where the electron radiates a very hard photon at the beginning if its trajectory and never reach the ECAL.

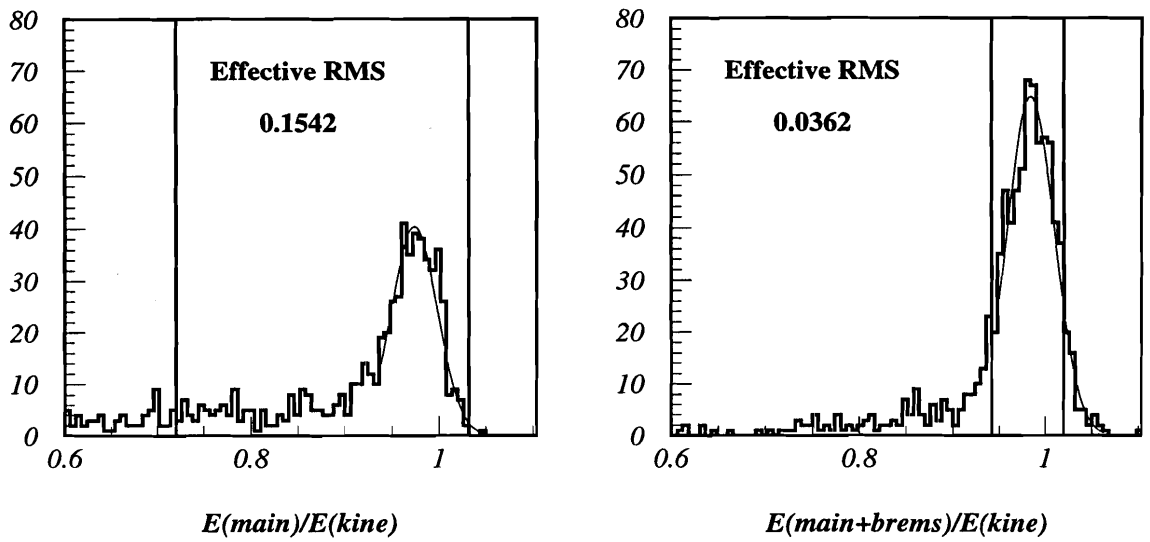

FIGURE 101. An illustration of the effective RMS, defined as the half width of the window around maximum containing 68.3% of the distribution. The distance between vertical lines corresponds to $2 \cdot RMS_{eff}$. The distributions are for 10 p_T GeV electrons.

		RMS_{eff}	2σ efficiency	3σ efficiency
p_T = 10 GeV	no brems recov.	0.154	0.45	0.50
	brems recov.	0.036	0.75	0.82
p_T = 30 GeV	no brems recov.	0.0665	0.53	0.59
	brems recov.	0.0208	0.69	0.77

TABLE 7. Effective RMS, 2σ and 3σefficiency for 10 GeV and 30 GeV E_T electrons without and with bremsstrahlung photon recovery.

5.5.3 Hard bremsstrahlung photons recovery

In the previous section, for the electron cluster identification we have used the GEANT informations. The electron cluster have been chosen as the closest to the electron ECAL impact point extracted from GEANT. In reality, the cluster belonging to the electron is determined through the cluster-track matching procedure. As we will show, the usual matching procedure of comparing each cluster with each track should be modified to be able to deal with the case of hard bremsstrahlung, taking into account all possible electron plus bremsstrahlung photons clusters combinations in the matching procedure.

In this section we will present two algorithms, called 'simple' and 'fit' matching algorithms. In the simple matching algorithm the electron cluster is determined as the cluster with the best χ^2 in ϑ, ϕ and *E/p* in a cone of $\Delta R = 0.1$ around the track extrapolation to ECAL, and having an *E/p* matching ratio greater than 0.2. Figure 102 presents the phi distance between the electron cluster and the track extrapolation to ECAL as a function of *E/p* ratio, using this algo-

rithm, for both 10 and 30 GeV p_T electrons. In addition to well matched electrons, there are two populations with bad *E/p* matching, one correlated with increasing phi distance, and another with negative phi distance. The first population with bad *E/p* matching corresponds to the cases for which the electron cluster is correctly assigned, with a certain amount of the original electron energy radiated as bremsstrahlung photons. The more the radiated photon takes energy, the more distant is the electron cluster from the track extrapolation. The population with bad *E/p* matching and negative phi distance corresponds to the cases where the track is wrongly assigned to the photon, rather than to the electron cluster. This happens when photons takes more than a half of the electron energy and thus both populations have $E/p > 0.5$. Also shown in figure 102 is the distribution of the transverse energy of the cluster associated to the track, without and with bremsstrahlung recovery method, described in the section 5.5. The improvement using the recovery method is evident, but still some low energy tail remains, due to the cases of hard bremsstrahlung, when the photon cluster is wrongly associated to the track. As expected these effects are more important for lower electron transverse momentum.

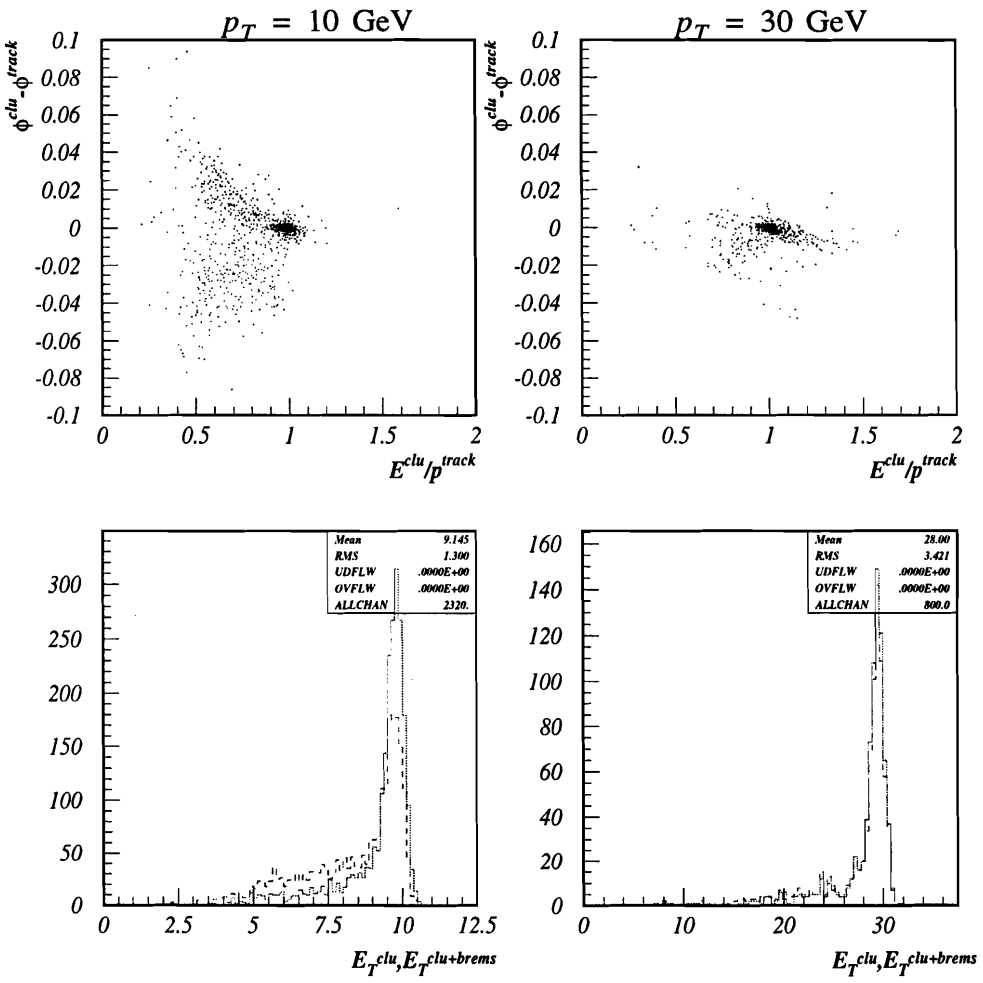

FIGURE 102. Phi distance between cluster and associated track vs. *E/p* for simple matching algorithm (up), and the cluster transverse energy without and with brems recovery (down), for 10 GeV (left) and 30 GeV (right) p_T electrons generated in the barrel acceptance.

To better understand this problem of electron misidentification, it is instructive to look at the distribution of the transverse position of the outermost measured track hit. As already mentioned, the tracks reconstruction starts from the pixel layers and goes outward, propagating track from layer to layer while a hit in the vicinity of extrapolated point is found. The distribution of the last found hit transverse position is shown in figure 103, for both 10 and 30 GeV p_T electrons. One can see that a significant fraction of the tracks is not reconstructed up to the outermost tracker layer (≈ 120 cm). This comes from hard bremsstrahlung, where the change of curvature is such that the track finding algorithm fails to find the hit following the emission point. In the cases of very hard bremsstrahlung for which the photon takes more than half of the electron energy, the track is even better matched with the photon cluster, both geometrically and in momentum, but the bremsstrahlung recovery goes in wrong direction.

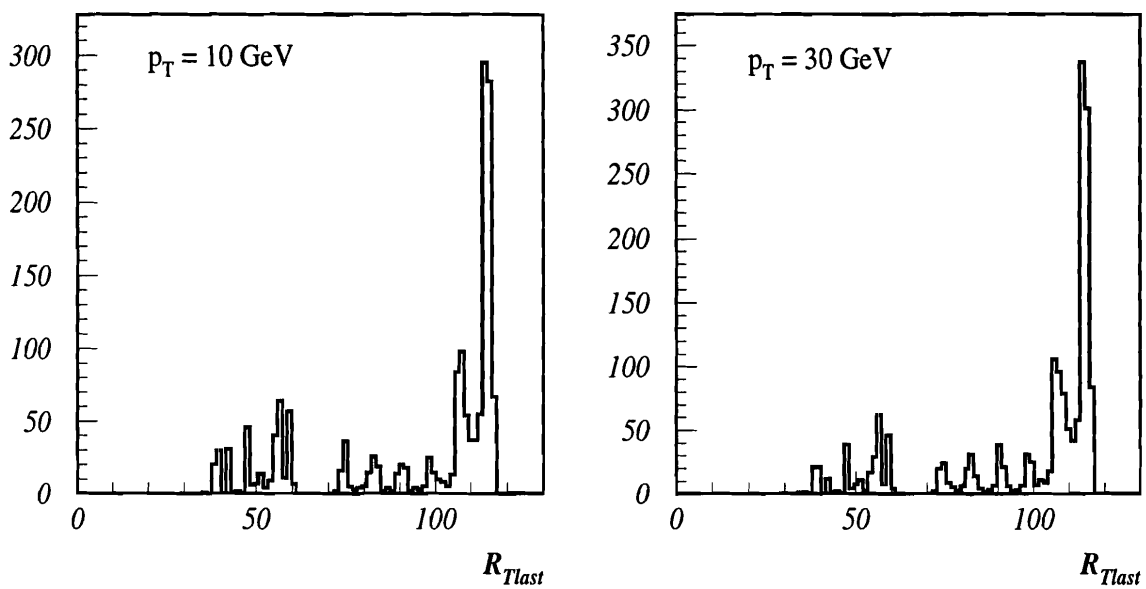

FIGURE 103. Transverse radius of the outermost track hit found by the track finding algorithm (left).

In order to better match electron clusters and tracks we have developed a procedure which consists of the two following steps:

1. All clusters in a road along ϕ axis around the track extrapolation and up to $\Delta\phi = \pm 0.1$ are considered as electron clusters candidates. These clusters are sorted in decreasing phi order (charge -1 case). Starting from each cluster taken in turn as electron cluster, the bremsstrahlung search is performed taking the ϕ road size and direction from the cluster measured transverse energy and the track charge. At the end of this step a set of electron plus bremsstrahlung clusters is defined.
2. The best set is obtained by minimizing a χ^2 in terms of two quantities:
   - the distance between track extrapolation and energy weighted average of the clusters position ($y_{\text{barycenter}}$ in the equation 64),
   - the distance between E/p and the fraction of energy remaining to the electron, with E given by the electron cluster candidate (α in the equation 65).

Figure 104 shows the ϕ and the E/p distances for all electron plus bremsstrahlung photon clusters sets and the same distributions for the selected ones, for 10 GeV p_T electrons in whole ECAL acceptance. In figure 105 the same is shown for 30 GeV p_T electrons.

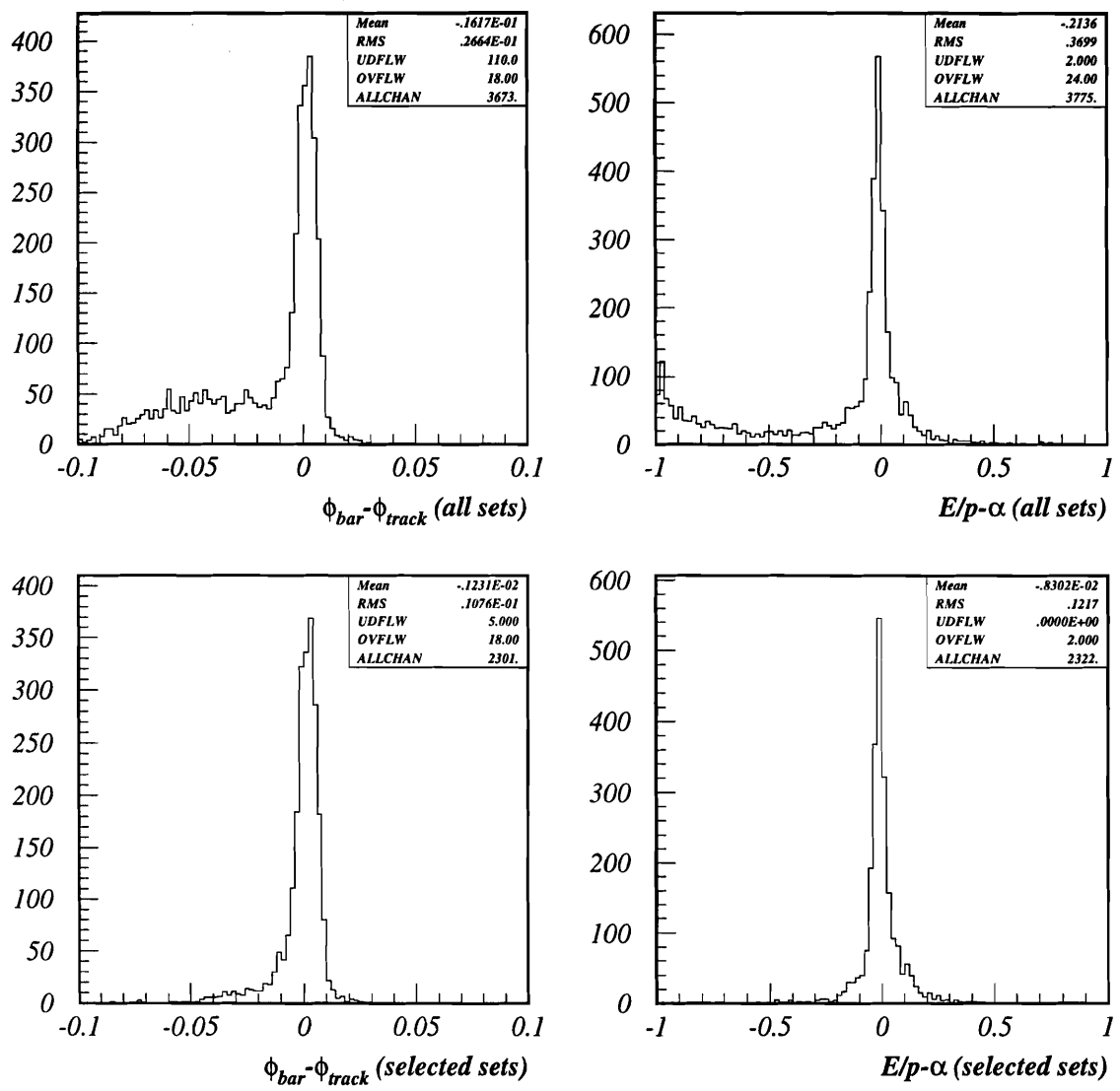

FIGURE 104. Distributions of the ϕ and the $E/p - \alpha$ distances for all sets electron plus bremsstrahlung photon clusters (top) and the same distributions for the selected ones (bottom), for 10 GeV p_T electrons.

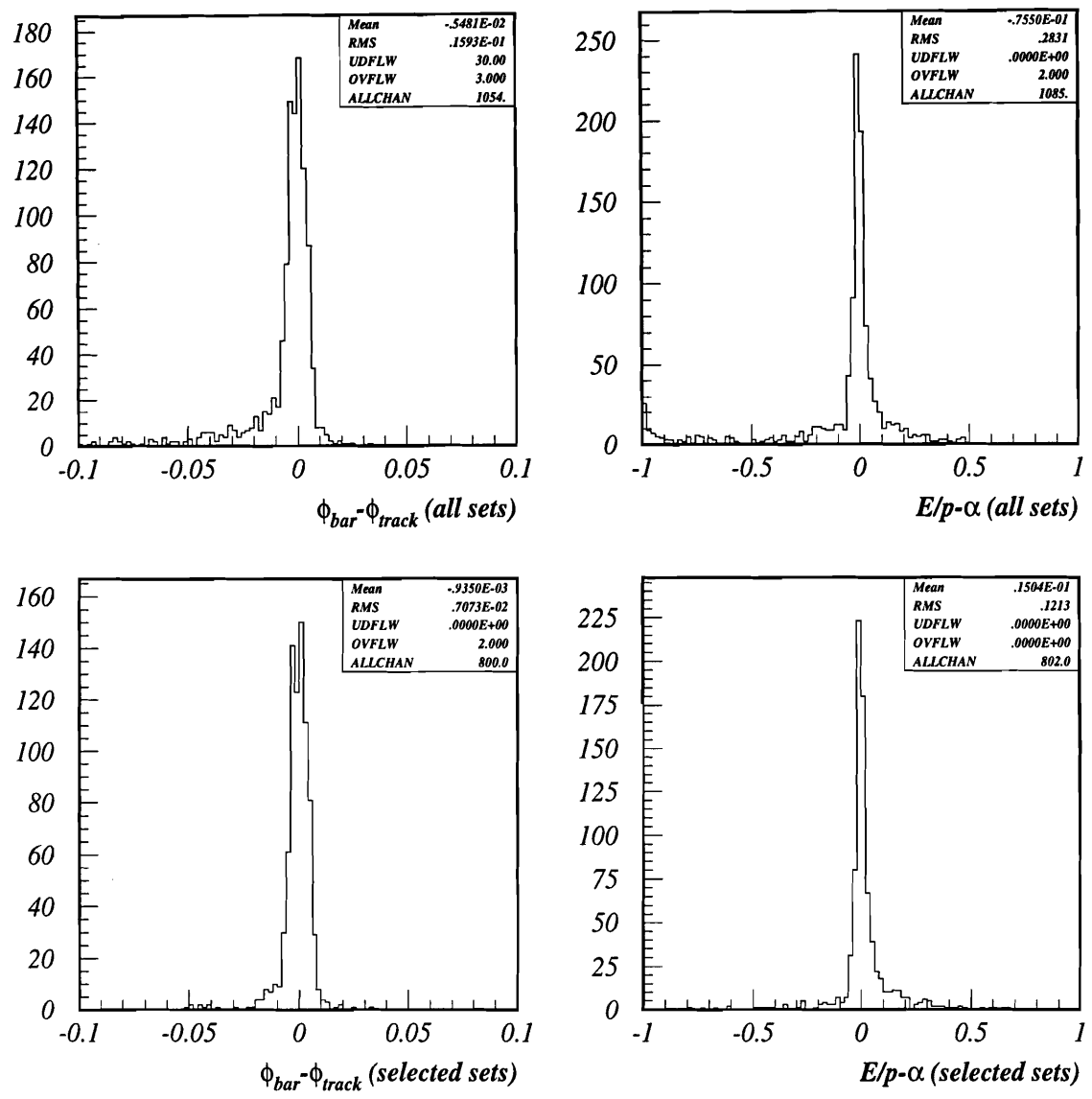

FIGURE 105. The same as on figure 104 for 30 GeV p_T electrons.

To compare this algorithm with the simple matching one, in figure 106 we show the phi distance between barycenter of matching clusters and extrapolated tracks versus *E/p* ratio. Comparing with the same distributions in figure 102, one can see that the population corresponding to the photon cluster wrongly identified as electron have moved from negative to positive $\Delta\phi$. Since the electron cluster is now properly identified, the electron cluster energy to track momentum ratio is now lower than 0.5. The distribution of the electron cluster transverse energy and electron plus bremsstrahlung photon clusters recovered are also shown on figure 105. Both a gain with respect to the electron energy only and with respect to the simple matching algorithm are visible. The efficiencies as the fractions of events within $E/p \pm 0.2$ are given in table 8.

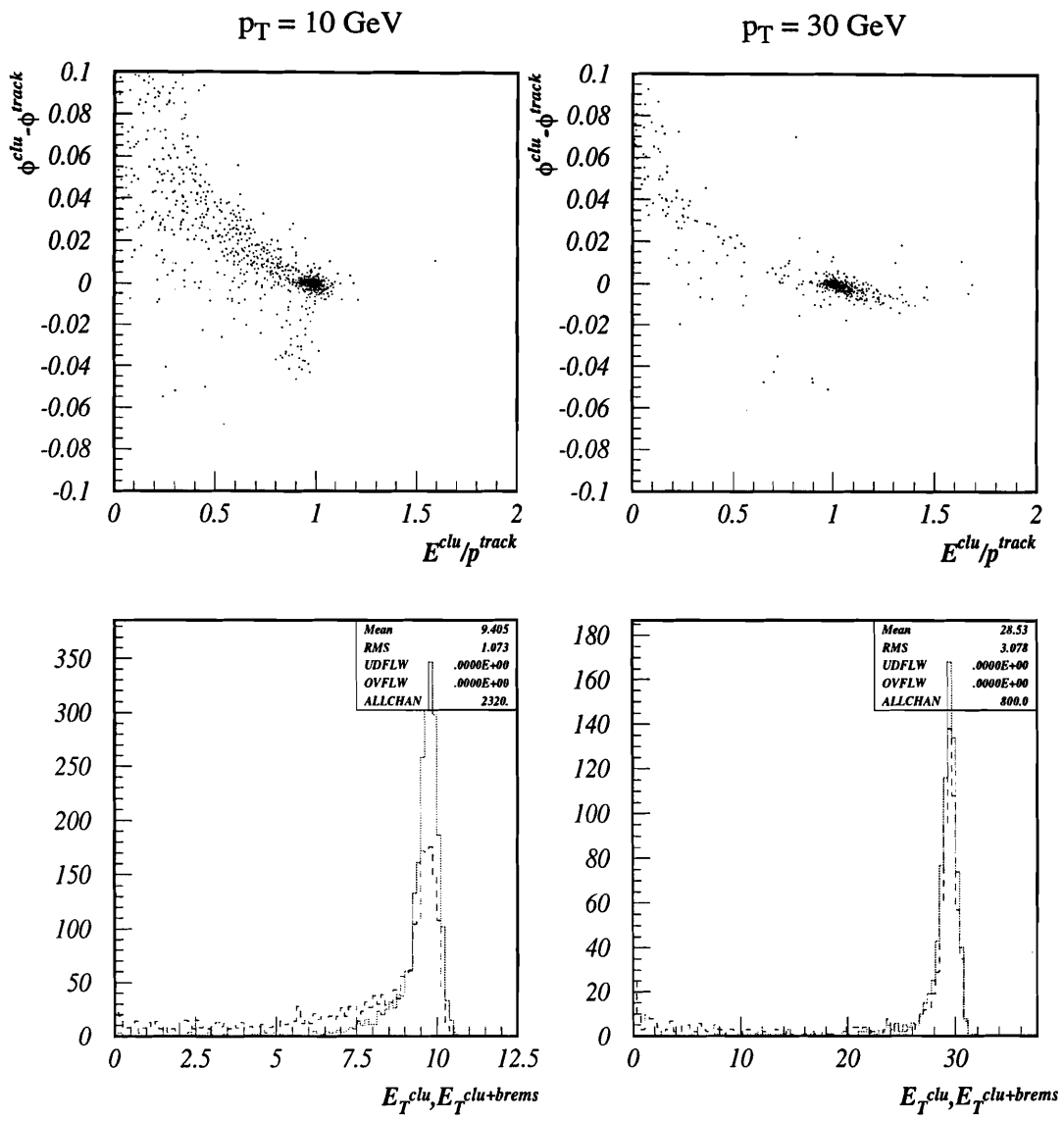

FIGURE 106. Phi distance between cluster and associated track versus *E/p* for fit matching algorithm (top), and the cluster transversal energy without and with recovered photon clusters (bottom), for 10 GeV (left) and 30 GeV (right) p_T electrons generated in the barrel acceptance.

$\varepsilon(E/p \pm 0.2)$	p_T = 10 GeV	p_T = 30 GeV
simple	86.4%	90.8%
fit	94.4%	95.8%

TABLE 8. The fraction of events within $E/p \pm 0.2$ for 10 and 30 GeV p_T electrons with simple and fit clusters-track matching algorithms.

5.6 Electron momentum estimation

In the section 5.4 we have presented the dynamical clustering algorithm which allows to construct the set of crystals following the event by event variations of the particle impact position and direction. However, corrections are still needed to account for small residual lateral leakage. In addition, an estimator of the particle energy as a sum of all the crystals energies is not optimal with respect to the noise contribution. Assuming that we can predict the mean expected energy in each crystal, another estimator can be constructed which will correct for the lateral leakage and will treat properly the noise contribution. This will be the subject of this section. To predict the shower energy deposit in each crystal the track impact point and direction at ECAL entrance and a shower model are necessary. For the impact position and the direction we will use the track extrapolation to the calorimeter and a shower parametrization will be used as the shower model.

Having optimized the energy estimate in the ECAL we will combine it with the tracker momentum estimation to construct a final electron momentum estimator.

5.6.1 Weighting method

5.6.1.1 Method description

The simplest estimator of the energy deposited by the particle in the electromagnetic calorimeter is given by the sum of the energies measured by the crystals (e_i) belonging to the cluster associated to the particle:

$$E_s = \sum_i e_i. \qquad \text{(EQ 70)}$$

In what follows we will call this estimator the *'cluster energy sum'*. Its variance is given by

$$\sigma^2_{E_s} = \sum_{i,j} cov(e_i, e_j) = \sum_{i,j} \sigma_{e_i}\sigma_{e_j}\rho_{ij}, \qquad \text{(EQ 71)}$$

where ρ_{ij} are the correlation coefficients.

The variance of the cluster energy sum estimator has a significant contribution from the noise. Adding N crystals with the noncorrelated noise σ_{noise} contributes to

$$\sqrt{N}\sigma_{noise} \qquad \text{(EQ 72)}$$

to the variance of this estimator. The mean multiplicity of the electromagnetic clusters is about 25 (35) for the electron cluster only and about 35 (43) for the electron plus bremsstrahlung photons clusters, for 10 (30) GeV p_T electrons. Therefore, for the expected energy resolution of the CMS electromagnetic calorimeter, the noise dominates the resolution for energies smaller than about 20 GeV.

Another energy estimator can be constructed in the following way: for a given impact position and direction every crystal in which the particle deposits a fraction (f_i) of its energy gives an estimator ($\tilde{E}_i$) of the total particle energy:

$$\left\{\tilde{E}_i = \frac{e_i}{f_i}\right\} \quad i = 1, \ldots, n, \tag{EQ 73}$$

where e_i is the measured energy in the ith crystal. The optimal combination of these estimators is given by the weighted sum:

$$\tilde{\mathrm{E}} = \sum_{i=1}^{n} w_i' \tilde{E}_i = \sum_{i=1}^{n} w_i' \frac{e_i}{f_i} = \sum_{i=1}^{n} w_i e_i, \tag{EQ 74}$$

where w_i is the weight of the ith crystal. The requirement of having an unbiased estimator $\langle \tilde{\mathrm{E}} \rangle = E$, leads to the constraint:

$$\sum_i w_i f_i = 1. \tag{EQ 75}$$

The variance of the estimator $\tilde{\mathrm{E}}$ is given by

$$\sigma^2_{\tilde{\mathrm{E}}} = \sum_{i,j} w_i w_j cov(e_i, e_j). \tag{EQ 76}$$

The weights are obtained by minimizing the variance with constraint introduced by the Langrange multiplier:

$$\Theta = \sigma^2_{\tilde{\mathrm{E}}} + 2\lambda\left(\sum_i w_i f_i - 1\right). \tag{EQ 77}$$

Minimization with respect to w_i gives:

$$\frac{\partial \Theta}{\partial w_i} = 2 w_i cov(e_i, e_i) + \sum_{i \neq j} w_j (cov(e_i, e_j) + cov(e_j, e_i)) + 2\lambda f_i = 0, \tag{EQ 78}$$

which can be expressed in a matrix form

$$SW = -\lambda F \Rightarrow W = -\lambda S^{-1} F, \tag{EQ 79}$$

with

$$W = \begin{bmatrix} w_1 \\ w_2 \\ \ldots \\ w_n \end{bmatrix} \qquad S = \begin{bmatrix} \sigma_1^2 & \sigma_1\sigma_2\rho_{12} & \ldots & \sigma_1\sigma_n\rho_{1n} \\ \sigma_1\sigma_2\rho_{12} & \sigma_2^2 & \ldots & \sigma_2\sigma_n\rho_{2n} \\ \ldots & \ldots & \ldots & \ldots \\ \sigma_1\sigma_n\rho_{1n} & \sigma_2\sigma_n\rho_{2n} & \ldots & \sigma_n^2 \end{bmatrix} \qquad F = \begin{bmatrix} f_1 \\ f_2 \\ \ldots \\ f_n \end{bmatrix}. \tag{EQ 80}$$

Using the equation 75, written in the matrix form as $F^T W = 1$, from relation 79 one obtain:

$$\lambda = -\frac{1}{F^T S^{-1} F}. \tag{EQ 81}$$

Therefore, the weights are:

$$W = \frac{S^{-1}F}{F^T S^{-1} F}. \qquad \text{(EQ 82)}$$

In the case of a diagonal covariance matrix S (i.e. $\rho_{ij} = 0, i \neq j$), the weights become:

$$w_i = \frac{1}{\sum_{j=1}^{n} \frac{f_j^2}{\sigma_j^2}} \cdot \frac{f_i}{\sigma_i^2}. \qquad \text{(EQ 83)}$$

Moreover, for variances being parametrized as

$$\sigma_i = a\sqrt{\varepsilon_i} = a\sqrt{p_{inc} f_i}, \qquad \text{(EQ 84)}$$

where ε_i is the expected energy and p_{inc} is the electron momentum at ECAL entrance, all weights are the same and equal to:

$$w_i = \frac{1}{\sum_{j=1}^{n} f_i}, \qquad \text{(EQ 85)}$$

and the energy estimator becomes:

$$\tilde{E}_{sw} = \frac{\sum_{i=1}^{n} e_i}{\sum_{j=1}^{n} f_j}. \qquad \text{(EQ 86)}$$

In a general case, the weights are functions of the expected fractions and covariance matrix,

$$w_i = f(f_1, f_2, \ldots, f_n, \sigma_1, \sigma_2, \ldots, \sigma_n, \rho_{12}, \rho_{13}, \ldots, \rho_{nn}), \qquad \text{(EQ 87)}$$

in total $n(n+5)/2$ parameters. But, because of the electromagnetic shower compactness most of informations is contained in a relatively small number of crystals. Thus, one can limit the number of parameters by considering only few crystals. To demonstrate this, the energy resolution for 10 GeV electrons is shown in figure 107 as a function of the cumulated energy fraction. Electrons enter the central crystal in three different points (center, near corner, and near one side on the half height) in the direction of the crystal axis. Every step in the cumulated fraction corresponds to the addition of one crystal. The covariance matrix and expected fractions are extracted from Monte Carlo simulation. We can see that, as the cumulated fraction reach the level of about 90%, the energy resolution improvements when adding more crystals become negligible.

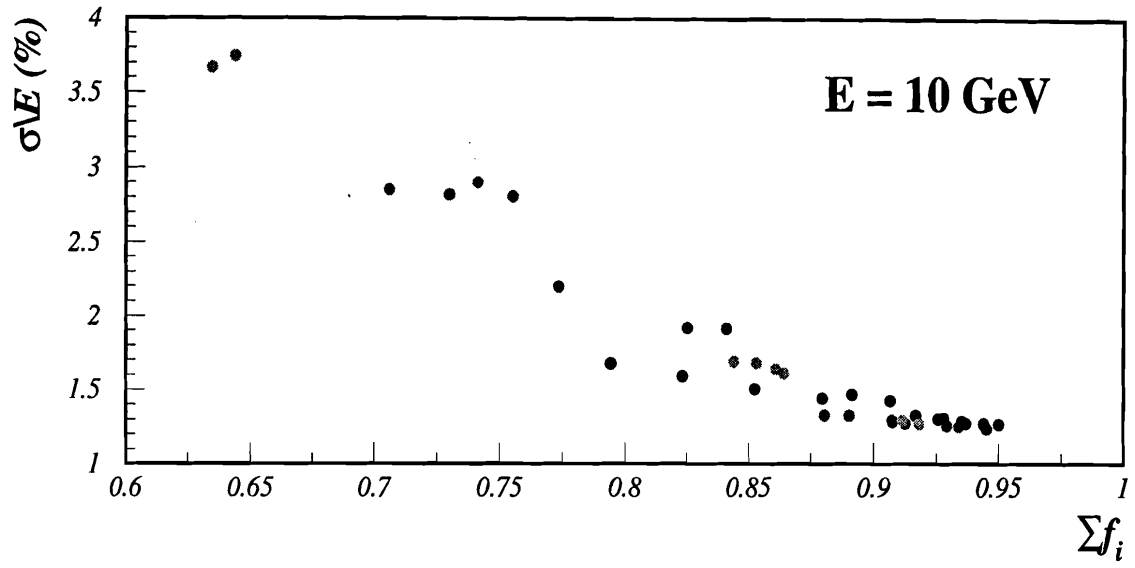

FIGURE 107. Energy resolution as a function of the cumulated energy fraction for 10 GeV electrons, for three different electron impact points. Results are obtained using weighted estimator, with the expected fractions and covariance matrix obtained from the Monte Carlo simulation.

As we have seen, the weights are functions of the expected fractions and of the covariance matrix. The expected fractions will be obtained from shower parametrization, using the extrapolated track momentum to predict the impact position and direction. The covariance matrix, i.e. the covariance and the correlations between crystal energy measurements will be studied in a following section.

5.6.1.2 Shower model

A high energy electron or photon deposits its energy in the electromagnetic calorimeter through a shower development process. The basic physics of this process can be found in [67][85], and references therein. The final results of the showering is the absorption of the incident particle energy. In our implementation of the shower model, the elementary energy deposit points (hits) are generated according to a parametrized shower profile. The mapping of the energy deposition coordinates to readout channels is done using the electromagnetic calorimeter geometry. In what follows we will shortly described the shower parametrization used and the tuning of the parameters, needed to obtain the requested precision of the predicted fractions.

Following reference [86], the shower energy distribution is written as:

$$\frac{d^3E}{dxdydz} = E\frac{dL(z)}{dz}\frac{dT(r,z)}{2\pi r dr}, \qquad \text{(EQ 88)}$$

where z is the shower axis and r is the radial distance from the shower axis. The longitudinal profile is well described according to the standard gamma function:

$$\frac{dL}{dz} = E_{inc}\frac{\beta^{\alpha}}{\Gamma(\alpha)}z^{\alpha-1}e^{-\beta z}, \qquad \text{(EQ 89)}$$

with z in units of radiation length X_0. The parameters α and β are related with the first ($\langle z \rangle$) and second (σ_z) moments of the distributions as

$$\frac{1}{\langle z \rangle} = \frac{\beta}{\alpha} \qquad \frac{\sigma_z^2}{\langle z \rangle^2} = \frac{1}{\alpha}, \qquad \text{(EQ 90)}$$

and are parametrized as a function of the shower energy by linear functions of $\ln E$.

A well known characteristic of the transversal profile is its hard core, followed by a long tail. The parametrization chosen in reference [86] is:

$$\frac{dT(r,z)}{drdz} = a\frac{2(\gamma-1)rR_1^{2(\gamma-1)}}{(r^2+R_1^2)^{\gamma}} + (1-a)\frac{2(\gamma-1)rR_2^{2(\gamma-1)}}{(r^2+R_2^2)^{\gamma}}, \qquad \text{(EQ 91)}$$

where r is in units of Molière radius, $\gamma = 1.70$, and a, R_1 and R_2 are simple functions of $\ln E$ and z. The transversal fluctuations are known experimentally to be very small at high energies and are therefore neglected.

The longitudinal and transversal profiles, generated with the parametrization and obtained with the full Monte Carlo (GEANT) simulations for electron energies from 0.5 to150 GeV are given in figure 108. One can remark a good agreement between both models.

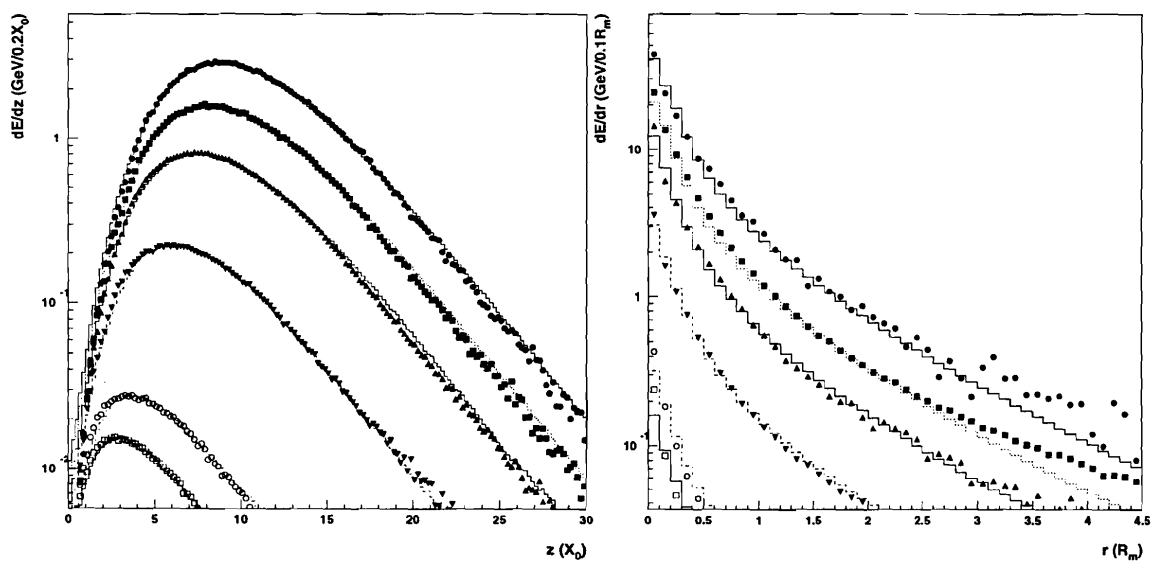

FIGURE 108. $PbWO_4$ longitudinal (left) and transversal (right) shower profiles for 0.5, 1, 10, 40, 80 and 150 GeV electrons from full Monte Carlo simulation (lines) and from the parametrization (symbols) [86].

A fine tuning of the parameters was necessary to use this shower model to provide the expected fractions in each crystal. The first parameter to be optimized is the number of generated points per unit of incident particle energy. In order to limit the effect of the statistical uncertainty to the energy resolution we demand it to be about one order of magnitude smaller than the variance of the energy distribution. This gives a requirement of about 10000 points/ GeV of incident particle energy.

A difference between the expected and measured energy mean values would produce a bias on the weighted estimator. In order to have a negligible influence of such bias to the energy resolution it should be bring to the level of about one order of magnitude smaller than the variance. For a typical variance of about 1.5% at 10 GeV energy, this implies to have an agreement between expected and measured energy mean values of the order of 0.15%. To obtain such degree of agreement we have tuned the shower transversal parametrization by scaling the initial values of R_1, R_2 and a, between 0.9 and 1.1. The parameter R_1 is mostly related to the transversal profile behavior at small transverse radius, while R_2 parametrizes the behavior at bigger transverse radius. The two regions are connected with the parameter a. The difference between the sum of expected and the sum of Monte Carlo mean energies is shown in figure 109 as a function of the scaling factors. We can notice an insensitivity on parameters R_1 and positive correlations between R_2 and a. Minimizing the differences between expected and Monte Carlo values, and repeating the same procedure for several electron impact configurations, we have obtained the following values of the scaling factors:

$$\frac{R_1}{R_1^{inital}} = 1.02; \frac{R_2}{R_2^{initial}} = 1.02; \frac{a}{a^{initial}} = 0.9. \qquad \text{(EQ 92)}$$

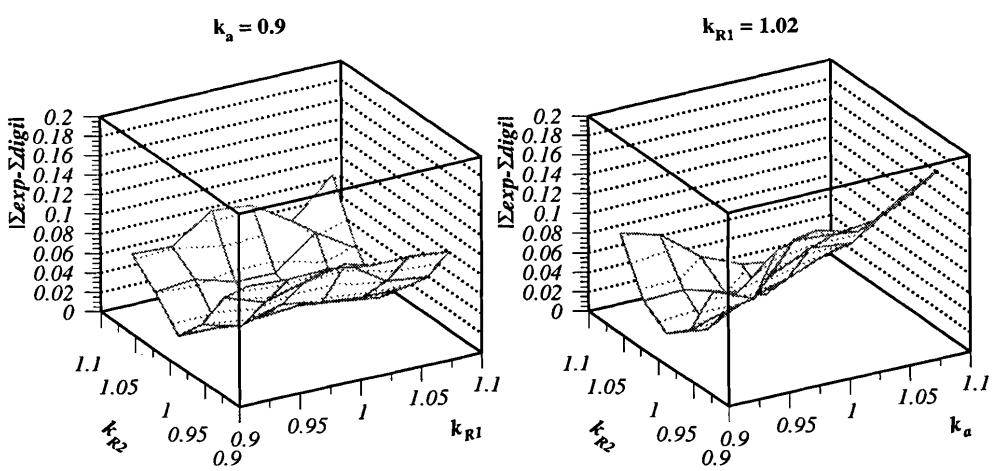

FIGURE 109. Optimization of the shower transversal parameters R_1, R_2 and a. The absolute value of difference of the predicted and the simulated energy sum in 3×3 matrix around the electron impact point is shown as a function of the scaling factors.

Magnetic field effects

In presence of a magnetic field, the shower profile is slightly changed, due to the curling of electrons and positrons in the shower. Although these effects are small, the needed level of precision requires to optimize the shower description accordingly.

The magnetic field effects on the shower profile depend on the angle between the shower axis (i.e. impact particle momentum direction) and the magnetic field direction. To study these effects we have generated events without and with 4 T magnetic field, with electrons entering crystal in the front face barycenter and parallel to its axis, for 3 different pseudorapidities (0.17, 0.85 and 1.24), which corresponds to three different momentum versus magnetic field angles ($80.2°, 46.4°$ and $32.4°$). The fractions of the energy deposited in the 3×3 matrix around the impact crystal are shown in figure 110, separately for central (figure a) and border (figures b, c and d) crystals. There are two important effects to be noticed:

1. With the magnetic field, the enlargement of the shower in the ϕ direction causes a decrease of the energy deposit in the central (figure a) and η neighboring crystals (figure b) and an increase in the ϕ neighboring crystals (figure c). For the crystals in the corners (figure d) these two effects almost compensate and the energy content remains at the same level.
2. The differences between the energy deposits without and with magnetic field decrease with increasing pseudorapidity because of the smaller angle between the magnetic field and the electron directions. The observed small differences in energy content for the corner crystals (figure d) at a given value of the magnetic field are caused by the nonsymmetrical crystals shapes.

To account for these effects in the shower parametrization we have applied a stretching factor in the ϕ direction to the points produced in the shower generation process. This factor has been optimized by minimizing a χ^2 of expected and Monte Carlo deposited energies for all three electron impact configurations. The results are shown in figure 111, together with a straight line fit of the stretching factor with respect to the angle (α) between the electron momentum and the magnetic field direction. The fit gives:

$$B_{factor} = 1 + 0.00232 \cdot \alpha. \qquad \text{(EQ 93)}$$

At the end of this subsection, let us outline two main advantages of the chosen shower model:

- The chosen shower parametrisation is simple, with a small number of relevant parameters which could be relatively easily tuned, as we have just demonstrated. To use this model in the real experiment, the tuning will have to be done on the beam test data or/and selected clean electron samples.
- Since we are interesting only in the prediction of the average energy deposited in crystals, this model is much less CPU time consuming than other models implementing the details of the physical processes (like for example GEANT).

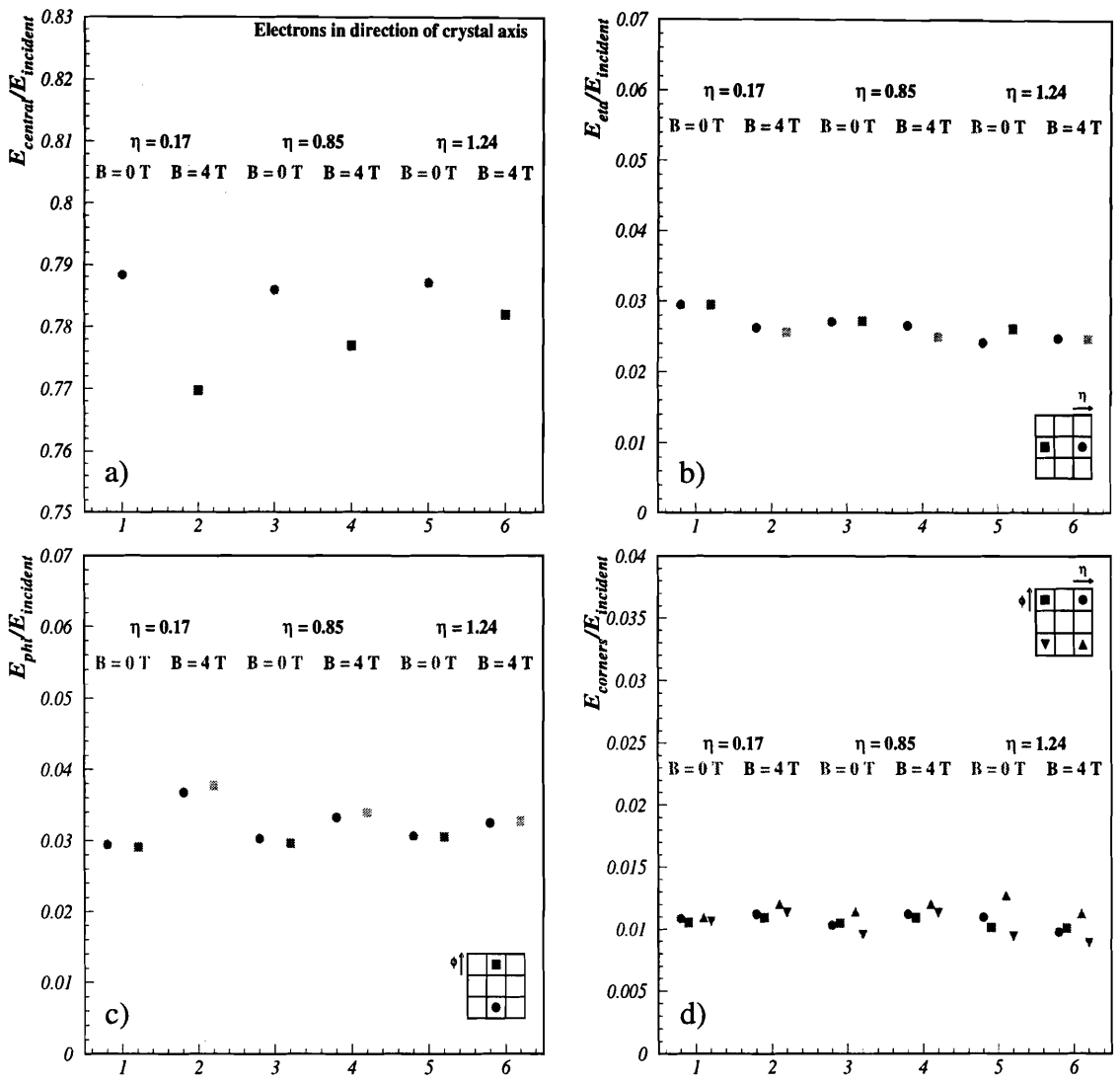

FIGURE 110. Effects of the magnetic field on the electromagnetic shower in GEANT, expressed as changes in the normalized energy deposited in the 3×3 crystal matrix. Electrons enters at the center of the middle crystal along the crystal axis at 3 different pseudorapidities and for 2 values of the magnetic field.

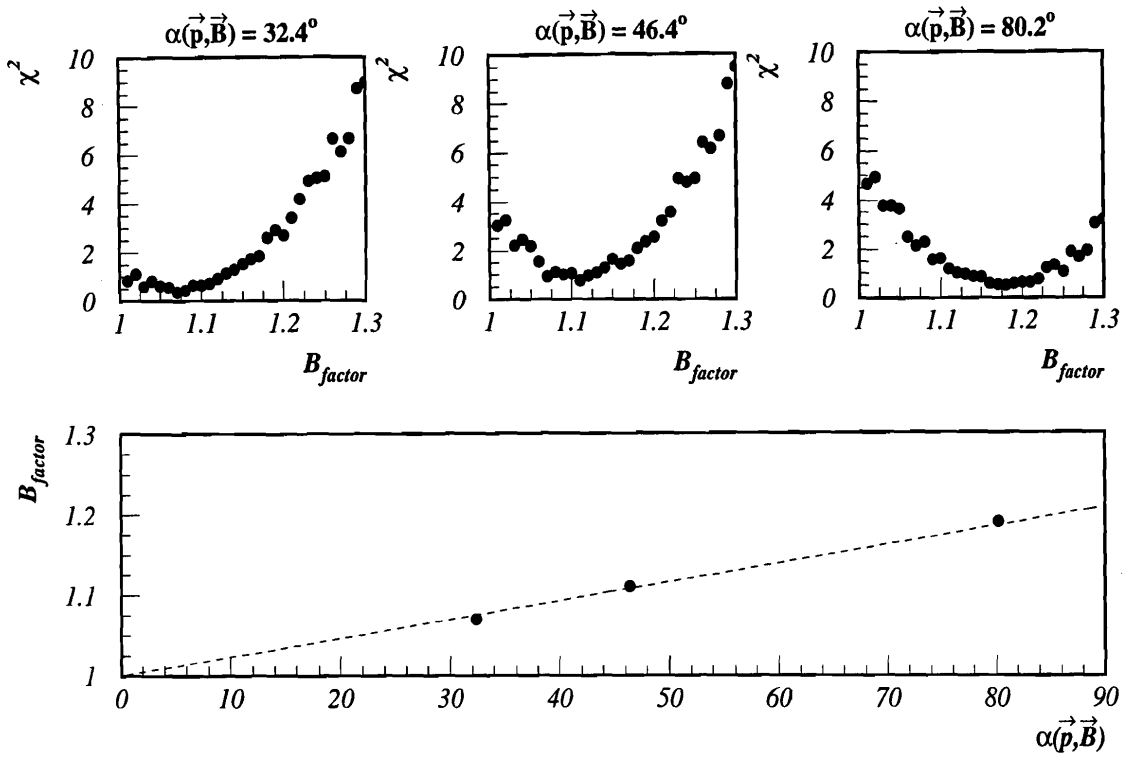

FIGURE 111. Upper plots: χ^2 between predicted and simulated energies in the 3×3 crystal matrix centered around the impact crystal as a function of the magnetic field stretching factor B_{factor}. The plots are given for different values of the angle (α) between electron momentum and magnetic field. Lower plot: A fit of the B_{factor} versus the angle α. The points corresponds to the values of the B_{factor} for which χ^2 reaches its minimum for a given α.

5.6.1.3 Covariance matrix

The covariance matrix consists of the variances and the correlations between the energy measurements in the crystals. The energy conservation in the shower process generates strong correlations between the energy deposit in different regions of the calorimeter. Because of the granular structure of the calorimeter these correlations have a strong dependence on the electron impact position and direction. To study the covariance matrix, we have generated 10 GeV electrons samples in several configurations of impact points and directions. The energy distributions for the crystals in a 3×3 matrix, for electrons incident at center of middle crystal in direction of its axis are shown in figures 112. The significant width and slightly nongaussian form of the distributions are due to the correlations in the energy deposit between the crystals.

The correlations coefficients for the 8 crystals with respect to the central one and the normalized variances for all nine impact electron configurations (3 impact positions with 3 impact angles at each) are shown in figure 113 as a function of the crystal mean energy. The bottom figure also shows the lines parametrizing the energy resolution with different stochastic term, keeping a noise term of 30 MeV. We can notice that neither correlation coefficients nor resolutions do follow simple parametrization as a function of the energy.

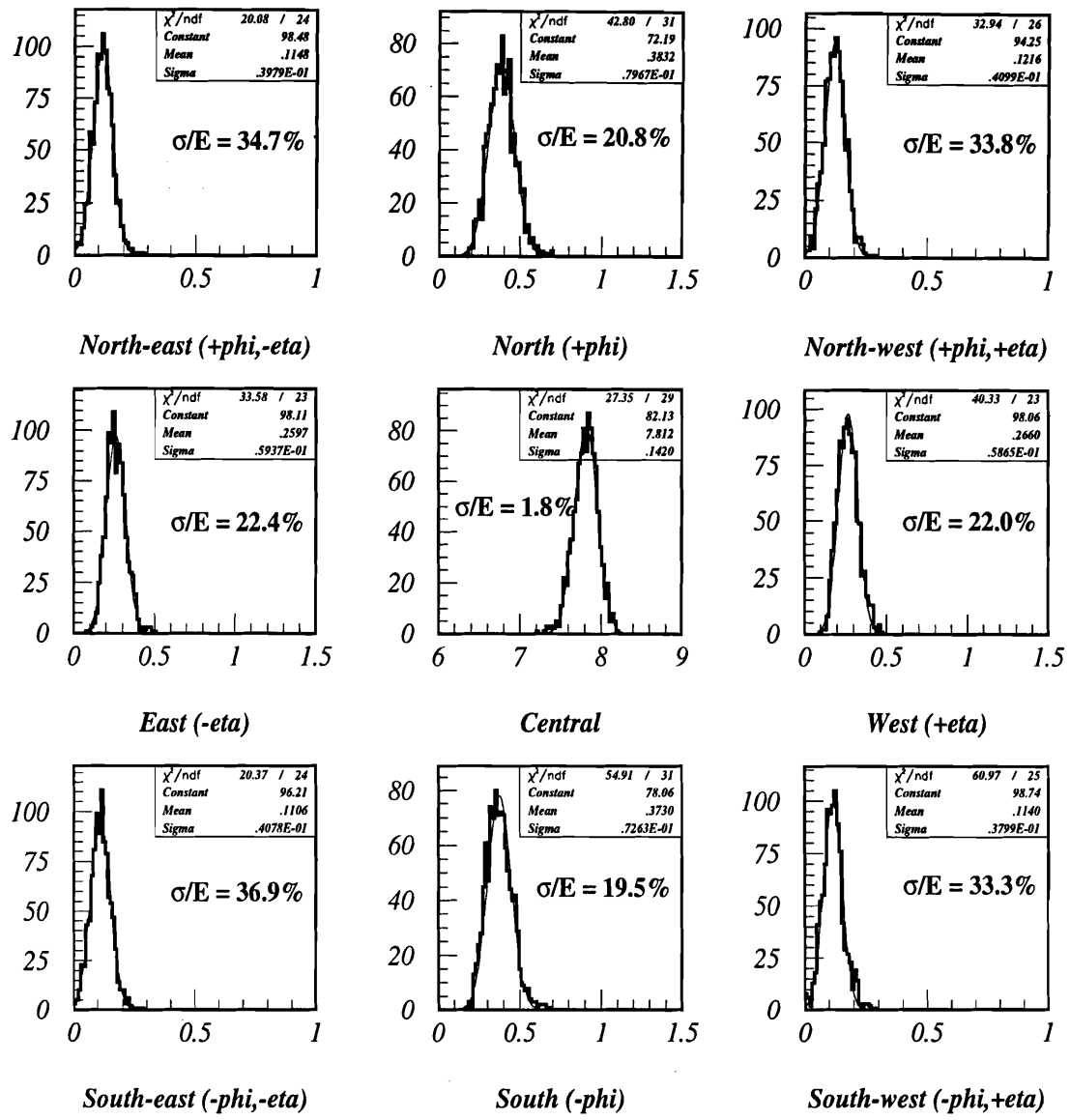

FIGURE 112. Energy response in a 3x3 crystal matrix for 10 GeV electrons entering the central crystal at its front face barycenter and along its axis.

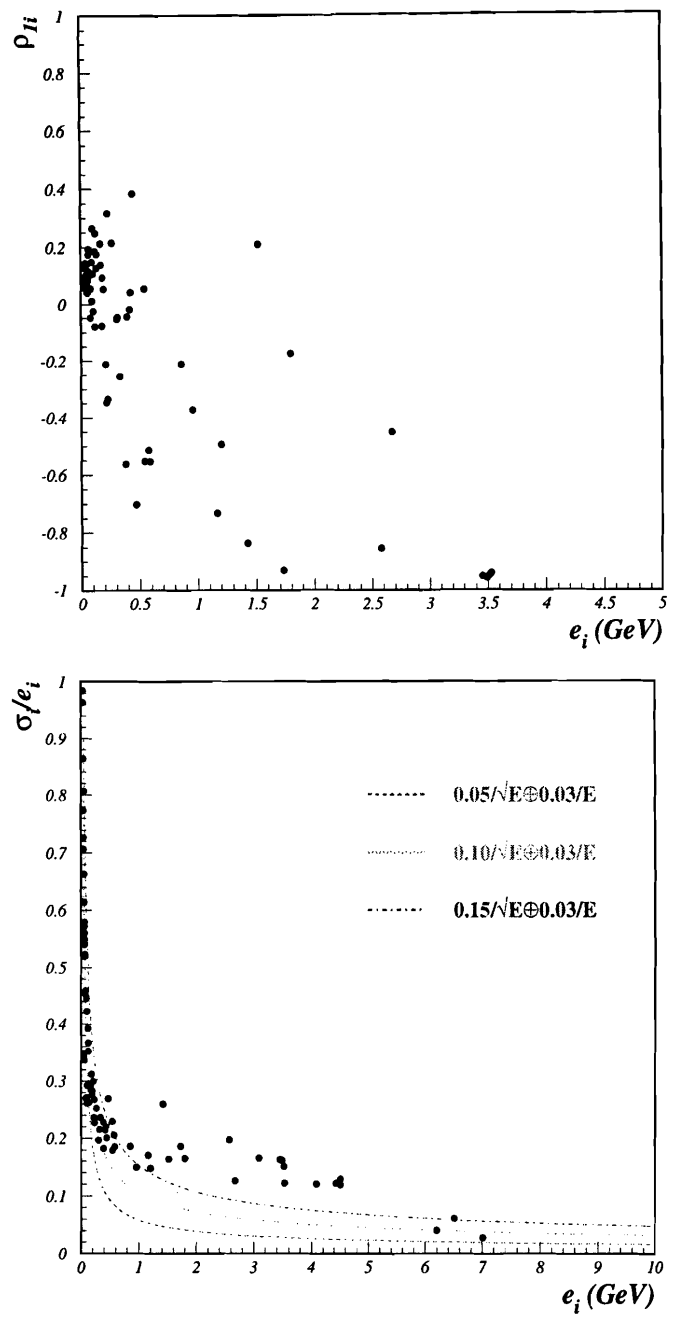

FIGURE 113. Correlation coefficients between central and other crystals (up) and normalized variances of the energy measurements in 3×3 matrix for 10 GeV electron entering central crystal in nine configurations (down).

In conclusion, the presence of important correlations do not allow for a simple description of the covariance matrix. In what follows we will assume a behavior $\sigma_i \sim \sqrt{e_i}$ so that all the weights in the weighting method are equal and given by the equation 85. The weighted estimate reduces therefore to a correction factor and hence the method will be referred from hereafter as the *'single weight method'*.

5.6.1.4 Results

In this sections we present the results obtained with the single weight method and compare them with the cluster energy sum estimator. We start with the example of 10 and 30 GeV electrons generated at the ECAL entrance, to decouple the influence of the tracker material and track reconstruction from the influence of the expected energy deposit predictions with the shower model. Hence, in this example the electron impact position and momentum will be extracted from the Monte Carlo simulations.

Then we will include the tracker and study the samples with fixed p_T of 10 and 30 GeV. As estimations of the electron ECAL impact point and direction, as well as the electron impact momentum, the reconstructed track extrapolated to ECAL will be used. We will also consider the case of a bigger value for the electronic noise.

The parametrisation of the crystal variances in the form $\sigma_i \sim \sqrt{e_i}$, introduced in the previous section, is justified for crystals with energy e_i well above the noise level. Therefore, in the application of the single weight method, only the crystals with $e_i > 2\sigma_{noise}$ will be considered. This will also reduce the number of crystals used for energy estimation and therefore the noise influence on the energy measurement.

E = 10 GeV and E = 30 GeV electrons at ECAL entrance

In this example electrons have been generated at the ECAL entrance, with fixed energy and uniformly distributed impact points in the barrel acceptance.

In the previous sections the shower model has been tuned using few electron impact configurations. To verify this agreement in a more realistic sample we have compared the relative difference between the expected and Monte Carlo values in this example. The results are shown in figure 114, for a 3×3 crystals matrix centered on the crystal with the highest expected energy. The crystals are sorted by their energy contents in decreasing order. One can remark a very good agreement of the values for the crystal with highest energy deposit, and a good agreement for all the others. The increase in the width of the distribution as going to smaller values of energy is the consequence of the resolution degradation.

The energy estimator obtained with the single weight method and the one obtained as the cluster energy sum, both normalized to the generated energy, are compared in figure 115 for 10 and 30 GeV electrons. About 30% better energy resolution for 10 GeV electrons and 25% for 30 GeV electrons of the single weight estimator and improved normalization can be seen.

These results are summarized in figure 116. As the reference, two curves corresponding to the intrinsic energy resolution for 3×3 and 5×5 crystal matrices, i.e. for an electron entering in the center of the matrix in the direction of the crystal axis, are presented. The improvements with the single weighting method with respect to the cluster energy sum is evident.

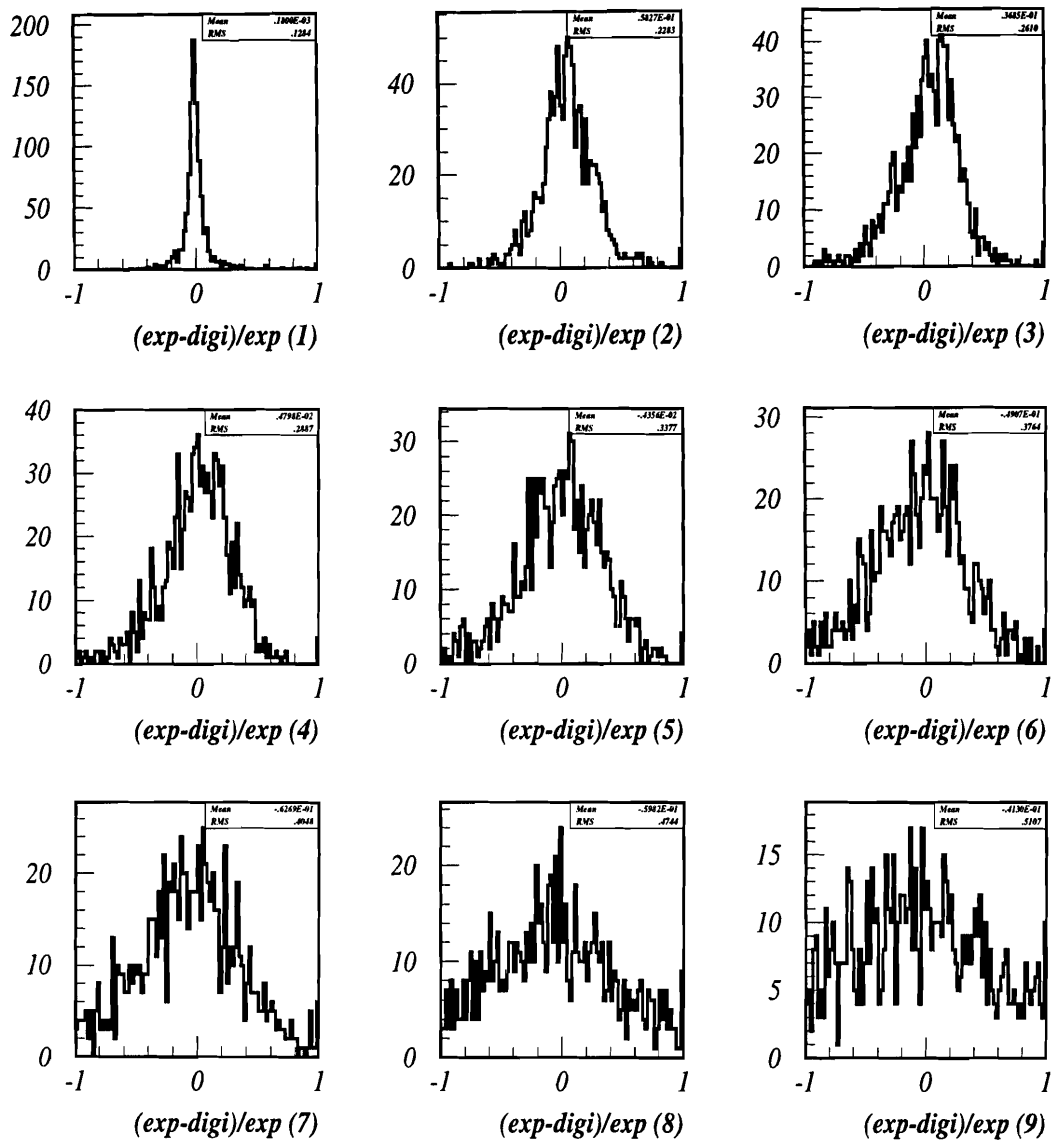

FIGURE 114. Relative differences between the predicted and GEANT simulated energy deposited by 10 GeV electrons in a 3×3 crystal matrix, centered around the crystal with the highest predicted energy. The crystals are sorted by their energy contents, in decreasing order.

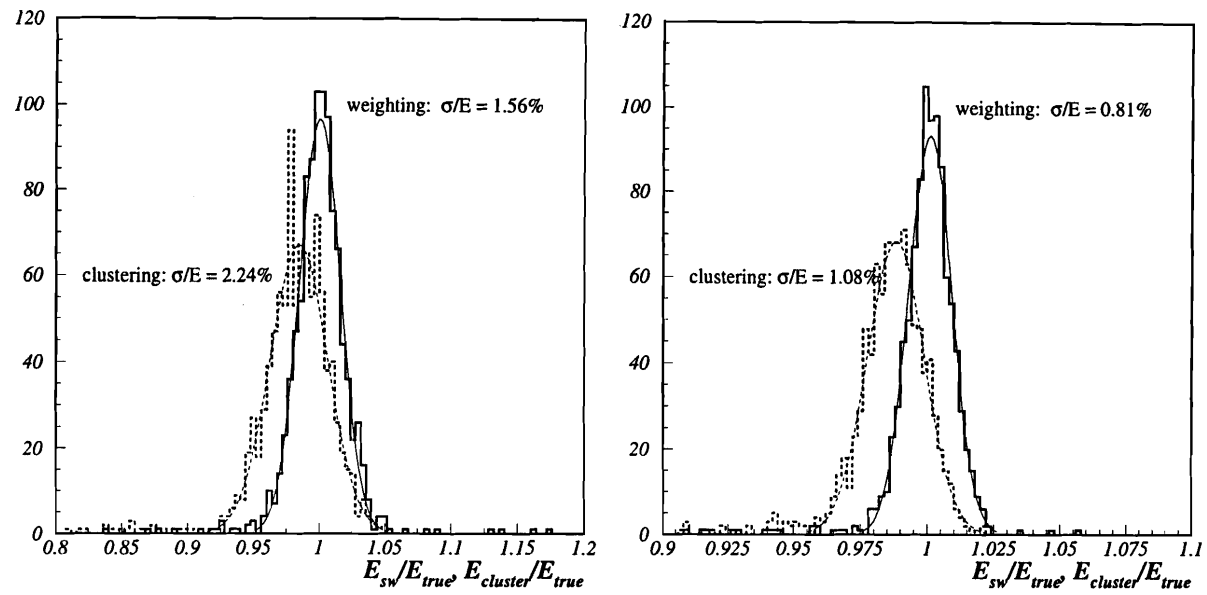

FIGURE 115. Results of the energy estimation with the single weight method and the cluster energy sum, for 10 GeV (left) and 30 GeV (right) electrons generated at the ECAL entrance, normalized to the generated electron energy. The electron impact points are uniformly distributed in the barrel acceptance.

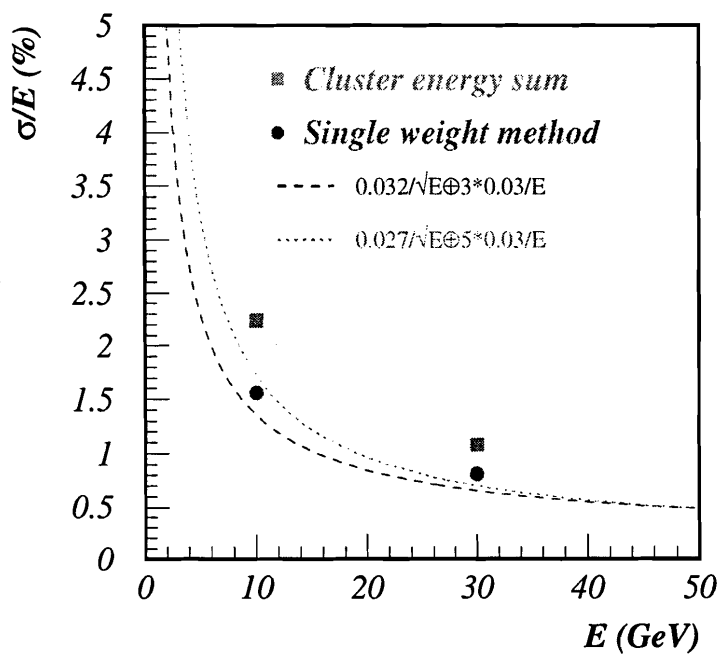

FIGURE 116. Comparison of the results with the single weight method and the cluster energy sum. The lines correspond to the intrinsic energy resolutions with 3x3 (dashed curve) and 5x5 (dotted curve) crystal matrices assuming perfect lateral leakage corrections.

p_T = 10 GeV and p_T = 30 GeV electrons with reconstructed tracks

We now present the influence of the track reconstruction on the single weight method. On the contrary from the previous example the fixed transverse momentum samples are used. Electrons are generated from the beam interaction point in the barrel acceptance, with the appropriate vertex fluctuations.

As a reference we first show in figure 117 results for 10 and 30 GeV p_T electrons without tracker material in front of ECAL. Electron ECAL impact position, direction and momentum, used for the shower generation, are still extracted from the Monte Carlo simulation. The results are in agreement with those presented in figure 116 (the mean energy for 10 GeV p_T electrons is about 14 GeV and for 30 GeV p_T is about 42 GeV).

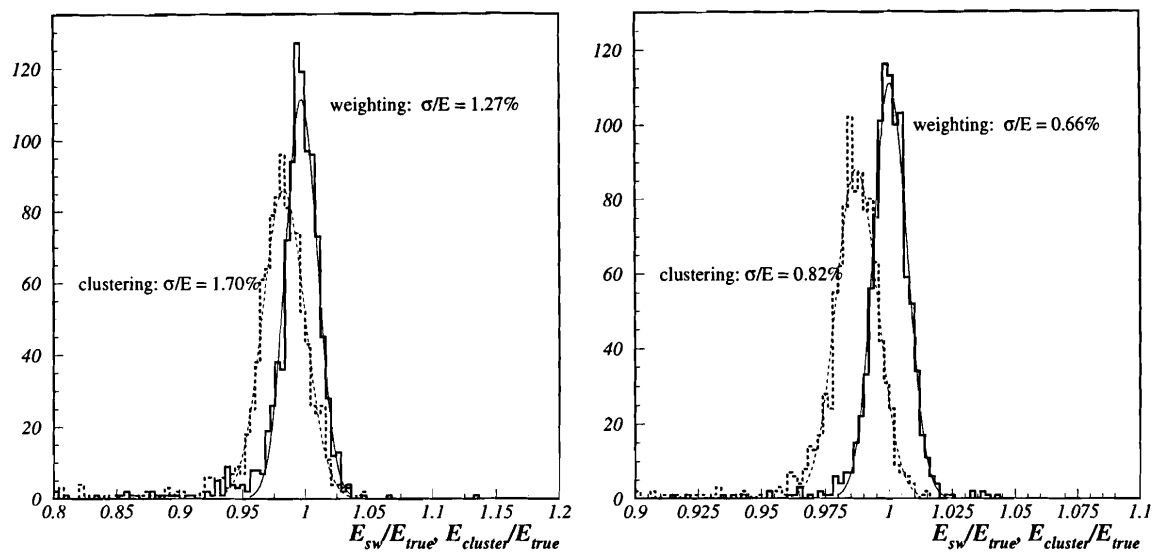

FIGURE 117. Comparison between the single weight estimator and the cluster energy sum for 10 GeV (left) and 30 GeV (right) p_T electrons, generated from the beam interaction point, still using Monte Carlo tracks. The tracker material is not included.

The influence of the tracker on the energy estimation with the single weight method comes from two effects. The first effect is electron bremsstrahlung in the tracker material, which changes the pattern of the energy deposited in the crystals. For the events with partially merged electron and photons clusters, the energy measured by the crystals will be less in agreement with the predicted energy. These events can be identified by a sizeable χ^2 between measured and predicted energy deposits. The bremsstrahlung effect is expected to be more important for the smaller electron transverse momenta, because of the larger average separation of the electron and radiated photons. The second important effect is related to the precision of the electron track momentum estimation and the precision of the track extrapolation to the electromagnetic calorimeter. In the single weight method these informations, together with the shower model, are used to predict the fractions of the total energy deposited in the crystals. In the track reconstruction process the track parameters are estimated from its curvature in the

magnetic field. As a consequence, the transverse momentum resolution deteriorates with increasing track p_T. In the first approximation this effect is not expected to affect the proposed method, since we use fractions of the incident particle and since the transversal shower profile shape changes little with energy. On the other hand the precision of the track extrapolation is increasing toward higher p_T as a consequence of the smaller track curvature. Therefore, we can expect to have better behavior of the single weight method for higher p_T electrons, since both the bremsstrahlung effects and the track reconstruction effects become less important.

In figure 118 the results obtained with the single weight method and cluster energy sum, for the whole set of 10 GeV p_T electrons events are shown. The cluster energy sum has better efficiency while the single weight estimator has a better resolution. To compare these two estimators when the extrapolated track better corresponds to the real electron impact track we choose as criterion an effective χ^2 between the simulated and the predicted energy fractions. In the χ^2 calculation the variance of the measured energy for each crystal has been parametrized as $\sigma_{e_i} = 0.09 \cdot \sqrt{e_i}$. The distributions of the two estimators for events which pass the cut $\chi^2 < 15$ are shown in figure 119. The acceptance of this cut is about 50%. For this set of events 15% better efficiency and 19% better resolution for the single weight estimator is obtained. The better resolution for the single weight estimator is the consequence of reducing the noise contribution in the energy estimation by using only crystals with energy well above the noise value ($e_i > 2\sigma_{noise}$). With this condition the average number of crystal considered is 9.9 ± 2.1, while the cluster energy sum uses 25.0 ± 5.9 crystals.

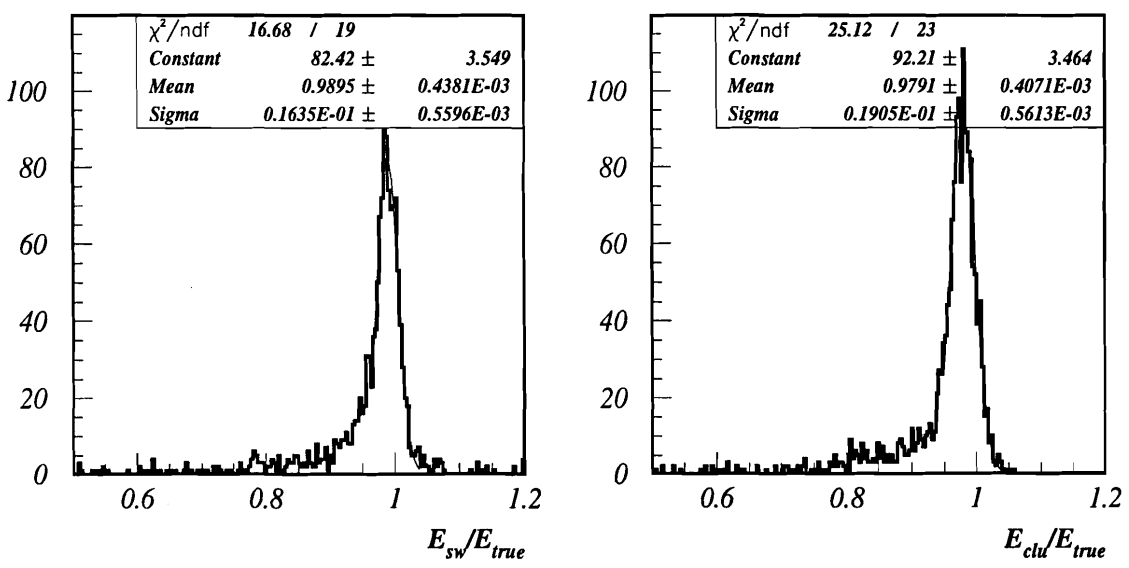

FIGURE 118. Distributions of the single weight estimator (left) and the cluster energy sum (right) for the full sample of 10 GeV p_T electrons, normalized to the generated energy. Fits are obtained by an iterative procedure in the region of $[-1.5\sigma, 3\sigma]$ around mean.

The acceptance as a function of the effective RMS and of the resolution is shown in figure 120. Event selection is based on the χ^2 value. For what concerns efficiency, by tighten-

ing the χ^2 cut the single weight method improves faster than the cluster energy sum. The resolution remains at about the same level since the sigma was extracted by a fit of the upper part of the distribution.

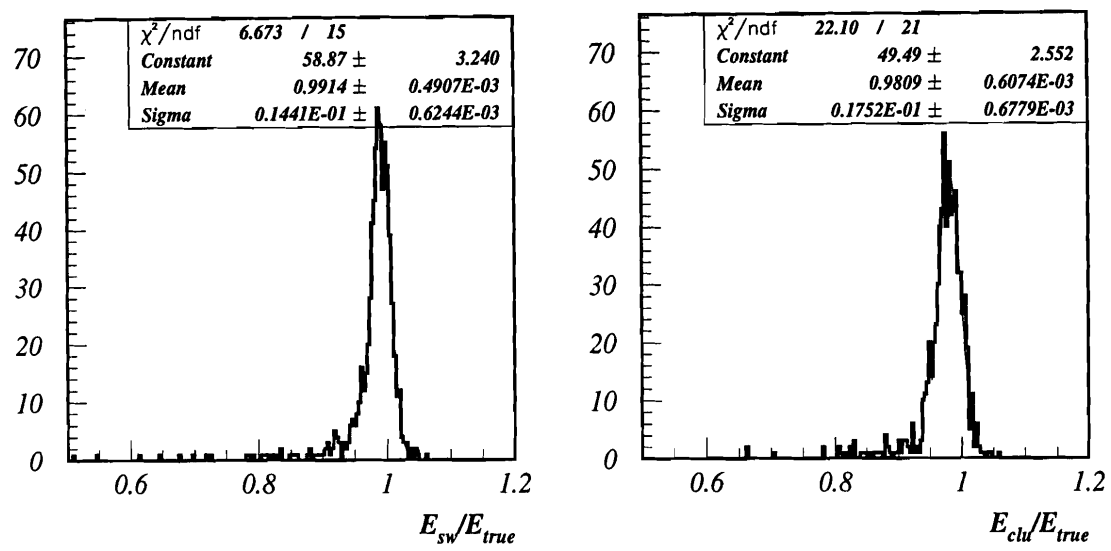

FIGURE 119. Distributions of the single weight estimator (left) and the cluster energy sum (right) for the sample of 10 GeV p_T electrons satisfying the $\chi^2 < 15$ cut.

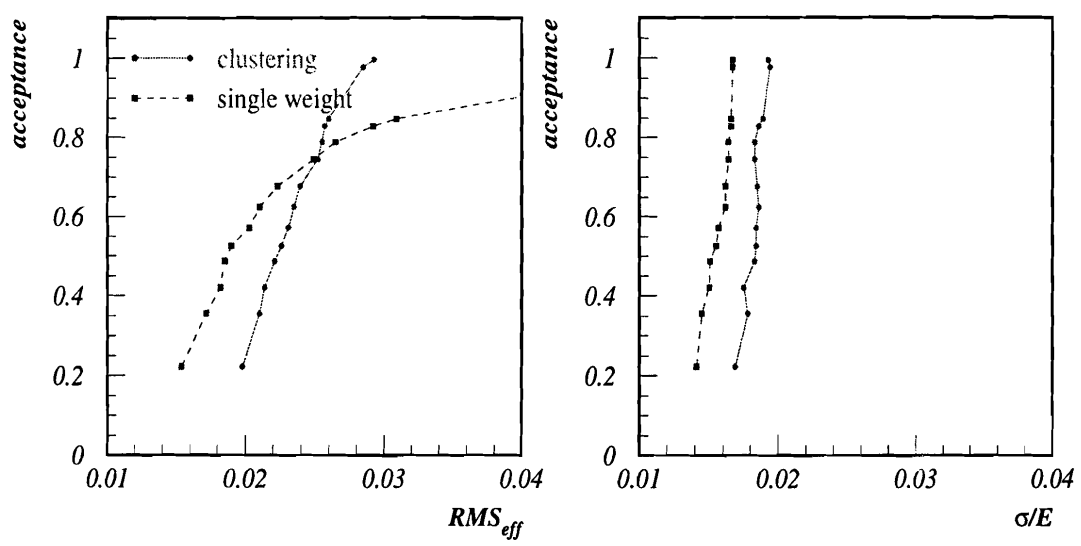

FIGURE 120. Acceptance as a function of the effective RMS (left) and of the resolution (right) for the single weight and the cluster energy sum estimators for 10 GeV p_T electrons. Event selection is based on the χ^2 between the simulated and the predicted energy fractions.

The electronic noise used up to now in the simulation was 30 MeV per channel. It is likely that in the experiment the noise will exceed this value. To study the performances of the single weight method in the case of bigger noise we have performed the study for 100 MeV noise per crystal. The results are shown in figures 121 and 122 for the whole set of events and with the additional cut of $\chi^2 < 15$, respectively. Figure 123 shows the acceptance of events for different χ^2 cuts as a function the effective RMS and of the resolution. For this value of noise the single weight method gives 18% smaller effective RMS and 29% better resolution for about 60% of events.

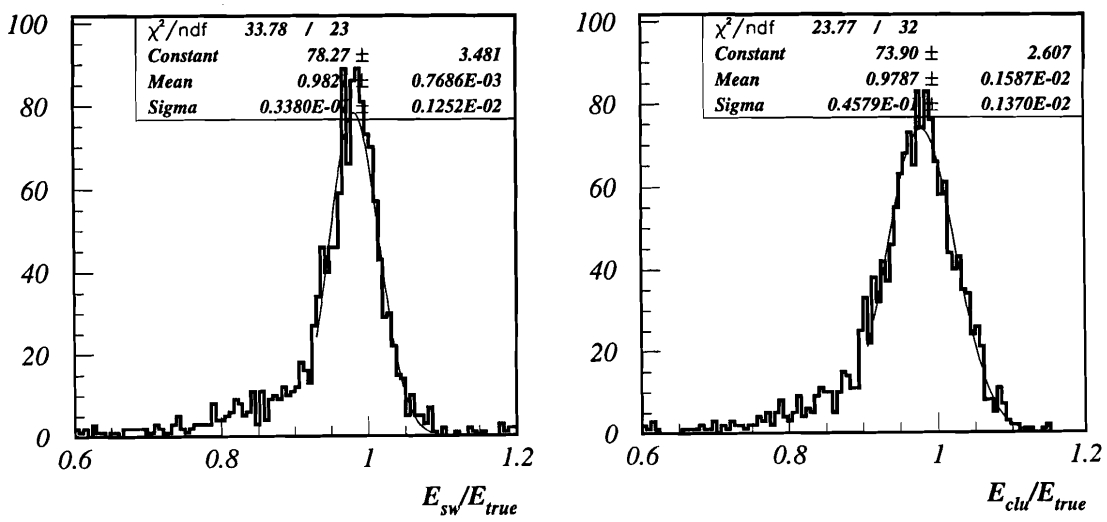

FIGURE 121. Distributions of the single weight estimator (left) and the cluster energy sum (right) for the full sample of 10 GeV p_T electrons, with 100 MeV electronic noise per channel.

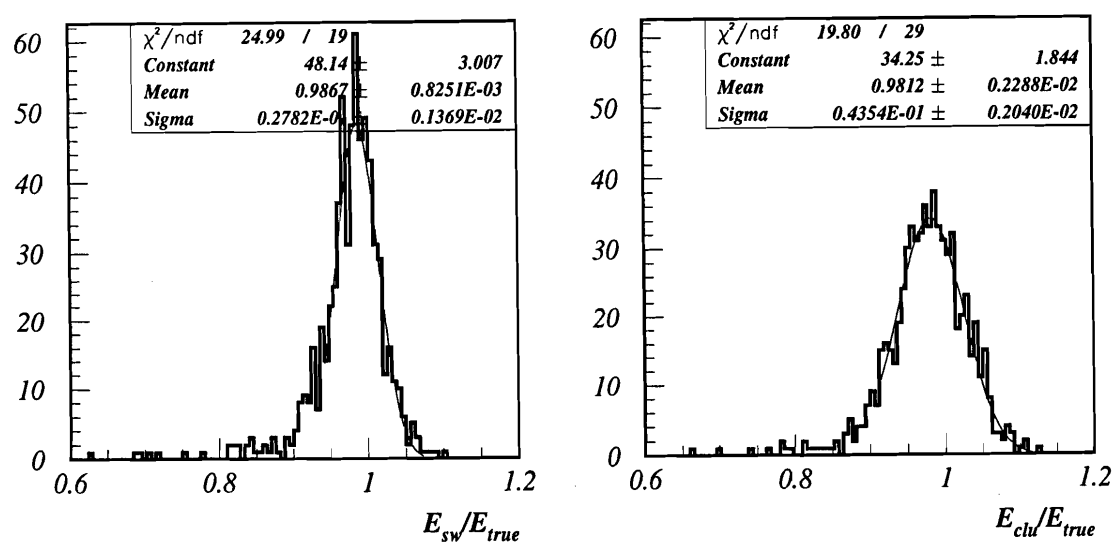

FIGURE 122. Distributions of the single weight estimator (left) and the cluster energy sum (right) for the sample of 10 GeV p_T electrons satisfying the $\chi^2 < 15$ cut. The value of the electronic noise is 100 MeV per channel.

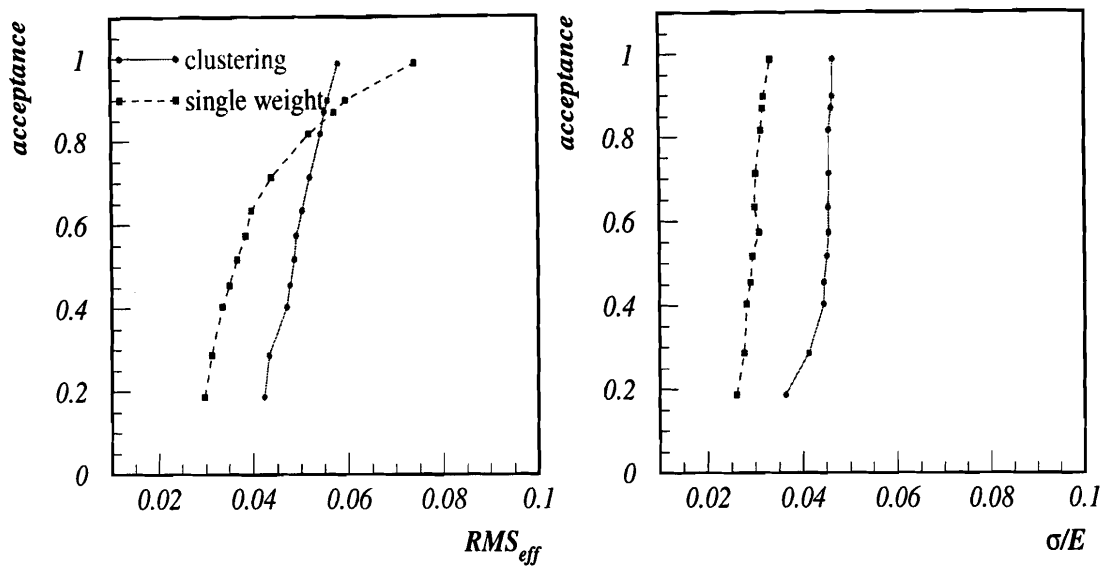

FIGURE 123. Acceptance as a function of the effective RMS (left) and of the resolution (right) for the single weight and the cluster energy sum estimators for 10 GeV p_T electrons. The value of the electronic noise is 100 MeV per channel.

The results for 30 GeV p_T electrons, for the nominal noise of 30 MeV per crystal, are shown in figures 124 and 125, for the whole set of events and those satisfying $\chi^2 < 15$ cut. Figure 126 presents an acceptance as a function of the effective RMS and of the resolution. For about 70% of events the single weight estimator gives about 10% better effective RMS and about 15% better resolution.

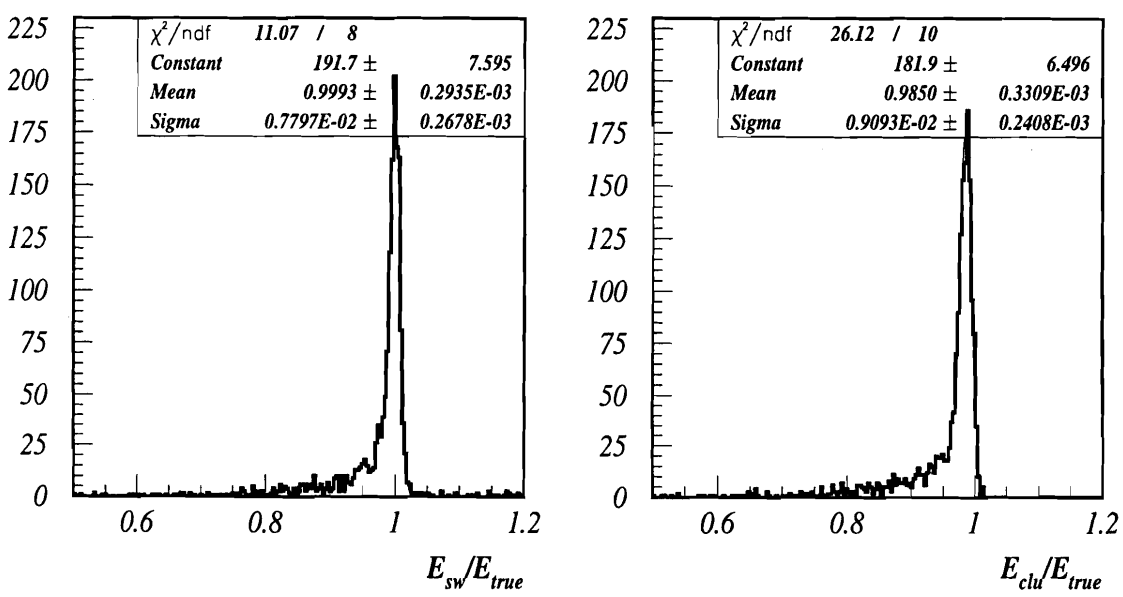

FIGURE 124. Distributions of single weight estimator (left) and the cluster energy sum (right) for the full sample of 30 GeV p_T electrons.

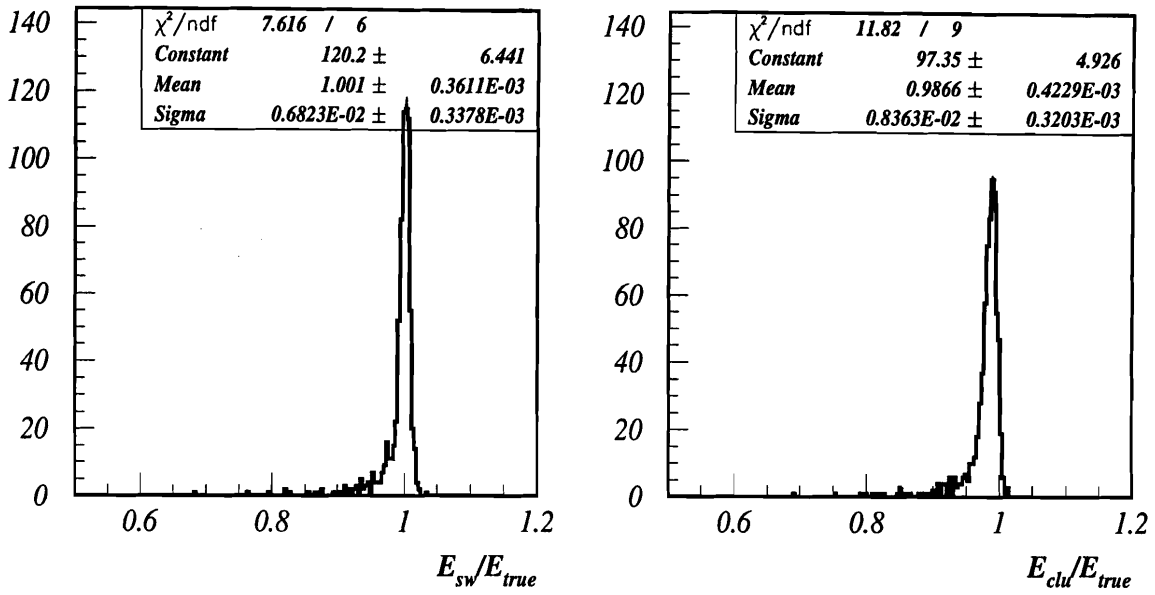

FIGURE 125. Distributions of the single weight estimator (left) and cluster energy sum (right) for the sample of 30 GeV p_T electrons satisfying the $\chi^2 < 15$ cut.

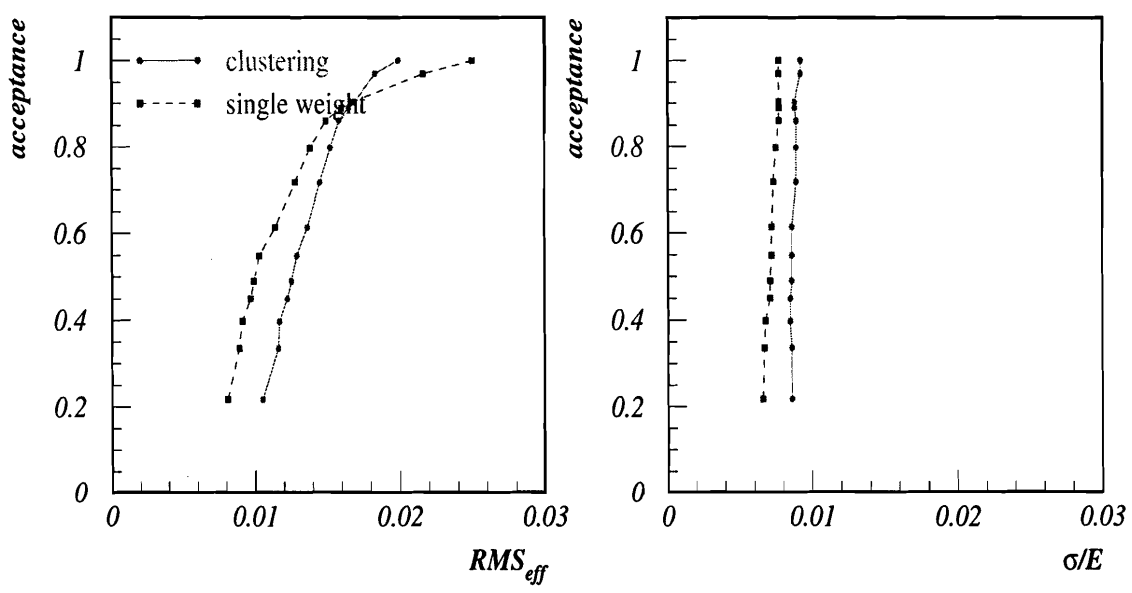

FIGURE 126. Acceptance as a function of the effective RMS (left) and of the resolution (right) for the single weight and cluster energy sum estimators for 30 GeV p_T electrons.

5.6.1.5 Summary and discussion

Let us at the end of this section summarize and discuss the main results obtained with the proposed method for the electron energy estimation:

- The presence of strong correlations between energies deposited in neighboring crystals does not allow for a simple parametrization of the covariance matrix. Choosing the parametrization of the variances in the form $\sigma_i \sim \sqrt{e_i}$, the weights for all crystals are identical and the weighted estimate reduces to a correction factor for the leakage outside the crystal set used for the energy estimation.
- As the above variance parametrization is justified only for crystal with signal well above the noise level, only the crystal with energy $e_i > 2\sigma_{noise}$ are used. This condition reduces the number of crystals used for the energy estimation, from about 25 for the cluster energy sum to about 10 for the single weight estimator, for 10 GeV p_T electrons. Studying the cases with noise values of 30 MeV and 100 MeV per crystal, we have shown that the single weight estimator improves with respect to the cluster energy sum, as the noise increases. This is particularly important for high luminosities, since the pile-up will result in an effective increase of the noise (f.g. in average about 20 MeV per crystal at high luminosity).
- The performances of the single weight method, comparing with the cluster energy sum, improve with increasing electron transverse momentum since both the bremsstrahlung effects and the track extrapolation effects become less important. Since this method uses the predicted energy fractions rather than predicted energies directly, and since the shape of the transversal shower profile changes little with the energy, the method is fairly insensitive to the deterioration of the tracker momentum resolution with increasing transverse momentum, as soon as the impact point and direction are correctly estimated.
- The effective χ^2 between the predicted and measured energy fractions in the considered set of crystals can be used to identify events with considerable bremsstrahlung effect resulting in a significant shower profile change. For these events the cluster energy sum gives better results and will be taken as the energy estimate. The acceptance for the typical value $\chi^2 < 15$ is about 50%, and can be relaxed as the electron energy increases, accepting therefore more events for which the single weight method is used for the electron energy estimation.
- As the shower model a simple parametrization of the electromagnetic shower longitudinal and transversal profiles has been used. We have demonstrated the ability to tune the shower parameters in order to reach the requested level of precision in the energy estimation. In the real experiment the tuning of the shower model will have to be performed using the selected samples of clean electrons and/or test beam data.

Several other algorithms for the energy estimation using the predicted or presimulated energy deposit pattern in the crystals could be also envisaged:

- *The shower fit.*
  Such an algorithm uses measured and predicted energy fractions to fit the electron energy. For a successful fit the covariance matrix model has to be included and possible limitations of this method could arise from a limited description of strong correlations between the energy measurements in the neighboring crystals.
- *The neural networks.*
  Here, a large number of generated patterns are used to train the neural network. The obtained network is then applied to the observed pattern to estimate the electron energy.

Possible limitations of this method is in the huge number of different energy deposited patterns which are to be generated to train the network as to be able to reach the requested precision in energy estimation.

- *The shower library.*
  Observed patterns are interpolated between preselected patterns stored in a shower library. Possible limitations of such method are, as in the case of the neural networks, of statistical origin.

5.6.2 Electron momentum estimator

Finally, in this section we present a combination of the tracker and the ECAL momentum estimation to obtain a final electron momentum estimator.

An optimal linear combination of two estimators is given by their weighted sum:

$$\tilde{p} = w_E \cdot E + w_p \cdot p. \qquad \text{(EQ 94)}$$

Here E stands for ECAL energy and p for tracker momentum estimators and the weights are inverse of the variances.

To apply such combination of E and p estimators we have to look more carefully to their distributions, shown in figure 127. The ECAL energy estimator is a combination of single weight and cluster energy sum estimators, properly normalized. For the events satisfying the condition $\chi^2 < 15$, i.e. with a good agreement between expected and Monte Carlo energy values, we take the single weight method energy estimator. Otherwise the cluster energy sum is taken. As we can see, at 10 GeV p_T the tracker has better resolution and efficiency than the ECAL measurement. From the shapes of the distribution, with the characteristic left tail caused by the bremsstrahlung, we see that these estimators are not unbiased and the above weighted sum cannot be used for the complete set of events.

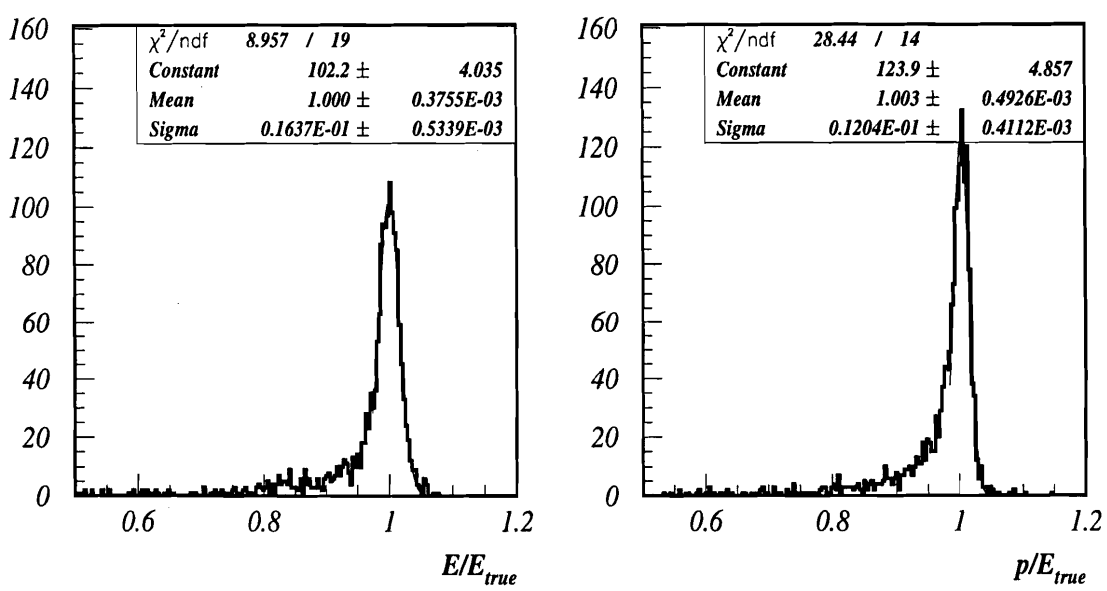

FIGURE 127. Comparison of the ECAL energy and tracker momentum estimators, normalized to the generated momentum, for 10 GeV p_T electrons.

In figure 128 the correlation between the ECAL energy and tracker momentum estimators, normalized to the generated energy, is shown. It is interesting to remark that most of the tail of one distribution is contained in the region around the peak of the other.

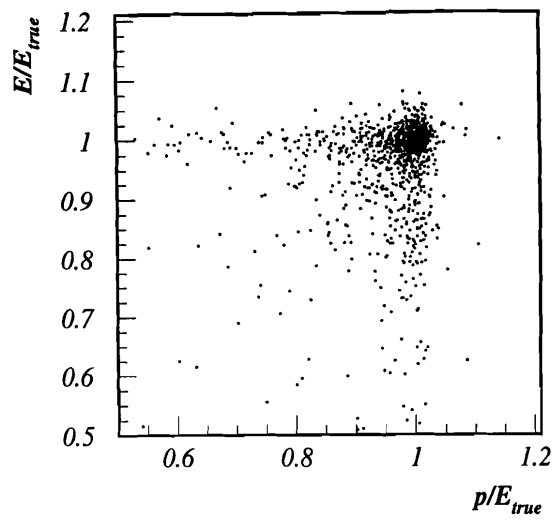

FIGURE 128. Energy versus momentum estimators, both normalized to the generated momentum, for 10 GeV p_T electrons.

Using this property we can construct a variable which will serve as a criterion for the application of the weighted sum. This variable is the ratio *E/p* and its correlations with the energy and momentum estimators are shown in figure 129. From the shape of the correlations one can distinguish three regions: one around $E/p = 1$ where both estimators are unbiased and we can combine them, one for the bigger values where the ECAL energy is a better estimator of the particle momentum and one for smaller values where the tracker momentum is better.

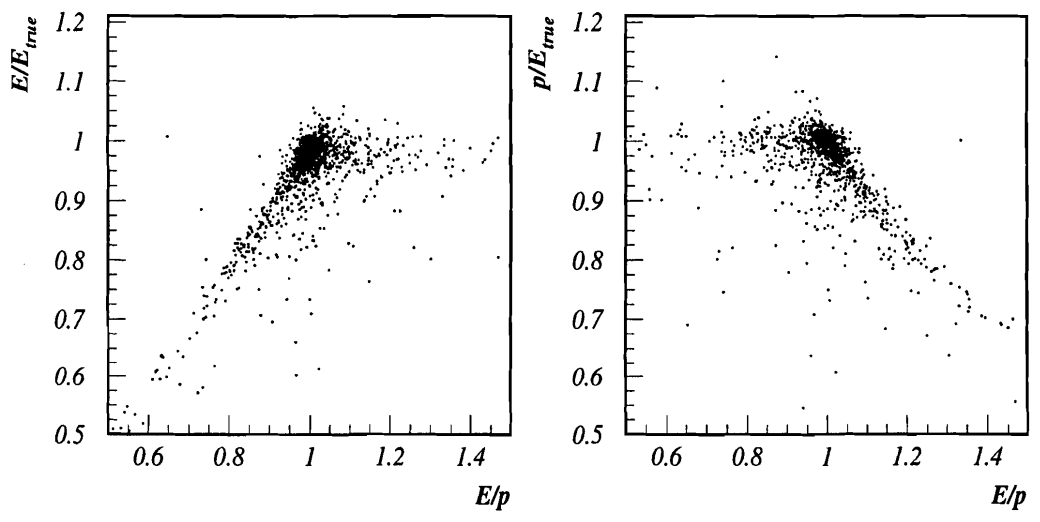

FIGURE 129. Correlations of the ECAL energy (left) and the tracker momentum (right) estimators normalized to the generated momentum and their ratio, for 10 GeV p_T electrons.

As a combination of the electromagnetic calorimeter and the tracker measurements we therefore take:

$$\tilde{p} = \begin{cases} w_E \cdot E + w_p \cdot p \ , \text{if} \left|\frac{E}{p} - 1\right| \leq 2\sigma_{E/p} \\ E \qquad , \text{if} \ \frac{E}{p} > 1 + 2\sigma_{E/p} \\ p \qquad , \text{if} \ \frac{E}{p} < 1 - 2\sigma_{E/p} \end{cases} \qquad \text{(EQ 95)}$$

The $\sigma_{E/p}$ is the variance of the E/p ratio where σ_E and σ_p are parametrized by their expected resolutions. The results for 10 GeV p_T electrons are shown in figure 130. Comparing them with the previous distributions the improvement is clear.

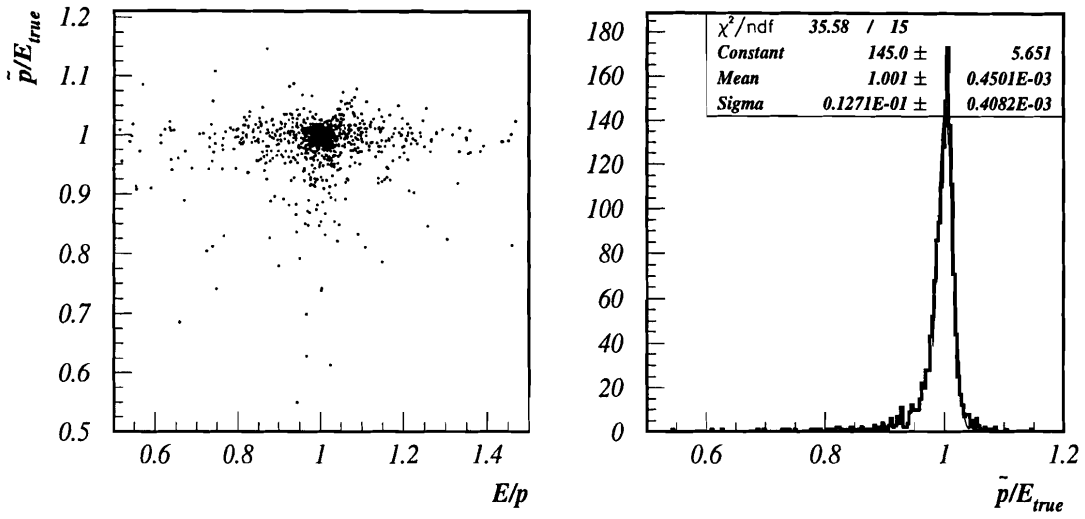

FIGURE 130. Combined electron momentum estimator normalized to the generated energy versus E/p ratio (left) and the distribution of the combined estimator (right).

The same results for 30 GeV p_T are shown in figures 131, 132, 133 and 134. Although at this energy the ECAL energy estimator dominates, there are still improvements with combining ECAL and tracker measurements.

The summary of the results is shown in table 9, expressed through σ, effective RMS and efficiency in $\pm 2\sigma$ and $\pm 3\sigma$ regions around the mean. The combined estimator has the energy resolution of the tracker momentum estimator at the smaller energy and the ECAL energy estimator resolution at the higher energy. The effective RMS and efficiencies are improved with respect to both single estimators. $\pm 2\sigma$ ($\pm 3\sigma$) efficiencies are 78% (87%) for 10 GeV p_T and 66% (76%) for 30 GeV p_T electrons.

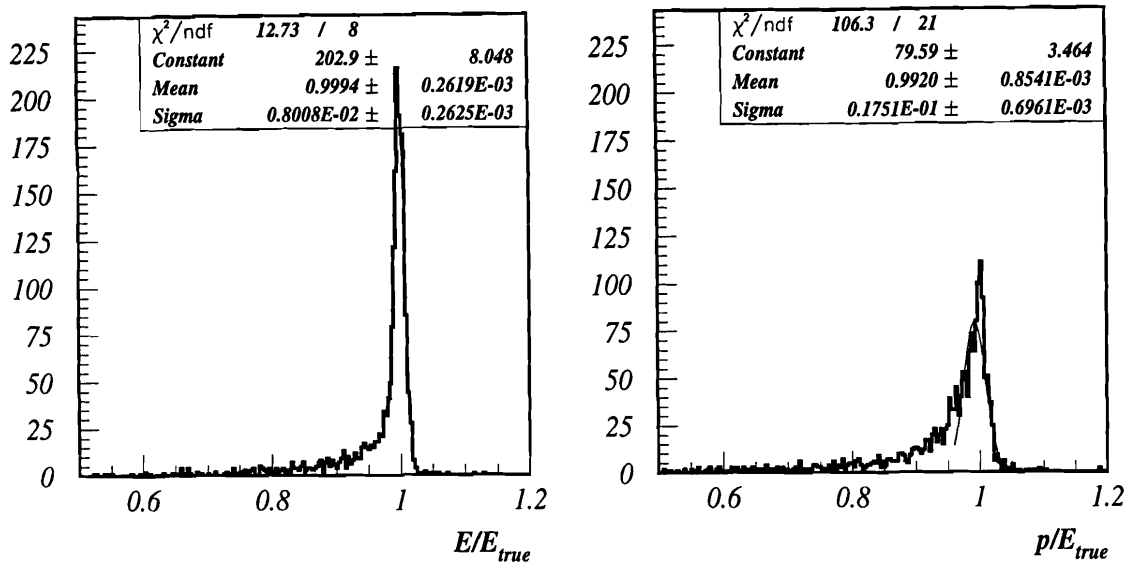

FIGURE 131. Comparison of the ECAL energy and tracker momentum estimators, normalized to the generated momentum, for 30 GeV p_T electrons.

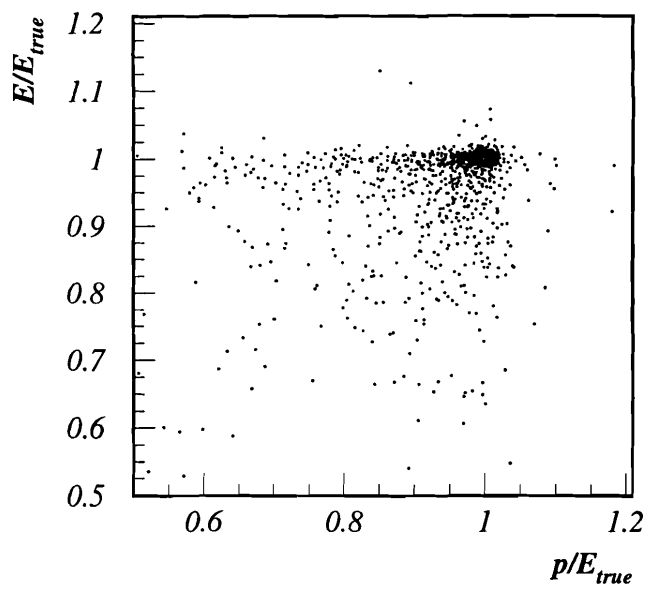

FIGURE 132. Energy versus momentum estimators, both normalized to the generated momentum, for 30 GeV p_T electrons.

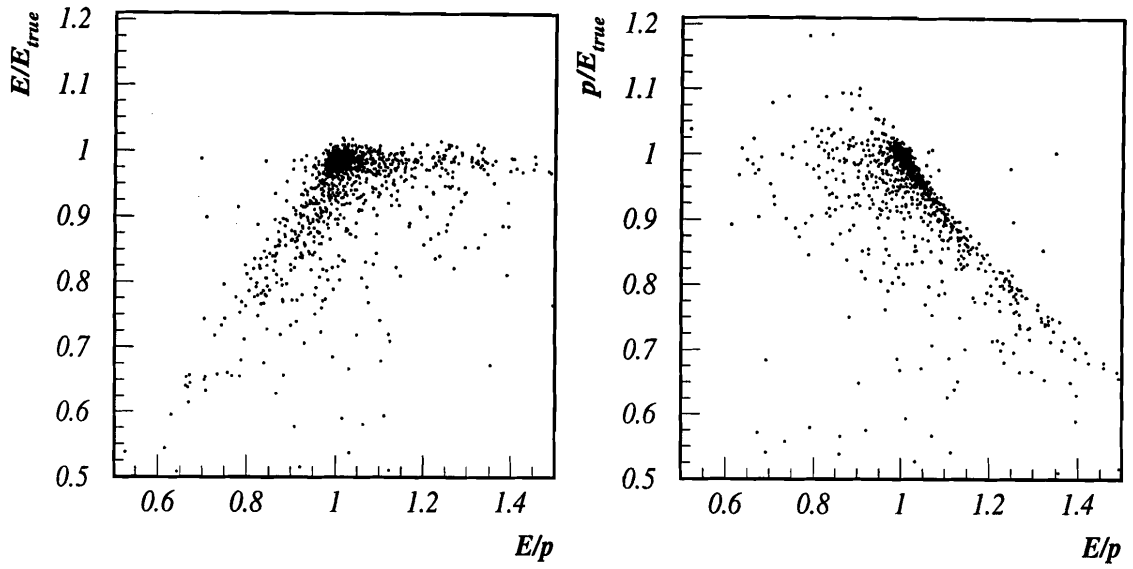

FIGURE 133. Correlations of the ECAL energy and tracker momentum estimators normalized to the generated momentum and their ratio, for 30 GeV p_T electrons.

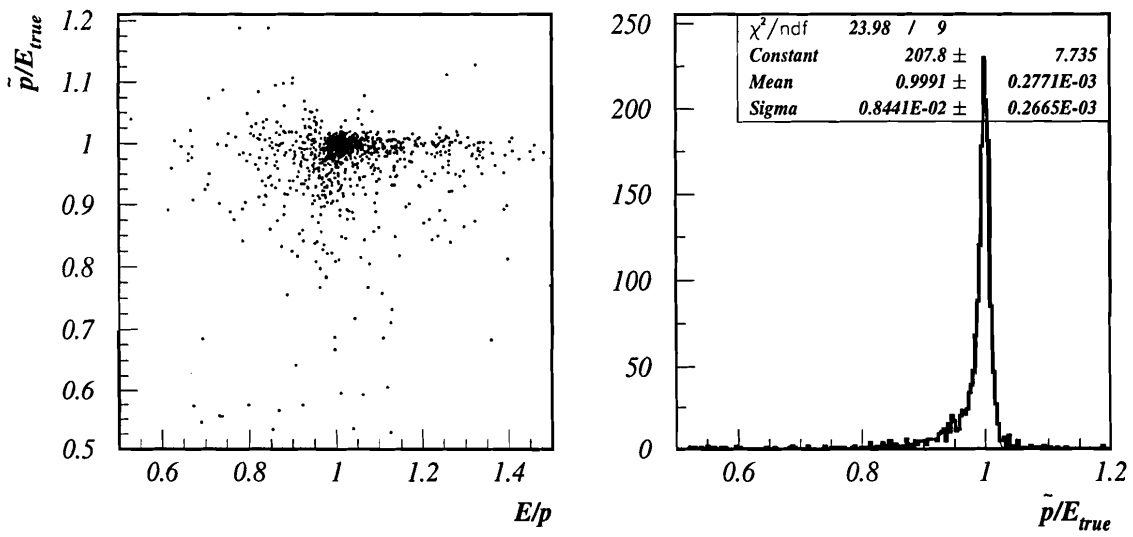

FIGURE 134. Combined estimator normalized to the generated momentum versus E/p (left) and distribution of the normalized combined estimator (right).

		RMS_{eff}	σ	$\varepsilon(\pm 2\sigma)$ (%)	$\varepsilon(\pm 3\sigma)$ (%)
p_T = 10 GeV	E	0.029	0.0164	71.5	78.5
	p	0.025	0.0120	67.1	74.2
	$\tilde{p}$	0.017	0.0127	79.1	86.5
p_T = 30 GeV	E	0.020	0.0080	62.3	69.9
	p	0.045	0.0175	59.7	68.1
	$\tilde{p}$	0.016	0.0084	69.4	75.5

TABLE 9. Summary of the results ($\tilde{p}$) combining the ECAL energy (E) and tracker momentum (p) estimators.

5.7 Results and discussion

In this section the developed electron reconstruction algorithms are applied on the reconstruction of the $H \rightarrow ZZ^* \rightarrow 4e^{\pm}$ events. Representative samples are taken for Higgs masses of 130, 150 and 170 GeV, covering the Higgs mass region explorable with this channel. The events with at least 2 e^+ and 2 e^- with $p_T > 6.5$ GeV and in the barrel acceptance ($|\eta| < 1.48$) are preselected. In addition to the stochastic term of 2.3% and noise of 30 MeV per crystal already present in the simulations, the reconstructed electron energy in the electromagnetic calorimeter has been smeared by a gaussian fluctuation of $0.55\% \cdot E$ in order to account for the constant term in the energy resolution. Therefore, the ECAL energy resolution now corresponds to the one introduced in the particle level analysis, studied in the previous chapter.

The reconstructed 2-electrons invariant mass closest to the Z boson nominal mass (referred from hereafter as Z boson) and the 4-electrons invariant mass (referred as Higgs boson) are presented in figures 135, 136 and 137, for 130, 150 and 170 GeV Higgs respectively. For the Z boson reconstruction, the charge constrain and the p_T electron cuts, summarized in the section 4.9 are applied. The Z* and the Z mass constraints are imposed in addition for the Higgs mass reconstruction. The Z mass resolution varies from 1.8 GeV for 130 GeV Higgs mass to about 2.2 GeV for a Higgs of 170 GeV. The resolution of the Higgs boson are 1.3, 1.6 and 1.8 for 130, 150 and 170 GeV Higgs masses respectively. We can also notice an increase of the lower mass tail on the Z reconstructed mass as going toward lower Higgs masses, which is mainly due to the increasing fraction of Z*Z* events in the Higgs decay.

The reconstruction results are summarized in table 10, and compared with those from particle level analysis. Comparing the acceptances in the table, we conclude that the most important contribution comes from the initial electron reconstruction acceptance, which reflects a rather low track finding efficiency. We have to recall here that the tracker performances are still not completely optimized, opening the possibility to increase the signal acceptance. The acceptance for the p_T electrons cuts are slightly lower comparing with the particle level results,

while the acceptance for the Z* and the Z mass constraints remains at the same level. The widths of the reconstructed mass distributions are about twice larger than those from the particle level analysis, where the energy resolution was optimistically introduced as a smearing of the electron energy. The reason of such resolution degradation is in electron bremsstrahlung in the tracker material. Although the electron reconstruction algorithms, presented in the previous sections, threat correctly the bremsstrahlung effect for a large fraction of electron configurations, the presence of 4 electrons in the signal final state makes this effects still the dominating one. The $\pm 2\sigma_{m_H}$ and $\pm 3\sigma_{m_H}$ efficiency are about 10-15% lower than the particle level ones. The overall efficiencies in the $\pm 2\sigma_{m_H}$ mass window are 26%, 31% and 37% for the Higgs masses of 130 GeV, 150 GeV and 170 GeV respectively, which is about half of those obtained with the particle level analysis.

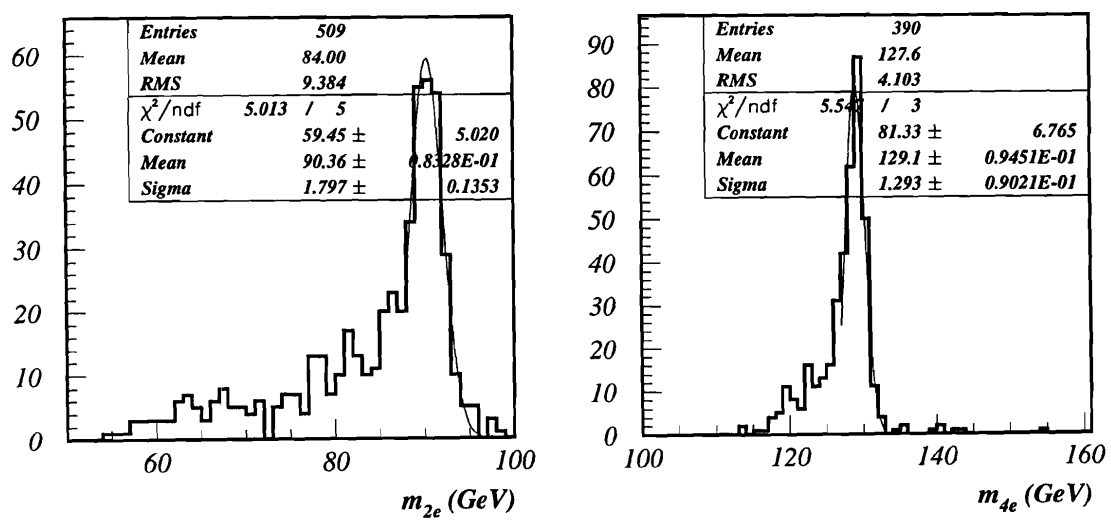

FIGURE 135. 2-electrons reconstructed invariant mass closes to the nominal Z boson mass (left) and 4-electrons reconstructed invariant mass (right), for 130 GeV Higgs mass.

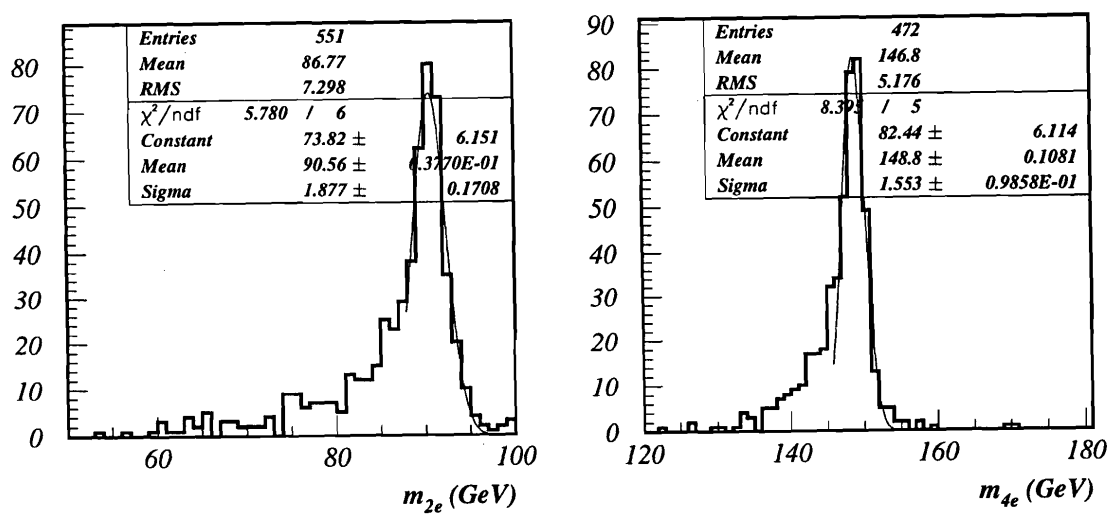

FIGURE 136. 2-electrons reconstructed invariant mass closes to the nominal Z boson mass (left) and 4-electrons reconstructed invariant mass (right), for 150 GeV Higgs mass.

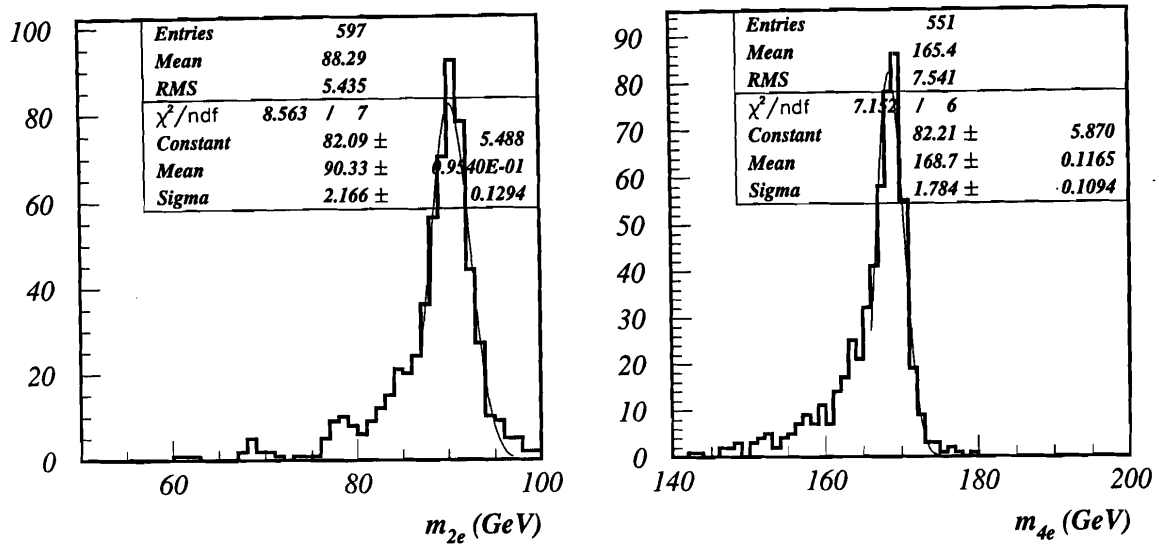

FIGURE 137. 2-electrons reconstructed invariant mass closes to the nominal Z boson mass (left) and 4-electrons reconstructed invariant mass (right), for 170 GeV Higgs mass.

	m_H = 130 GeV		m_H = 150 GeV		m_H = 170 GeV	
	full reconst.	particle level	**full reconst.**	particle level	**full reconst.**	particle level
$e^{\pm}$ reconstruction acc.	**0.64**	1.00	**0.65**	1.00	**0.67**	1.00
p_T $e^{\pm}$ cuts	**0.89**	0.96	**0.91**	0.99	**0.94**	1.00
Z* mass cuts	**0.90**	0.90	**0.94**	0.95	**0.95**	0.96
Z mass cut	**0.77**	0.82	**0.86**	0.90	**0.92**	0.94
σ_{m_H} (GeV)	**1.29**	0.66	**1.58**	0.72	**1.78**	0.87
2σ efficiency	**0.68**	0.81	**0.67**	0.80	**0.67**	0.74
3σ efficiency	**0.77**	0.87	**0.77**	0.85	**0.76**	0.81
total acceptance	**0.26**	0.56	**0.31**	0.68	**0.37**	0.67

TABLE 10. Summary of the results on the Higgs reconstruction using the detailed detector simulation and from the particle level analysis. For the total acceptance calculation the 2σ efficiency is taken.

Studies of the Higgs reconstruction through the $H \rightarrow ZZ^* \rightarrow 4e^{\pm}$ channel have been already performed in the CMS collaboration. The early study of the detector induced effects, described in reference [82], used a detector description which was actual on that time. It had a tracker material budget of about 0.2 X_0 in the central region $|\eta| < 1$, increasing to about 0.4 X_0 around $\eta = 1.6$, which is about 50% less than in the tracker design used in our study. The second major difference concerns the energy resolution of $5\%/\sqrt{E} + 0.5\%$ with a noise of 50

MeV per crystal, which is about twice the value for the resolution we have used in the ECAL barrel. The main results obtained with this study are Higgs mass resolutions of 1.5, 1.7 and 2.4 GeV and Z mass resolutions of 2.1, 2.1 and 2.2 GeV for Higgs of 130, 150 and 170 GeV respectively. Comparing these values with those in table 10, we conclude that the improvement in the reconstructed Higgs mass resolution expected from a better electron energy resolution, are compromized by a significant increase of the tracker material budget. By looking at the distributions we found that the sophisticated electron recontruction algorithms employed in our analysis significantly improve the signal acceptance.

To conclude this section with the signal visibility we will include the endcap part of the detector by using the assumptions that the overall electron finding efficiency remains at the same level, i.e. about 66% and that the Higgs mass resolution increases for about 15%, with the $\pm 2\sigma_{m_H}$ efficiency remaining the same. These assumption are based on combining our reconstruction results with the particle level analysis.

For the ZZ* background we use acceptances results obtained also with full detector simulations: 0.63 for the initial electron reconstruction efficiency, 0.85 for electrons p_T cuts, 0.78 for the Z* mass constraint and 0.89 for the Z mass constraint. For the $t\bar{t}$ and $Zb\bar{b}$ backgrounds, as for the Higgs masses other than 130, 150 and 170 GeV, the full reconstruction results have been combined with the particle level analysis results.

The final number of signal and background events expected in the $H \rightarrow ZZ^* \rightarrow 4e^{\pm}$ channel are given in figure 138 for one year of LHC running at high luminosity. As we can see from figure one could expect about 15, 30 and 10 signal events for 130, 150 and 170 GeV respectively, while the total number of bacground events remains below 8.

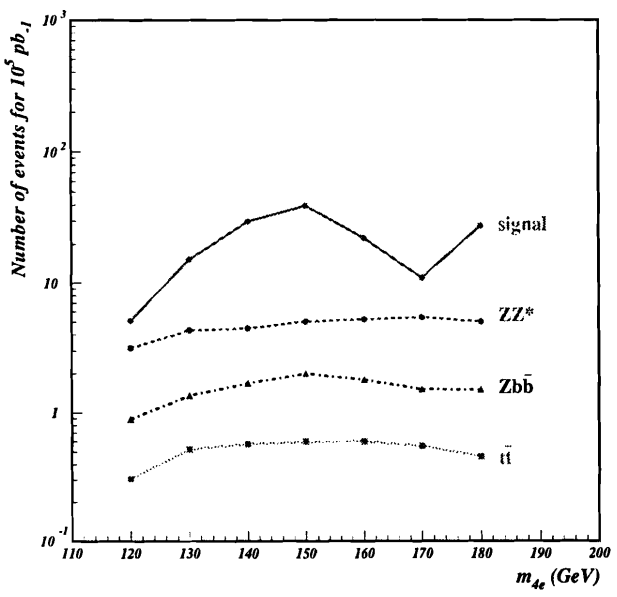

FIGURE 138. Number of expected signal and background events in the mass window $m_H \pm 2\sigma_{m_H}$ after one year of LHC running at high luminosity. The numbers are obtained combining the full detector simulation and results from the particle level analysis.

The statistical significance of the signal is shown in figure 139. Comparing these results with those obtained after the particle level analysis only (figure 87) one can notice an important reduction of the signal significance, when considering the detector effects. This reduction is a consequence of a rather low electron finding efficiency (about 0.9 per electron), and about two times larger Higgs mass resolution. Further optimization of the tracker electron finding algorithms is expected to improve this efficiency. For an electron finding efficiency of 0.95 the signal significance would increase by about 11%. Another possible improvement could be expected from developing an internal bremsstrahlung recovery algorithm, as it was proposed in reference [87]. A precise evaluation of such algorithm request more detailed study including the pile-up effects.

In conclusion, we have found that the Higgs boson can be discovered through the $H \rightarrow ZZ^* \rightarrow 4e^{\pm}$ decay channel for one year of the LHC running at high luminosity if its mass is in the region between 127 GeV and 168 GeV, and above 172 GeV to the kinematically allowed limit $2m_Z$. In the vicinity of 150 GeV the Higgs could be found after the first year of LHC running at low luminosity.

By combining this channel with the Z muonic decay, the signal and background number of events would increase by about factor 4, while the signal significance would increase by a factor 2. It means that the Higgs boson could be discovered through the $H \rightarrow ZZ^* \rightarrow 4l^{\pm}$ ($l = e, \mu$) channel from about 120 GeV all the way up to $2m_Z$, for the integrated luminosity of 10^5 pb^{-1}.

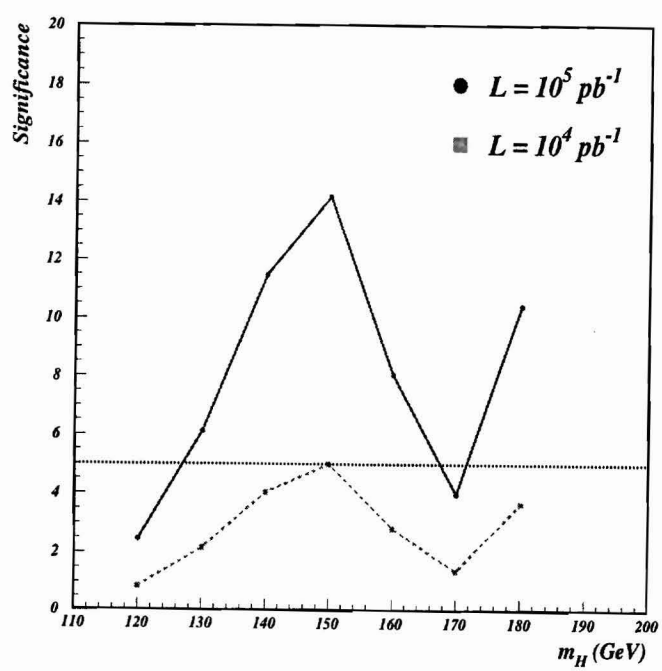

FIGURE 139. The signal significance for the Higgs search through the $H \rightarrow ZZ^* \rightarrow 4e^{\pm}$ channel, for one year of LHC running at high and low luminosity. The results are obtained combining the full detector simulation with the particle level analysis.

Conclusion

The work presented in this thesis consists of the study of the CMS potential for the Higgs search through the $H \rightarrow ZZ^* \rightarrow 4e^{\pm}$ channel. To make this search possible it is necessary to have a high performance electromagnetic calorimeter. Our contribution to the construction of the electromagnetic calorimeter was in developing the alveolar structures production quality control process. To estimate the potential for Higgs discovery through $H \rightarrow ZZ^* \rightarrow 4e^{\pm}$ decay channel, a particle level analysis, followed by a detailed reconstruction study have been performed.

After several years of research and developments, the CMS electromagnetic calorimeter has entered into a mass production phase for most of its components. The alveolar containers, designed to hold the crystals, have been developed in the laboratory and their production was entirely given to a factory. The two most important design characteristics of the alveolar containers are the precise mechanical structure and the optical quality of the inner reflective material. In order to assure these properties to be at the level requested by the physics we have developed a quality control procedure consisting of the production process monitoring, precise geometrical and detailed optical measurements. For the optical control we have developed an instrument allowing to measure the reflexivity and the diffusivity of the alveolar container inner material, a specially developed aluminum foil. The optical control procedure consists of measuring the aluminum sample before production and the alveolar structure after the full production process. The most important criteria requests the reflexivity of the alveolar container inner material to be bigger than 85% of the raw material reflexivity. The proposed procedure has been tested on the alveolar containers made in the preproduction phase in the laboratory. It has confirmed that all the alveolar containers produced conform to the established criteria. The entire quality control process has been transmitted to the producer and is currently in use.

Although the Higgs mass is a free parameter in the Standard Model and therefore can not be predicted, theoretical arguments and experimental data from the electroweak precision measurements tend to prefer an intermediate mass Higgs boson. In the mass range from about 120 GeV to $2m_Z$ one of the main Higgs search channel is $H \rightarrow ZZ^* \rightarrow 4l^{\pm}$, where the leptons are electrons or muons. In this thesis we have studied the channel with the four electrons final state. The signal cross section and branching ratios have been calculated with the programs implementing the most recent theoretical calculations, including the QCD and QED next-to-leading order corrections. The final state particles have been generated using the PYTHIA Monte Carlo program, with the cross section calculated at the leading order. The normalization of the Monte Carlo obtained cross section to the one calculated with more rigorous theoretical models requires an agreement between the kinematical variables. We have studied the distribution of the Higgs transverse momentum comparing the predictions from two models: one based on the parton shower formalism implemented in the Monte Carlo particle genera-

tors and the other based on the soft gluon resummation. We conclude that both methods agree in the region of small and intermediate p_T, which dominates the total distribution. In the high p_T region, the resummation calculation matches the exact matrix elements, while the parton shower moedl can be either adjusted by allowing more parton shower activity or the merging with exact matrix elements calculations should be implemented. Another important aspect in the $H \rightarrow ZZ^* \rightarrow 4e^{\pm}$ channel study was the evaluation of the $Zb\bar{b}$ background. For the cross sections calculations and the event generation the CompHEP Monte Carlo program has been used, which treats correctly the phase space generation in this process. We have studied both the gluon fusion and the quark annihilation production processes and found that later contributes to about 16% of the total cross section. From the about 20% variation of the leading order cross section with changes of the QCD scale, the size of the higher orders corrections have been estimated as important. For the other two background processes, $t\bar{t}$ and ZZ^*, the recent theoretical calculation have been reviewed and accordingly the Monte Carlo generator cross sections have been normalized. We have then studied the optimization of the analysis cuts. The cuts on the p_T of the first two electrons have been chosen as 20 GeV and 15 GeV in order to obtain more than 99% signal acceptance. Because of the very small total number of events in this channel, particularly at the lower reachable masses, we conclude that p_T cuts as low as 10 GeV and 7 GeV on third and fourth electrons respectively, are optimal. The irreducible backgrounds, $t\bar{t}$ and $Zb\bar{b}$ can be effectively suppressed by the isolation cut, requiring the absence of the charged tracks with $p_T > 2.5$ GeV in a cone $R = 0.2$ around all four electrons.

The results of the particle level analysis of the $H \rightarrow ZZ^* \rightarrow 4e^{\pm}$ channel leads to very stringent requirements on the electron reconstruction. The signal significance is roughly proportional to the electron reconstruction efficiency squared and inversely proportional to the squared root of the reconstruction Higgs mass width. In addition, the small number of expected signal events, the low transverse momentum of two lightest electrons and the detector resolution dominance in the reconstructed Higgs width require to have good electron reconstruction efficiency and precision. This has been studied using a detailed detector description. For the tracks reconstruction, the kalman filter based track finding algorithm has been used. For the clusters reconstruction in the electromagnetic calorimeter, a dynamical clustering algorithm has been used, specially developed follow the event by event fluctuations of the particle impact point and direction. The biggest problem in the electron reconstruction in the CMS comes from the bremsstrahlung in the tracker material. In this work we have studied a bremsstrahlung photon recovery algorithm. The photons clusters are searched for in a region determined from the measured electron transverse energy and then associated to the electron cluster. The intrinsic properties of this method, when using the Monte Carlo informations for the electron track identification, shows about 30% better reconstruction efficiency for 10 GeV p_T electrons, with respect to the electron cluster only. For 30 GeV p_T electrons the gain with the recovery method is about 15%. The recovery algorithm is also used to improve the electron identification efficiency. Instead of using a single cluster barycenter to match with the extrapolated track, the set of all possible electron-photons cluster combinations is firstly determined, and their barycenter matched with the electron track. This algorithm gives about 10% better efficiency for 10 GeV p_T electrons and about 5% for 30 GeV p_T electrons. Furthermore, we have studied an optimization of the electron momentum estimator. Using expectations of the electron energy deposit pattern in the electromagnetic calorimeter the energy resolution can be improved by more than 15% for 10 GeV p_T electrons, for about 50% of events. The improvement increases with increasing the noise value per channel as well as with increasing the electron transverse momentum. For the final electron momentum estimation we

have combined the momentum estimator from the tracker and the ECAL energy estimator. Significant improvements in the efficiency have been obtained, with the resolution given by the tracker resolution at the smaller energies and by the ECAL resolution at the higher energies. The developed algorithms have been applied to the $H \rightarrow ZZ^* \rightarrow 4e^{\pm}$ events reconstruction. The obtained results for the reconstructed Higgs mass width are 1.3 GeV, 1.6 GeV and 1.8 GeV for 130 GeV, 150 GeV and 170 GeV Higgs masses respectively, with the $m_H \pm 2\sigma_{m_H}$ efficiency of 67%. Combining the reconstruction results with those from the particle level analysis, we conclude that the Higgs boson could be found through the $H \rightarrow ZZ^* \rightarrow 4e^{\pm}$ in the mass range from 127 GeV to 168 GeV and from 172 GeV to $2m_Z$, for one year of LHC running at nominal luminosity. In the vicinity of 150 GeV the Higgs could be found through this channel after the first year of LHC running at low luminosity.

Bibliography

[1] F. Abe et al, The CDF Collaboration, *Phys. Rev. Lett.* **74**, 2626 (1995);
S. Abachi et al, The D0 Collaboration, *Phys. Rev. Lett.* **74**, 2632 (1995).

[2] R. D. Field, *"Perturbative QCD"*, Addison-Wesley, Redwood City, 1989;
Yu. L. Dokshitzer and al, *"Basic of Perturbative QCD"*, Ed. Frontieres, Gif-sur-Yvette, 1991;
F. J. Yndurain, *" The Theory of Quark and Gluon Interactions"*, Springer-Verlag, Berlin, 1993.

[3] S. Weinberg, *Phys. Rev. Lett.* **19**, 1264 (1967);
A. Salam, in *"Elementary Particle Theory"*, W. Svartholm, ed., Almquiest and Wiksell, Stockholm (1968);
S.L. Glashow, J. Iliopoulos and L. Maiani, *Phys. Rev.* **D2**, 1285 (1970).

[4] B. W. Lee, *"Chiral Dynamics"*, Gordon and Breach, New York, 1972;
S. Coleman, *"Aspects of Symmetry"*, Cambridge Univ. Press, Cambridge, 1985.

[5] G. 't Hooft and M. Veltman, *Nucl. Phys.* **B50**, 318 (1972), and references therein.

[6] P. Higgs, *Phys. Lett.* **12** (1964) 132.

[7] A. Linde, *JETP Lett.* **23** (1976) 64; *Phys. Lett.* **B62** (1976) 435;
S. Weinberg, *Phys. Rev. Lett* **36** (1976) 294;
S. Coleman and E. Weinberg, *Phys. Rev.* **D7** (1973) 188.

[8] S. Dawson, *"The Standard Model intermediate mass Higgs boson"*, in the Perspectives on Higgs Physics II, ed. Gordon L. Kane, World Scientific, 1997.

[9] G. Altarelli and G. Isidori, *Phys. Lett.* **B337** (1994);
J. A. Casas, J. R. Espinosa and M. Quirós, *Phys. Lett.* **B342** (1995) 171; **B382** (1996) 374;
T. Hambye and K. Riesselmann, *Phys. Rev.* **D55** (1997) 7255.

[10] A. Gurtu, *"Precision tests of the electroweak gauge theory"*, talk presented at the XXXth International Conference on Higs Energy Physics, Osaka, Japan, July 27 - August 2, 2000;

[11] C. Tully, *"Status of LEP-wide Higgs searches"*, talk presented at LEPC Seminar, CERN, Geneva, September 5, 2000

[12] *"Report of the Higgs working group"*, in Physics at Run II, Supersymmetry/Higgs Workshop, Version 6, June, 2000, http://fnth37.fnal.gov/higgs.html

[13] K. Wilson, as quoted by L. Susskind, *Phys. Rev.* **D20** (1979) 2619;
G. 't Hooft, in Recent Developments in Gauge Theories, ed. by G. 't Hooft et al. (Plenum Press, 1980)

[14] J. R. Espinosa and M. Quirós, *Phys. Rev. Lett.* **81** (1998);
J. R. Espinosa and M. Quirós, *"What is the upper limit on the lightest supersymmetric*

Higgs mass?", work presented at the Sixth International Symposium on Particles, Strings and Cosmology, Northeastern University, Boston, USA, March 22-29 1998.

[15] J. F. Gunion, A. Stange and S. Willenbrock: *"Weakly-coupled Higgs boson"*, UCD-95-28, ILL-(TH)-95-28, hep-ph/9602238

[16] H. Georgi, S. Glashow, M. Machacek and D. V. Nanopoulos, *Phys. Rev. Lett.* **40** (1978) 692.

[17] M. Spira, A. Djouadi, D. Graudenz and P. M. Zerwas, *Nucl. Phys.* **B453** (1995) 17.
A. Djouadi, M. Spira and P. M. Zerwas, *Phys. Lett.* **B264** (1991) 440
D. Graudenz, M. Spira and P. M. Zerwas, *Phys. Rev. Lett.* **70** (1993) 1372.

[18] M. Spira, *"QCD Effects in Higgs Physics"*, hep-ph/9705337

[19] R. N. Cahn and S. Dawson, *Phys. Lett.* **B136** (1984) 196
K. Hikasa, *Phys. Lett.* **B164** (1985) 341;
G. Altarelli, B. Mele and F. Pitolli, *Nucl. Phys.* **B287** (1987) 205;

[20] T. Han, G. Valencia and S. Willenbrock, *Phys. Rev. Lett.* **69** (1992) 3274.

[21] D. Rainwater and D. Zeppenfeld, JHEP **9712**:005, 1997
D. Rainwater, D. Zeppenfeld and K. Hagiwara, Phys. Rev. **D59**:014037, 1999

[22] S. L. Glashow, D. V. Nanopoulos and A. Yildiz, Phys. Rev. **D18** (1978) 1724;
Z. Kunzst, Z. Trocsanyi and W. J. Striling, Phys. Lett. **B271** (1991) 247.

[23] T. Han and S. Willenbrock, *Phys. Lett.* **71** (1993) 2699.

[24] Z. Kunszt, *Nucl. Phys.* **B247** (1984) 339;
J.F. Gunion, *Phys. Lett.* **B253** (1991) 269
W.J. Marciano and F.E. Paige, *Phys. Rev. Lett.* **66** (1991) 2433.

[25] Z. Kunszt, S. Morreti and W. J. Stirling, Z. Phys. **C74** (1997) 479.

[26] D. Zeppenfeld, R. Kinnunen, A. Nikitenko and E. Richter-Was, *Phys.Rev.* **D62** (2000) 013009

[27] J. Ellis, M. K. Gaillard and D. V. Nanopoulos, *Nucl. Phys.* **B106** (1976) 292.
L. Resnick, M. K. Sundaresan and P. J. S. Watson, Phys. Rev. **D8** (1973) 172.

[28] E. Braaten and J. Leveille, *Phys. Rev.* **D22** (1980) 715;
N. Sakai, *Phys. Rev.* **D22** (1980) 2220;
T. Inami and T. Kubota, *Nucl. Phys.* **B179** (1981) 171;
S. G. Gorishny, A. L. Kataev and S. A. Larin, *Sov. J. Nucl. Phys.* **40** (1984) 329;
M. Drees and K. Hikasa, *Phys. Rev.* **D41** (1990) 1547; *Phys. Lett.* **B240** (1990) 455. and (E) **B262** (1991) 497.

[29] A. Djouadi, M. Spira and P. Zerwas, *Z. Phys.* **C70** (1996) 427

[30] B. A. Kniehl, *Phys.Rep.* **240** (1994) 211.

[31] B. W. Lee, C. Quigg and H. B. Thacker, Phys. Rev. **D16** (1977) 1519.

[32] T. G. Rizzo, *Phys. Rev.* **D22** (1980) 389;
W. Y. Keung and W. J. Marciano, *Phys. Rev.* **D30** (1984) 248.

[33] R. N. Cahn, Rep. Prog. Phys. **52** (1989) 389.

[34] A. Djouadi, J. Kalinowski and M. Spira, *"HDECAY: a Program for Higgs Boson Decays in the Standard Model and its Supersymmetric Extension"*, *Comput. Phys. Commun.* **108**

(1998) 56. The HDECAY program is available to the public from http://home.cern.ch/~mspira/proglist.html

[35] D. Denegri, *"Standard Model phycis at the LHC (pp collisions)"*, in Proceedings of the Large Hadron Collider Workshop, Vol. I (1990) 55, CERN 90-10

[36] The LHC Study Group, *"The Large Hadron Collider Conceptual Design."* CERN/AC/95-05

[37] UA4/2 Collaboration, *Phys.Lett.* **B315** (1993), 503

[38] CMS Technical Proposal, CERN LHCC/94-38

[39] ATLAS Technical Proposal CERN LHCC/94-43

[40] LHCb Technical Proposal, CERN LHCC/98-4

[41] ALICE Technical Proposal, CERN LHCC/95-71

[42] CMS Collaboration, *"The Tracker Project. Technical Design Report"*, CERN/LHCC 98-6;

[43] CMS Collaboration, *"Addenum to the CMS Tracker TDR"*, CERN/LHCC 2000-016

[44] CMS Collaboration, *"The Electromagnetic Calorimeter. Technical Design Report"*, CERN/LHCC 97-33.

[45] G. Aleexev et al, *Nucl. Instr. Meth.* **A358** (1997) 425-434.
E. Auffray et al, *Nucl. Instr. Meth.* **A412** (1998) 223-237.

[46] R. Depasse t al, *"Analysis from August 1999 beam tests of a PbWO4 Crystal matrix"*, CMS Note 2000/009

[47] CMS Collaboration, *"The Hadron Calorimeter Project. Technical Design Report"*, CERN/LHCC 97-31

[48] CMS Collaboation, *"The Muon Project. Tecnical Design Report"*, CERN/LHCC 97-32

[49] W. Badgett t al, *"CMS Calorimeter Level 1 Regional Trigger Electron Identification"*, CMS Note 1999/026

[50] A. Givernaud, M. Lebeau and J.-P. Vialle, *"Barrel ECAL simulation and optimisation in CMS"*, CMS TN 1995/151

[51] D. J. Graham and C. Seez, *"Simulation of Longitudinal Light Collection Uniformity in $PbWO_4$ Crystals"*, CMS Note 1996/002

[52] F. Gautheron, *"Etudes de cristaux scintillants de tungstate de plomb and de prototypes de calorimètre électromagnétique pour le projet CMS au LHC"*, thèse de l'Université Claude Bernard, Lyon I, 1997.

[53] P. Baillon and M. Montecchi, private communications

[54] J.-M. Le Goff et al, *"C.R.I.S.T.A.L., A data capture and production management tool for the assembly and construction of the CMS ECAL detector"*, CMS Note 1996/003
J.-M. Le Goff et al, *"From Desing to Production Control Through the Integration of Engineering Data Management and Workflow Management Systems"*, CMS Note 1997/104.
J.-M. Le Goff et al, *"Detector Construction Management and Quality Control: Establishing and Using a CRISTAL System"*, CMS Note 1998/033.

[55] R. P. Kauffman, *Phys. Rev.* **D44** (1991) 1415.

[56] J. C. Collins, D. E. Soper and G. Sterman, *Nucl. Phys.* **B261** (1985) 104;
G.T. Bodwin, *Phys. Rev.* **D31** (1985) 2616, E. **D34** (1986) 3932;
J. C. Collins, D. E. Soper and G. Sterman, *Nucl. Phys.* **B308** (1988) 833;
J. C. Collins, D. E. Soper and G. Sterman, in "*Perturbative QCD*", ed. A. H. Müller (World Sientific, Singapore, 1989).

[57] G. Miu and T. Sjöstrand, *Phys. Lett.* **B349**, 313 (1999).

[58] By C. Balázs and C.P. Yuan, *Phys.Rev.* **D56** (1997) 5558-5583.

[59] C. Balázs, J. Huston and I. Puljak, *"Higgs Production: A Comparison of Parton Showers and Resummation"* hep-ph/0002032

[60] H. L. Lai et al, *Phys. Rev.* **D55**, 1280 (1997).

[61] T. Sjöstrand, *Computer Phys. Commun.* **82**, 74 (1994).

[62] T. Sjöstrand, PYTHIA manual update for version 6.1, http://www.thep.lu.se/~torbjorn/Pythia.html

[63] G. Marchesini, B. R. Webber, G. Abbiendi, I. G. Knowles, M. H. Seymour and L. Stanco, *Computer. Phys. Commun.* **67**, 465 (1992).

[64] G. Corcella and M. H. Seymour, RAL-TR-1999-051, hep-ph/9908388.

[65] E. Barberio and Z. Was, *Comput. Phys. Commun.* **79** (1994) 291-308.

[66] The programs HIGLU, VV2H, V2HV, HQQ, written by M. Spira, are accesible at http://home.cern.ch/~mspiraproglist.html

[67] C. Caso et al, PDG, *Eur. Phys. Jour.* **C3, 1-4** (1998), 1-794.

[68] J. Ohnemus and J. F. Owens, *Phys. Rev.* **D43,** (1991), 3262.

[69] J. M. Campbell and R. K. Ellis, *Phys. Rev.* **D60** (1999), 113006.

[70] C. Balázs and C.-P. Yuan, hep-ph/9810319, FERMILAB-PUB-98/202-T

[71] T. Han, R. Meng and J. Ohnemus, *Nucl. Phys.* **B384** (1992) 59-77.
D. Zürcher in 1999 CERN Workshop on SM Physics at LHC, CERN, 1999

[72] E. W. N. Glover and J. J. van der Bij, *Nucl. Phys.* **B321** (1989) 561 and *Phys. Lett.* **B219** (1989) 488.

[73] P. Nason, S. Dawson and R. K. Ellis, *Nucl. Phys.* **B303** (1988) 607;
W. Beenakker et al, *Phys. Rev.* **D40** (1989) 54;
P. Nason, S. Dawson and R. K. Ellis, *Nucl. Phys.* **B327** (1989) 49; (E) *ibid.* **B335** (1990) 260;
W. Beenakker and al, *Nucl. Phys.* **B351** (1991) 507

[74] M. Dittmar and H. Dreiner, *" LHC Higgs Search with $l^+\nu l^-\bar{\nu}$ Final States"*, CMS Note 1997/083.

[75] M. Mangano in 1999 CERN Workshop on SM Physics at LHC, CERN, 1999

[76] B. van Eijk and R. Kleiss in Proceedings of the Large Hadron Collider Workshop, ed. G. Jarlskog and D. Rein, Aachen, 1990., CERN 90-10, vol II, page 183.

[77] M. Della Negra, and al, in Proceedings of the Large Hadron Collider Workshop, ed. G. Jarlskog and D. Rein, Aachen, 1990., CERN 90-10, vol II, page 510.

[78] A. Pukhov et al, *"CompHEP user's manual, v.3.3"*, Preprint INP MSU 98-41/542 and hep-ph/9908288

[79] C. Charlot et al, *"CMSIM - CMANA: CMS simulation facilities"*, CMS TN-1993/063; CMS detector simulation software group, *"CMS Simulation Package CMSIM. Users' Guide and Reference Manual"*, available at CMS internal web pages.

[80] *"GEANT - Detector description and simulation tool"*, CERN, Geneva, 1993.

[81] D. Stickland et al, *"Object Oriented Reconstruction for CMS Analysis"*, CMS IN/1999-001.

[82] I. Iashvili, R. Kinnenen, A. Nikitenko, *" Study of the $H \to ZZ^* \to 4l^{\pm}$ Channel Including radiation effects"*, CMS TN-1995/059;
D. Bomestar, A.Nikitenko, P.Verrecchia, *"1) $Z \to e^+e^-$ and $H \to 4e^{\pm}$ Mass Reconstruction in PbWO4 Crystal ECAL with GEANT Simulation of CMS detector. 2) Electrons of E_T = 30 GeV at η = 0.1 and 1.3 in CMS detector: E/p Matching Calibration, Resolution"* CMS TN-1995/019;
D. Bomestar, R. Kinnunen, D. Denegri, A. Nikitenko, *"Study of the $H \to ZZ \to 4l^{\pm}$ with a full GEANT simulation of CMS"*, CMS TN-1995/018;

[83] P. Busson, C. Charlot, *"A method for electron/photon reconstruction in CMS $PbWO_4$ crystal ECAL"*, CMS TN-1995-074.

[84] A.Givernaud, E.Locci, *"Study of the azimuthal cracks in the electromagnetic calorimeter: the photon case"*, CMS Note 1996/014;
V. Daponte, A. Givernaud, E. Locci, *"Study of the Polar Cracks in the Electromagnetic Calorimeter: the Photon Case"*, CMS Note 1997/087;
A.Givernaud, E.Locci, *"Study of the azimuthal cracks in the electromagnetic calorimeter: the electron and positron case"*, CMS Note 1998/032

[85] B. Rossi, *"High Energy Particle"*, Prentice-Hall, New York 1952.

[86] C. Charlot, *"Electromagnetic shower parametrisation in CMSIM"*, CMS-TN/94-312.

[87] C. Charlot and I. Puljak, *"External and final state internal bremsstrahlung effects and Higgs mass reconstruction in $H \to ZZ^* \to 4e^{\pm}$ for M_H = 130 GeV"*, CMS Note 1995/043

Abstract

The subject of this thesis is the study of CMS potential for the Higgs boson search through the $H \rightarrow ZZ^* \rightarrow 4e^{\pm}$ channel. The theoretical arguments and the experimental data from the electroweak precision measurements, combined with the direct search results, tend to prefer the intermediate mass Higgs boson where this channel is expected to be used for the Higgs boson search at the LHC. The short introduction to the Standard Model, emphasizing the Higgs sector is given and the main Higgs production processes at the LHC are reviewed, as well as the main decay channels.

After indicating an importance of the electromagnetic calorimeter in the electron reconstruction process, the mechanical structure and the optical properties of alveolar containers are described. The system for the quality control of the alveolar structures is developed, consisting of the production process monitoring system, the precise geometrical measurements and the optical quality control. For the optical quality control, the apparatus is constructed for measuring the reflexivity and the diffusivity of the raw material before the production and the alveolar structure after the complete production process. The developed quality control system ensures that the alveolar containers properties remain on the level not deteriorating the properties of the electromagnetic calorimeter.

The evaluation of the CMS potential for the Higgs search through its four electrons decay consists of the signal and background studies at the particle level and the reconstruction studies including the precise detector description. To combine the Monte Carlo generated events with the recent theoretical calculations, the distributions of the Higgs transverse momentum predicted by the parton shower model and the soft gluon resummation calculations are compared. The agreement is found for the low transverse momentum, while for the agreement at higher values the parton shower model can be adjusted. The evaluation of the $Zb\bar{b}$ background is done with properly modeling the phase space generation and the up to date theoretical results and Monte Carlo simulations are used for two other important backgrounds, ZZ^*/γ^* and $t\bar{t}$. The kinematical and topological cuts are studied and optimized in order to maximize the signal visibility.

The precise detector description is used for the $H \rightarrow ZZ^* \rightarrow 4e^{\pm}$ reconstruction in the CMS. The electron reconstruction algorithms are developed. The dynamical clustering algorithm is used for electromagnetic calorimeter clusters reconstruction, and the bremsstrahlung photons recovery method is implemented. The algorithm using the predicted energy deposit in the electromagnetic calorimeter is developed in order to improve the energy estimator precision and efficiency. The electron energy estimation from the electromagnetic calorimeter and the electron momentum estimation from the tracker detector are combined to construct the final electron momentum estimator. The developed electron reconstruction algorithms are applied to the $H \rightarrow ZZ^* \rightarrow 4e^{\pm}$ reconstruction, giving the Higgs mass resolution of 1.3, 1.6 and 1.8 GeV for 130, 150 and 170 GeV Higgs respectively. By combining the reconstruction results with those from the particle level analysis the signal significance is evaluated. The results show that the Higgs could be found through $H \rightarrow ZZ^* \rightarrow 4e^{\pm}$ channel in the region of about 127 GeV to 168 GeV and from 172 GeV to the kinematically allowed limit $2m_Z$, for one year of the LHC running at nominal luminosity. In the vicinity of 150 GeV the Higgs could be found through this channel after the first year of the LHC running at low luminosity.

Key words:
Higgs boson, LHC, CMS, electromagnetic calorimeter, alveolar container, Higgs transverse momentum, electron reconstruction, bremsstrahlung

Résumé

Le sujet de cette thèse est l'étude des possibilités de détection du boson de Higgs à CMS dans le canal $H \rightarrow ZZ^* \rightarrow 4e^{\pm}$. Des arguments théoriques ainsi que les données expérimentales provenant des mesures de précision dans le secteur électrofaible et les recherches directes favorisent un Higgs dans le domaine de masse intermédiaire, dans lequel ce canal sera utilisé pour la recherche du Higgs au LHC. Une brève introduction au modèle standard est donnée, avec une attention particulière au secteur de Higgs, et les principaux modes de production du Higgs au LHC sont rappelés.

Après avoir souligné l'importance du calorimètre électromagnétique pour la détection des électrons, sa structure mécanique et les propriétés optiques des structures alvéolaires sont décrites. Le système développé pour le contrôle de la qualité des alvéoles est présenté. Il consiste en un système de contrôle du processus de production, de mesures précises des caractéristiques géométriques et du contrôle de la qualité optique des structures. Pour ce dernier, un appareil a été construit pour mesurer la réflexivité et la diffusivité du matériau constituant les alvéoles, avant et après le processus complet de fabrication. Le système de contrôle-qualité développé permet de s'assurer que les propriétés des structures produites restent compatibles avec les spécifications permettant de conserver les performances du calorimètre électromagnétique au niveau requis pour la physique.

L'évaluation du potentiel de CMS pour la recherche du Higgs dans le canal de désintégration en quatre électrons consiste en une étude du signal et des bruits de fond au niveau générateur et en une étude de reconstruction incluant une description précise du détecteur. De façon à pouvoir combiner les évènements simulés à l'aide des programmes Monte Carlo avec les calculs théoriques récents, les distributions du moment transverse du Higgs obtenus par le modèle des gerbes de partons et le calculs de resommation des gluons mous sont comparés. Un bon accord est trouvé à petit moment transverse, alors qu'à plus haut moment transverse le modèle de gerbes de partons doit être ajusté. L'évaluation du bruit de fond $Zb\bar{b}$ est effectuée en utilisant une modélisation correcte de l'espace de phase et les résultats théoriques les plus récents, des simulations Monte Carlo étant utilisées pour les deux autres bruits de fond importants, ZZ^*/γ^* et $t\bar{t}$. Des coupures cinématiques et topologiques sont étudiées en vue de maximiser la visibilité du signal.

La description précise du détecteur est ensuite utilisée pour l'étude de la reconstruction du $H \rightarrow ZZ^* \rightarrow 4e^{\pm}$ dans CMS. Les algorithmes spécialement développés pour la reconstruction des électrons sont décrits. Un algorithme dynamique est utilisé pour la reconstruction des clusters électromagnétiques et une méthode pour la récupération des pertes dues au bremsstrahlung est mise en oeuvre. Enfin, un algorithme utilisant les valeurs attendues pour les signaux dans le calorimètre électromagnétique et développé en vue d'améliorer l'estimation de l'énergie des électrons est présenté. Cette estimation est ensuite combinée avec l'estimation fournie par le trajectomètre interne. Ces algorithmes de reconstruction sont finalement appliqués à la reconstruction du $H \rightarrow ZZ^* \rightarrow 4e^{\pm}$, et des résolutions de 1.3, 1.6 et 1.8 GeV sont obtenues pour des masses de Higgs de 130, 150 et 170 GeV respectivement. En combinant les résultats de reconstruction avec ceux de l'analyse au niveau générateur, la significance du signal est évaluée. Ces résultats montrent que le Higgs pourra être trouvé dans ce canal si sa masse est comprise entre 127 GeV et 168 GeV ou entre 172 GeV et la limite cinématique correspondant à $2m_Z$, après un an de prise de données à la luminosité nominale du LHC. Au voisinage de 150 GeV, le Higgs pourrait être trouvé dans ce canal dés la première année de fonctionnement du LHC à basse luminosité.

Mots clés:
boson de Higgs, LHC, CMS, calorimètre électromagnétique, structures alvéolaires, moment transverse du Higgs, reconstruction des électrons, bremsstrahlung